Elucidating the Structures of Cationic Metal-Nitrous Oxide Complexes using Infrared Action Spectroscopy

Ethan M. Cunningham

Magdalen College



A thesis submitted for the degree of

Doctor of Philosophy

Physical & Theoretical Chemistry Laboratory

University of Oxford

Trinity Term 2019

Elucidating the Structures of Cationic Metal-Nitrous Oxide Complexes using Infrared Action Spectroscopy

Ethan M. Cunningham, Magdalen College

A thesis submitted for the degree of Doctor of Philosophy

Trinity Term 2019

Abstract

Gas-phase metal ion-molecule complexes provide model environments within which to study fundamental molecular interactions involved in ligand activation and metal ion solvation. These complexes also represent entrance-channel species for catalytic reactions. The ligand of interest in this thesis is nitrous oxide, which accounts for 5% of anthropogenic emissions and is a potent greenhouse gas with a warming potential 300 times greater than carbon dioxide. Thus, there is considerable interest in reducing N_2O emissions particularly *via* metal-catalysed N_2O reduction. $M^{+/0/-}(N_2O)_n$ complexes represent entrance-channel species for such reactions and yet, little attention has been given to the structures of $M^{+/0/-}(N_2O)_n$ complexes. This thesis presents the first experimental investigation on $M^+(N_2O)_n$ and $M_n^+(N_2O)$ complexes studied *via* infrared action spectroscopy. The infrared spectra are further interpreted and assigned from simulated spectra based on density functional theory (DFT). A range of $M^+(N_2O)_n$ complexes (M = group 11, group 9, and Li, Al) have been studied in an attempt to draw comparisons between the different M^+ electron configurations (d^{10}, d^8, and closed s-shell, respectively). Spectroscopic signatures for N- and O-bound N_2O ligands are observed in all cases however the importance of low-lying electronic states is revealed for the group 9 cations, and insertion complexes inferred for the Li^+ ion.

Infrared multi-photon dissociation (IRMPD) studies on $M_n^+(N_2O)$ complexes (M = Au, Co) also present N- and O-bound spectroscopic signatures. However, as the metal cluster size increases, N_2O binds preferentially *via* the terminal N-atom. Larger clusters represent a more effective energy "bath" facilitating annealing to the lowest energy structure.

Acknowledgements

My time at Oxford has been an enjoyable one, and I wish to thank all my friends for making it such an unique experience. Firstly, I wish to thank my supervisor Professor Stuart Mackenzie for his invaluable advice and guidance throughout all stages of my DPhil. I will forever be grateful for his supervision and, in particular, his teachings on effective communication in science.

Particular thanks goes to Dr Alexander Gentleman for all of his help in the laboratory, on the computational simulations, and for his continuous help in publications and this very thesis. He truly is a thoroughly good egg. I wish to thank (soon to be) Dr Hansjochen Köckert for being with me every step of the way in the DPhil. Our contemplative walks kept me sane during the later stages (in addition to the early and middle stages). I have had the pleasure to work with the following members of the Mackenzie group: Alice Green, to whom special thanks goes for i) all the enthusiasm in the laboratory (both in Oxford and Berlin) and ii) very kindly reading thesis chapters, your keen eye and diligence have very much strengthened the thesis presented here. Dr Andreas Iskra, your friendly demeanour was a leading cause for me to apply for this research group and this institution in particular. Dr Dean Sheppard and (soon to be) Dr Katie Buckton, I wish to extend special thanks as, without whom, my experience in the group would not be the same. Fellow summer and Part II students Peter Beardsmore and Jess Walton, your inquisitive minds kept for an intellectually stimulating environment both in and outside of the laboratory, in addition to being great friends. New to the Mackenzie (P. Hore) group, Dr Shane Chandler, for all your help using LateX, without which this thesis would not have been produced. Indeed, I wish to thank all the members of the Mackenzie group as, for the most part, it's the interactions

with people that make for a congenial and productive environment.

I am grateful to Dr André Fielicke for his help and supervision on the experimental runs at the free electron laser facility in the Fritz-Haber Institute, Berlin.

The friends I have made at Magdalen College and other Oxford Colleges, my sincerest thanks for making my four years here memorable.

I am grateful to my previous mentor, Professor Andy Ellis, for introducing me to molecular spectroscopy and for his continued inspiration, and in particular for encouraging me to undertake a DPhil.

To my family, friends and parents, for whom I would not be where I am now and almost certainly would not have been able to complete the doctorate without your continued help and support.

Lastly, I would like to thank the EPSRC and Magdalen College for their financial support.

List of Publications

Publications arising from this work:

[1] Cunningham, E. M.; Gentleman, A. S.; Beardsmore, P. W.; Iskra, A.; Mackenzie, S. R., Infrared Signature of Structural Isomers of Gas–Phase $M^+(N_2O)_n$ (M = Cu, Ag, Au) Ion-Molecule Complexes, *J. Phys. Chem. A*, **2017**, 121, 7565-7571

[2] Cunningham, E. M.; Gentleman, A. S.; Beardsmore, P. W.; Mackenzie, S. R., Structural Isomers and Low-Lying Electronic States of Gas-Phase $M^+(N_2O)_n$ (M = Co, Rh, Ir) Ion-Molecule Complexes, *Phys. Chem. Chem. Phys.*, **2019**, 21, 13959-13967

[3] Cunningham, E. M.; Gentleman, A. S.; Beardsmore, P. W.; Mackenzie, S. R., Infrared Spectroscopy of Closed s-shell Gas-Phase $M^+(N_2O)_n$ (M = Li, Al) Ion-Molecule Complexes, *Mol. Phys.*, **2019** DOI: 10.1080/00268976.2019.1595202

Other publications:

[4] Gentleman, A. S.; Green, A. E.; Price, D. R.; Cunningham, E. M.; Iskra, A.; Mackenzie, S. R., Infrared Spectroscopy of $Au^+(CH_4)_n$ Complexes and Vibrationally-Enhanced C-H Activation Reactions, *Top. Catal.*, **2018**, 61, 81-91

[5] Iskra, A.; Gentleman, A. S.; Cunningham, E. M.; Mackenzie, S. R., Carbon Dioxide Binding to Metal Oxides: Infrared Spectroscopy of $NbO_2^+(CO_2)_n$ and $TaO_2^+(CO_2)_n$ Complexes, *Int. J. Mass. Spec.*, **2019**, 435, 93-100

Contents

1 Introduction **1**

1.1 Catalysis 1

1.2 Clusters 4

1.2.1 Cluster Sources 5

1.3 Probing the Structure of Metal Clusters 7

1.3.1 Ion Mobility 8

1.3.2 Trapped Ion Electron Diffraction 9

1.3.3 Vibrational Action Spectroscopy 9

1.4 Metal Ion-Molecule Complexes 12

1.5 Motivation to Study N_2O 14

1.6 Thesis Overview 17

2 Experimental and Theoretical Methodology **19**

2.1 Vibrational Energy Levels 19

2.2 Infrared Absorption 23

2.3 Cluster Source 24

2.4 Time-of-Flight Mass Spectrometry 24

2.5 IRPD Spectroscopy 26

2.6 IRMPD Spectroscopy 28
2.7 Computational Methods 30
2.7.1 Electronic Structure 30
2.7.2 Density Functional Theory 32
2.7.3 Computational Methodology 36

3 Infrared Signature of Structural Isomers of Gas-Phase $M^+(N_2O)_n$ (M = Cu, Ag, Au) Ion-Molecule Complexes **39**

3.1 Introduction 40
3.2 Experimental Methods 43
3.3 $M^+(N_2O)_n$-Ar Time-of-Flight Spectra 44
3.4 IRPD Spectra of $M^+(N_2O)_n$-Ar Complexes 46
3.4.1 $Cu^+(N_2O)_n$-Ar Infrared Spectra 46
3.4.2 $Ag^+(N_2O)_n$-Ar Infrared Spectra 54
3.4.3 $Au^+(N_2O)_n$-Ar Infrared Spectra 58
3.4.4 $M^+(N_2O)_n$-Ar Spectral Trends 63
3.5 $(N_2O)_n^+$ IRPD Spectra of (n = 3-5) complexes 72
3.6 Conclusions 73

4 Structural Isomers and Low-Lying Electronic States of Gas-Phase $M^+(N_2O)_n$ (M = Co, Rh, Ir) Ion-Molecule Complexes **75**

4.1 Introduction 76
4.2 Experimental Methods 79
4.3 $M^+(N_2O)_n$-Ar Time-of-Flight Spectra 80
4.4 $M^+(N_2O)_n$-Ar IRPD Spectra 81

4.4.1 $Co^+(N_2O)_n$-Ar IRPD Spectra 82
4.4.2 $Rh^+(N_2O)_n$-Ar IRPD Spectra 93
4.4.3 $Ir^+(N_2O)_n$-Ar IRPD Spectra 102
4.5 Discussion 108
4.6 Conclusions 109

5 Infrared Spectroscopy of Closed *s*-Shell Gas-Phase $M^+(N_2O)_n$ (M = Li, Al) Ion-Molecule Complexes 111

5.1 Introduction 112
5.2 Experimental Methods 114
5.3 Time-of-Flight Mass Spectra 115
5.4 $Li^+(N_2O)_n$-Ar IRPD Spectra 115
5.5 $Li^+(N_2O)_n$-N_2 IRPD Spectra 123
5.6 $Al^+(N_2O)_n$-Ar IRPD Spectra 128
5.7 Discussion 132
5.8 Conclusions 135

6 Adsorption of Nitrous Oxide on Gold and Cobalt Cationic Clusters 137

6.1 Introduction 138
6.1.1 Gold 138
6.1.2 Cobalt 140
6.2 Experimental and Theoretical Methods 143
6.3 Results and Discussion 144
6.3.1 $Au_n^+(N_2O)$ Clusters 144
6.3.2 $Co_n^+(N_2O)$ Clusters 154

6.4 Conclusions 165

7 Conclusions **168**

A Appendix **173**

Bibliography **179**

Chapter 1

Introduction

1.1 Catalysis

Catalysis is of crucial importance for all aspects of modern life. Estimations predict as much as 85% of the everyday items upon which modern society relies all, somewhere in the production line, involve a catalyst.[1] Thus, these items, along with their production, have a considerable influence on energy expenditure (e.g. the petrochemical industry),[2–4] healthcare (e.g. the pharmaceutical industry),[5–7] material science (e.g. plastics),[8,9] transport (e.g. catalytic converters in the automotive industry),[10–12] and environmental impact (e.g. water and air quality).[13,14] The Haber-Bosch process, the production of ammonia from its constituent elements, is perhaps one of the most well-known chemical reactions to be heavily reliant on a catalyst. This reaction laid the foundations for large-scale production of fertilizer and consumes *ca.* 1-2% of the world's energy production per year.[15]

The word catalysis was first coined in 1835 by Jöns Jakob Berzelius, after observing that some substances accelerate the reaction rate (up to equilibrium) without themselves being consumed in the reaction. Considering the reaction kinetics, a catalyst is known as a ma-

terial which opens up an alternate reaction pathway with lower reaction barriers compared to the pathway without the catalyst. As reaction rates are governed by the barrier height of the rate-determining step, a reduction in this barrier height equates to an increase in reaction rate. The intermediate steps associated with a particular reaction do not, however, affect the location of chemical equilibrium. Usually only the energy differences between the reagents and products (*i.e.* whether endo- or exothermic), and the entropic changes associated with a reaction, can influence the point of chemical equilibrium. However, if a reaction yields multiple products, a catalyst can also raise the abundance or fraction of a particular product relative to the others; which is termed "selectivity". Considering again the reaction kinetics framework, a resultant new reaction pathway, facilitated by the catalyst, is favoured forming the dominant product. The larger the difference in barrier heights between the catalysed and non-catalysed reaction pathways, the greater the degree of selectivity.

There exist three main categories of catalysts: homogeneous, heterogeneous and biological. Homogeneous catalysts are those where the catalyst and the reagents exist in the same phase, typically the solution-phase. Biological catalysts are those which are exploited by nature and are heavily reliant on enzymes. Heterogeneous catalysts are in a different phase to the reagents; generally a solid catalyst with the reagents in either the solution or gas phase. Sadly, the mechanistic understanding of heterogeneous catalysis is not as advanced as homogeneous, due to the difficulty in characterising experimentally the catalyst surface accurately. Heterogeneous catalysts typically consist of finely dispersed particles of a transition metal on a support, normally a silicate or metal oxide. The surfaces of these catalysts tend to be rough, offering many different chemical environments. Thus, it is challenging to experimentally verify and characterise the relationship between key structures

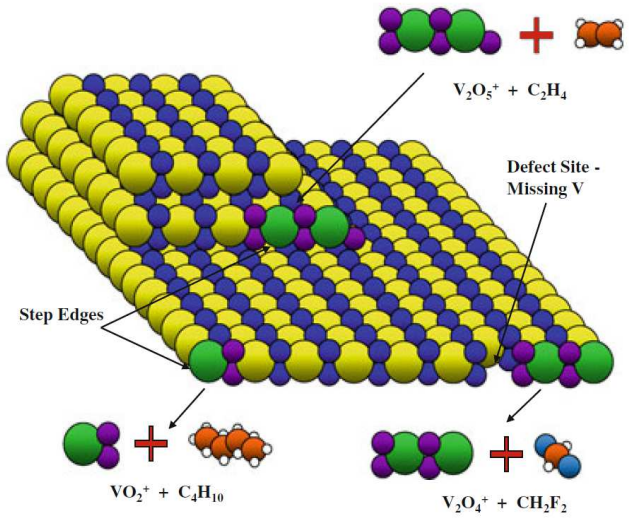

Figure 1.1: Kinks, corners, step edges which compose the defect sites. Figure adapted from Castleman, A. W. *Catal Lett*, 2011, 141, 1243-1253.[22]

and catalytic activity.[16] Novel developments on single crystal surfaces led to breakthroughs concerning these challenges, providing a detailed description of the surface and attached adsorbates. The emergence of techniques such as scanning tunnelling microscopy (STM) and atomic force microscopy (AFM) resulted in atom-scale precision of the surface.[17,18] It was quickly realised that these single crystal surfaces exhibited different chemical behaviour when compared to the highly-dispersed, real catalysts. These differences lead to reactions being classified as "structure-sensitive", or "structure-insensitive".[19] Structure-sensitive reactions were found to exhibit greater reactivity at so-called "defect" sites, *i.e.* kinks, corners, vacancy sites (see, for example figure 1.1).[20] Thus, the term "active site" was coined for the area which is responsible for the observed catalytic activity.[21] These sites represent special geometrical and electronic configurations, which control catalytic activity and selectivity. Accurate characterisation of the active site is thus important in elucidating the underlying mechanisms which control the observed chemistry, giving direction for the development of next-generation catalysts.

There exist myriad techniques allowing for the investigation of surfaces. However, the development of molecular beams, together with methods generating small metallic particles entrained within these molecular beams,[23] unlocked new research directions including "gas-phase surface science". Gas-phase metallic particles possess a finite number of atoms, resulting in many surface atoms along with different chemical environments of atypical coordination. These chemical environments are often viewed as defect sites, and thus, metal particles in many ways are ideal model systems for heterogeneous catalysis. The study of small metal particles, or clusters of metal atoms in isolation, allow for direct investigation of the active site in the absence of complications due to solvent molecules, counter-ions, or from perturbations from the surface.

1.2 Clusters

Metal clusters are defined as n = 1-1000 atoms bound together *via* substantial chemical bonds, forming a cohesive unit. The cluster properties for larger clusters present a smooth variation, for example in magnetism or ionisation energy, which converge to the bulk value with increasing cluster size.[24,25] Smaller clusters, however, present different behaviour and quantum mechanical effects dominate, with cluster properties often changing starkly with the addition of just one atom.[26] This really is a regime where "every atom counts".

The unique behaviour associated with clusters is not only present in the gas phase; finely-dispersed metal particles also present properties different from bulk material. As discussed above, these species often display catalytic properties. One example is the difference in physico-chemical properties associated with gold. Bulk gold is famously unreactive; resilient to tarnishing in standard conditions. However, highly dispersed gold either in solution or as nanoparticles on a surface behave much differently, in some cases catalysing a number

of reactions.[27,28] One prominent example is the catalytic oxidation of carbon monoxide to carbon dioxide by molecular oxygen.[29] This catalytic reaction, using gold, proceeds at lower temperatures when compared to the same reaction using different metals.[29]

Gas-phase metal clusters can be readily produced with defined parameters such as charge state, size, and adsorption site number. By changing these parameters, the general underlying concepts can be constructed. Understanding these concepts is not just important to the chemical and catalytic properties of isolated metal clusters, but also serve as a conceptual basis for the investigation and optimisation of active sites of more-complicated catalytic systems under different thermodynamic and kinetic conditions.

1.2.1 Cluster Sources

There are many experimental techniques employed in investigating the stability and abundance of gas-phase metal clusters. The earliest, developed by Robbins and coworkers,[30] were thermally-heated oven sources. A low melting point metal (typically an alkali metal) is heated in an oven, the gaseous metal then expands adiabatically through a nozzle, resulting in a continuous, effusive beam expansion. These sources produced small clusters of $n =$ 1-10 atoms. Later designs used pressurised ovens, in which the oven is filled with an inert gas.[31] The metal vapour is entrained in the inert gas, again expanding, often supersonically, to produce a molecular beam. The presence of the inert gas leads to more collisions within the molecular beam, which include three-body collisions, key to cluster growth, resulting in colder and larger metal clusters. Collisions with the inert gas atoms disperse any excess energy resulting from newly-formed exothermic metal-metal bonds. Clusters of as many as $n = 100$ can be produced utilising these sources. Oven sources, however, suffer from high consumption rate of the metal sample and so initial studies were limited to low-boiling point metals (e.g. alkali metals).[32]

Another technique used to produce both neutral and ionic metal clusters is the pulsed-arc cluster ion source (PACIS)[33] developed in the early 1990s. Here, a backing gas of helium is pulsed between two electrodes, a discharge between the electrodes then produces a plasma partly vaporising the metal surface. Metal ions and clusters are formed *via* collisions with the carrier gas. PACIS is able to operate at high repetition rates, producing a high intensity cluster beam. However, since PACIS produces a plasma, additional cooling is required and, similar to oven sources, suffers from high consumption of the metal sample.

One such technique is the sputtering source, in which an ion gun generates rare-gas ions which are accelerated towards the metal target.[34,35] Typical kinetic energies of the rare-gas ions are on the order of several keV,[34] enough to eject metal atoms from the metal surface. Clusters can be produced in all three common charge states and with relative stability, as observed in the investigation of coinage metal anions (Cu_n^-, Ag_n^-, Au_n^-; n = 1-10) by Lineberger and coworkers.[36]

The technique of vaporising (ablating) high melting point metals using laser radiation has been utilised widely for years.[37] Laser vaporisation sources were developed independently by Smalley and Bondybey in 1981.[23,38] Heating, and subsequent vaporisation, of the metal surface is achieved by focussing a beam of a pulsed laser, typically the 2nd (532 nm) harmonic of a Nd:YAG laser. Upon vaporisation, the neutral and ionised metal atoms are emitted from the surface, with free electrons also emitted which can attach to the ablated atoms. The resulting metal plasma is then entrained into a gas pulse, often through a clustering channel. This channel promotes three-body collisions necessary for cluster formation.[39] The metal targets are usually discs or rods and are continuously rotated throughout the experiment ensuring ablation of a fresh surface at each laser shot. A schematic view of a laser vapourisation source is presented in figure 1.2.

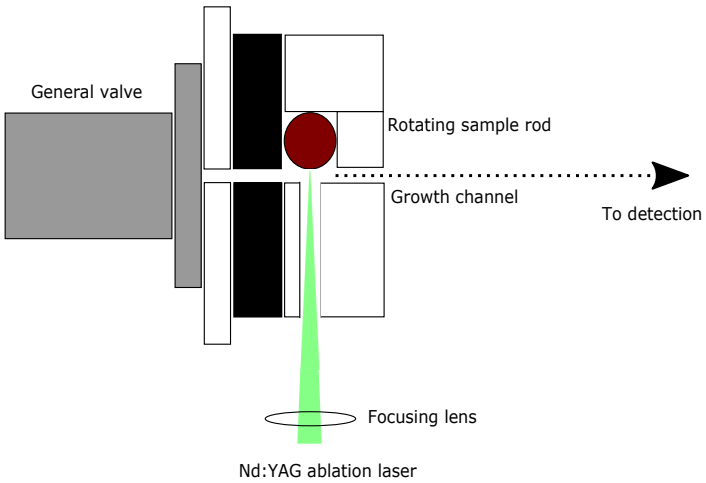

Figure 1.2: Schematic design of the general laser ablation cluster source.[39]

Many modifications to this conventional cluster source have been implemented, including cyrogenically cooling the cluster channel using liquid nitrogen. Cooling down to 77 K enhances the production of larger metal clusters and results in cooler clusters, often permitting the adsorption of weakly-bound messenger species. Knickelbein and coworkers observed neutral nickel clusters as far as $n = 90$.[40] An additional cooling block, attached to the cluster channel, was used by Fielicke *et al.* to produce cationic vanadium clusters with attached, weakly-bound, argon atoms.[41] Mixed-metal binary clusters can be produced efficiently *via* a dual-rod ablation source, first implemented by Kaya and coworkers investigating Co_nV_m, Si_nNa_m, $Co_nAl_m^-$, and $Au_nPd_m^-$ clusters.[42–45]

1.3 Probing the Structure of Metal Clusters

Accurate structure determination of metal clusters still remains a challenge for experimentalists and theoreticians alike. However, high-resolution characterisation techniques typically used for condensed-phase samples cannot be directly applied to isolated, gas-phase metal clusters as the accessible number densities are too low. For example, in absorption spectroscopy, attenuation in light intensity is typically measured. The low number density

results in extremely low detection efficiency. Characterisation is thus obtained *via* indirect methods, usually based on mass spectrometry, where sensitive detection can be utilised for spectroscopic measurements.

Quantum chemical computational techniques are often coupled with such experimental studies to aid interpretation. Transition metals possess many electrons in d orbitals, and thus, accurate structure determination is challenging with theoretical treatment. The computational techniques used in this thesis will be explained further in chapter 2.

1.3.1 Ion Mobility

Ion mobility is a powerful method for structure determination of gas-phase molecular ions. Kappes and coworkers were the first to investigate metal cluster ions using ion mobility.[46] Briefly, studies involve measuring the time taken for a particular cluster ion to traverse a cell pressurised with a buffer gas. The cluster ion is guided by an electric field through the cell, and by using the flight time the cluster collisional cross section can be determined and directly compared with theoretical calculations. Combined with mass spectrometry, the cluster is first mass-selected *via* time-of-flight before entering the drift cell, with a quadrupole mass spectrometer positioned after the drift cell preventing detection of unwanted, fragment ions.[47]

Cationic and anionic gold clusters were investigated using ion mobility coupled with density functional theory calculations by Kappes and coworkers.[48,49] For the cations, planar structures were found for n = 3-7, with 3-dimensional structures occurring at n = 8. In contrast, the anionic clusters presented planar structures for n = 3-11, with the first 3-dimensional geometry at n = 12.

1.3.2 Trapped Ion Electron Diffraction

Parks and coworkers developed the trapped ion electron diffraction (TIED) technique by investigating the C_{60}^+ cluster.[50] Size-selected clusters are stored in a radio-frequency quadrupole ion trap for an adequate time (typically minutes) so that electron-diffraction measurements can be undertaken. The resulting diffraction pattern is detected by a microchannel phosphor screen detector (MCP) and imaged using a charge-coupled-device (CCD) camera. This diffraction pattern can then be readily compared to scattering functions from predicted geometries based on density functional theory.

TIED has also been used to investigate large metal clusters, exploring M_{55}^- structures for the $3d$ and $4d$ elements, M = Sc-Cu and Zr-Ag.[51] The authors observed general correlations of cluster structure with bulk lattice morphology.

1.3.3 Vibrational Action Spectroscopy

A wide range of high-resolution spectroscopic techniques, allowing for direct structural characterisation, have been applied to diatomic and triatomic metal cluster species, such as laser-induced fluorescence (LIF), resonance enhanced UV/VIS multiphoton ionisation, and pulsed-field ionisation zero electron kinetic energy (ZEKE) photoelectron spectroscopy.[52–57] However, high-resolution techniques require large number densities which are difficult to attain as the cluster size increases. Thus, structural characterisation of gas-phase metal clusters using spectroscopy relies on alternative, indirect methods to measure the absorption of photons.

One such technique, yielding detailed structural information on metal clusters, is infrared (IR) action spectroscopy.[58–61] There are four main categories of IR action spectroscopy: infrared resonance enhanced multiple photon ionisation (IR-REMPI), infrared

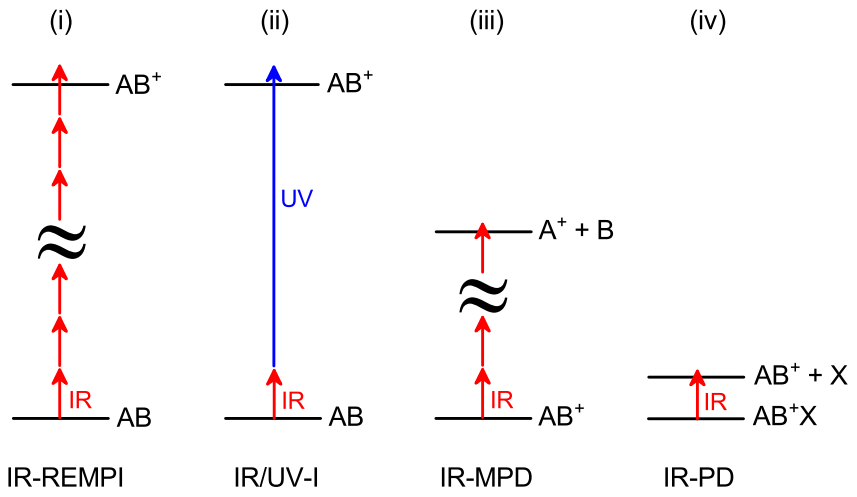

Figure 1.3: Schematic illustrating the four main categories of IR action spectroscopy: i) infrared resonance enhanced multiple photon ionisation (IR-REMPI), ii) IR/UV two-colour ionisation, iii) infrared multiple photon dissociation (IRMPD), and iv) infrared photodissociation (IRPD) of a messenger-tagged cluster.

ultraviolet (IR/UV) two-colour ionisation, infrared multiple photon dissociation (IRMPD), and infrared photodissociation (IRPD) of messenger-tagged clusters. These experimental techniques are shown schematically in figure 1.3. Investigations on neutral clusters utilise IR-REMPI and IR/UV ionisation techniques, whilst charged clusters typically employ IRMPD and IRPD techniques. In all four techniques, a vibrational spectrum is obtained by recording mass spectra with and without IR radiation (mass spectral yield) as a function of wavelength. The IR action spectrum produced cannot be treated as an IR absorption spectrum, but can well reflect the major observations, e.g. band position. In light of the thesis, only techniques utilising characterisation on charged clusters (IRMPD and IRPD) will be discussed further.

IRMPD usually consists of a dissociative event which is easily detected *via* mass spectrometry. An intense and tunable IR radiation source (typically a free electron laser (FEL)) is required to resonantly heat the metal cluster in a sequential incoherent photon absorption process (equation 1.1 and figure 1.3 (iii)).

$$AB^+ \xrightarrow{h\nu} (AB^+)^* \xrightarrow{h\nu} ... \xrightarrow{h\nu} A^+ + B \tag{1.1}$$

When the IR radiation is resonant with a fundamental vibrational transition, the cluster (represented here as AB^+) will absorb these IR photons. In principle, this technique takes advantage of the cluster being charged, so the cluster could easily be a negatively charged anion. However, since the body of work in this thesis investigates cationic species, for clarity equation 1.1 represents the cationic process. Charged clusters are much easier to manipulate compared to neutral clusters; ions are easily mass-selected prior to IR-irradiation, which removes cross-communication (cascading effects) of different photodissociation channels coming from different parent ion signal channels, leading to fragment ions of the same mass. In contrast, IR measurements where ions are not mass-selected have an advantage in that the complete sample of cluster sizes can be recorded in one scan. Metal clusters with an attached adsorbate normally occupy strong M-ligand dissociation energies of several eV, thus the IRMPD process involves the absorption of many IR photons. A useful approach reducing the number of IR photons absorbed is the inert-messenger technique.[60]

A weakly-bound messenger species, typically a rare-gas atom or inert molecule, is adsorbed to a metal ion (or cluster) and will desorb from the rest of the complex *via* intramolecular vibrational energy redistribution (IVR) breaking the weak ion-messenger bond (figure 1.3 (iv)):

$$AB^+X \xrightarrow{h\nu} (AB^+)^*X \xrightarrow{IVR} AB^+ + X \tag{1.2}$$

The perturbation of X on the AB^+ ion should be small so that the structural information gained from the complex approximates the structural information of the bare, untagged ion. He atoms are usually used as the inert messenger as these offer a weak perturbation

on the ion of interest plus increase the density of states and hence, the IVR rate. The measured IRPD spectra of He-tagged ions usually reflect the linear absorption spectrum quantitatively.[62–66] Heavier rare-gas atoms (e.g. Ar or Kr) have been known to bind to metal ions quite strongly, and thus, can in some cases significantly perturb the metal ion, leading to shifts in vibrational frequencies compared to the un-tagged ion. In such cases, the rare-gas atom should be included in the simulations. IRPD of messenger-tagged species often involves greater than a single photon being absorbed.

IRPD spectra, coupled with density function theory (DFT), of clusters up to $n \approx 20$ atoms can often be unambiguously assigned based on comparison of the observed spectra with the simulated spectra of generated low-lying isomers. Compared to IRMPD spectra, the bands yielded in IRPD spectra are very narrow (7-12 cm^{-1}), which is normally limited by the spectral linewidth of the probe laser, and/or dynamical effects. A detailed perspective article highlighting the advances in vibrational spectroscopy in the structural characterisation of metal clusters has been outlined by Knut Asmis.[67]

1.4 Metal Ion-Molecule Complexes

Metal ions, along with their interactions with ligands, are widespread in chemistry as prototypes for: bonding in inorganic and organometallic chemistry, species involved in a wide variety of catalytic processes, and as suitable models for active sites present in enzymes.[68–71] Investigation of gas-phase metal ion-molecule complexes yields a deeper understanding of key metal-ligand interactions, ligand activation, and metal ion solvation all at the molecular level and unperturbed by influences such as solvent, aggregation, and counter-ion effects, which are prevalent in the condensed-phase. Understanding these fundamental processes will further knowledge across the fields of chemistry, biology, geochemistry, and astro-

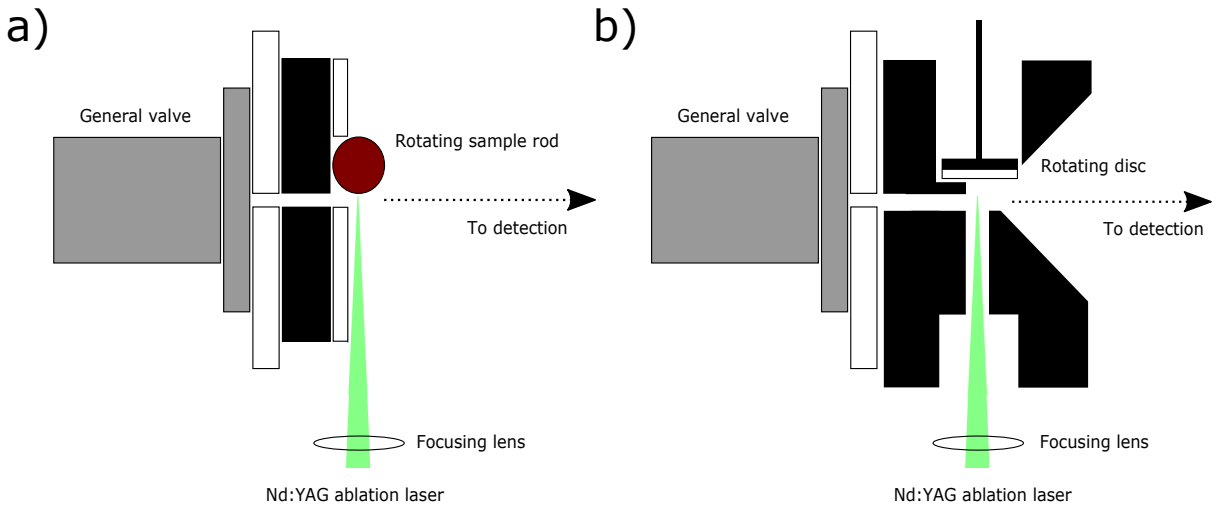

Figure 1.4: a) Schematic design of the so-called "cutaway" laser ablation cluster source from Duncan and coworkers.[39] b) Schematic design of the laser ablation cluster source used in the Mackenzie laboratory facilitating the formation of metal ion-ligand complexes.

physics.[72] Metal ions, in particular alkali metals such as Na and K, and alkaline earth metals Mg and Ca, are atmospherically significant. As a consequence of meteor ablation, hundreds of tons of these metals enter the atmosphere every day, acting as a sink for positive charge.[73] Mg cations have also been observed in other planetary atmospheres, e.g. Jupiter.[74] Gas-phase metal-ligand complexes also serve as models for reaction intermediates, an active area which has been studied extensively both experimentally and theoretically.[75–77]

As mentioned previously in section 1.2.1, the laser vaporisation source is an effective method of producing gas-phase metal clusters in high abundance and stability. Duncan and coworkers developed the so-called "cutaway" source, designed to produce a metal ion surrounded by weakly-bound ligands or rare-gas atoms.[39] A schematic representation of the cutaway source is illustrated in figure 1.4.

Weakly-bound complexes (especially those which are messenger-tagged) require extremely cold supersonic expansion conditions, such as that of a free-jet expansion. The typical laser-ablation cluster source does not allow for a free-jet expansion as the growth channel, allowing metal-metal collisions for growth of the metal cluster, forbids it. The

cutaway design removes the cluster channel allowing for a (near) free-jet expansion. Duncan and coworkers have produced very cold complexes using this source design, such as the Mg^+-Ne complex, yielding rotationally-resolved electronic spectra, quoting a rotational temperature of 4 K.[78]

Electrospray ionisation (ESI) is becoming a dependable source for the production of metal-ligand complexes. With this technique, a liquid sample (normally a salt solution with the metal and ligand of interest) is forced through a small capillary set at a potential difference typically of *ca.* 3000 V. The liquid is dispersed into vacuum *via* electrospray, into fine aerosols. These aerosols are charged, thus unstable, and will undergo solvent evaporation yielding the isolated ion of interest. Beyer and coworkers utilised ESI to produce and investigate the spectroscopy of salt clusters doped with organic molecules, $[Na_nCl_{n-2}(C_2HO_3)]^+$, n = 5-11.[79]

1.5 Motivation to Study N_2O

Nitrous oxide (N_2O) is a potent greenhouse gas with a warming potential 300 times greater than carbon dioxide and accounts for 5% of anthropogenic greenhouse emissions.[80,81] In addition to its climate change potential, tropospheric N_2O emissions are the major source of stratospheric NO_x species, thus N_2O represents the dominant ozone-depleting emission of the 21st century.[80,81] A wide range of human activities such as manufacturing, fossil fuel use, and agriculture have led to an increase in N_2O emissions, with concentrations rising by 0.5-0.9 ppb per volume per year.[77]

Although N_2O is unregulated by the Montreal Protocol,[82] there is considerable interest in reducing nitrous oxide emissions due to its detrimental effect on the environment. One effective route to reduce emissions is *via* heterogeneous metal-catalysed N_2O decomposi-

tion and reduction,[83,84] which has been an active area of extensive research in conventional heterogeneous catalysis and cluster science.[85] A vital research goal is to understand the reactivity of N_2O at metal centres in contrasting environments, e.g. gas-phase, solid supports, in enzymes and in the condensed-phase. By considering a combination of these investigations, novel and provocative insights into the fundamental binding mechanisms between N_2O and metal ions, including bond activation or scission, is yielded.

N_2O possesses a low dipole moment of 0.161 D and exists as two major canonical structures, shown at the top of figure 1.5. The valence molecular-orbitals of N_2O are presented at the bottom of figure 1.5, showing the occupied HOMO-1 7σ and HOMO 2π orbitals along with the unoccupied LUMO 3π orbital. Thermodynamically, nitrous oxide is a strong oxidant but kinetically, is defiant towards decomposition. The presence of metal ions have the ability of lowering these kinetic barriers *via* activation.[86] N_2O is a weak σ electron donor and a weak π electron acceptor and as such, is considered a poor ligand to metal centres. As a result, only two metal-N_2O complexes (one with a V^{III}, d^2, centre, and another with a Cu^{I}, d^{10}, centre) have been characterised by single-crystal X-ray diffraction.[87,88] In both cases, N_2O is bound linearly to the metal centre *via* the terminal N-atom.

In terms of fundamental binding interactions, gas-phase $M^{+/0/-}(N_2O)_n$ complexes represent model entrance-channel species on the N_2O decomposition potential energy surface (PES), in which these interactions can be studied in isolation. Metal atom-N_2O binding has been studied both theoretically[89–97] and experimentally,[98,99] and the reaction kinetics of N_2O with charged metal atoms and clusters have been investigated under thermal and single-collision conditions.[100–110] N_2O can act as both an O and N source for ionic species, leading to oxide and nitride formation.[100] Theoretical studies of these binding interactions support terminal O-coordination to the metal centre.[89–93] However, matrix isolation in-

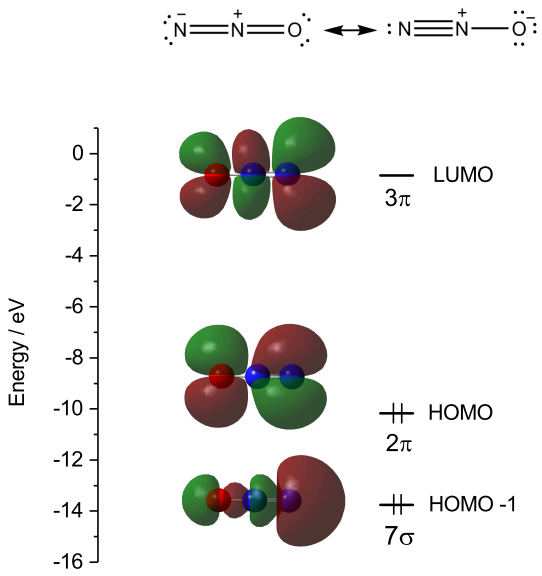

Figure 1.5: *Top*: Major canonical structures of nitrous oxide. *Bottom*: Valence molecular-orbital energies calculated from density functional theory computed at the B3P86 level of theory employing the Def2TZVP basis set.

frared studies report terminal N-coordination to Ni, Pd, and Pt centres,[98] and also to MCl centres (M = Cu, Ag).[99] The authors of these studies invoke a bonding scheme, shown in figure 1.6. This mechanism involves synergistic σ donation from the occupied 7σ orbital of N_2O into an empty σ orbital on the metal ion along with π back-bonding from the metal d orbitals into the unoccupied $3\pi^*$ orbital of N_2O. The findings in this thesis, however, are interpreted in terms of an alternative binding mechanism, detailed in chapter 3. The fundamental binding interactions are also interpreted by considering the force constant of the N=N bond.

Relevant gas-phase infrared spectroscopic studies are limited to pure $(N_2O)^{\pm}$ complexes,[111,112] free electron laser studies of N_2O on Rh_n^+ clusters,[113–115] and blackbody infrared radiative dissociation.[116] The studies of N_2O on Rh_n^+ clusters demonstrated that the decomposition of nitrous oxide on size-selected clusters can be initiated using resonant infrared excitation, with the cluster-N_2O entity representing an entrance-channel complex

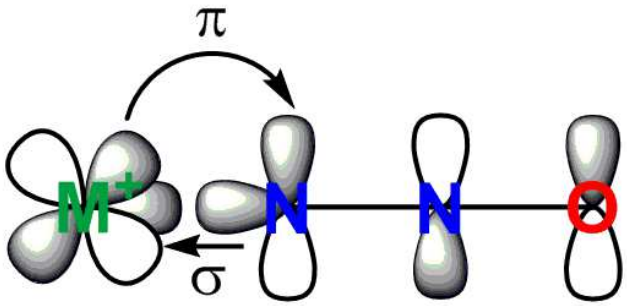

Figure 1.6: Proposed binding mechanism for N-coordination to a metal ion presenting synergistic σ donation to the M centre from the N_2O 7σ orbital and π back-bonding from M to the $3\pi^*$ orbital of N_2O.[98]

on the reactive potential energy surface. Driving the reactivity from pre-reactive states producing non-statistical reaction products represents a longstanding goal in cluster science.[117]

Little attention has thus far been given to the structural information of gas-phase $M^{+/0/-}(N_2O)_n$ complexes, where coordination numbers and trends in binding energies/motifs can be readily extracted. Such studies offer the possibility of gaining a deeper and more detailed insight into the intricacies of N- and O-binding of N_2O to metal centres. As described in section 1.3.3, infrared photodissociation (IRPD) spectroscopy is a viable technique to probe gas-phase metal-ligand complexes. This approach has been employed by several groups providing reliable information on the structures of many gas-phase metal-ligand complexes;[118–120] however this thesis presents the first experimental studies of $M^+(N_2O)_n$ complexes.

1.6 Thesis Overview

This chapter has provided a brief introduction to heterogeneous catalysis, and how clusters and metal-ligand complexes can provide more information in this field. Chapter 2 details the experimental and theoretical methods used in this thesis. The main body of work is presented in chapters 3-6, forming an ongoing series of infrared studies of $M^+(N_2O)_n$ species

as entrance-channel complexes for the metal-centred nitrous oxide reduction reaction. We have undertaken a systematic study comparing N_2O binding to a range of metals from across the periodic table in an attempt to draw comparisons between them and elucidate trends in their behaviour. Group 11 metals (chapter 3) were the first chosen to investigate as in their cationic form, they offer a closed-shell d^{10} electron configuration, and thus, metal ion-N_2O interactions were expected be simpler. To complement these findings, open-shell group 9, d^8 (chapter 4) ions were complexed with nitrous oxide, presenting evidence of low-lying electronic states. For an interesting comparison with these transition metal ions, closed s-shell ions, Li^+ and Al^+ (chapter 5) were ligated with N_2O. By way of comparison with the $M^+(N_2O)_n$ studies, chapter 6 presents an infrared study of nitrous oxide binding to cationic gold and cobalt clusters ($M_n^+(N_2O)$, M = Au, Co) using the free electron laser facility at the Fritz-Haber Institute, Berlin. Chapter 7 concludes the thesis highlighting the main findings of this work and discusses future work.

Chapter 2

Experimental and Theoretical Methodology

2.1 Vibrational Energy Levels

An example of internal motion of a diatomic molecule is its periodic vibrational motion. This motion, along with the transitions between the allowed quantum levels, can be approximated by a simple harmonic oscillator (SHO), which obeys Hooke's Law:

$$F = -k_F x \tag{2.1}$$

where F is the force, k_F is the force constant and x is the displacement from equilibrium. The molecular potential energy is a parabolic potential and is expressed:

$$V(x) = \frac{1}{2} k_F x^2 \qquad x = R - R_e \tag{2.2}$$

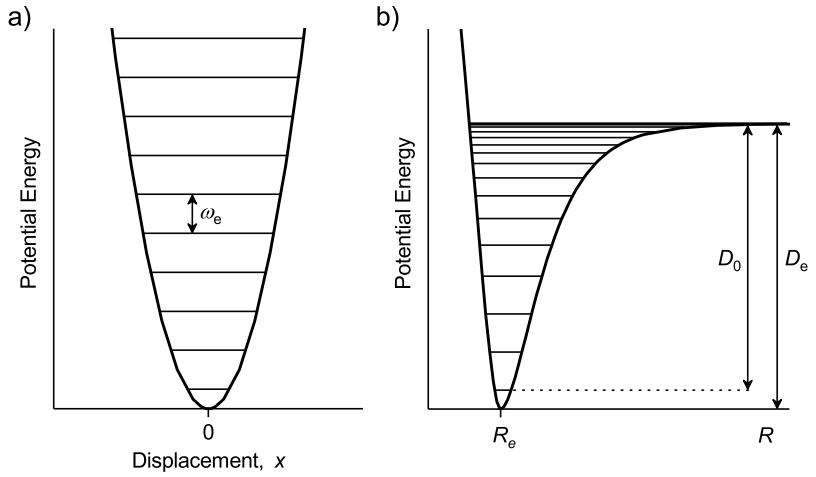

Figure 2.1: a) Molecular potential energy curve of the simple harmonic oscillator displaying equally spaced, non-degenerate energy levels, and b) Morse molecular potential energy curve illustrating the finite energy levels converging toward the dissociation energy.

Where R is the bond distance from the equilibrium bond distance, R_e. The classical frequency of oscillation is expressed:

$$\nu_{vib} = \frac{1}{2\pi}\sqrt{\frac{k_F}{\mu}} \tag{2.3}$$

where μ is the reduced mass.

The energy eigenvalues (*i.e.* vibrational terms) of a SHO are expressed as:

$$\tilde{G_\nu} = (\nu + \frac{1}{2})\omega_e \qquad \omega_e = \frac{\nu_{vib}}{\tilde{c}} = \frac{1}{2\pi\tilde{c}}\sqrt{\frac{k_F}{\mu}} \tag{2.4}$$

where ν is the vibrational quantum number which is a positive integer value, or zero, ω_e is the vibrational constant, and $\tilde{c}$ is the speed of light expressed in cms^{-1}. The molecular potential energy curve of a simple harmonic oscillator is shown in figure 2.1(a). Vibrational transitions obey the selection rule $\Delta\nu = \pm 1$, with the separation between energy levels given by ω_e. The simple harmonic oscillator gives a reasonable approximation of vibrations in molecules at small displacement (x) values. However, this parabolic energy curve cannot provide an accurate approximation for large displacement values as it does not allow the

bond to dissociate.

Real molecular bonds do not act as harmonic oscillators since they can be broken, thus allowing for finite dissociation energies to be identified. Also, as the bond is stretched the restoring force is not proportional to the displacement. The motion and behaviour of real systems is "anharmonic". To calculate the energy levels of anharmonic systems, one must use a function which more accurately resembles the potential energy curve, such as the Morse potential energy curve:[121]

$$V(x) = D_e[1 - exp(-\sqrt{\frac{k_F}{2D_e}}x)]^2 \tag{2.5}$$

where k_F is the force constant near the potential minimum and D_e is the dissociation energy. Figure 2.1(b) shows the anharmonic, Morse potential energy curve with the vibrational energy levels no longer equally spaced but which converge on the dissociation energy. The energy eigenvalues are represented by:

$$\tilde{G_\nu} = (\nu + \frac{1}{2})\omega_e - (\nu + \frac{1}{2})^2\omega_e\chi_e \qquad \nu = 0, 1, 2, 3, ...\nu_{max} \tag{2.6}$$

where χ_e is the dimensionless, anharmonicity constant:

$$\chi_e = \frac{\omega_e}{4D_e} \tag{2.7}$$

The asymmetry of the anharmonic potential energy curve relaxes the selection rules $\Delta\nu = \pm1, \pm2, \pm3, ..., \pm n$. However, the overtones ($0 \rightarrow 2$, $0 \rightarrow 3$) are typically much weaker than the fundamental ($0 \rightarrow 1$) transition.

A molecule of N atoms occupies $3N$ degrees of freedom, of which $3N$ - 6 are normal vibrational modes ($3N$ - 5 for linear molecules).[122] The vibrational frequencies of these modes depend on: i) the mass of each atom, ii) the strength of the chemical bonds, and

iii) the molecular geometry. For a vibrational transition to be allowed (*i.e.* to be infrared active), there must be a change in the molecular dipole moment. In such a case, the molecule is excited *via* the absorption of photons at the same frequency as the vibration.[122] The intensity of these vibrational transitions is proportional to the square of the electric dipole transition moment, R. A transition from a lower vibrational state, described by the wavefunction $\psi_{\nu}^{'}$, and a higher vibrational state, described as ψ_{ν}, is expressed:

$$R_{\nu\nu'} = \int \psi_{\nu}^{'*} \mu \psi_{\nu} d\tau_{\nu} \tag{2.8}$$

R is a vector with x, y, and z components and μ is the electric dipole moment operator. For a transition to be allowed, the integral defining the dipole transition moment must be nonzero, in which case, the integrand must be an even function. Such transitions occur between an even state (orbital) and an odd state.

For the transition moment $R_{\nu\nu'}$ between two non-degenerate states to be non-zero, it must follow:

$$\Gamma(\psi_{\nu}^{'}) \otimes \Gamma(\mu) \otimes \Gamma(\psi_{\nu}) = TSIR \tag{2.9}$$

where TSIR indicates a totally symmetric irreducible representation with Γ indicating an irreducible representation. The electric dipole moment operator, μ, can be further separated into three Cartesian axes: μ_x, μ_y, and μ_z.[123]

$$\Gamma(\psi_{\nu}^{'}) \otimes \Gamma(\mu_x) \otimes \Gamma(\psi_{\nu}) = TSIR \tag{2.10}$$

$$\Gamma(\psi_{\nu}^{'}) \otimes \Gamma(\mu_y) \otimes \Gamma(\psi_{\nu}) = TSIR \tag{2.11}$$

$$\Gamma(\psi_{\nu}^{'}) \otimes \Gamma(\mu_z) \otimes \Gamma(\psi_{\nu}) = TSIR \tag{2.12}$$

For $R_{\nu\nu'}$ to be non-zero, at least one of these components must transform as the totally symmetric irreducible representation, giving rise to an infrared-allowed vibrational transition.

2.2 Infrared Absorption

Vibrational spectra are typically recorded *via* direct absorption methods, reliant upon a frequency-dependent extinction coefficient, ε. A typical absorption experiment involves irradiating the sample with light: the light intensity before and after passing through the sample, given as I_0 and I respectively, is recorded. The Beer-Lambert law relates the extinction coefficient, ε, and the light intensity *via* the equation:

$$I = I_0 e^{-\varepsilon c l} \tag{2.13}$$

where c is the sample concentration and l is the path length of light travelled through the sample. This technique, when applied to gas-phase molecular beam experiments, suffers two experimental challenges. First, cluster sources, in particular laser ablation sources, produce a broad distribution of cluster sizes entrained in the molecular beam. Thus, it is impossible to record the absorption spectrum for a particular cluster size as the recorded difference in light intensity will be a result of many different cluster sizes, all absorbing and re-emitting light, producing convoluted signals. Second, the number densities of the sample produced in a molecular beam are typically too low to measure significant changes in light intensity. By increasing the path length, for example in cavity ring down experiments, this challenge can be overcome.[124] This technique has been used successfully to measure the absorption

spectrum of AuSi and WO,[125,126] but fails for weakly-absorbing or larger systems.

Highlighted earlier in section 1.3, infrared spectra of gas-phase systems are typically recorded *via* indirect methods. One such method, termed "action spectroscopy" utilises mass spectrometry and records changes in ion signals upon irradiation with light. Mass spectrometry offers greater sensitivity and, in addition, species can be size-selected.

2.3 Cluster Source

Gas-phase $M^+(N_2O)_n$ ion-molecule complexes studied in this thesis (chapters 3-5) were produced using a "cutaway" laser ablation source similar to that of Duncan and coworkers.[39] A schematic of the laser ablation source has been shown previously in figure 1.4(b). This source was designed to minimise the production of metal-metal clusters and maximise the production of metal-ligand complexes along with their inert-messenger analogues, which require cold, free-jet supersonic expansion. The design was first employed successfully by the Mackenzie group investigating $M^+(CO_2)_n$ complexes.[127] In this design, the 2nd harmonic (532 nm, E = 5-10 mJ/pulse) output of a pulsed Nd:YAG laser (Continuum Minilite) is used to ablate a rotating metal disc. The rotation ensures continuous ablation of a fresh surface. The metal vapour/plasma produced is entrained in a 6-8 bar pulse of argon carrier gas seeded with 0.6-1.0% N_2O. The gas pulse is delivered *via* a pulsed solenoid valve (Parker-Hannifin General valve, series 9) with a typical pulse duration of 500 μs.

2.4 Time-of-Flight Mass Spectrometry

The metal-ligand complexes are formed immediately in a free-jet supersonic expansion in the source chamber. The complexes are then passed through the skimmer, forming a uniform molecular beam, into the extraction chamber and are perpendicularly extracted into a time-of-flight mass spectrometer (TOF-MS). The complexes studied in chapter 3 were detected

via linear TOF-MS,[128] whilst the complexes in chapters 4 and 5 were detected *via* reflectron TOF-MS.[129] A schematic of the experimental setup is illustrated in figure 2.2. The time-of-flight mass spectrometer used for these experiments is based on that developed by Wiley and McLaren.[128] In this design, a large potential difference is applied between a set of plates (figure 2.2, (2)) which accelerate the ions into the time-of-flight tube. Ions with a given charge q are accelerated by the electric field (E_E or E_S) and traverse a distance, (S_E or S_S). For example, the electric field of the extractor electrode is represented by $E_E = V_E/S_E$. The kinetic energy, KE, of a particular ion of mass m and charge q can be expressed:

$$KE = \frac{1}{2}mv^2 = q(E_R + E_E) \tag{2.14}$$

Ions with a lower mass gain a higher velocity and traverse through the flight tube faster, arriving sooner at the detector. Assuming each ion is singly-charged ($q = e$), equation 2.14 can be rearranged so that the ion mass can be determined from the arrival time:

$$m = 2\frac{e(E_R + E_E)}{L^2}t^2 \tag{2.15}$$

Where L is the length of the flight tube (thus, $v = L/t$). The mass resolution is governed by the ion spatial distribution and velocity distribution. As the molecular beam traverses through the extraction chamber, there is an initial spread in the ion spatial distribution, leading to a range of different velocities and arrival times at the detector. This problem is mitigated by separate electric fields provided by the repeller and extractor electrodes (which comprise the extraction grids, figure 2.2. (2)), developed by Wiley and McLaren.[128] The supersonic expansion conditions also contribute to a spread in the velocity distribution of ions. Utilising reflectron lenses (figure 2.2, (3)) can compensate for this spread; ions with

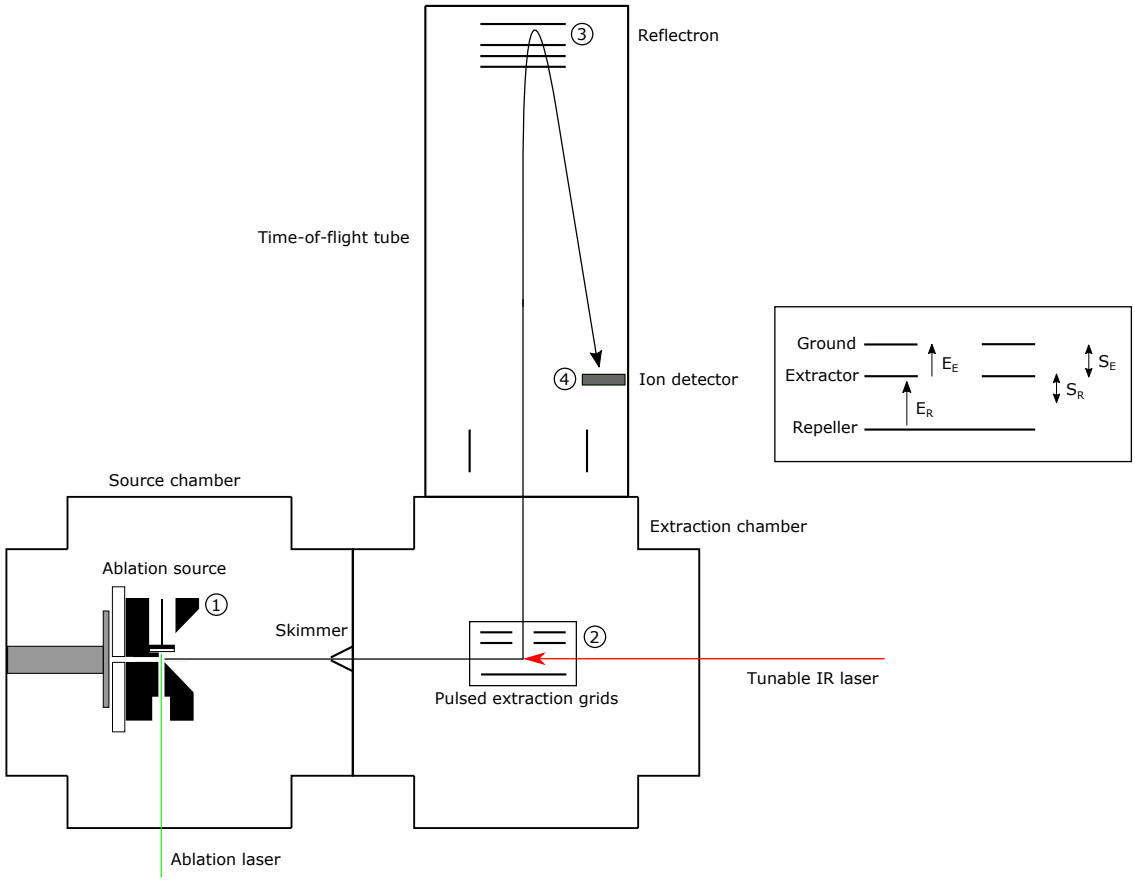

Figure 2.2: Schematic of the IRPD experiment in the Oxford laboratory.

a higher velocity penetrate deeper into the reflectron region, thus spend more time in this region which compensates for the shorter time spent in the time-of-flight tube.

2.5 IRPD Spectroscopy

Infrared photodissociation (IRPD) spectroscopy is a variant of action spectroscopy, utilising the sensitivity of mass spectrometry for spectroscopic measurements. As described earlier in section 1.3.3., to obtain an IRPD spectrum the molecule of interest is irradiated with infrared radiation and the ion signal is monitored as a function of wavelength. The first IRPD experiments were performed by Y.T. Lee and coworkers, investigating protonated hydrogen clusters, H_5^+, H_7^+ and H_9^+.[60]

In this thesis, IRPD is utilised together with the "inert-messenger" technique.[130] A

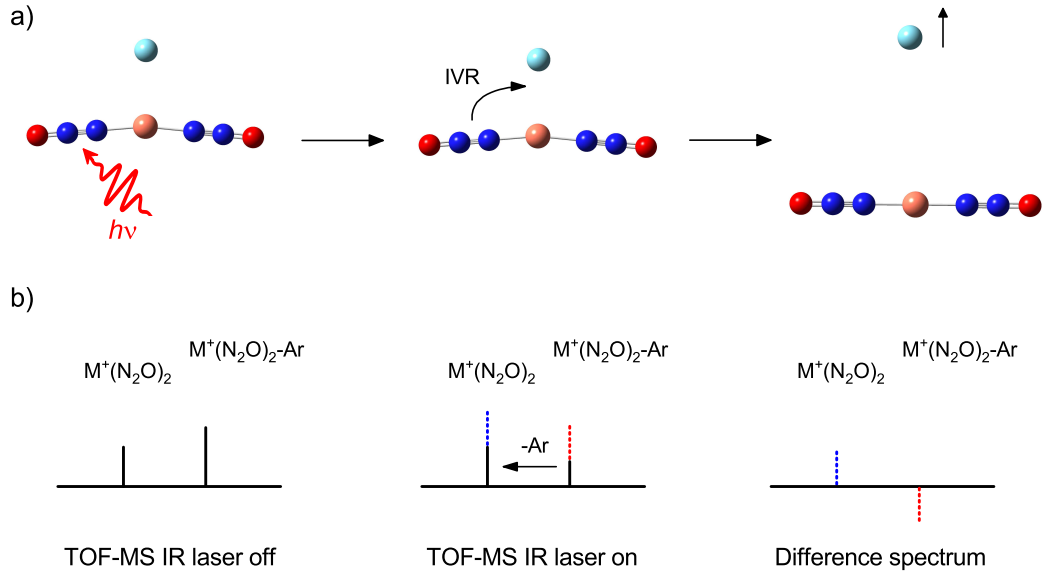

Figure 2.3: a) IRPD utilising the inert messenger technique; absorption of a photon by $M^+(N_2O)_2$-RG leads to dissociation of the weak M^+-RG bond, and b) Schematic mass spectra of the $M^+(N_2O)_2$-Ar complex. As IR radiation is introduced, the $M^+(N_2O)_2$-Ar dissociates *via* the loss of Ar, leading to a decrease in the ion signal intensity of the $M^+(N_2O)_2$-Ar parent channel, and corresponding increase in the $M^+(N_2O)_2$ daughter channel.

schematic of this dissociative event is illustrated in figure 2.3(a). A weakly-bound rare-gas atom is adsorbed to a $M^+(N_2O)_2$ complex, which is irradiated with infrared radiation. If a photon is resonant with a vibrational mode in the N_2O ligand, the photon is absorbed and induces heating of the complex. Through intramolecular vibrational redistribution (IVR),[131] where energy is redistributed over available vibrational degrees of freedom in the complex, desorption of the rare-gas atom from the complex occurs. Thus, recording the loss of this rare-gas atom provides the mass spectrometric signature for photon absorption. Monitoring the fractional depletion of the $M^+(N_2O)_n$-Ar complex as a function of IR wavenumber yields the infrared spectrum of the $M^+(N_2O)_n$ complex of interest.

Adsorption of Ar atoms is found to have a weak perturbation on the structure of the $M^+(N_2O)$ complex. The addition of this extra atom also results in a higher density of states, facilitating IVR thus increasing the fragmentation yield. Argon has been used as

the inert messenger in many IRPD studies of metal ion-ligand complexes.[132–134] Infrared studies on $M^+(N_2O)_n$ complexes (chapters 3-5) utilised a table-top optical parametric oscillator/amplifier system (LaserVision), providing tunable infrared radiation in the region of the fundamental ν_3 stretch (N=N) of nitrous oxide, *i.e.* 2150-2400 cm^{-1}.

2.6 IRMPD Spectroscopy

Chapter 6 presents an investigation of cationic metal clusters with an attached nitrous oxide ligand. In some cases, N_2O is bound to the cluster by as much as 1 eV, corresponding to *ca.* 8066 cm^{-1}. The fundamental vibrational modes probed in this study cover 1100 - 2450 cm^{-1}, thus more than one photon must be absorbed by the cluster in order to induce photodissociation of the N_2O ligand. Infrared multiphoton photodissocation (IRMPD) spectroscopy is therefore employed to investigate these systems.

For this study, a free electron laser (FEL) is used as the infrared radiation source, providing high photon fluences and a broad tunable range which other light sources fail to provide. Many FELs operate, broadly, by the same scheme, as illustrated in figure 2.4. A beam of electrons, generated by an electron gun, is introduced close to the speed of light into an undulator system. The undulator produces a magnetic field with periodicity λ_w, which forces the electrons into an oscillating trajectory *via* the Lorentz force. The acceleration due to the oscillations causes the electrons to emit dipole radiation, which is initially weak and incoherent. To improve the intensity and create coherent radiation, the undulator is situated within an optical cavity. The cavity causes a standing wave, formed by spontaneous emission, which induces newly injected electrons to radiate coherently, bunching the electrons together. This electron bunching increases the intensity of the emitted radiation. As a consequence of the cavity, this effect causes a positive feedback loop causing the spacing

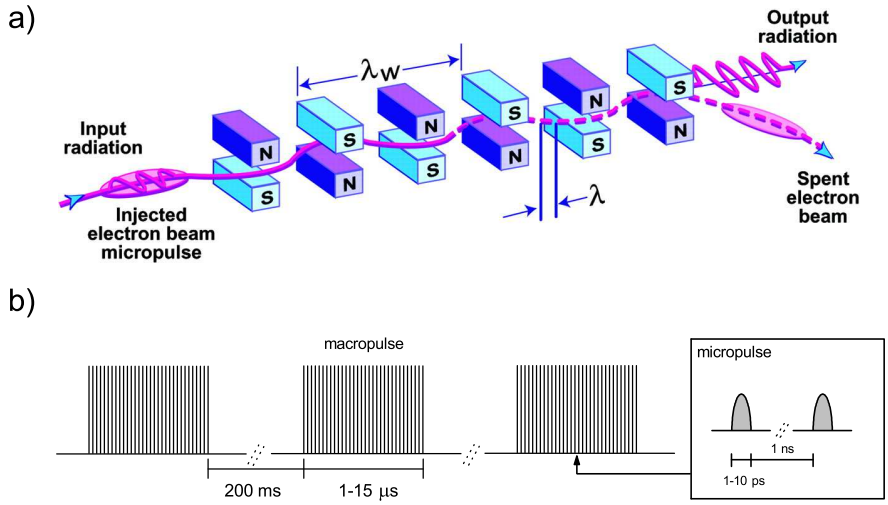

Figure 2.4: a) Schematic illustrating the typical layout of a free electron laser. An electron beam traverses through a periodic arrangement of magnets, their acceleration caused by the Lorentz force results in emission of radiation. Figure reproduced with permission from O'Shea, P. G.; Freund, H. P. *Science*, 2001, 292, 1853-1858.[135] b) Pulse structure of the laser light showing the macropulse composed of micropulses.

of the electron bunches to oscillate in unison with the radiation wavelength. The emitted radiation is a resonance between the radiation field and the electron beam. Thus, the wavelength of radiation can be adjusted by altering the spacing between the undulator magnets, the magnetic field, and electron energy. The IR pulses are composed of macropulses and micropulses (figure 2.4b). The macropulses are typically between 1-15 μs in duration, with a repetition rate of 20 Hz and a pulse energy of up to 100 mJ. Each macropulse is composed of micropulses, which are typically of picosecond duration, separated by a nanosecond.

The IRMPD experiments presented in chapter 6 were performed at the free electron laser (FEL) facility at the Fritz-Haber-Institut (FHI) der Max-Planck-Gesellschaft in Berlin,[137] in collaboration with Dr André Fielicke. The IR radiation generated by the FEL is focused into the extraction area of the TOF-MS within the FHI cluster experiment. A schematic overview of the FHI experiment is shown in figure 2.5. The cluster source is similar to that in the Mackenzie laboratory, however there are some key differences. First, the metal target

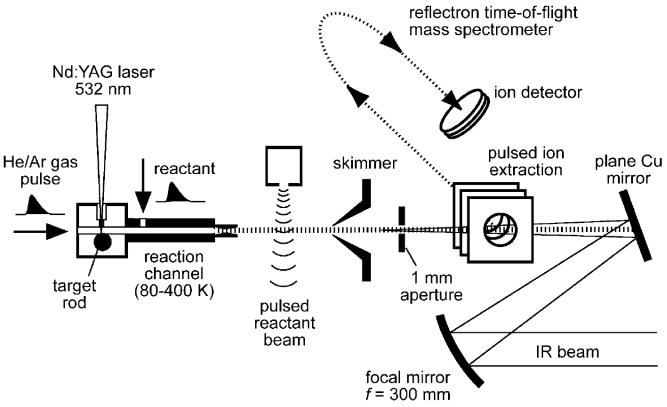

Figure 2.5: Schematic of the IRMPD experiment at the Fritz-Haber-Institut, Berlin. Figure reproduced with permission from Harding, D. J.; Fielicke, A, *Chem.: Eur. J.*, 2014, 20, 3258-3267.[136]

is a rod, and not a disc. Second, the FHI cluster source is fitted with a cluster channel, facilitating the growth of metal-metal clusters. In these experiments, the metal clusters were first produced, with nitrous oxide introduced *via* the reaction channel, forming the $M_n^+(N_2O)$ clusters of interest. This is different from the Oxford source where the reactant gas (N_2O) is seeded and introduced *via* the backing gas (argon). Similar to the experiments performed in Oxford, these cluster ions, along with their IRMPD action spectra, were detected *via* reflectron TOF-MS.

2.7 Computational Methods

2.7.1 Electronic Structure

To determine the electronic structure of atoms and molecules, computational techniques can be used to solve the time-independent Schrödinger equation:

$$\hat{H}\Psi_0(r_n, R_m) = E_0\Psi(r_n, R_m) \tag{2.16}$$

where $\hat{H}$ is the Hamiltonian operator, Ψ_0 is the ground-state wavefunction and E_0 is the ground-state energy. Unfortunately, a direct solution to the Schrödinger equation is

only possible for the simplest system, thus a series of approximations must be employed. The proton mass is *ca.* 1800 times greater than the mass of the electron, as a consequence the protons move significantly slower than the electrons. The nuclei are thus fixed, allowing the electrons to move in a field generated by static nuclei. This is the basis of the Born-Oppenheimer approximation, which allows the following simplifications to be made: i) the molecular ground-state wavefunction, $\Psi_0(r_n, R_m)$ becomes dependent only on electron coordinates *i.e.* $\Psi_0(r_n, R_m) \longrightarrow \Psi_0^{el}(r_n)$, ii) All kinetic energy contributions from nuclei equate to zero, and iii) all potential energy terms from nuclear interactions equate to a constant value, for fixed nuclear positions.

One of the crucial complications in all electronic structure calculations is the electron-electron repulsion term. To simplify and approximate the wavefunctions of the molecule, inexact methods were introduced; the earliest is the Hartree-Fock method. Formulation of the approach is based on the orbital approximation, in which the overall wavefunction Ψ^0 is treated as a product of one electron wavefunctions (or orbitals):

$$\Psi^0 = \psi_a^0(1)\psi_b^0(2)...\psi_z^0(N_e) \tag{2.17}$$

However, the electronic wavefunction must obey the Pauli principle, and as such, this expression does not take into account the electron spin. To ensure the Pauli principle is obeyed, the expression can be written as a Slater determinant in terms of spin-orbitals (product of an orbital wavefunction and the spin function):

$$\Psi^0(x; R) = (N_e!)^{-1/2} \det \mid \varphi_a(1)\varphi_b(2)...\varphi_z(N_e) \mid \tag{2.18}$$

or more simply

$$\Psi = \| \varphi_a \varphi_b ... \varphi_z \| \tag{2.19}$$

The Hartree-Fock (HF) method treats the electron-electron interactions in an average way; each electron is considered to be moving in an electrostatic field generated by the nuclei and the average field of the remaining electrons. Thus, HF is an inexact method with Ψ^0 treated as an inexact wavefunction, as this average behaviour of electrons does not consider the instantaneous electronic interactions, nor the quantum mechanical effects on electron distributions. Thus, in the HF approach, electron correlation is ignored.

2.7.2 Density Functional Theory

Density functional theory (DFT) is one of the most dominant computational techniques for molecular electronic structure determination and is used in this thesis determining structural assignments based on simulated vibrational spectra. The basis of this method is that the energy of an electronic system can be expressed in terms of the electron probability density, ρ. For a system of N_e electrons, $\rho(r)$ denotes the total electron density at a point, r, in space. DFT calculates the total electron density

$$\rho(r) = N_e \mid \Psi_{tot} \mid^2 \tag{2.20}$$

where Ψ_{tot} is the total electronic wavefunction. In 1964 Pierre Hohenberg and Walter Kohn theorised a proof known as the Hohenberg-Kohn existence theorem: "**The ground-state energy and all other ground-state electronic properties are uniquely determined by the electron density.**" Hence, the ground-state energy of a molecular system, E_0, is a function of the ground-state electron density, ρ_0, of the system, and as such, can be expressed as:

$$E_0[\rho_0(r)] = T[\rho_0(r)] + V_{ee}[\rho_0(r)] + V_{ne}[\rho_0(r)] \tag{2.21}$$

The V_{ne} term is the attractive potential energy term between the electrons and nuclei. The T and V_{ee} terms represent the kinetic energy and the potential energy electron-electron interaction, respectively. These two terms are independent; their expressions do not depend on the electron number or the coordinates and charges of the nuclei. The sum of these terms form the Hohenberg-Kohn functional. Unfortunately, the exact form of this functional is unknown, thus approximate functions must be used. The development of new approximate functions remains a big challenge in density functional theory.

In 1965, Walter Kohn and Lu Jeu Sham devised a different approach to deal with the inexact terms in the functional - accurately describing the kinetic energy of electrons by treating them as non-interacting fermions. This is known as the Kohn-Sham (KS) approach, which separates the electron kinetic energy functional into two parts, one which can be calculated exactly, and a small correction term. The KS approach is closely related to the HF method, as they both share identical formulae for the kinetic, electron-nuclear, and electron-electron energies. Separating the electron kinetic energy term (the major contribution equivalent to the HF kinetic energy) can be expressed:

$$H_\lambda = T + V_{ext}(\lambda) + \lambda V_{ee} \tag{2.22}$$

where V_{ext} is the external potential energy, which is equal to V_{ne} for $\lambda = 1$. For intermediate λ values, V_{ext} is adjusted to the same density obtained for when $\lambda = 1$ (*i.e.* the real system) and for non-interacting electrons, $\lambda = 0$. In the case where $\lambda = 0$, electrons are non-interacting so the exact solution to the Schrödinger equation can be expressed as a Slater determinant, composed of orbitals, ϕ_i, yielding an exact kinetic energy functional.

$$T_s = \sum_{i=1}^{N_e} \langle \phi_i \mid -\frac{1}{2}\nabla^2 \mid \varphi_i \rangle \tag{2.23}$$

This expression is only an approximation to the real kinetic energy, however it is a substantial improvement over the Thomas-Fermi (TF) formula. The exact kinetic energy can also be calculated from natural orbitals arising from the exact density matrix. However, representing the exact density requires an infinite number of natural orbitals, thus the density matrix is unknown. However, the density can be approximated and expressed as a set of one-electron functions (orbitals).

$$\rho_{(approx)} = \sum_{i=1}^{N_{elec}} \mid \phi_i \mid^2 \tag{2.24}$$

As stated earlier, the Kohn-Sham approach is to accurately describe the kinetic energy of electrons, assuming they are non-interacting fermions. In reality, however, electrons are interacting. This interaction needs to be included in the expression, and is stated as an exchange-correlation term. A general DFT expression can then be yielded:

$$E_{DFT}[\rho] = T_s[\rho] + E_{ne}[\rho] + J[\rho] + E_{xc}[\rho] \tag{2.25}$$

where $J[\rho]$ is the electron-electron repulsion energy. $E_{xc}[\rho]$ is the electron-electron exchange energy (electron-correlation functional) which accounts for kinetic energy of the interacting electrons and the quantum mechanical electron-electron interactions. The one-electron functions (orbitals) required to solve this expression are generated *via* the self consistent field (SCF) method. A set of orbitals are chosen as an initial guess and the Kohn-Sham expression is solved. The new, resultant orbitals generated are then used to solve the KS expression again. This process is repeated until the difference between the new and old orbitals is sufficiently small to a certain threshold.

The central task in DFT is to improve the approximation of the exchange-correlation functional. There exist a myriad of functionals whose coefficients have been adjusted for a better agreement with experimental data or with high level *ab initio* calculations. The simplest approximation is the local density approximation (LDA) which assumes the exchange-correlation functional depends only on a uniform electron gas. A more sophisticated approximation is the generalised gradient corrected (GGA) approach, accounting for changes (gradients) in the electron density which contribute to the exchange-correlation functional. BP86[138,139] is an example of a GGA functional and is widely used in the physical chemistry community. The performance of a particular functional, however, depends on the system under investigation. Typically, experimental data is required to compare with the functional to decide whether the functional is suitable. Another popular type of functional is the hybrid model, whereby a GGA functional is used but a certain fraction of the exchange interaction is calculated *via* Hartree-Fock exchange, attempting to improve the accuracy. An example of this was proposed by Perdew, Burke and Enzerhof,[140,141] taking 20% of the HF exchange energy, creating their PBE0 functional.[140–142] The fraction of HF exchange used is normally adjusted to fit a set of experimental data for a specific hybrid functional. Beyond these are meta-GGA functionals which include second order derivatives of the electron density $\nabla^2\rho(r)$ and/or the orbital kinetic energy. As a consequence, the computational costs of utilising meta-GGA functionals are usually significantly higher than that of GGA or hybrid functionals. Tao, Perdew, Staroverov and Scuseria produced the TPSS meta-GGA functional which includes the orbital kinetic energy terms.[143]

2.7.2.1 Basis Sets

A basis set is a combination of atom-centred mathematical functions used to represent atomic orbitals. The employed functions describe the radial and angular distributions of

electron density. These sets can then be employed to describe molecular orbitals. In DFT calculations, Kohn-Sham orbitals can be constructed from linear-combinations of a set of predefined basis functions, χ_α.

$$\phi_i = \sum_{\alpha}^{M_{basis}} c_{\alpha i}\chi_\alpha \tag{2.26}$$

This greatly reduces the optimisation time as the coefficients $c_{\alpha i}$ are the only variables. However, the accuracy of the calculation will depend on the choice and the number of basis functions. Minimal basis sets implement one function per atomic orbital, higher-level basis sets will include multiple basis functions per atomic orbital. Basis sets can be further augmented using polarisation and/or diffuse functions, allowing a greater distortion and/or radial extension from atomic symmetry and orbital size, yielding a more accurate molecular binding model. However the use of large basis sets increases the computational time significantly. For improved calculation efficiency the core electrons can be replaced with an effective core potential (ECP), which represents the electron-nucleus and inner electron interactions and takes relativistic effects into account.[144–146] As an example, calculations on the $Au^+(N_2O)_n$ complexes, employing the Def2TZVP basis set,[147,148] implements the ECP-60 effective core potential, whereby the 60 inner (core) electrons (along with the electron-electron and electron-nucleus interactions) are replaced with a pseudopotential. This is useful as, in most cases, it is the valence electrons (19 in the case of Au^+) that determine many of the chemical properties.

2.7.3 Computational Methodology

In chapters 3 and 4, geometry optimisation calculations were performed on starting geometries of $M^+(N_2O)_n$ complexes in a range of different spin states employing the B3P86 hybrid functional[149] coupled with the Def2TZVP basis set[147,148] using the Gaussian09 suite of pro-

grams.[150] To aid comparison with the experimental spectra, the wavenumbers of infrared bands in the simulated spectra were scaled by a factor of 0.932, derived from the calculated ν_3 stretch of isolated N_2O.[151] The functional and basis set were chosen as the simulated IR spectra generated are in reasonable agreement with experimental spectra. This functional and basis set combination has also been utilised successfully for similar metal-ligand complexes, $M^+(CO_2)_n$.[127] Harmonic vibrational frequency calculations were subsequently performed determining whether the optimised structures were true minima (possessing zero imaginary frequencies). For reaction profiles, detailed in chapter 4, transition states were also verified using vibrational frequency analysis (*i.e.* structures possessing one imaginary frequency). Transition states along these reaction profiles were linked to calculated minima by employing intrinsic reaction coordinate (IRC) calculations.

Calculations performed in chapter 5 employed the B3PW91-D3 hybrid density functional[149,152] coupled with the aug-cc-pVDZ basis set.[153,154] This combination produced simulated spectra in better agreement with the experimental IRPD spectra, when compared to using the B3P86 hybrid functional[149] coupled with the Def2TZVP basis set,[147,148] implemented in chapters 3 and 4.

The calculations presented in chapter 6 on $M_n^+(N_2O)$ clusters employed the hybrid version of the meta-GGA functional TPSS, including 10% exact exchange (TPSSh)[155] together with the Def2TZVP basis set.[147,148] This functional has been employed successfully on gold cluster-ligand complexes.[156] First, initial geometries of the bare cationic clusters were calculated, based on previous work on Au_n^+ clusters by Kappes,[48] and on Co_n^+ by Fielicke and coworkers.[157] Once the lowest energy geometry and spin state was identified, geometry optimisation along with frequency calculations were performed on various starting geometries of $M_n^+(N_2O)$ clusters (both dissociatively- and molecularly-bound). Simulated vibrational

spectra of $M^+(N_2O)_n$ and $M_n^+(N_2O)$ clusters were then compared to the observed spectra elucidating structures and binding motifs.

Chapter 3

Infrared Signature of Structural Isomers of Gas-Phase $M^+(N_2O)_n$ (M = Cu, Ag, Au) Ion-Molecule Complexes

This chapter presents the first study on the interactions involved between individual metal cations and nitrous oxide, combining infrared photodissociation (IRPD) spectroscopy and density functional theory (DFT) calculations. Group 11 metals were chosen as, in their cationic form, they offer a closed-shell, d^{10} electron configuration so that interactions with nitrous oxide are expected to be simpler than open-shell cations. The IRPD spectra show clear evidence of both nitrogen- and oxygen-bound ligands, giving a wide range of structural isomers for each complex. The evolution of the structures observed, as well as spectral trends for each metal center, are interpreted by considering the molecular orbitals involved in the

binding interactions and resulting calculated ligand binding energies. Many of the findings in this chapter are based on the publication: Infrared Signature of Structural Isomers of Gas-Phase $M^+(N_2O)_n$ (M = Cu, Ag, Au) Ion-Molecule Complexes, Cunningham, E. M.; Gentleman, A. S.; Beardsmore, P. W.; Iskra, A.; Mackenzie, S. R.; *J. Phys. Chem. A.*, **2017**, 121, 7565-7571.

3.1 Introduction

Extensive studies of N_2O reactions with atomic metal ions have been carried out, in particular by Lavrov *et al.*[100] 46 different metal cations with N_2O were surveyed with primary reaction channels identified including O-atom transfer, N-atom transfer, and N_2O addition. In this study, the authors modelled their inductively coupled plasma source to determine the relative populations of ground and excited electronic states at 5500 K. They found that excited states contributed 20% or less toward the overall populations of Cu^+, Ag^+, and Au^+. For the O-atom transfer reaction (forming the monoxide cation) to proceed exothermically, the oxygen atom affinity of the metal cation must exceed the oxygen atom affinity of nitrogen. Based on the oxygen atom affinities of the group 11 cations, the O-atom transfer reactions for all three metals are endothermic and as such, no reactions were observed. The N_2O addition reaction was observed exclusively for the group 11 monocations. Table 3.1 presents the primary and higher-order products for the reactions of metal cations with nitrous oxide. These addition reactions were presumed to occur by the collisional stabilisation reaction (shown in reaction 3.1) at 0.35 Torr of helium, rather than radiative association. Primary addition reactions were observed to proceed with small bimolecular rate coefficients, on the order of $k \leqslant 2.4 \times 10^{-12}$ cm^3 molecule^{-1} s^{-1}. The authors rationalised this low efficiency of addition to the weak binding energy of N_2O to the metal cation, governed

Table 3.1: Primary and higher-order product ions for reactions of atomic ions M^+ with nitrous oxide in helium at 0.35 ± 0.01 Torr and 295 ± 2 K. Table reproduced with permission from Lavrov, V. V.; Blagojevic, V.; Koyanagi, G. K.; Orlova, G.; Böhme, D. K. *J. Phys. Chem. A.*, **2004**, 108, 5610-5624.[100]

M^+	Primary Products	Higher-Order Products
Cu^+	$Cu^+(N_2O)$	$Cu^+(N_2O)_2$
Ag^+	$Ag^+(N_2O)$	$Ag^+(N_2O)_2$
Au^+	$Au^+(N_2O)$	$Au^+(N_2O)_2$

by electrostatic interactions which are weak due to the low dipole moment of N_2O (0.161 D). The rate coefficients for secondary N_2O addition were always higher than for primary addition, $k \leqslant 5$ x 10^{-12} cm^3 molecule^{-1} s^{-1}, which was attributed to the increased number of degrees of freedom in the secondary reaction intermediate, leading to longer lifetimes and thus higher rates of collisional stabilisation.

$$M^+ + N_2O + He \longrightarrow M^+N_2O + He \tag{3.1}$$

The tendency of ions with d^{10} electron configurations (Cu^+, Ag^+, Au^+, and Hg^{2+}) to form compounds in which the metal centre is ligated to only two ligands was first postulated by L. E. Orgel in 1958.[158] In particular, Au^+ and Hg^{2+} strongly tend to form compounds of low coordination number, in most cases linear XY_2 compounds. Treating ions as charged, non-polarisable spheres, the most stable arrangement of ligands about a given cation occupies high symmetry, yielding tetrahedral and octahedral coordinated cations. Distortion away from these symmetrical geometries is achieved through orbital mixing, or hybridisa-

tion. If the stabilisation due to orbital hybridisation is sufficiently large, it will compensate for the energy lost in distortion away from the electrostatically stable octahedral geometry. The most likely orbitals to be involved in the hybridisation are the d_{z^2} and s orbitals, since the energy separation between d and s orbitals is small for Cu^+, Ag^+, Au^+, and Hg^{2+}. It was also found that the expenditure of energy required for s-d hybridisation is proportional to the s-d energy separation. The low coordination of these ions was thus rationalised as the stabilisation due to s-d hybridisation which compensated for the energy lost by distorting from an octahedral geometry.

Matrix isolation studies on $ClCuN_2O$, $ClAgN_2O$, and AuN_2O complexes present the first experimental, infrared spectroscopic studies on group 11 atoms with nitrous oxide.[99,159] In each case, N_2O was co-deposited with laser-ablated metal halide (or pure Au) in excess argon onto a 11 K (4 K) CsI window. Infrared spectra were recorded using a Fourier transform infrared spectrometer. These spectra, coupled with simulated spectra from DFT calculations and isotopic substitution experiments, were then used to predict the structures of the observed reaction products. The copper- and silver-chloride were both found to react with N_2O to form linear ClMNNO complexes, with the terminal N atom of N_2O bound to the metal atom. Whereas the reactions of laser ablated gold atoms with N_2O yielded exclusively anionic products; $AuNO^-$ and $OAuNN^-$. No evidence was found for the formation of neutral or cationic products.

Infrared photdissociation studies on group 11 nitrosyl complexes, $M^+(NO)_n$ have been performed by Zhou and coworkers.[133,134] In a similar fashion to the study in this chapter, these complexes were formed by laser ablation of a metal disc in the presence of a helium/argon carrier gas and nitric oxide gas mixture, and detected *via* time-of-flight mass spectrometry. Complexes of interest were mass-selected and dissociated using tunable in-

frared radiation. Calculated vibrational spectra of low-lying structures, using density functional theory, were compared to the observed IRPD spectra to identify these gas-phase metal-nitrosyl structures. The group 11-nitrosyl complexes all exhibited different coordination numbers; Ag^+ with the largest of five, followed by Cu^+ of four, and Au^+ with a coordination number of two. The NO ligand was found to bind *via* the N-atom in a bent geometry, indicative of NO acting as a one-electron donor. Evidence was also found of ligand-ligand interactions in higher-order complexes, involving the $(NO)_2$ dimer bound *via* the two O atoms. Different from the work presented in this chapter, the Ar atom, when bound to the metal complex, has a strong influence on the geometric and electronic structures of the $M^+(NO)_n$ complexes.

Metal ion-ligand complexes are of significant importance, offering model environments to study molecular interactions that are key to a wide range of scientific fields, including catalytic processes. Despite this, experimental structural determination of metal ion-nitrous oxide complexes, $M^+(N_2O)_n$, has attracted little attention. This chapter presents the first infrared action spectroscopy study on gas-phase $M^+(N_2O)_n$ complexes, elucidating structural isomers, periodic trends, and ligand binding energies, all in a molecular orbital framework.

3.2 Experimental Methods

The instrument and technique employed in these studies has been described in detail in the previous chapter, hence only brief details will be given here. Gas-phase $M^+(N_2O)_n$ (M = Cu, Ag, Au) complexes along with their argon-tagged analogues are formed by 532 nm pulsed laser ablation of a rotating metal disc in the presence of an argon carrier gas seeded with 0.6-1.5 % nitrous oxide (with a backing pressure of 6 bar). The resulting molecular beam

is skimmed and charged species are detected by linear time-of-flight mass spectrometry.[128] Tunable pulsed infrared radiation in the region of 2150-2400 cm^{-1} (covering the asymmetric stretch of N_2O) is provided by an optical parametric oscillator/amplifier system. The infrared beam counterpropagates with the molecular beam and IRPD spectra are collected employing the "inert messenger" technique,[132,160–164] in which the loss of a weakly-bound argon atom from $M^+(N_2O)_n$-Ar complexes provides the signature of IR photon absorption as a function of wavenumber.

To aid in the assignment and interpretation of the experimental IRPD spectra, the structures and infrared spectra of energetically low-lying isomers were calculated using density functional theory employing the B3P86 hybrid functional[149] coupled with the Def2TZVP basis set.[147,148] All calculations were performed using the Gaussian09 suite of programs.[150]

3.3 $M^+(N_2O)_n$-Ar Time-of-Flight Spectra

Figure 3.1a shows the time-of-flight mass spectrum illustrating the production of $Cu^+(N_2O)_n$ complexes following the ablation of a copper disc in the presence of an argon carrier gas seeded with 0.6% N_2O. $Cu^+(N_2O)_n$ complexes and their argon-tagged counterparts are clearly identifiable. Additional ion-signals in the mass spectrum, indicated with asterisks, are assigned to $M^+(N_2O)_n(H_2O)$ complexes arising from contaminant background H_2O in the experimental chamber. The equivalent mass spectra presenting $Ag^+(N_2O)_n$ and $Au^+(N_2O)_n$ complexes are shown in figures 3.1b and 3.1c.

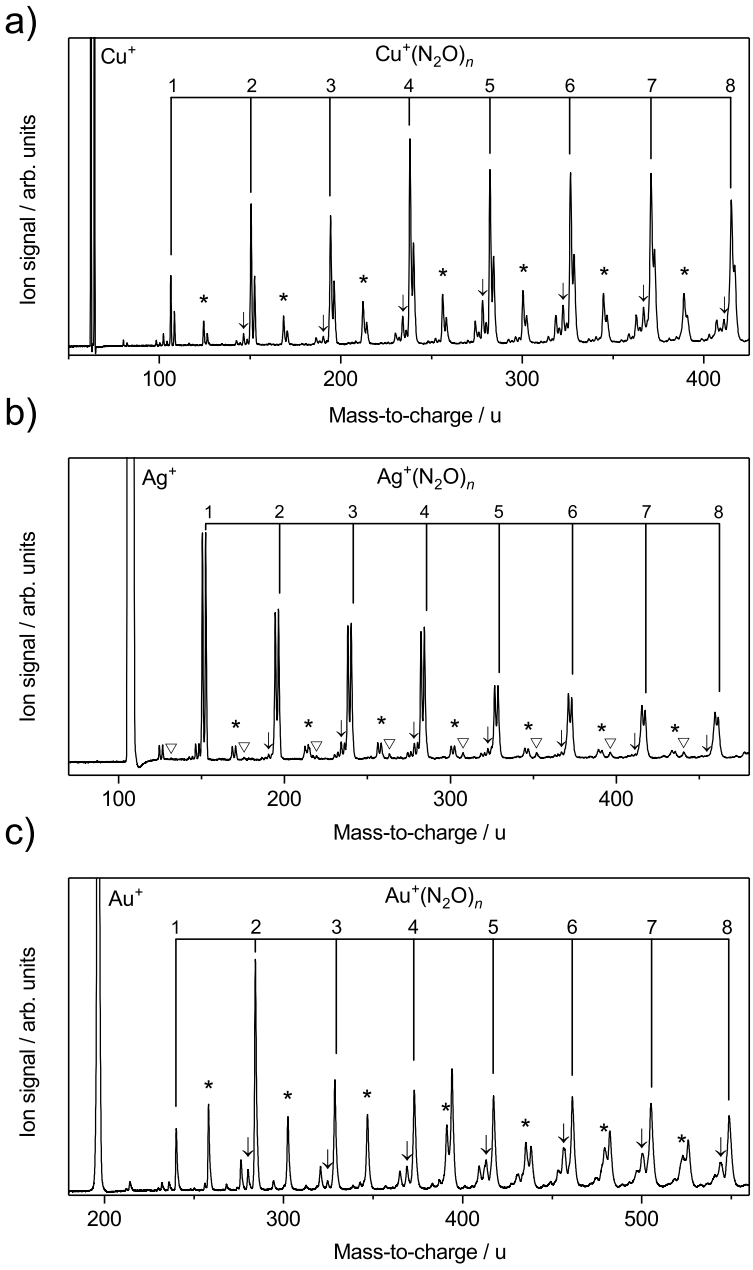

Figure 3.1: Time-of-flight mass spectra of $M^+(N_2O)_n$ complexes (M = (a) Cu, (b) Ag, and (c) Au) produced by laser ablation of a metal disc in an argon carrier gas seeded with 0.6-1.0% N_2O. Asterisks (*) mark $M^+(N_2O)_n(H_2O)$ complexes and arrows indicate Ar-tagged complexes. $(N_2O)_n^+$ complexes can also be identified ($\bigtriangledown$) in (b).

3.4 IRPD Spectra of $M^+(N_2O)_n$-Ar Complexes

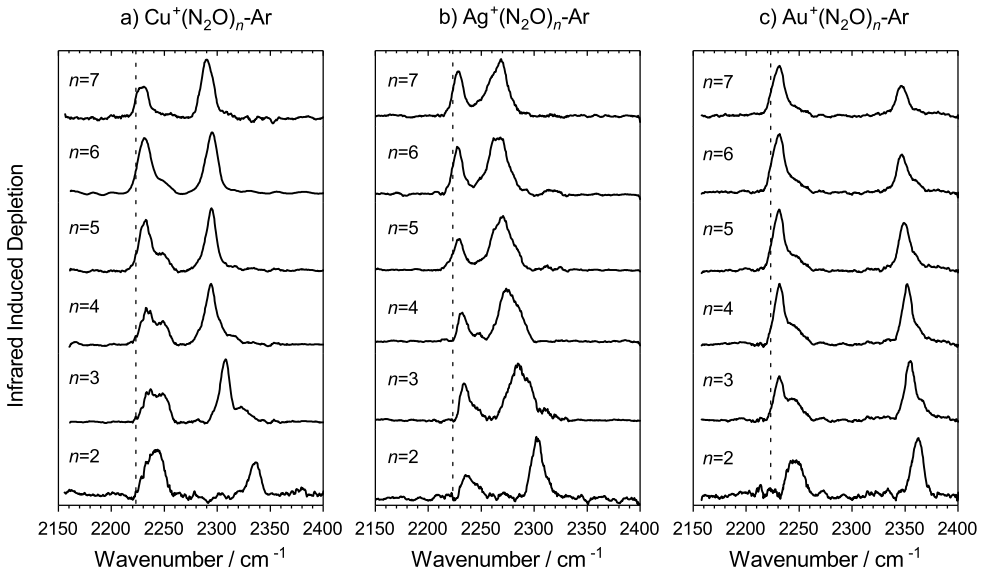

Figure 3.2: Experimental IRPD spectra of $M^+(N_2O)_n$-Ar (n = 2-7) complexes (M = (a) Cu, (b) Ag, and (c) Au). In each case, depletion occurs due to the loss of the Ar messenger atom. For comparison the depletion intensity for each spectrum was normalised with the maximum value in this region. The vertical dashed line indicates the wavenumber of the ν_3(N=N) asymmetric stretching mode in isolated N_2O at 2223.5 cm^{-1}.[151] Figure reproduced with permission from *J. Phys. Chem. A.*, **2017**, 121, 7565-7571.

The experimental IRPD spectra of the Ar-tagged $M^+(N_2O)_{2-7}$ (M = Cu, Ag, Au) complexes are shown in figure 3.2. In each case, two distinct bands are observed: one close to the asymmetric stretching frequency of isolated N_2O at 2223.5 cm^{-1},[151] and the other significantly blue-shifted by between 50 and 140 cm^{-1}. It is convenient in what follows to discuss each of the group 11 metal-N_2O complexes separately.

3.4.1 $Cu^+(N_2O)_n$-Ar Infrared Spectra

Figure 3.2a shows the experimental infrared depletion spectra of the $Cu^+(N_2O)_{2-7}$-Ar complexes. The most blue-shifted band ($n = 2$) is 112 cm^{-1} away from free N_2O and undergoes a smooth red-shift until $n = 4$. Confirmed by DFT calculated structures, $n = 4$ represents the coordination number, explaining the cease in red-shift for the n = 5-7 complexes.

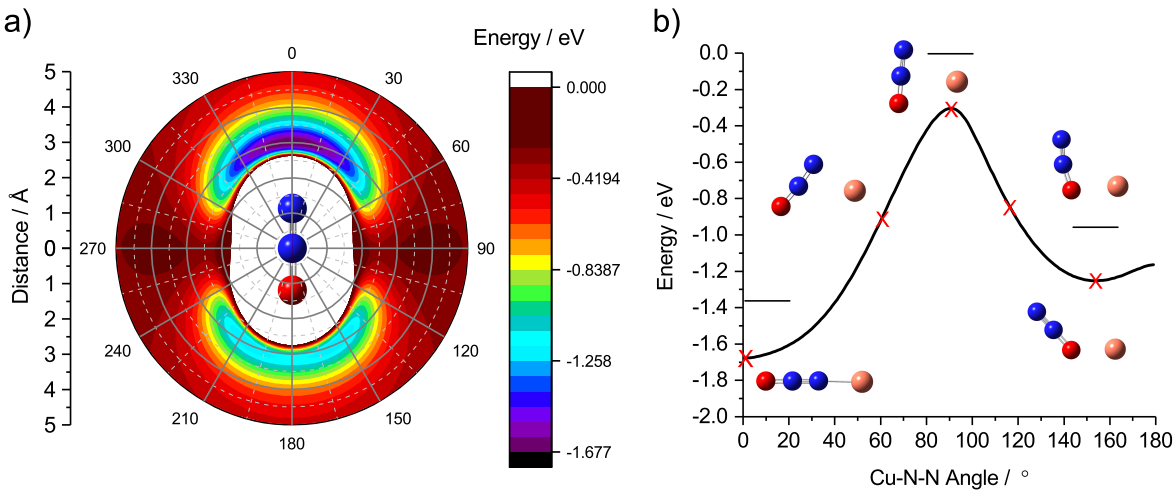

Figure 3.3: (a) Potential energy surface for the Cu^+N_2O complex showing a linear Cu^+NNO global minimum geometry and a secondary, non-linear Cu^+ONN minimum geometry. The surface was generated by fixing the N_2O molecule at its equilibrium geometry. (b) Minimum-energy pathway as a function of Cu-N-N bond angle illustrating the relative energies of the N- and O-bound minima. For this pathway the N_2O geometry was allowed to relax. Horizontal lines indicate the energy of the respective geometry-optimised structures including zero-point correction.

The first understanding of the observed spectra is provided when considering the Cu^+-N_2O potential energy surfaces. Figure 3.3a shows the calculated potential energy surface (PES) for the Cu^+N_2O complex illustrating a linear Cu^+NNO (*i.e.* bonding *via* the terminal N-atom) putative global minimum structure, together with a pronounced secondary minimum corresponding to the bent Cu^+ONN, O-bound isomer. This PES was generated by fixing the N_2O molecule at its equilibrium geometry and varying the distance and angle of Cu^+ relative to the N_2O. Distances were measured in increments of 0.1 Å and angles in measurements of 1°. The minimum energy pathway, figure 3.3b, shows the two minima separated by a barrier to internal rotation of *ca.* 1 eV. This pathway was generated by allowing the N_2O geometry to relax as a function of Cu-N-N bond angle (measured in increments of 1°).

During the clustering process within the molecular beam expansion, it is highly likely that excited isomeric forms will be trapped behind such barriers observed in the minimum-

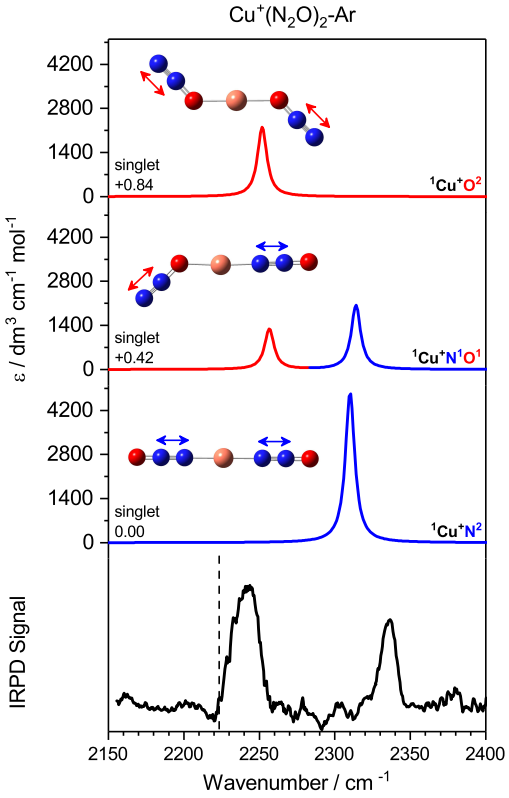

Figure 3.4: Experimental IRPD spectrum of the $Cu^+(N_2O)_2$-Ar complex along with simulated vibrational spectra of energetically low-lying isomers of the ground singlet state in the region of the N_2O asymmetric (N=N) stretch. Simulated vibrational bands corresponding to N-bound and O-bound ligands are indicated in blue and red, respectively. The relative energies are given in eV. The vertical dashed line indicates the wavenumber of the ν_3(N=N) asymmetric stretching mode in isolated N_2O at 2223.5 cm^{-1}.[151]

energy pathway leading to the presence of isomers with both N- and O-bound ligands. It is also clear from the PES shown in figure 3.3a that within each of these minima, ligands are free to undergo wide-amplitude motion. In what follows, a notation is adopted: $^{2S+1}M^+N^xO^y$, which represents a structure where x and y are integer values indicating the number of N- and O-bound ligands, where $x + y = n$ for a particular complex. As an example, $^1M^+N^1O^2$ represents a singlet-state complex of $M^+(N_2O)_3$ with one N-bound and two O-bound ligands.

The interpretation of multiple isomers present in the molecular beam is supported when

comparing the DFT spectral simulations of low-lying singlet isomers with the observed IRPD spectrum of $Cu^+(N_2O)_2$-Ar, figure 3.4. The doubly N-bound isomer, $^1Cu^+N^2$, represents the putative global minimum structure with the $^1Cu^+N^1O^1$ and $^1Cu^+O^2$ isomers representing higher-lying local minima. It is clear that the global minimum $^1Cu^+N^2$ structure cannot account for the two spectral bands observed, and as such, O-bound ligands must be present.

The spectrum is interpreted as followed: The band around 2240 cm^{-1} arises from isomers containing O-bound ligands. This binding motif *via* the terminal O-atom only weakly-perturbs the N=N bond, vibrational excitation of which occurs in this region. In contrast, the spectral feature at 2335 cm^{-1} is a signature of the presence of N-bound ligands. Binding *via* the terminal N-atom has a much larger effect on both the force constant of the N=N bond and the effective reduced mass, thus leading to the pronounced blue-shift observed in the spectrum relative to the free N_2O at 2223.5 cm^{-1} (table 3.5). The exact spectral position of each band is weakly dependent on the isomeric form. In this case the low wavenumber (O-bound) band in the $^1Cu^+O^2$ isomer is 6 cm^{-1} red-shifted relative to the same feature in the $^1Cu^+N^1O^1$ isomer. In a similar fashion, the N-bound band in the $^1Cu^+N^2$ is itself 6 cm^{-1} red-shifted to the same feature in the $^1Cu^+N^1O^1$ isomer. These differences in spectral position in different isomers are reflected in the widths of the spectral bands in the observed IRPD spectrum. These features may be resolvable as distinct peaks at higher resolution.

The linear global minimum structure, $^1Cu^+N^2$, presents one active IR band in this region (*i.e.* the antisymmetric combination of the N=N ligand stretches) and hence, the band at 2240 cm^{-1} is clear evidence of the presence of O-bound ligands. At this resolution, it is not possible to distinguish spectrally between: (i) a mixture of isomers, and (ii) a pure population of the $^1Cu^+N^1O^1$ isomer. Given the spectral widths of the observed bands, the

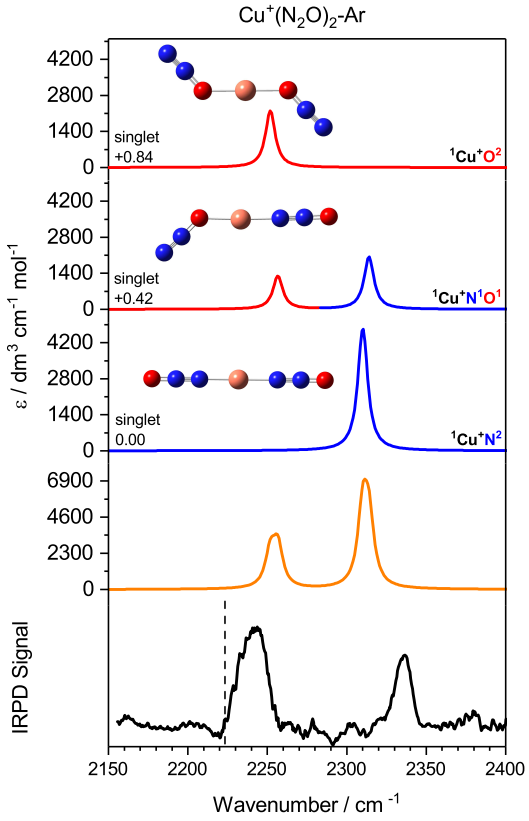

Figure 3.5: Experimental IRPD spectrum of the $Cu^+(N_2O)_2$-Ar complex along with simulated vibrational spectra of energetically low-lying isomers of the ground singlet state in the region of the N_2O asymmetric (N=N) stretch. Simulated vibrational bands corresponding to N-bound and O-bound ligands are indicated in blue and red, respectively. The combined IR spectrum assuming a 1:2:1 weighting of the three isomers is indicated in orange. The relative energies are given in eV. The vertical dashed line indicates the wavenumber of the ν_3(N=N) asymmetric stretching mode in isolated N_2O at 2223.5 cm^{-1}.[151]

former is much more likely.

The range of possible $^1Cu^+N^xO^y$ structural combinations in the molecular beam scales linearly with the number of ligands. The fractional population of each isomer, and hence, the contribution to the observed IR spectrum is a complicated function of the cluster growth mechanism. This mechanism is highly unlikely to produce a binomial coefficient (*i.e.* Pascal triangle) distribution. By virtue of the deeper well on the potential energy surface, a new N-bound ligand can always displace an existing O-bound ligand, but the reverse is not true. The final population distribution of isomers, although not necessarily thermal, is therefore

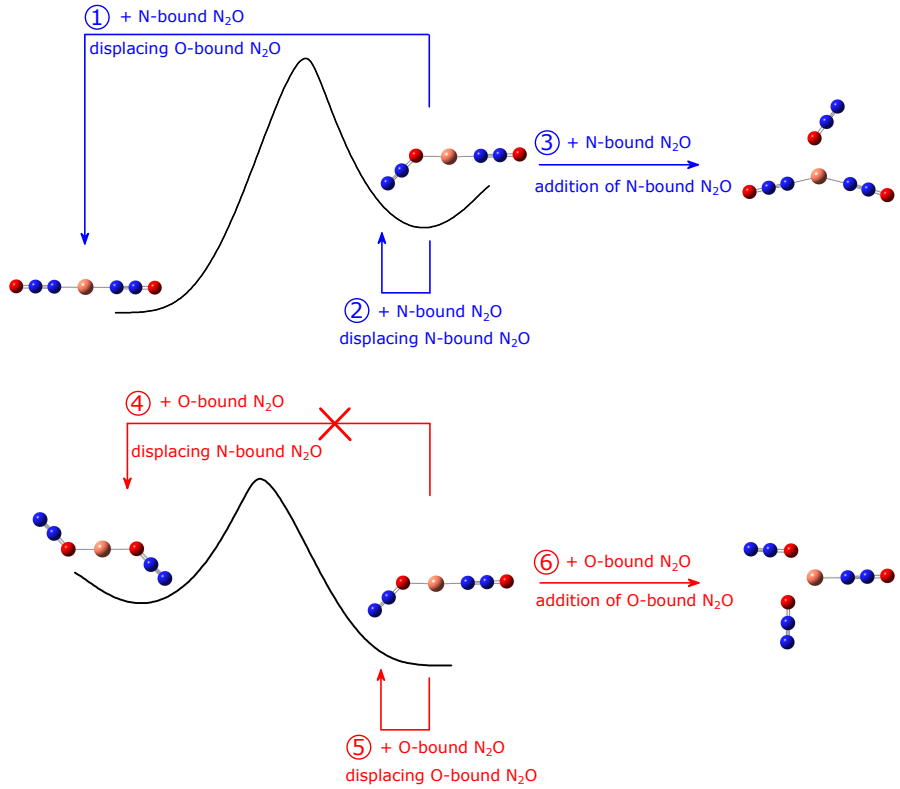

Figure 3.6: Schematic diagram illustrating how N_2O can either displace an existing ligand, or bind to the metal centre forming a higher-order complex, both of which rely on the incoming N_2O orientation. Scenarios in blue indicate an incoming N-bound N_2O ligand, and red an incoming O-bound N_2O ligand.

expected to be richer in the energetically lower-lying N-bound isomers. It is also likely that the addition of a new ligand, with the increase in internal energy this brings, will lead to further annealing of the parent cluster, enriching the lower-energy structures.

With the absence of quantitative information on the isomeric fractional population distribution in the molecular beam, the simulated IR spectra for the $Cu^+(N_2O)_2$ complexes were fitted to a convolution assuming a binomial distribution of isomers (figure 3.5). This produces satisfactory, however imperfect, agreement with the observed IRPD spectra.

Figure 3.6 shows a cartoon representation of the metal complex growth mechanisms for the small $n = 2$ and 3 complexes. Given the energy separation between $^1Cu^+N^2$ and $^1Cu^+N^1O^1$ (0.42 eV), an N-bound ligand can displace an O-bound ligand (figure 3.6 (1)),

but the reverse is less likely (figure 3.6 (4)). An N-bound ligand can replace an N-bound ligand (figure 3.6 (2)), or bind to the metal centre, forming the $^1Cu^+N^2O^1$ complex (figure 3.6 (3)). Similarly, an O-bound ligand can displace an O-bound ligand (figure 3.6 (5)), or bind to the metal centre forming the $^1Cu^+N^1O^2$ complex (figure 3.6 (6)).

Figure 3.7 presents the same spectral convolutions for the $Cu^+(N_2O)_3$ and $Cu^+(N_2O)_4$ complexes. In the case of $n = 4$, the isomer-specific spectral shifts of individual bands accounts for the spectral widths in the observed spectrum (particularly for the broad feature at 2240 cm^{-1}, presenting a FWHM of 25 cm^{-1}, despite an infrared laser linewidth of 4 cm^{-1}). The presence of a pure distribution of either the $^1Cu^+N^4$ or $^1Cu^+O^4$ minima can be ruled out, since in the case of $n = 2$, these would lead to a single feature in the observed spectrum. It is clear for all complex sizes that structures containing both N- and O-bound ligands are present, however, the relative abundances of each isomer cannot be inferred from the relative intensities of each spectral band.

Table 3.2: Zero-point corrected relative energies of the isomers of $Cu^+(N_2O)_n$ (n = 1-4) complexes calculated at the B3P86/Def2TZVP level of theory. Energies are relative to the global minimum geometry and electronic state for each complex.

Species	Isomer	$E_{rel.}$ / eV	Species	Isomer	$E_{rel.}$ / eV
$^1Cu^+(N_2O)$	N^1	0.00	$^1Cu^+(N_2O)_3$	N^3	0.00
	O^1	0.40		N^2O^1	0.24
$^3Cu^+(N_2O)$	N^1	3.36		N^1O^2	0.58
	O^1	3.41		O^3	0.97
$^1Cu^+(N_2O)_2$	N^2	0.00	$^1Cu^+(N_2O)_4$	N^4	0.00
	N^1O^1	0.42		N^3O^1	0.18
	O^2	0.84		N^2O^2	0.39
				N^1O^3	0.68
				O^4	1.03

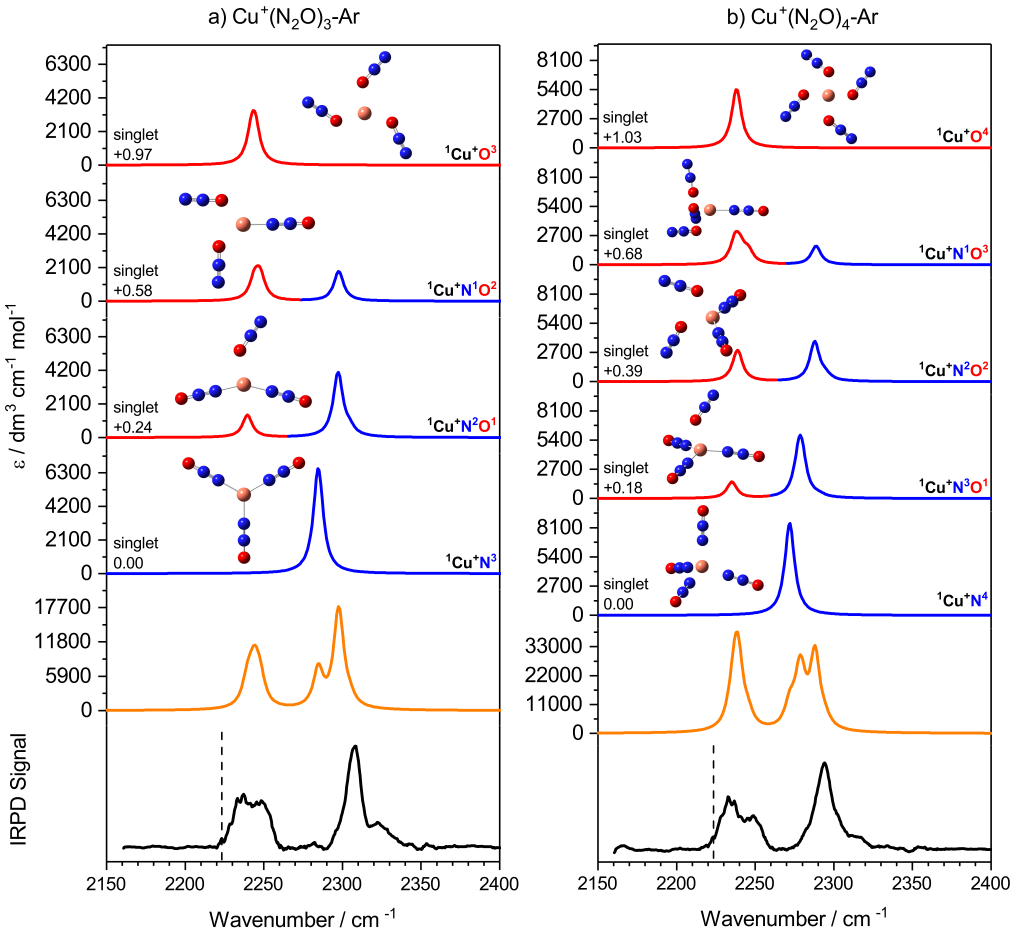

Figure 3.7: Experimental IRPD spectrum of the a) $Cu^+(N_2O)_3$-Ar and b) $Cu^+(N_2O)_4$-Ar complex along with simulated vibrational spectra of energetically low-lying isomers of the ground singlet state in the region of the N_2O asymmetric (N=N) stretch. Simulated vibrational bands corresponding to N-bound and O-bound ligands are indicated in blue and red, respectively. The combined IR spectrum in a) assumes a 1:3:3:1 weighting of the four isomers and in b) assumes a 1:4:6:4:1 weighting of the five isomers. In each case the IR spectrum is indicated in orange. The relative energies are given in eV. The vertical dashed line indicates the wavenumber of the ν_3(N=N) asymmetric stretching mode in isolated N_2O at 2223.5 cm^{-1}.[151]

3.4.2 $Ag^+(N_2O)_n$-Ar Infrared Spectra

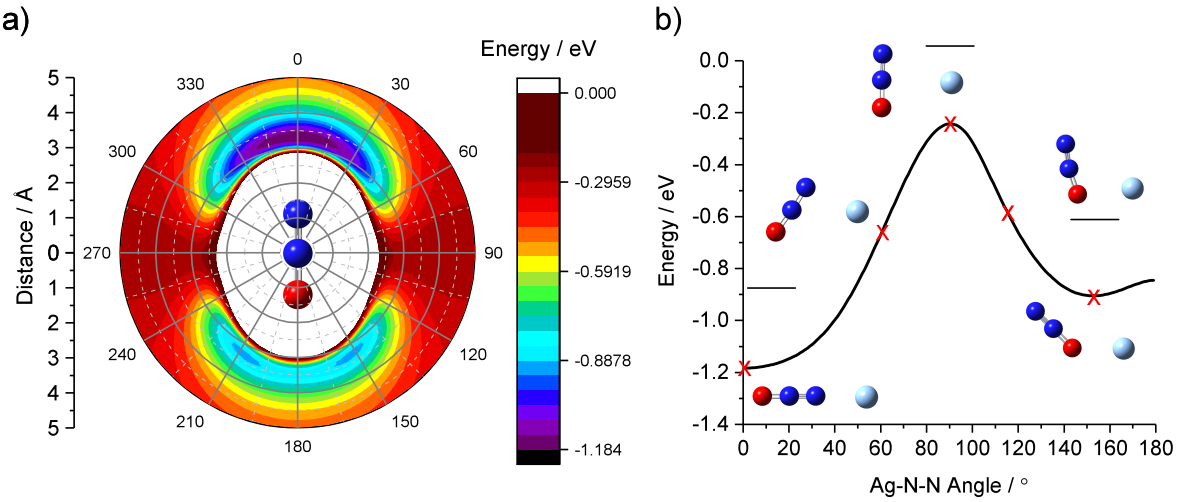

Figure 3.8: (a) Potential energy surface for the Ag^+N_2O complex showing a linear Ag^+NNO global minimum geometry and a secondary, non-linear Ag^+ONN minimum geometry. The surface was generated by fixing the N_2O molecule at its equilibrium geometry. (b) Minimum-energy pathway as a function of Ag-N-N bond angle illustrating the relative energies of the N- and O-bound minima. For this pathway, the N_2O geometry was allowed to relax. Horizontal lines indicate the energy of the respective geometry-optimised structures including zero-point correction.

The IRPD spectra for the $Ag^+(N_2O)_{2-7}$-Ar complexes are presented in figure 3.2b. A similar trend observed in the $Cu^+(N_2O)_n$-Ar complexes is found here in which the most blue-shifted band is observed at $n = 2$, with this band displaying a smooth red-shift upon increasing complex size up to $n = 4$. Just as with the $Cu^+(N_2O)_n$ complexes, and confirmed by DFT calculations, $n = 4$ represents a coordination number. Similar also to the $Cu^+(N_2O)_n$ complexes, each spectrum presents a band near the asymmetric stretch of isolated N_2O, displaying a weak dependence on the number of ligands attached, apart from an increase in relative intensity and a slight shift towards the free N_2O stretch.

As with the $Cu^+(N_2O)_n$ complexes, understanding these spectra becomes clear when considering the calculated potential energy surfaces, figure 3.8. The potential energy surface for the Ag^+N_2O complex also presents a putative global minimum linear N-bound structure, with a secondary O-bound minimum structure displaying a bent geometry. These minima

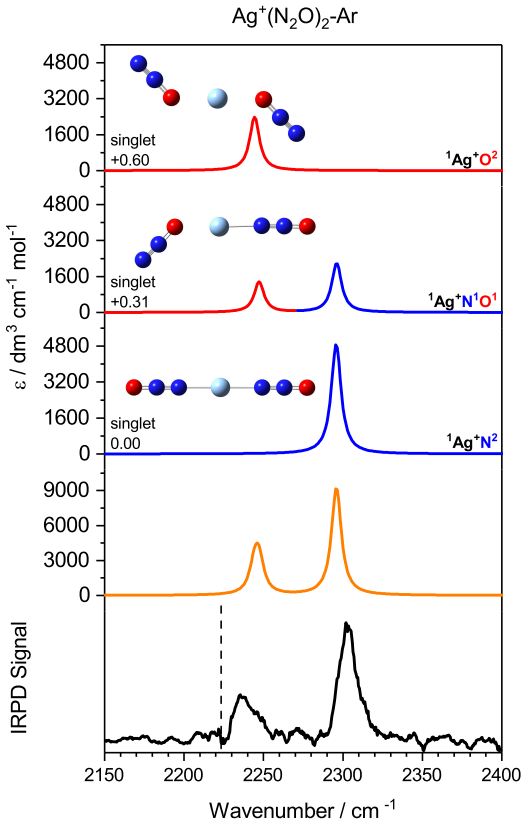

Figure 3.9: Experimental IRPD spectrum of the $Ag^+(N_2O)_2$-Ar complex along with simulated vibrational spectra of energetically low-lying isomers of the ground singlet state in the region of the N_2O asymmetric (N=N) stretch. Simulated vibrational bands corresponding to N-bound and O-bound ligands are indicated in blue and red, respectively. The combined IR spectrum assuming a 1:2:1 weighting of the three isomers is indicated in orange. The relative energies are given in eV. The vertical dashed line indicates the wavenumber of the ν_3(N=N) asymmetric stretching mode in isolated N_2O at 2223.5 cm^{-1}.[151]

are also separated by a significant barrier to internal rotation.

To interpret the observed IRPD spectra, DFT calculations on the $Ag^+(N_2O)_n$ complexes were performed to find minimum structures along with their simulated vibrational spectra. Figure 3.9 shows the observed IRPD spectrum of $Ag^+(N_2O)_2$-Ar, along with calculated low-lying minima and their corresponding simulated IR spectra for the $Ag^+(N_2O)_2$ complexes fitted to a convolution assuming a binomial distribution of isomers (*i.e.* 1:2:1). The spectral positions (2303 cm^{-1} and 2239 cm^{-1}), along with the relative intensities of these bands, agree well with the combined simulated spectrum shown in orange. Just as the case for

Table 3.3: Zero-point corrected relative energies of the isomers of $Ag^+(N_2O)_n$ (n = 1-4) complexes calculated at the B3P86/Def2TZVP level of theory. Energies are relative to the global minimum geometry and electronic state for each complex.

Species	Isomer	$E_{rel.}$ / eV	Species	Isomer	$E_{rel.}$ / eV
$^1Ag^+(N_2O)$	N^1	0.00	$^1Ag^+(N_2O)_3$	N^3	0.00
	O^1	0.26		N^2O^1	0.14
$^3Ag^+(N_2O)$	N^1	4.34		N^1O^2	0.37
	O^1	4.39		O^3	0.61
$^1Ag^+(N_2O)_2$	N^2	0.00	$^1Ag^+(N_2O)_4$	N^4	0.00
	N^1O^1	0.31		N^3O^1	0.11
	O^2	0.60		N^2O^2	0.24
				N^1O^3	0.42
				O^4	0.62

$n = 2$ for the $Cu^+(N_2O)_n$ series, the observed spectrum comprises a mixture of the three isomers $^1Ag^+N^2$, $^1Ag^+N^1O^1$ and $^1Ag^+O^2$.

This interpretation can be applied to higher order complexes (n = 3,4), the calculated structures along with simulated spectra of which are shown in figure 3.10. Similar to the $Cu^+(N_2O)_n$ complexes, the agreement between the experimental IRPD spectra and the binomial distribution of isomers (orange spectra) is satisfactory. In particular, for $n = 3$, the broad feature at *ca.* 2286 cm^{-1} is a convolution of isomers containing an N-bound ligand, all of which present a unique spectral shift accounting for the broadness of the observed band.

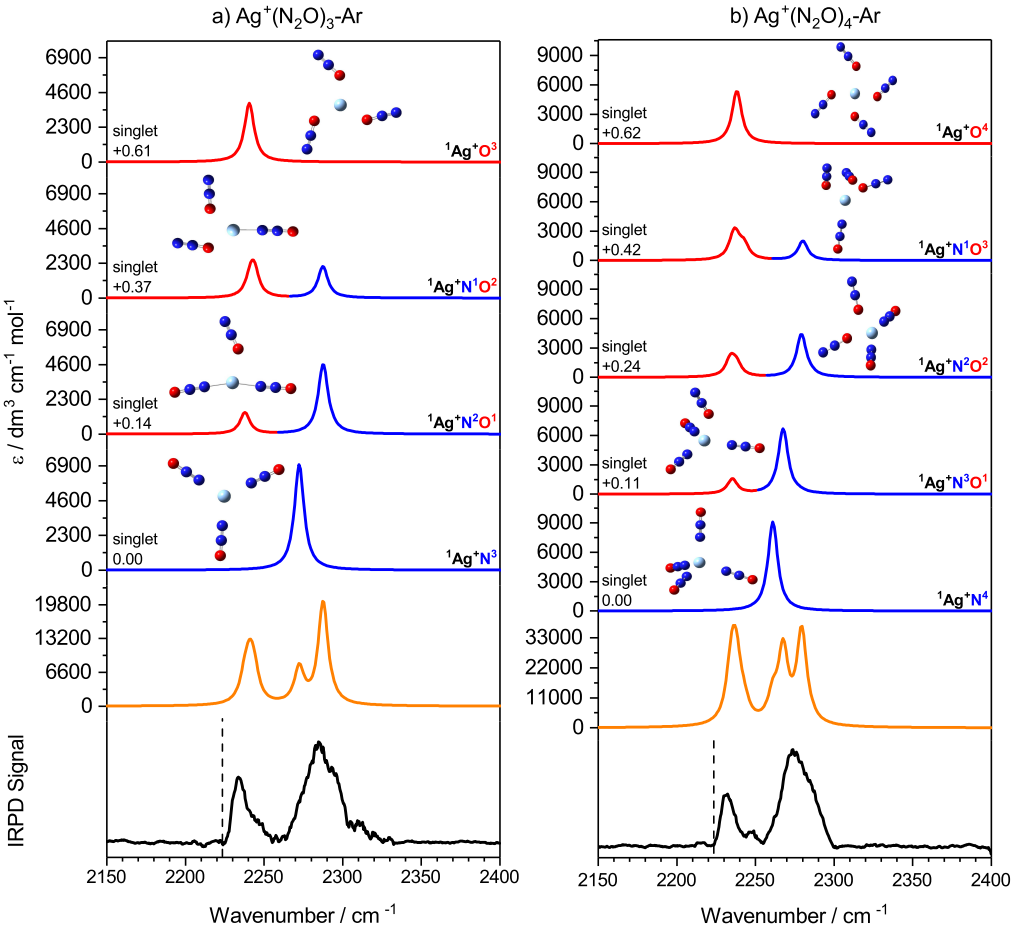

Figure 3.10: Experimental IRPD spectrum of the a) $Ag^+(N_2O)_3$-Ar and b) $Ag^+(N_2O)_4$-Ar complex along with simulated vibrational spectra of energetically low-lying isomers of the ground singlet state in the region of the N_2O asymmetric (N=N) stretch. Simulated vibrational bands corresponding to N-bound and O-bound ligands are indicated in blue and red, respectively. The combined IR spectrum in a) assumes a 1:3:3:1 weighting of the four isomers and in b) assumes a 1:4:6:4:1 weighting of the five isomers. In each case the IR spectrum is indicated in orange. The relative energies are given in eV. The vertical dashed line indicates the wavenumber of the ν_3(N=N) asymmetric stretching mode in isolated N_2O at 2223.5 cm^{-1}.[151]

3.4.3 $Au^+(N_2O)_n$-Ar Infrared Spectra

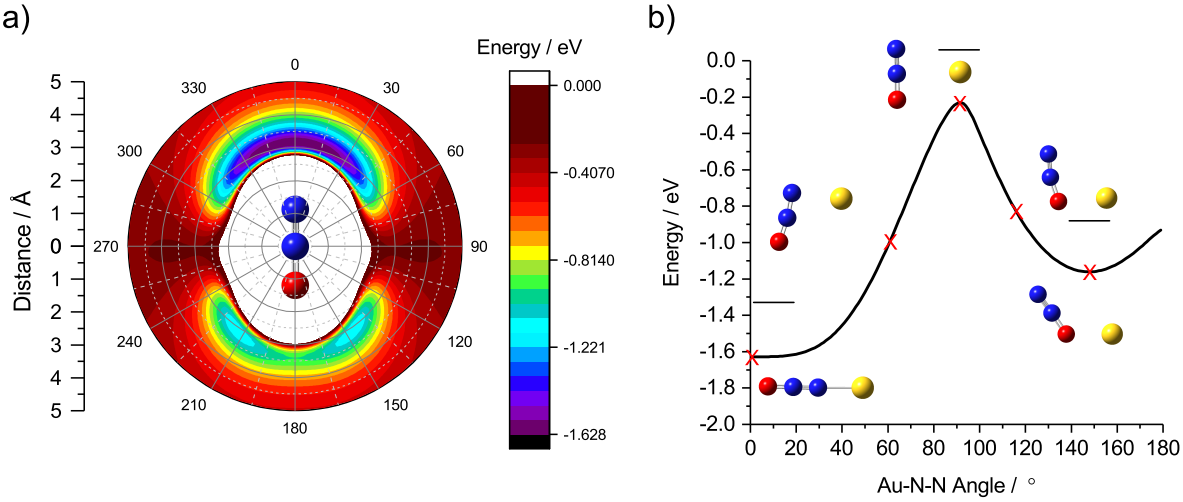

Figure 3.11: (a) Potential energy surface for the Au^+N_2O complex showing a linear Au^+NNO global minimum geometry and a secondary, non-linear Au^+ONN minimum geometry. The surface was generated by fixing the N_2O molecule at its equilibrium geometry. (b) Minimum-energy pathway as a function of Au-N-N bond angle illustrating the relative energies of the N- and O-bound minima. For this pathway, the N_2O geometry was allowed the relax. Horizontal lines indicate the energy of the respective geometry-optimised structures including zero-point correction. Figure reproduced with permission from *J. Phys. Chem. A.*, **2017**, 121, 7565-7571.

The experimental IRPD spectra for the $Au^+(N_2O)_n$-Ar complexes are presented in figure 3.2c. The trend in the blue-shifted band is different to that found in the $Cu^+(N_2O)_n$-Ar and $Ag^+(N_2O)_n$-Ar complexes. Here, the blue-shifted band only slightly decreases in shift upon addition of N_2O ligands (a reduction of 15 cm^{-1} from $n = 2$ to $n = 7$). Different also from the $Cu^+(N_2O)_n$ and $Ag^+(N_2O)_n$ complexes, in which the coordination number was found to be four, the coordination number in the case of gold is two. In each spectrum shown in figure 3.2c, there is a feature close to the asymmetric stretch of isolated N_2O. Upon increasing complex size, this band becomes more intense relative to the blue-shifted band, also lending to the proposed idea of a coordination number of two. Considering the $n = 7$ spectrum, the band at 2231 cm^{-1} is 1.68 times more intense than the blue-shifted band at 2347 cm^{-1}. Core N-bound ligands are assigned to the blue-shifted band in all spectra,

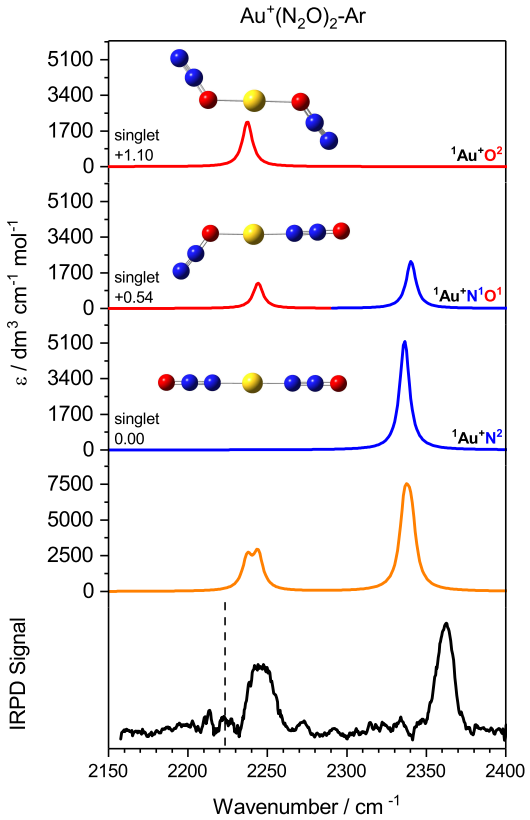

Figure 3.12: Experimental IRPD spectrum of the $Au^+(N_2O)_2$-Ar complex along with simulated vibrational spectra of energetically low-lying isomers of the ground singlet state in the region of the N_2O asymmetric (N=N) stretch. Simulated vibrational bands corresponding to N-bound and O-bound ligands are indicated in blue and red, respectively. The combined IR spectrum assuming a 1:2:1 weighting of the three isomers is indicated in orange. The relative energies are given in eV. The vertical dashed line indicates the wavenumber of the ν_3(N=N) asymmetric stretching mode in isolated N_2O at 2223.5 cm^{-1}.[151]

whereas the band close to the isolated N_2O stretch is assigned as either an O-bound core ligand, or N-/O-bound ligands in the outer coordination sphere. Hence, at $n = 7$, the intense feature at 2231 cm^{-1} is assigned as a convolution of: (i) five outer N_2O ligands (N-/O-bound), and (ii) O-bound core ligands, with the blue-shifted band at 2347 cm^{-1} assigned as two N-bound core ligands. Since there are more contributions from the outer sphere ligands due to a low coordination number, this can help rationalise the increase in intensity of the band close to the isolated N_2O stretch upon increasing ligation.

These assignments are strengthened when considering the calculated potential energy

surface (figure 3.11), along with the simulated vibrational spectra of low-lying isomers for $n = 2$ (figure 3.12). Just as with the Cu^+N_2O and Ag^+N_2O complexes, the calculated potential energy surface for Au^+N_2O shows a putative global minimum linear Au^+NNO structure with a secondary O-bound, bent minimum with both minima separated by a significant barrier to internal rotation. The band positions, along with the spectral widths and relative intensities of the observed spectrum for $n = 2$, agrees well with the combined simulated IR spectrum (orange). The interpretation here is the same; the experimental IRPD spectrum of $Au^+(N_2O)_2$-Ar comprises a mixture of the isomers $^1Au^+N^2$, $^1Au^+N^1O^1$ and $^1Au^+O^2$.

The coordination number of two for the $Au^+(N_2O)_n$ complexes can be further identified when considering the calculated structures and simulated IR spectra presented in figure 3.13. The triply N-bound isomer (*i.e.* $^1Au^+N^3$) shows a T-shaped structure, with two core N-bound ligands and an outer N-bound ligand. The two core Au^+-N distances are calculated at 1.99 Å with the third considerably longer at 3.16 Å. The simulated spectrum shows that this third N_2O ligand is weakly-bound to the metal-centre as its N=N stretch is close to the isolated N_2O stretch and therefore resides in an outer coordination sphere.

Table 3.4: Zero-point corrected relative energies of the isomers of $Au^+(N_2O)_n$ (n = 1-4) complexes calculated at the B3P86/Def2TZVP level of theory. Energies are relative to the global minimum geometry and electronic state for each complex.

Species	Isomer	$E_{rel.}$ / eV	Species	Isomer	$E_{rel.}$ / eV
$^1Au^+(N_2O)$	N^1	0.00	$^1Au^+(N_2O)_3$	N^3	0.00
	O^1	0.45		N^2O^1	0.52
$^3Au^+(N_2O)$	N^1	2.51		N^1O^2	0.54
	O^1	2.58		O^3	1.05
$^1Au^+(N_2O)_2$	N^2	0.00	$^1Au^+(N_2O)_4$	N^4	0.00
	N^1O^1	0.54		N^3O^1	0.49
	O^2	1.10		N^2O^2	0.50
				N^1O^3	0.51
				O^4	1.02

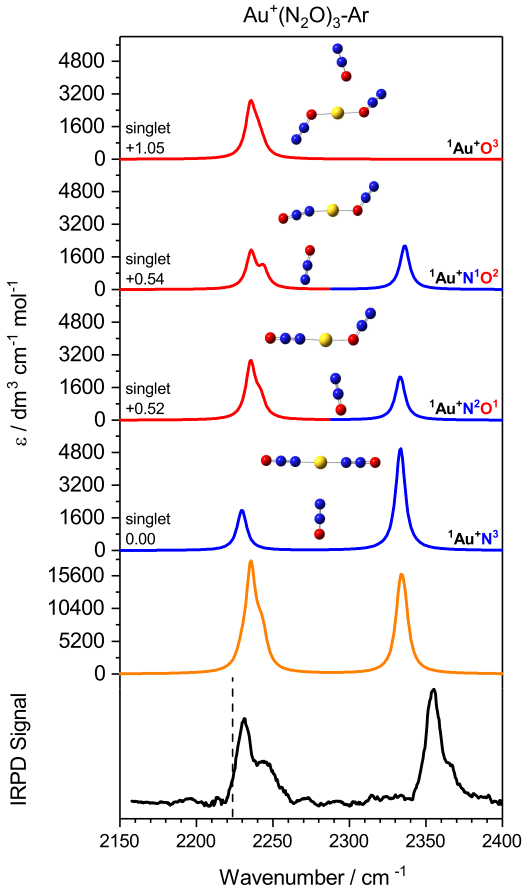

Figure 3.13: Experimental IRPD spectrum of the $Au^+(N_2O)_3$-Ar complex along with simulated vibrational spectra of energetically low-lying isomers of the ground singlet state in the region of the N_2O asymmetric (N=N) stretch. Simulated vibrational bands corresponding to N-bound and O-bound ligands are indicated in blue and red, respectively. The combined IR spectrum assuming a 1:3:3:1 weighting of the four isomers is indicated in orange. The relative energies are given in eV. The vertical dashed line indicates the wavenumber of the ν_3(N=N) asymmetric stretching mode in isolated N_2O at 2223.5 cm^{-1}.[151]

3.4.4 $M^+(N_2O)_n$-Ar Spectral Trends

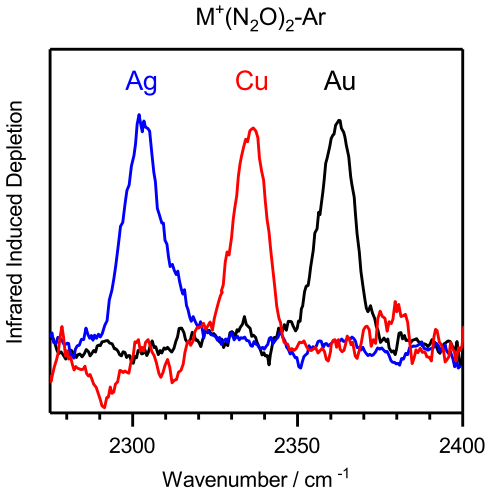

Figure 3.14: Experimental IRPD spectra of the $M^+(N_2O)_2$-Ar (M = Cu, Ag, Au) complexes in the region of N-bound N_2O ligands. IRPD spectra for the copper, silver and gold species are indicated in red, blue and black, respectively.

For ease of comparison, the N-bound bands in the $n = 2$ case for all three metals are presented in figure 3.14. As can be seen, the extent of blue-shift is the largest for gold, followed by copper and the smallest for silver. These differences in blue-shift can be understood when considering the valence orbitals involved in the M^+-N_2O interaction. Figure 3.15 shows the calculated valence orbital energies of the group 11 cations along with the lowest unoccupied molecular orbital (LUMO) (3π), highest occupied molecular orbital (HOMO) (2π), and HOMO-1 (7σ) orbital of nitrous oxide. As discussed previously in section 1.5, the 7σ orbital of N_2O is antibonding with respect to the N=N bond. Therefore, σ-donation from this HOMO-1 orbital into the metal centre will strengthen the N=N bond resulting in a spectral blue-shift.

Inspection of the resulting molecular orbitals involved, presented in figure 3.16, shows that the interaction between N-bound ligands and the metal centre is dominated by σ-donation from nitrous oxide to metal-centred s-d_{z^2} hybrid orbitals, formed from the vacant

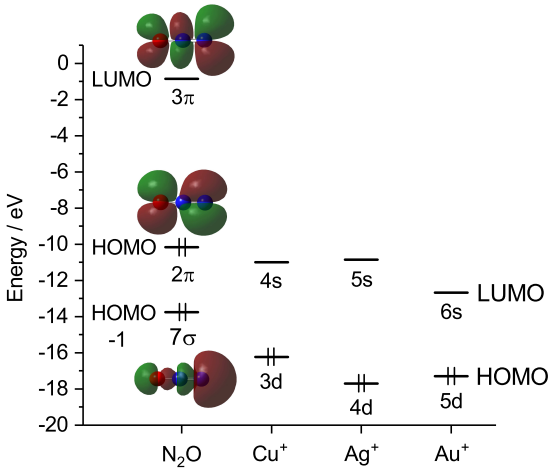

Figure 3.15: Valence orbital energies calculated at the B3P86/Def2TZVP level of theory for N_2O, Cu^+, Ag^+, and Au^+. Figure reproduced with permission from *J. Phys. Chem. A.*, **2017**, 121, 7565-7571.

n*s* and the HOMO d_{z^2} orbitals on the metal cation. Hybridisation of *s*-*d* orbitals was first postulated by Orgel to account for the special stability of linear d^{10} metal cation M^+-L_2 complexes relative to their tetrahedral and octahedral counterparts, in particular for Au^+ complexes.[158] The molecular orbital of the $Au^+(N_2O)_2$ complex (N-bound) presenting the same orbital interaction behaviour within a linear geometry is shown in figure 3.17. The interaction here is also between the *s*-d_{z^2} hybrid orbital on Au^+ and the 7σ orbital of N_2O. The strength of the M^+-N_2O interaction, and in turn the observed spectral blue-shift, does not correlate with the 7σ-M^+ LUMO energy gap, but instead on the degree of *s*-*d* hybridisation induced on the metal cation upon complexation. The degree of *s*-*d* hybridisation depends inversely on the M^+ HOMO-LUMO energy gap.

As shown in figure 3.18, the magnitude of the energy gap does indeed follow the trend $Au^+ < Cu^+ < Ag^+$. The small HOMO-LUMO energy gap in Au^+ arises from relativistic effects and reflects the relative stability of linear Au^+-L_2 complexes compared with the Cu^+ and Ag^+ counterparts. This argument can be extended to explain the coordination numbers

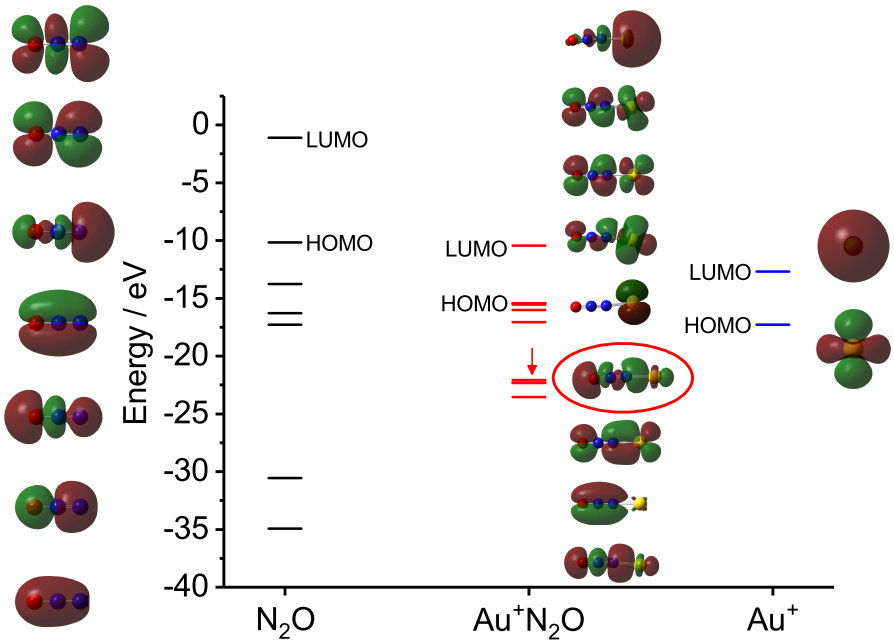

Figure 3.16: Valence orbital energies of N_2O, Au^+N_2O (N-bound) and Au^+ calculated at the B3P86/Def2TZVP level of theory. The ordering of the valence orbital energies (represented by bars) corresponds to the molecular orbitals shown. The highlighted molecular orbital shows the first bonding interaction between the 7σ orbital of N_2O and the s-d_{z^2} hybridised orbital of Au^+.

observed in the spectra for each metal cation. With each successive ligand addition, the degree of σ-donation decreases, reducing the spectral blue-shift associated with N-bound ligands. As discussed before, this can be seen in the IRPD spectra in figure 3.2, whereby the reduction in blue-shift of the N-bound band ceases at $n = 2$ for Au^+ but continues to $n = 4$ for Cu^+ and Ag^+.

The coordination numbers of the three metals is further proved when considering the calculated ligand dissociation energies. Figure 3.19 shows the calculated binding energies of successive N-bound N_2O ligands for $Cu^+(N_2O)_n$, $Ag^+(N_2O)_n$ and $Au^+(N_2O)_n$ complexes. Strongly-bound M^+-L_2 structures are evident in the clear marked drop in binding energy for the third ligand relative to that of the first two ligands. In the case of copper and silver there is a second, less pronounced drop between $n = 4$ and 5, consistent with the trend in spectral blue-shifts supporting the idea that four is the coordination number for these two

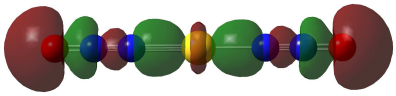

Figure 3.17: Molecular orbital of the $^1Au^+N^2$ isomer of $Au^+(N_2O)_2$ calculated at the B3P86/Def2TZVP level of theory showing the interaction of the s-d_{z^2} hybrid orbital on Au^+ with the 7σ orbital from two N_2O ligands, forming a linear complex.

metals.

Since this the first IRPD study on $M^+(N_2O)_n$ complexes, these findings can most appropriately be compared with IR studies of $M^+(NO)_n$ (M = Cu, Ag, Au) complexes, explored by Zhou and coworkers.[133,134] Findings on the nitrosyl complexes, consistent with the present work, show clear step decreases in the bond dissociation energies, for all coinage metals, between $n = 2$ and 3, with further evidence of coordination numbers at $n = 4$ for copper, and $n = 5$ for silver. Furthermore, the same pattern for stronger ligand binding to gold and copper ions compared to silver ions was observed. The core M-L binding energies in the two types of metal-ligand complex are surprisingly similar for the two ligands. One difference between the complexes of the two ligands is that within the nitrosyl complexes, there is evidence of a higher degree of ligand-ligand interaction than is observed in this study of N_2O complexes.

Contrastingly, O-bound N_2O interactions are dominated by electrostatic interactions. Orbital overlap between the occupied π orbitals on the O atom (HOMO of N_2O) and the unoccupied s orbitals on the metal cation is inefficient, so the metal cation centre interacts directly with one of the lone electron pairs on the O atom. This interaction accounts for the two equivalent, non-linear O-bound minima on the potential energy surfaces. The calculated barrier (obtained at 180 °) between the equivalent O-bound minima is small, but the largest

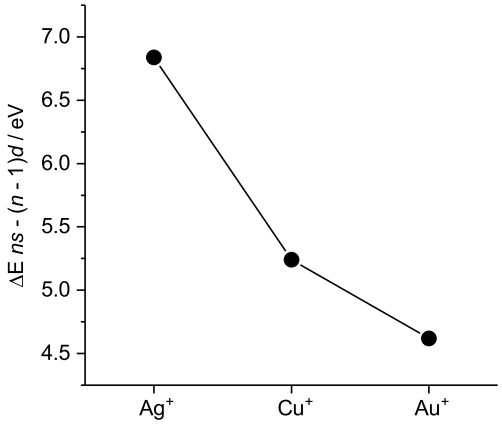

Figure 3.18: Valence orbital energy difference between the ns (LUMO) and $(n$ - $1)d$ (HOMO) for Ag^+, Cu^+, and Au^+ calculated at the B3P86/Def2TZVP level of theory.

for Au^+N_2O at 0.23 eV (figure 3.11), followed by Cu^+N_2O at 0.09 eV (figure 3.3) and then Ag^+N_2O at 0.06 eV (figure 3.8). This small barrier found in all metal complexes suggests O-bound ligands undergo large amplitude motion in this potential well. However, since the measured N=N stretch in O-bound ligands is largely unaffected by this interaction, there is no clear spectral signature of this effect at the resolution employed here.

Table 3.5 presents the calculated bond distances, force constants, and reduced masses of the group 11 nitrous oxide complexes. When compared to the calculated N=N and N=O bond distances of isolated N_2O, binding *via* the terminal N atom leads to a reduction in the N=O bond distance, and an increase in the N=N bond distance. Contrastingly binding *via* the terminal O atom leads to a decrease in the N=N bond distance and an increase in the N=O bond distance. However, the blue-shifts observed for the N-bound group 11 nitrous oxide complexes are more reflective of the force constant, k, rather than bond distances or the effective reduced mass. Shown in table 3.5, the force constant is increased for N-bound complexes and is increased the furthest for Au^+, followed by Cu^+, and then Ag^+. The blue-shifts observed in the IRPD spectra are thus a combination of the increased force

Table 3.5: Bond distances (nitrous oxide molecule along with M-X where X is the terminal atom, *i.e.* N or O), reduced masses, and force constants for the lowest energy N- and O-bound isomers of $M^+(N_2O)$ (M^+ = Cu, Ag, Au) complexes calculated at the B3P86/Def2TZVP level of theory.

Species	N=N / Å	N=O / Å	k / mDyn/Å	μ / Da	M-X / Å
N_2O	1.120	1.180	47.27	14.10	-
$^1Cu^+NNO$	1.123	1.150	51.21	14.13	1.879
$^1Cu^+ONN$	1.109	1.205	48.46	14.06	1.968
$^1Ag^+NNO$	1.123	1.152	50.34	14.13	2.173
$^1Ag^+ONN$	1.100	1.200	48.20	14.06	2.281
$^1Au^+NNO$	1.122	1.149	51.83	14.13	2.030
$^1Au^+ONN$	1.109	1.209	47.47	14.05	2.184

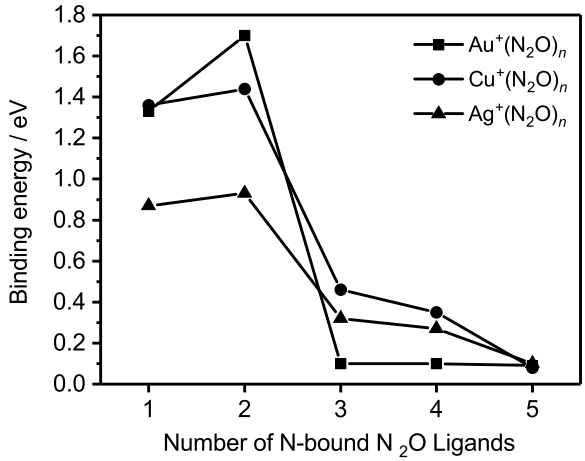

Figure 3.19: Successive ligand binding energies of N-bound $M^+(N_2O)_n$ complexes calculated as $E[M^+(N_2O)_n]$ - $E[M^+(N_2O)_{n-1}]$ - $E[N_2O]$ including zero-point correction. Figure reproduced with permission from *J. Phys. Chem. A.*, **2017**, 121, 7565-7571.

constant on the N=N bond (when bound *via* the terminal N-atom) and σ donation from the 7σ orbital into the metal centre, strengthening the N=N bond.

The IRPD spectra presented here investigated the photodissociation of a weakly-bound argon atom attached to the metal-ligand complex $M^+(N_2O)_n$-Ar, and were compared with simulated spectra and structures of naked complexes, $M^+(N_2O)_n$. Figure 3.20 shows the experimental IRPD spectrum of $Au^+(N_2O)_2$-Ar compared with the simulated spectra of non- and argon-tagged structures. As observed, negligible difference is found between the

simulated spectra of non-tagged and argon-tagged species. This finding was also observed for larger $Au^+(N_2O)_n$ complex sizes, and for the $Cu^+(N_2O)_n$ and $Ag^+(N_2O)_n$ complexes.

The IRPD spectra in this study probe the asymmetric stretch of N_2O, identifying two different binding motifs to d^{10} metal centres; *i.e.* terminal N- and O-bound N_2O ligands. Probing the symmetric stretch of nitrous oxide provides no additional diagnostic information on the binding motif to the metal centre. The symmetric region, just as with the asymmetric region, identifies two distinct spectral bands which are assigned as N- and O-bound ligands. Figure 3.21 provides an example, showing the $^1Au^+N^2$, $^1Au^+N^1O^1$, and $^1Au^+O^2$ isomers of $Au^+(N_2O)_2$. In both stretching regions, N-bound bands (blue) and O-bound bands (red) can clearly be identified.

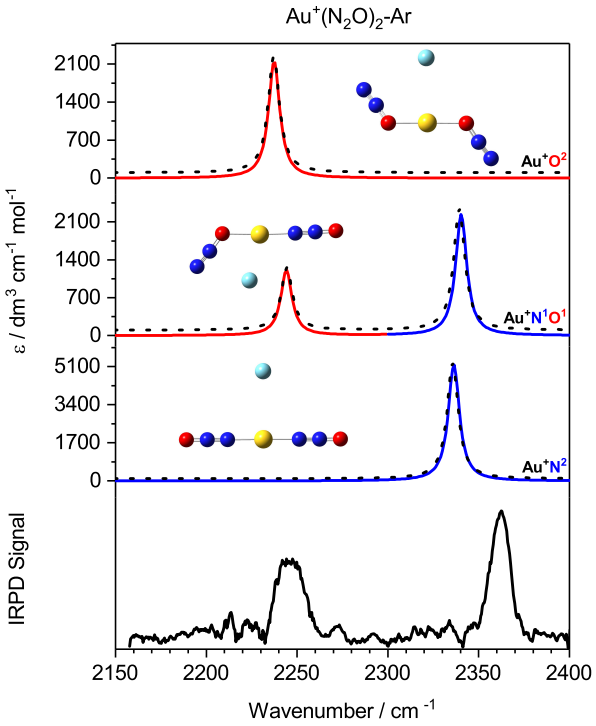

Figure 3.20: Experimental IRPD spectrum of $Au^+(N_2O)_2$-Ar along with the simulated spectra for non-tagged and Ar-tagged structures. Simulated IR bands corresponding to N-bound and O-bound ligands for non-tagged structures are indicated in blue and red, respectively, and as dotted spectra for Ar-tagged structures.

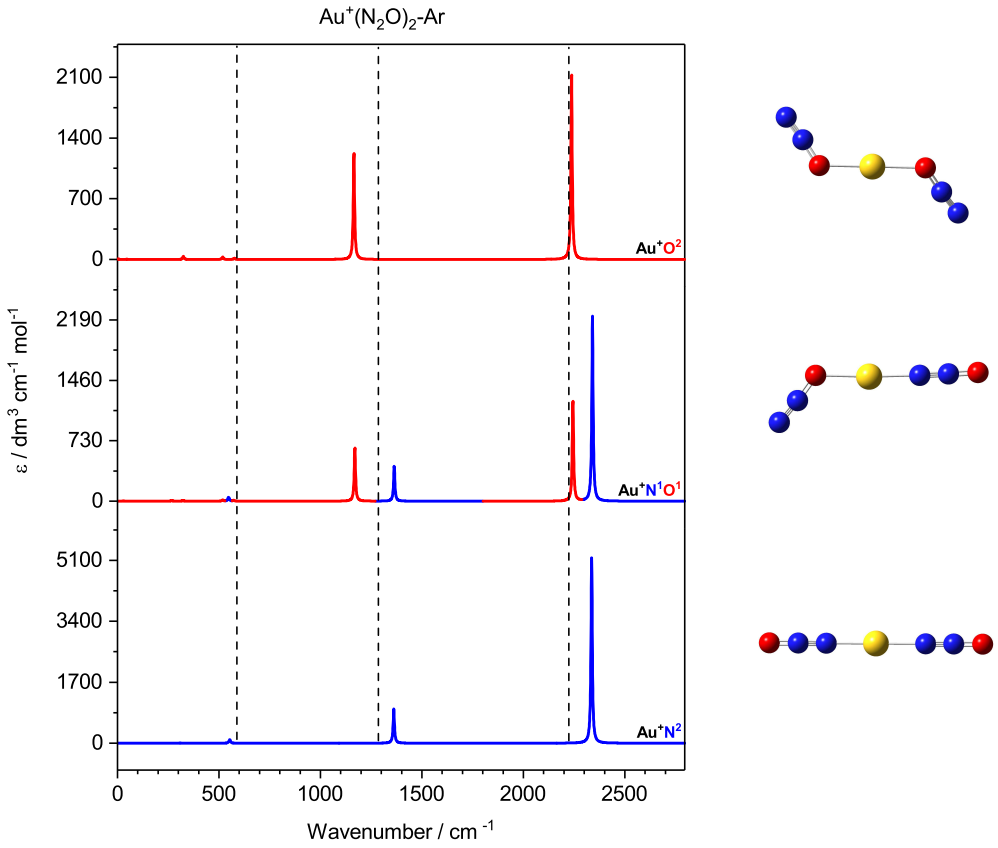

Figure 3.21: Geometry-optimised minima of the $^1Au^+N^2$, $^1Au^+N^1O^1$, and $^1Au^+O^2$ isomers of the $Au^+(N_2O)_2$ complex along with simulated spectra in the asymmetric, symmetric, and bending region of N_2O. Simulated IR bands corresponding to N- and O-bound ligands are indicated in blue and red, respectively. The vertical dashed lines at 588.8, 1285, and 2223.5 cm^{-1} indicate the wavenumber of the ν_2(N=N=O bend), ν_1(N=O symmetric stretch), and ν_3(N=N asymmetric stretch) modes in isolated N_2O, respectively.[151]

3.5 $(N_2O)_n^+$ IRPD Spectra of (n = 3-5) complexes

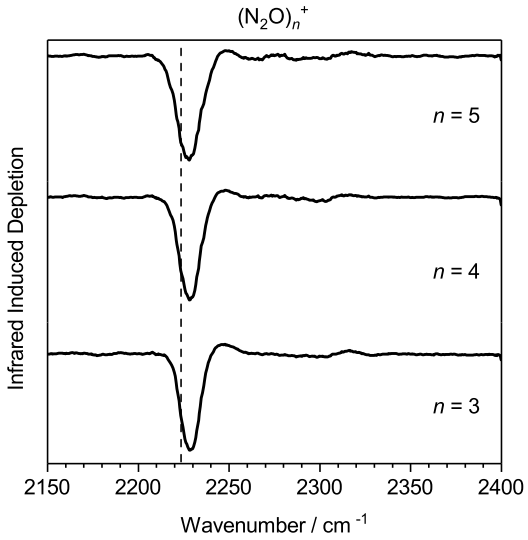

Figure 3.22: Experimental IRPD spectra of $(N_2O)_n^+$ complexes (n = 3-5) in the region of the N_2O asymmetric stretch. The vertical dashed line indicates the wavenumber of the ν_3(N=N) asymmetric stretching mode in isolated N_2O at 2223.5 cm^{-1}.[151]

During experiments on $Ag^+(N_2O)_n$ complexes, $(N_2O)_n^+$ complexes were also produced (see time-of-flight mass spectrum, figure 3.1b). The IRPD spectra for $(N_2O)_n^+$ (n = 3-5) are shown in figure 3.22 with all complexes presenting an enhancement in ion-signal (or negative depletion) close to the isolated stretch of N_2O. As these complexes are not argon-tagged, depletion in ion signal is due to the loss of one, (or multiple) N_2O molecules, therefore leading to the production of lower mass complexes (in this case n = 3-5) and as such, presenting an enhancement in ion signal. Despite this, these IRPD spectra are in excellent agreement with those recorded previously for $(N_2O)_n^+$ complexes by Inokuchi and coworkers.[111] By combining IRPD experiments together with calculated vibrational mode analysis it was shown that a $N_4O_2^+$ ion with a C_{2h} structure (bound together *via* terminal O-atoms) comprised the ion core for the $(N_2O)_n^+$ complexes ($n > 3$). The IRPD spectra of the n = 3-5 complexes presented bands near the isolated stretch of N_2O and were assigned to ν_3 vibrations of solvent (or outer-sphere) molecules relative to the $N_4O_2^+$ core. These

findings are mirrored in the IRPD spectra presented here (figure 3.22).

This study on coinage metal-nitrous oxide complexes presents bands in two distinct spectral regions (assigned as N- and O-bound N_2O ligands), with the N-bound band presenting differences in blue-shift relative to the metal centre (*i.e.* Cu, Ag, and Au). Since the measured IRPD spectra of the $(N_2O)_n^+$ complexes is in excellent agreement with that of previous measurements,[111] it is concluded that the assignments made for the coinage metal-nitrous oxide complexes are sound.

3.6 Conclusions

Small gas-phase nitrous oxide complexes of coinage metal cations have been studied using infrared photodissociation spectroscopy in the region of the ν_3(N=N) mode in N_2O. By comparing the experimental spectra with spectral simulations of different $M^+(N_2O)_n$ structures calculated *via* density functional theory, there is evidence for isomers containing both N- and O-bound ligands, with the spectral signature of the former significantly blue-shifted from the free N_2O stretch by as much as 140 cm^{-1}. The trends observed between the three metals, as well as those with increasing numbers of ligands, are interpreted from a molecular orbital approach to the binding interaction in which the approaching N_2O ligand induces s-d_{z^2} hybridisation of the metal cation.

As observed in figure 3.21, there are also N- and O-bound infrared signatures found in the ν_2 and ν_1 regions. Future work to follow up this study would involve investigating these N- and O-bound signatures in the ν_1 N=O symmetric stretching and ν_2 N=N=O bending regions.

It is comparatively unusual for the same ligand to occupy multiple competing binding motifs, and the ability to selectively excite one binding motif over another in three different

infrared regions may provide an opportunity to drive mode-selective intracluster chemistry, and ultimately direct a reaction spectroscopically, in different isomers.

Chapter 4

Structural Isomers and Low-Lying Electronic States of Gas-Phase $M^+(N_2O)_n$ (M = Co, Rh, Ir) Ion-Molecule Complexes

The structures of gas-phase group nine cation-nitrous oxide metal-ligand complexes, $M^+(N_2O)_n$ (M = Co, Rh, Ir), have been determined by a combination of infrared photodissociation spectroscopy and density functional theory. The infrared spectra were recorded in the region of the N_2O asymmetric (N=N) stretch using the inert messenger technique and show spectroscopically distinct features for N- and O-bound isomers. The evolution of the spectra with increasing ligand number is qualitatively different for each of the metal ions studied here with only $Co^+(N_2O)_n$ complexes behaving similarly to the coinage metal complexes studied in the previous chapter. The rich variety of electronic and isomeric structures

identified make these species attractive targets for infrared-driven, isomer selective intra-complex chemistry. Much of the work presented in this chapter is based on the publication: Structural isomers and low-lying electronic states of gas-phase $M^+(N_2O)_n$ (M = Co, Rh, Ir) ion-molecule complexes, Cunningham, E. M.; Gentleman, A. S.; Beardsmore, P. W.; Mackenzie, S. R. *Phys. Chem. Chem. Phys.*, **2019**, 21, 13959-13967.

4.1 Introduction

As discussed in previous chapters, the reactions of monocations with N_2O has been surveyed by Böhme and coworkers using inductively coupled plasma/selected-ion flow tube (ICP/SIFT) mass spectrometry.[100] Oxygen-atom transfer and N_2O addition were observed as the primary products for Co^+, whereas Rh^+ was found to produce adducts and Ir^+ was found to produce multiple oxides along with adduct formation. Table 4.1 summarises these findings.

The O-atom reaction efficiency will depend strictly on the overall exothermicity of the reaction, activation barriers in the reaction coordinate and overall conservation of spin multiplicity. The O-atom transfer reaction with Co^+ was found to proceed slowly and compete with adduct formation, despite the overall reaction being exothermic.

Given that both N_2O and N_2 occupy a singlet ground state, the O-atom transfer reaction

$$M^+ + N_2O \longrightarrow MO^+ + N_2 \tag{4.1}$$

is only spin-allowed for M^+ and MO^+ states of the same multiplicity.[100] The cobalt cation, Co^+ has a (d^8) ^{3}F ground-state,[165] whereas the ground-state of cobalt oxide, CoO^+, is $^5\Delta$. However, Armentrout and Beauchamp invoked a low-lying $^3\Sigma^-$ state of CoO^+ in their reactivity study.[166] Despite the O-atom transfer reaction being exothermic, the $Co^+ + N_2O$

Table 4.1: Primary and higher-order product ions for reactions of group 9 atomic ions with nitrous oxide in Helium at 0.35 ± 0.01 Torr and 295 ± 2 K. Table reproduced with permission from Lavrov, V. V.; Blagojevic, V.; Koyanagi, G. K.; Orlova, G.; Böhme, D. K. *J. Phys. Chem. A.*, **2004**, 108, 5610-5624.[100]

M^+	Primary Products	Higher-Order Products
Co^+	CoO^+	$CoO^+(N_2O)_n$, n = 1-3
	$Co^+(N_2O)$	$Co^+(N_2O)_m$, m = 2-3
Rh^+	$Rh^+(N_2O)$	$Rh^+(N_2O)_2$
Ir^+	IrO^+	IrO_n^+, n = 2-3, $IrO_2^+(N_2O)$

reaction is both spin-forbidden and experiences a significant barrier (0.50 eV, figure 4.4) on the ground-state surface. Unsurprisingly, this reaction was found to proceed slowly.[100] The reaction rate is, however, around 1 order of magnitude higher than those measured for the other spin-forbidden reactions of $M^+ + N_2O$ (M = Cr, Mn, Ni, Mo, Ru).[100] We find no evidence of the involvement of excited electronic states in any of the cobalt complexes. The excited ^{1}D surface shown in figure 4.4 is the lowest energy excited-state, with the same Co^+ d^8 electron configuration as the ^{3}F ground state (there are, however, lower ^{5}F and ^{3}F excited states at 0.4 eV and 1.2 eV, respectively, but these have $d^7(^4\text{F})4s$ electron configurations). As will become clear throughout this chapter, in all $M^+(N_2O)_n$ systems studied, low spin states are increasingly stabilised by successive ligation.

The $Rh^+ + N_2O$ O-atom transfer reaction is the only one within the group 9 cations to be fully spin-allowed, with RhO^+ occupying a $^3\Sigma^-$ ground state. Despite this reaction being exothermic, the reaction is very slow ($k < 4 \times 10^{-13}$ cm^3 molecule^{-1} s^{-1}),[100] two orders of magnitude lower than the those measured for other spin-allowed monocations (M

= Fe, Zn, Y, Hf). This is likely due to the large barrier (0.70 eV, figure 4.4) on the ground-state surface. The d^8 ^{1}D state is the lowest excited state of different multiplicity and the only excited state predicted at 5500 K by Böhme and coworkers in the modelling of their inductively coupled plasma source.[100]

In contrast with the other two group 9 metal cations, the reaction of Ir^+ with N_2O is fast, despite being spin-forbidden on the quintet ground state surface. A small (0.19 eV, figure 4.4) barrier to reaction was calculated on the ground state surface. Böhme and coworkers account for the fast reaction rate as arising from spin mixing (spin-orbit coupling) when forming the metal oxide cation - *i.e.* in the exit channel.[100]

Relevant infrared spectroscopic measurements on the group 9 monocations are limited to matrix isolation studies.[167–169] Reactions of laser-ablated cobalt, rhodium and iridium with nitric oxide were performed by Andrews and coworkers.[168,169] Upon laser-ablation, these metal atoms and ions were co-deposited with nitric oxide in excess argon or neon onto a 10 or 4 K CsI cryogenic window. Fourier-transform infrared (FT-IR) spectroscopy coupled with density functional theory calculations allowed the authors to identify the isomeric form and charge states of the group 9-nitrosyl complexes. The reaction with cobalt formed: (i) neutral species (the end-on bonded $Co(NO)_{1-3}$ and side-bonded $Co(\eta^2\text{-NO})$), (ii) the cationic $Co^+(NO)$ complex, and (iii) anionic $Co^-(NO)_{1-2}$ species. Reactions with rhodium and iridium formed: (i) neutral $M(NO)_{1-3}$ and NMO species, and (ii) cationic $M^+(NO)$ species.

Xu and coworkers performed similar experiments investigating the reactions of laser-ablated rhodium with nitrous oxide in matrix isolation.[167] Density functional theory calculations were also employed, with the agreement between the experimental and calculated vibrational frequencies inferring the presence of neutral $Rh(NNO)_{1-2}$ isomers (*i.e.* nitrous

oxide binding *via* the terminal N-atom).

Following the earlier work (chapter 3) on coinage metal ions, we expect similar binding motifs and entrance-channel complexes. Each of the potential energy profiles presented in figure 4.4 shows two entrance-channel complexes corresponding to nitrous oxide binding to the metal centre *via* the terminal N-atom or the O-atom, respectively. In every case the N-bound isomer is the lower in energy. These structures form the basis for the understanding of the IRPD spectra to follow.

4.2 Experimental Methods

The instrument and technique employed have been described in previous chapters so only brief details will be given. Gas-phase $M^+(N_2O)_n$ (M = Co, Rh, Ir) complexes and their argon-tagged counterparts are formed by entraining the products of focussed 532 nm pulsed laser ablation of a rotating metal disc in a dense pulse of argon carrier gas seeded with N_2O (0.6% with 6 bar backing pressure). As the gas expands into high vacuum, weakly-bound complexes are formed in many-body collisions and subsequently cooled in the ensuing expansion. The resultant molecular beam is skimmed and positively-charged species are detected by reflectron time-of-flight mass spectrometry.[129] All aspects of the instrument (*i.e.* ablation laser, IR-OPO/OPA laser and oscilloscope) were operated at 10 Hz.

The IRPD spectra are recorded using the inert messenger technique,[132,160–164] in this case using a weakly-bound argon atom. Pulsed infrared radiation is provided by an optical parametric oscillator/amplifier system. Monitoring the fractional depletion in the ion signal of the $M^+(N_2O)_n$-Ar complex as a function of wavenumber yields the infrared spectrum of the $M^+(N_2O)_n$ complex of interest.

To aid in the assignment and interpretation of the experimental spectra, structures along

with simulated infrared spectra of energetically low-lying isomers were calculated using density functional theory (DFT), employing the B3P86 hybrid density functional[149] coupled with the Def2TZVP basis set.[147,148] To aid comparison with experimental spectra, the simulated bands were convoluted with a Lorentzian function with full-width-half-maximum (FWHM) of 8 cm^{-1} and scaled by a factor of 0.932, derived from the calculated ν_3 stretch of isolated N_2O.[151]

4.3 $M^+(N_2O)_n$-Ar Time-of-Flight Spectra

Figure 4.1 shows the time-of-flight mass spectrum illustrating the production of $Co^+(N_2O)_n$ complexes which are generated following the laser ablation of a cobalt disc in the presence of an argon carrier gas (6 bar backing pressure) seeded with 0.6% N_2O. $Co^+(N_2O)_n$, $CoO^+(N_2O)_n$ and $Co^+(N_2O)_n$-Ar complexes can be identified clearly.

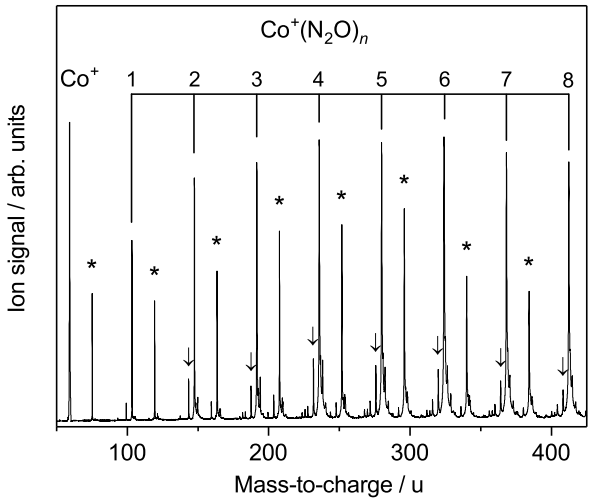

Figure 4.1: Time-of-flight mass spectrum of $Co^+(N_2O)_n$ complexes produced by laser ablation of a cobalt disc in an argon carrier gas seeded with 0.6% N_2O. Asterisks (*) mark $CoO^+(N_2O)_n$ complexes and arrows indicate Ar-tagged complexes. Figure reproduced with permission from *Phys. Chem. Chem. Phys.*, **2019**, 21, 13959-13967.

The equivalent mass spectra showing the $Rh^+(N_2O)_n$ and $Ir^+(N_2O)_n$ complexes are shown in figures 4.2 and 4.3. The size distribution of complexes generated can be controlled

crudely by varying the partial pressure of N_2O and/or the backing pressure behind the pulsed valve. $MO^+(N_2O)_n$ oxide complexes are the most prevalent ion signals in the cobalt mass spectrum, whilst the Ir^+ parent ion peak is extremely weak and almost undetectable suggesting highly efficient reaction and/or clustering with N_2O for this particular case. Uniquely in the case of the iridium mass spectrum, $M^+(N_2O)_n(N_2)$ complexes were also observed. These observations are consistent with the $M^+ + N_2O$ reactivity studies reported by Böhme and coworkers[100] and can be understood when considering the calculated reactive potential energy profiles for the first reactive collision, $M^+ + N_2O$, shown in figure 4.4.

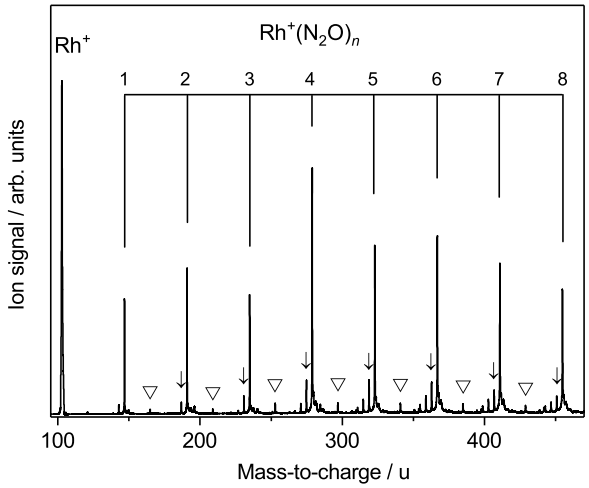

Figure 4.2: Time-of-flight mass spectrum of $Rh^+(N_2O)_n$ complexes produced by laser ablation of a rhodium disc in an argon carrier gas seeded with 0.6% N_2O. Ar-tagged complexes are indicated by arrows, with $Rh^+(N_2O)_n(H_2O)$ complexes (indicated by ($\bigtriangledown$)) also being formed.

4.4 $M^+(N_2O)_n$-Ar IRPD Spectra

The infrared spectra of $M^+(N_2O)_n$-Ar complexes (M = Co, Rh, Ir; n = 2-7) are shown in figure 4.5. It is clear that the evolution of the observed spectra with increased ligation are starkly different for each metal. Therefore, the spectra for each metal ion will be discussed separately.

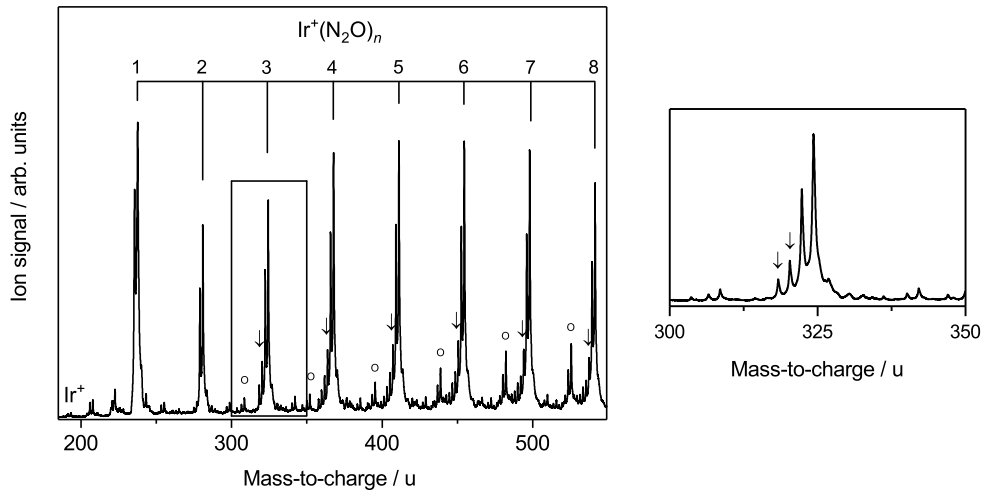

Figure 4.3: *Left*: Time-of-flight mass spectrum of $Ir^+(N_2O)_n$ complexes produced by laser ablation of an iridium disc in an argon carrier gas seeded with 0.6% N_2O. Ar-tagged complexes are indicated by arrows with $Ir^+(N_2O)_n(N_2)$ complexes (○) also being formed. *Right*: Inset showing the 300-350 mass region to highlight the ion signals of $^{193}Ir^+(N_2O)_3$ and $^{191}Ir^+(N_2O)_3$ along with $^{193}Ir^+(N_2O)_2$-Ar and $^{191}Ir^+(N_2O)_2$-Ar (both tagged complexes indicated by arrows).

4.4.1 $Co^+(N_2O)_n$-Ar IRPD Spectra

Figure 4.5a presents the IRPD spectra for the $Co^+(N_2O)_n$-Ar (n = 2-7) complexes. In each spectrum two distinct spectral features can be identified; one close to the asymmetric stretching frequency in isolated N_2O at 2223.5 cm^{-1},[151] and a second significantly blue-shifted from the first by between 93 and 50 cm^{-1}. The first spectral feature close to the isolated N_2O asymmetric stretch is broad, suggesting it is comprised of many vibrational bands and its intensity decreases with increasing complex size (up to n = 6). A distinct feature appearing at the isolated N_2O stretching frequency is apparent in the spectra for all complexes above $n > 2$, suggesting the presence of weakly-interacting ligands.

The second spectral feature undergoes a smooth red-shift (or a decrease in blue-shift relative to the first band for the smallest complex, n = 2) upon increasing ligand number from 2316 cm^{-1} for n = 2 to 2274 cm^{-1} for n = 7. The trends in the spectra of the $Co^+(N_2O)_n$-Ar complexes are similar to those reported for the coinage metal N_2O complexes

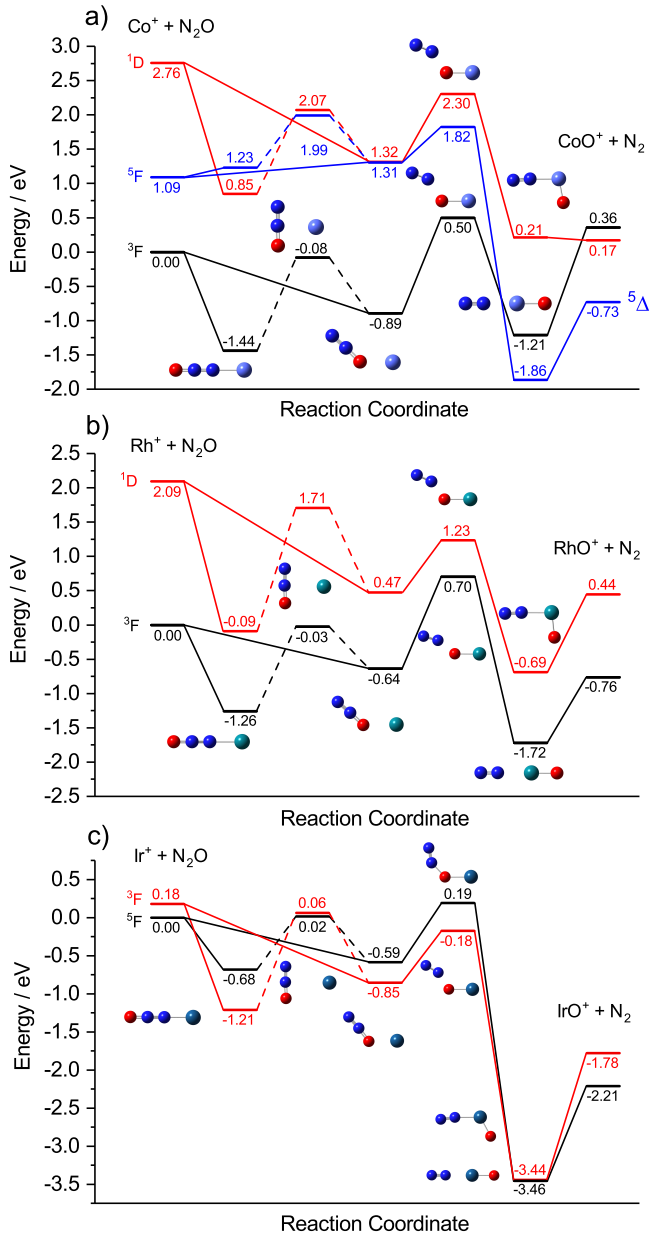

Figure 4.4: Calculated potential energy profiles for the M^+-N_2O insertion reaction (M = (a) Co, (b) Rh and (c) Ir). Black and red (blue in (a)) solid lines refer to ground and excited states of the metal cations, respectively. The M^+ + N_2O interaction can form either an N-bound or an O-bound complex, represented here as two pathways for each multiplicity (two lines originating from ground state cation and two lines from excited cation). Dashed lines represent the barrier to internal rotation. Figure reproduced with permission from *Phys. Chem. Chem. Phys.*, **2019**, 21, 13959-13967.

reported in chapter 3 and a similar rationale can be applied to their understanding in terms of N- and O-bound complexes.

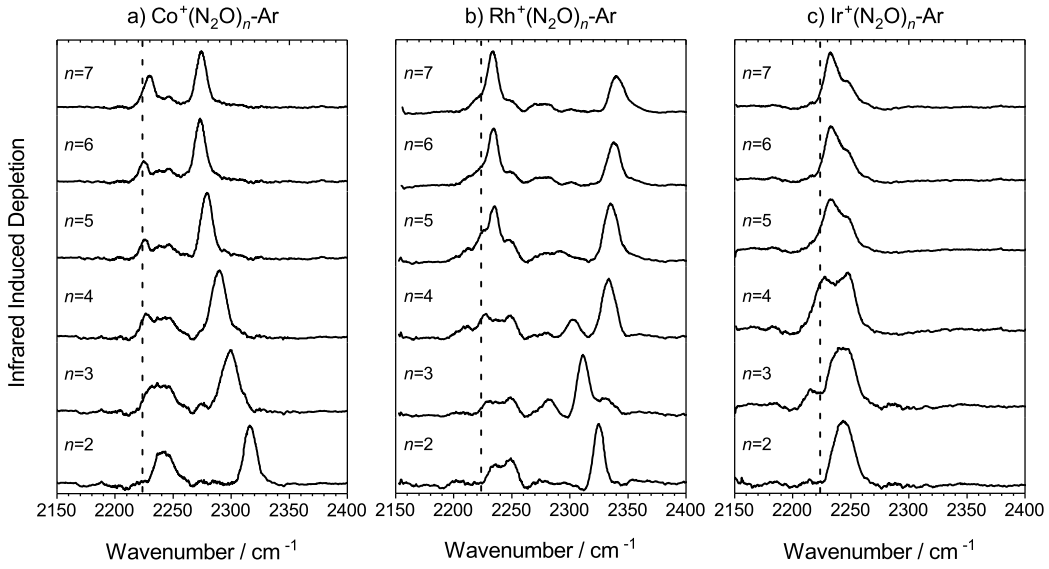

Figure 4.5: Experimental IRPD spectra of $M^+(N_2O)_n$-Ar (n = 2-7) complexes (M = (a) Co, (b) Rh and (c) Ir) in the region of the N_2O asymmetric (N=N) stretch. In each case, depletion of the ion signal occurs due to loss of the Ar messenger atom. To compare, the depletion intensity for each complex size was normalised with the maximum value in this region. The vertical dashed line indicates the wavenumber of the ν_3(N=N) mode in isolated N_2O at 2223.5 cm^{-1}.[151] Figure reproduced with permission from *Phys. Chem. Chem. Phys.*, **2019**, 21, 13959-13967.

Figure 4.6 shows a representation of the calculated Co^+N_2O potential energy surface in the entrance-channel. The surface (minimum energy pathway) was calculated by rotating the N_2O molecule about the metal centre by 1° increments and allowing the N_2O geometry to relax at each point between 0 and 180°. The line shown is the calculated minimum energy at each increment as a function of Co-N-N bond angle with 0° marking the linear Co^+NNO structure (*i.e.* η^1 *via* the terminal N atom) which represents the global-minimum entrance-channel structure. A second, higher-lying, double-well minimum corresponding to the bent Co^+ONN structure (η^1 *via* the terminal O atom) is observed at Co-N-N bond angles of 155° and 205°. These two principal minima, N- and O-bound, are separated by a large barrier to N_2O internal rotation of $>$ 1 eV. Rapid cooling within the free-jet expansion permits the formation of excited isomeric structures kinetically-trapped behind such barriers, leading to the possibility of isomers containing both N- and O-bound ligands. Since N_2O can bind to a

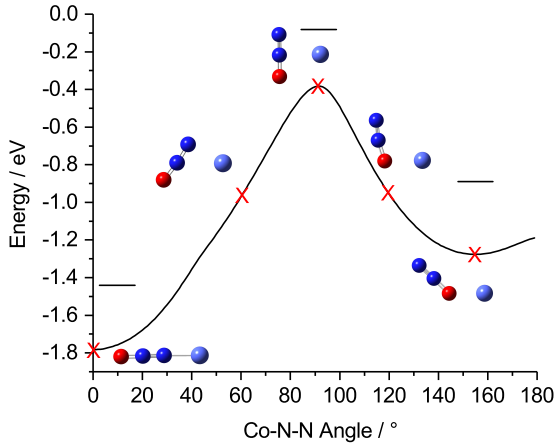

Figure 4.6: Minimum energy pathway of the triplet Co^+N_2O complex as a function of Co-N-N bond angle, illustrating the relative energies of the N- and O-bound minima. For each step along the pathway the N_2O geometry was allowed to relax. Horizontal lines indicate the energy of the respective geometry-optimised structures including zero-point correction. Figure reproduced with permission from *Phys. Chem. Chem. Phys.*, **2019**, 21, 13959-13967.

metal centre in two distinct orientations with differing binding energies, the growth kinetics become increasingly complicated upon successive ligation. As discussed before in chapter 3, figure 3.6, the binding of an N-bound ligand can potentially displace an existing O-bound ligand, however the reverse is less likely without the complex possessing significant internal energy. Therefore, the larger complexes will most likely possess more N-bound ligands.

As in chapter 3, the complexes will follow a succinct notation $^{2S+1}M^+N^xO^y$ for a particular structure in which x and y are integer values representing the number of N- and O-bound ligands, respectively. From this notation, $x + y = n$. As an example, $^1M^+N^2O^1$ represents a singlet state isomer of $M^+(N_2O)_3$ with two N-bound ligands and one O-bound ligand.

The $Co^+(N_2O)_n$-Ar spectra can be understood when considering the DFT calculations of the $Co^+(N_2O)_2$-Ar complex, which shows the N- and O-bound ligands to be spectroscopically distinct in the region of the N_2O asymmetric (N=N) stretch. Figure 4.7 shows the experimental IRPD spectra recorded for the $Co^+(N_2O)_2$-Ar complex together with spec-

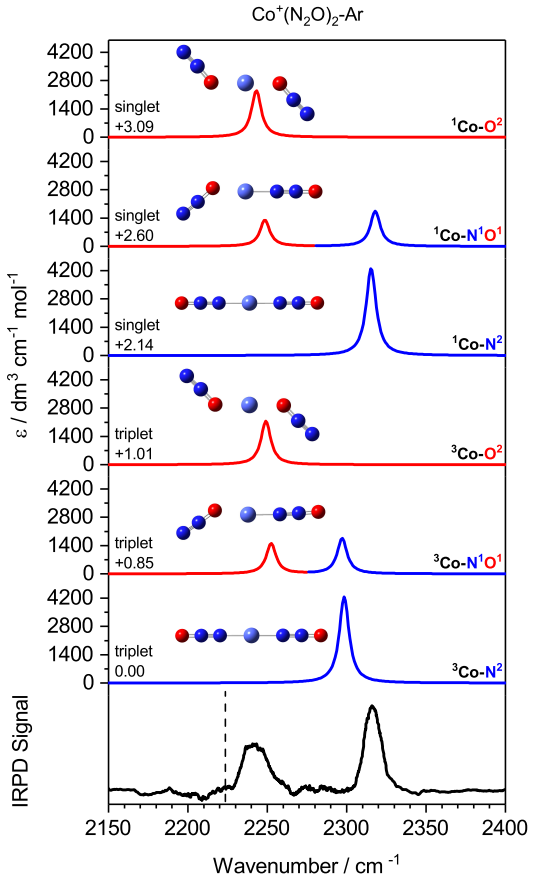

Figure 4.7: Experimental IRPD spectrum of the $Co^+(N_2O)_2$-Ar complex along with simulated IR spectra of low-lying triplet and singlet isomers in the region of the N_2O asymmetric (N=N) stretch. Simulated IR bands corresponding to N-bound and O-bound ligands are indicated in blue and red, respectively. The relative energies of the isomers concerned are given in eV. The vertical dashed line indicates the wavenumber of the ν_3(N=N) mode in isolated N_2O at 2223.5 cm^{-1}.[151]

tral simulations corresponding to triplet ($^3Co^+N^2$, $^3Co^+N^1O^1$ and $^3Co^+O^2$) and singlet ($^1Co^+N^2$, $^1Co^+N^1O^1$ and $^1Co^+O^2$) isomers.

Table 4.2 presents the relative energies of calculated structures of $Co^+(N_2O)_n$ (n = 1-4) in the lowest energy triplet, singlet and quintet states. Considering the relative energies calculated for the excited spin states (singlet and quintet) only the triplet states are likely to contribute significantly to the experimental spectra. The $^3Co^+N^2$ is calculated to be the lowest energy molecularly-bound structure. However, it is clear from figure 4.7 that this

structure alone cannot account for the two spectral bands observed experimentally and that O-bound ligands (in the form of $^3Co^+N^1O^1$ and $^3Co^+O^2$ isomers) must be present in our expansion. These two experimental bands are assigned as follows: the lower wavenumber band at 2240 cm^{-1} is attributed to the N=N stretch in O-bound ligands. Such binding represents minimal perturbation to the N=N bond on the ligand, leading to a fundamental band close to that of isolated N_2O. The higher wavenumber band at 2316 cm^{-1} arises from N-bound ligands. The binding mechanism for N-bound ligands, explained previously in chapter 3, is dominated by electron donation from the N_2O HOMO-1, 7σ orbital to the metal centre. The 7σ orbital is antibonding with respect to the N=N bond, electron donation from this orbital therefore results in a slightly stronger N=N bond, reflected by a spectral blue-shift.[91,98,170]

The two bands present in the observed spectrum clearly indicate the presence of structures possessing both N- and O-bound ligands. Given the relative energies of the different triplet isomers ($^3Co^+N^2$, $^3Co^+N^1O^1$ and $^3Co^+O^2$), it is inconceivable that we generate a pure population of the $^3Co^+N^1O^1$ structure. Therefore, it is concluded that a mixture of these triplet isomers is present in the molecular beam.

Figure 4.8 presents the experimental IRPD spectrum of the $Co^+(N_2O)_2$-Ar complex together with the lowest energy molecularly-bound quintet isomers ($^5Co^+N^2$, $^5Co^+N^1O^1$ and $^5Co^+O^2$) and inserted quintet isomers ($^5Co^+N^1$(ins.) and $^5Co^+O^1$(ins.)).

The N-bound inserted quintet isomer, $^5Co^+N^1$(ins.), is isoenergetic with the doubly N-bound triplet isomer,$^3Co^+N^2$, so both could be regarded as the ground state structure of $Co^+(N_2O)_2$. However, as discussed earlier, the PES presents a barrier to O-atom transfer (see figure 4.4) and the reaction is exothermic, so it is unlikely the N_2 molecule could remain bound once significant energy is released upon formation of the strong M^+-O bond.

Table 4.2: Zero-point corrected energies of structural isomers of $Co^+(N_2O)_n$ (n = 1-4) complexes calculated at the B3P86/Def2TZVP level of theory. Energies are relative to the global minimum geometry and corresponding electronic state for each complex size, n.

Species	Isomer	$E_{rel.}$ / eV	Species	Isomer	$E_{rel.}$ / eV
$^3Co^+(N_2O)$	N^1	0.00	$^3Co^+(N_2O)_3$	N^3	0.00
	O^1	0.54		N^2O^1	0.27
$^1Co^+(N_2O)$	N^1	2.28		$^*N^2O^1$	0.38
	O^1	2.57		N^1O^2	0.70
$^5Co^+(N_2O)$	N^1	2.67		O^3	1.22
	O^1	2.74	$^1Co^+(N_2O)_3$	N^3	1.62
				N^2O^1	2.02
				$^*N^2O^1$	2.07
				N^1O^2	2.48
				O^3	2.98
			$^5Co^+(N_2O)_3$	N^3	2.40
				N^2O^1	2.54
				N^1O^2	2.64
				O^3	2.74
$^3Co^+(N_2O)_2$	N^2	0.00	$^3Co^+(N_2O)_4$	N^4	0.08
	N^1O^1	0.85		N^3O^1	0.00
	O^2	1.01		N^2O^2	0.25
$^1Co^+(N_2O)_2$	N^2	2.14		N^1O^3	0.98
	N^1O^1	2.60		O^4	1.08
	O^2	3.09	$^1Co^+(N_2O)_4$	N^4	0.88
$^5Co^+(N_2O)_2$	N^2	2.28		N^3O^1	1.26
	N^1O^1	2.36		N^2O^2	1.68
	O^2	2.48		N^1O^3	2.05
				O^4	2.51
			$^5Co^+(N_2O)_4$	N^4	2.50
				N^3O^1	2.56
				N^2O^2	2.76
				N^1O^3	2.78
				O^4	2.83

The simulated spectra of the molecularly-bound quintet isomers ($^5Co^+N^2$, $^5Co^+N^1O^1$ and $^5Co^+O^2$) agree poorly with the experimental IRPD spectra. Given that these structures are calculated to lie much higher in energy, it is concluded that these quintet isomers

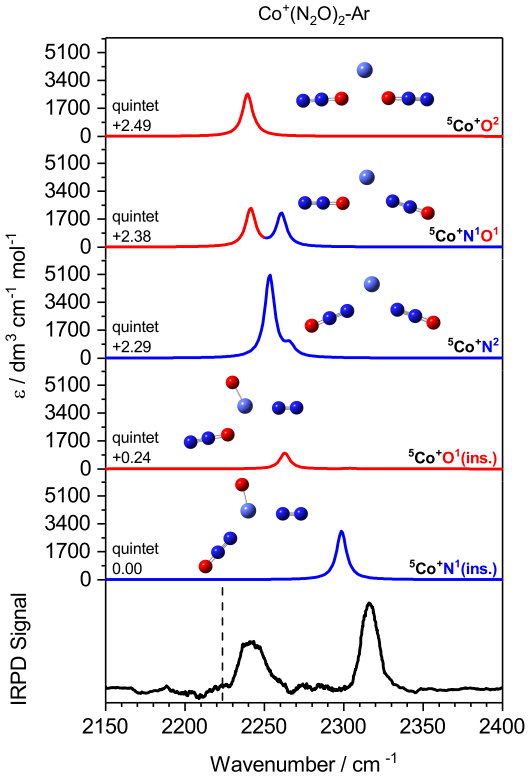

Figure 4.8: Experimental IRPD spectrum of the $Co^+(N_2O)_2$-Ar complex along with simulated IR spectra of low-lying quintet isomers along with inserted quintet isomers in the region of the N_2O asymmetric (N=N) stretch. Simulated IR bands corresponding to N-bound and O-bound ligands are indicated in blue and red, respectively. The relative energies of the isomers concerned are given in eV. The vertical dashed line indicates the wavenumber of the ν_3(N=N) mode in isolated N_2O at 2223.5 cm^{-1}.[151]

(molecularly-bound and inserted) do not contribute significantly to the observed IRPD spectrum. This argument is also mirrored in all calculated quintet isomers of higher-order complexes which are found to lie considerably higher in energy (table 4.2) with the simulated spectra agreeing poorly with the experimental spectra.

Figure 4.9 shows the experimental IRPD spectrum of the $Co^+(N_2O)_3$-Ar complex along with structures and simulated IR spectra of low-lying triplet-state and singlet-state isomers (a and b, respectively). As for the $n = 2$ case, two distinct spectral bands are observed which we assign as N- and O-bound N_2O ligands. There is slightly better agreement between the experimental band at 2299 cm^{-1} and the N-bound bands of simulated singlet-state isomers

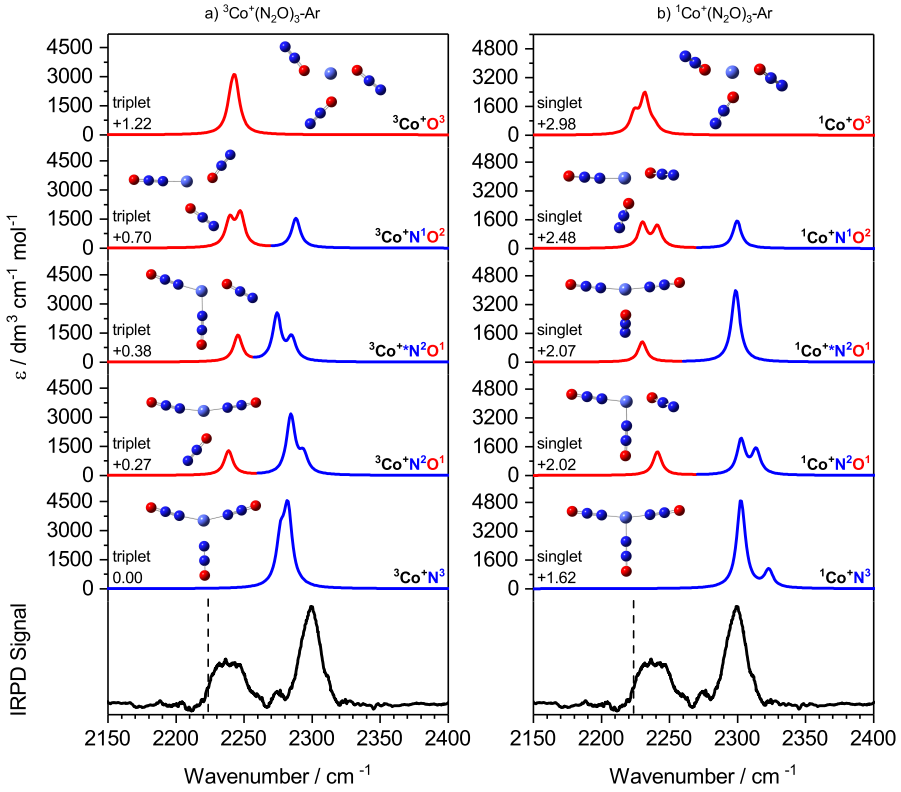

Figure 4.9: Experimental IRPD spectrum of the $Co^+(N_2O)_3$-Ar complex along with simulated IR spectra of low-lying: a) triplet-state isomers, and b) singlet-state isomers in the region of the N_2O asymmetric (N=N) stretch. Simulated IR bands corresponding to N-bound and O-bound ligands are indicated in blue and red, respectively. The relative energies of the isomers concerned are given in eV. The vertical dashed line indicates the wavenumber of the ν_3(N=N) mode in isolated N_2O at 2223.5 cm^{-1}.[151]

when compared with the N-bound bands of triplet-state isomers. However, considering these singlet-state isomers lie considerably higher in energy when compared to the global-minimum $^3Co^+N^3$ structure, there is a low probability these singlet-state isomers contribute significantly to the observed IRPD spectrum.

More evidence to suggest that singlet-state isomers do not contribute to the experimental IRPD spectra becomes apparent when considering the simulated spectra of the $n = 4$ triplet-state and singlet-state isomers (figure 4.10). As discussed previously, considering the IRPD spectra for the $Co^+(N_2O)_n$-Ar (n = 2-7) complexes (figure 4.5a), the most blue-shifted band red-shifts (or reduces in blue-shift) with increasing ligation. This effect is mirrored for the

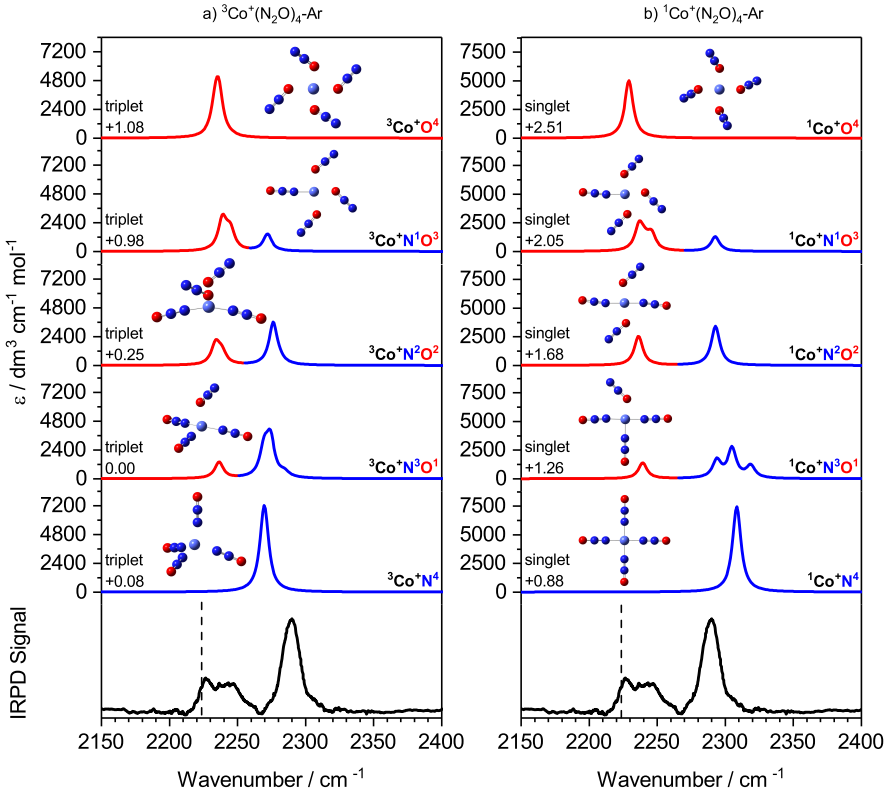

Figure 4.10: Experimental IRPD spectrum of the $Co^+(N_2O)_4$-Ar complex along with simulated IR spectra of low-lying: a) triplet-state isomers, and b) singlet-state isomers in the region of the N_2O asymmetric (N=N) stretch. Simulated IR bands corresponding to N-bound and O-bound ligands are indicated in blue and red, respectively. The relative energies of the isomers concerned are given in eV. The vertical dashed line indicates the wavenumber of the ν_3(N=N) mode in isolated N_2O at 2223.5 cm^{-1}.[151]

simulated N-bound bands for each of the simulated triplet isomers of $Co^+(N_2O)_n$. When considering the simulated bands of the singlet isomers of $Co^+(N_2O)_n$, the most blue-shifted band actually shifts further to the blue upon increased ligation, in contrast to the behaviour observed for the triplet counterparts. Since this effect is not mirrored in the observed IRPD spectra (figure 4.5a), it is highly likely that only triplet-state isomers in all of the complexes studied contribute significantly to the experimental spectrum.

The first two N_2O ligands bind to the Co^+ centre strongly, with a calculated M^+-L bond dissociation energy of 1.62 eV. Subsequent ligands are calculated to bind less-strongly. This is somewhat reflected in the lower wavenumber region of the experimental spectra, which

becomes broader with increasing ligand number as not only O-bound ligands contribute to this region, but also weakly-bound N-bound ligands. Interpreting the spectra in this region therefore becomes more difficult, especially for higher-order complexes.

As n increases, the efficiency of σ-donation from N-bound ligands decreases, which leads to a smooth red-shift in the higher-frequency (*i.e.*, more blue-shifted) band. This red-shift appears to cease at $n = 6$, suggesting the completion of a coordination shell which is both confirmed by DFT calculations, and consistent with the expected octahedral symmetry of high-spin d^8 complexes.

4.4.2 $Rh^+(N_2O)_n$-Ar IRPD Spectra

The IRPD spectra for the $Rh^+(N_2O)_n$-Ar (n = 2-7) complexes are shown in figure 4.5b. Similar to the $Co^+(N_2O)_n$-Ar complexes, two distinct spectral features are observed which are assigned to N- and O-bound core and outer-ligands. It is clear, however, both from the presence of new spectral features and a contrasting trend in the band positions upon increasing ligation that the $Rh^+(N_2O)_n$ complexes are more complicated than their $Co^+(N_2O)_n$ counterparts.

Figure 4.11 shows the IRPD spectrum of $Rh^+(N_2O)_2$-Ar along with the simulated spectra of energetically low-lying isomers of triplet and singlet states. Similar to $Co^+(N_2O)_2$, the observed bands at 2325 cm^{-1} and 2240 cm^{-1} can be attributed to N- and O-bound ligands, respectively, with a separation of *ca.* 85 cm^{-1}. The observed spectral splitting of the two bands is reproduced slightly better in the simulated spectra of the singlet-state structures ($\Delta\tilde{\nu}$ ($^1Rh^+N^1O^1$) = 96 cm^{-1} *c.f.* $\Delta\tilde{\nu}$ ($^3Rh^+N^1O^1$) = 66 cm^{-1}). However, for n = 2 the singlet-state structures are calculated to lie markedly higher in energy relative to the triplet-state structures. As such, there is no reason to believe that the singlet-state isomers contribute significantly to the observed spectrum. The presence of higher-lying O-bound ligands can be rationalised when considering the calculated potential energy surface of Rh^+N_2O, figure 4.12. Similar to the Co^+N_2O surface, a global minimum, linear N-bound structure can be identified along with a higher-lying, bent O-bound structure. A large barrier (*ca.* > 1 eV) between these minima permits the existence of higher-lying, kinetically-trapped O-bound isomers.

Quintet isomers of $Rh^+(N_2O)_2$-Ar along with simulated spectra were also calculated but were found to lie much higher than the triplet isomers. As observed in figure 4.13,

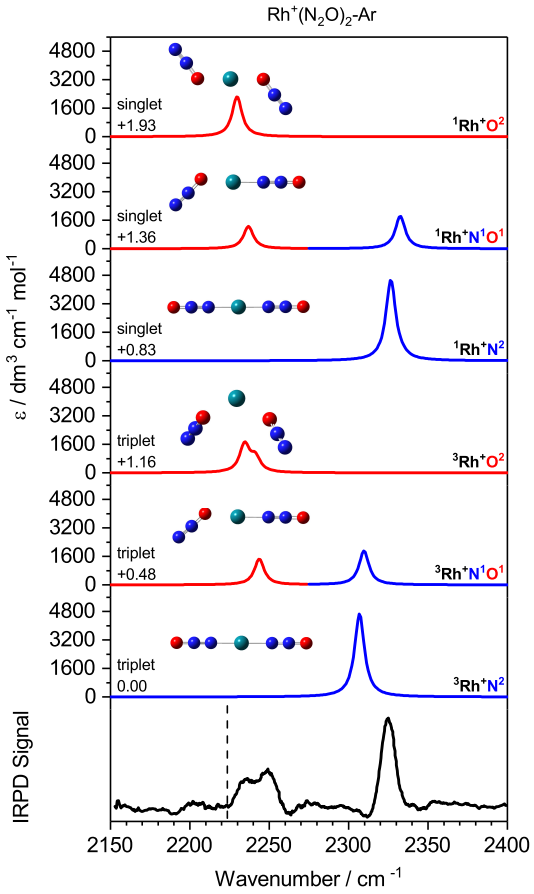

Figure 4.11: Experimental IRPD spectrum of the $Rh^+(N_2O)_2$-Ar complex along with simulated IR spectra of low-lying triplet- and singlet-state isomers in the region of the N_2O asymmetric (N=N) stretch. Simulated IR bands corresponding to N-bound and O-bound ligands are indicated in blue and red, respectively. The relative energies of the isomers concerned are given in eV. The vertical dashed line indicates the wavenumber of the ν_3(N=N) mode in isolated N_2O at 2223.5 cm^{-1}.[151] Figure reproduced with permission from *Phys. Chem. Chem. Phys.*, **2019**, 21, 13959-13967.

the simulated spectra of these isomers agree poorly with the observed IRPD spectrum so it is concluded that these quintet isomers are not present in significant quantities in the molecular beam.

The IRPD spectrum for the $Rh^+(N_2O)_3$-Ar species presents more bands than both its n = 2 and $Co^+(N_2O)_3$-Ar counterparts. Figure 4.14 shows the experimental IRPD spectrum for $Rh^+(N_2O)_3$-Ar together with simulated spectra for a range of $^{1/3}Rh^+N^xO^y$ isomers. The intense band at 2312 cm^{-1} and the broad feature between 2225-2250 cm^{-1} can be

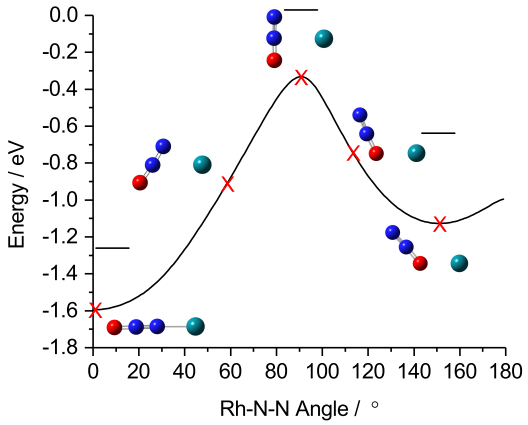

Figure 4.12: Minimum energy pathway for the triplet Rh^+N_2O complex as a function of Rh-N-N angle illustrating the relative energies of N-bound and O-bound minima. Horizontal lines indicate the energy of the respective geometry optimised structures including zero-point correction.

assigned as N- and O-bound ligands, respectively. The new band at 2281 cm^{-1} reflects a third N-bound ligand which binds less strongly than the two core ligands. Calculations show that this third ligand has an increased M^+-NNO bond distance of 2.23 Å compared to the core ligand distance of 2.07 Å. The core ligand band is clearly reproduced in the simulated spectra of the $^3Rh^+N^3$, $^3Rh^+N^2O^1$, $^3Rh^{+*}N^2O^1$ and $^3Rh^+N^1O^2$ isomers, whilst the third, weakly-bound N-bound ligand is reproduced in the $^3Rh^+N^3$, $^3Rh^{+*}N^2O^1$ and $^3Rh^{+*}N^1O^2$ isomers.

In the case of the rhodium complexes, the IRPD spectra become increasingly complex due to the presence of low-lying electronically excited states. For the bare cation, the d^8 ^{1}D state lies *ca.* 1.40 eV higher than the ^{3}F ground state.[171,172] However, upon complexation with N_2O, the singlet state is stabilised such that by $n = 3$ the $^1Rh^+N^3$ isomer is calculated to lie only 0.30 eV higher than the ground state $^3Rh^+N^3$ structure. The calculated relative energies of the lowest isomeric forms of singlet, triplet and quintet states of $M^+(N_2O)_n$ as a function of ligand number are presented in figure 4.15. Table 4.3 presents the calculated relative energies of the $Rh^+(N_2O)_n$ structural isomers (n = 1-4).

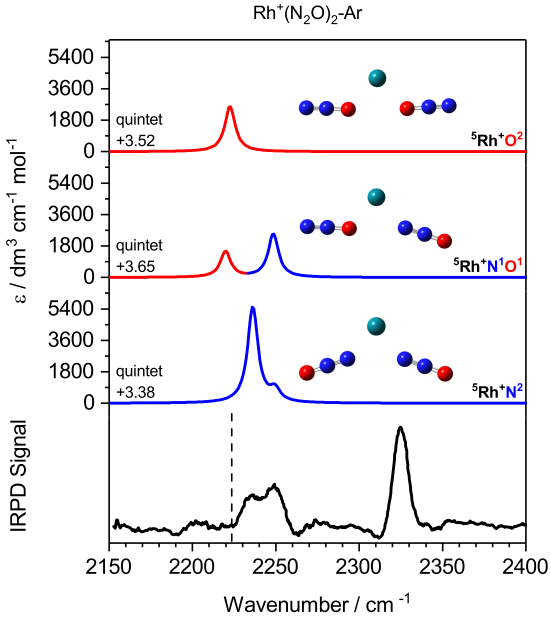

Figure 4.13: Experimental IRPD spectrum of the $Rh^+(N_2O)_2$-Ar complex along with simulated IR spectra of low-lying quintet-state isomers in the region of the N_2O asymmetric (N=N) stretch. Simulated IR bands corresponding to N-bound and O-bound ligands are indicated in blue and red, respectively. The relative energies of the isomers concerned are given in eV. The vertical dashed line indicates the wavenumber of the ν_3(N=N) mode in isolated N_2O at 2223.5 cm^{-1}.[151]

The shoulder at 2330 cm^{-1} in figure 4.14 is believed to be due to the emergence of a singlet-state isomer present in the spectrum. As shown in figure 4.15, the singlet-state isomer becomes comparable in energy with the triplet isomer at $n = 3$ and as such, becomes the ground state at larger n. It is likely that the observed IRPD spectrum of $Rh^+(N_2O)_3$-Ar is the result of a complex combination of multiple isomers of two different electronic states, triplet and singlet.

The singlet and triplet states are comparable in energy for the $n = 4$ complexes. However, at this complex size the ground state is now of singlet multiplicity, which is reflected in the intensity alternation, observed in figure 4.5b. Figure 4.16 shows the IRPD spectrum of the $Rh^+(N_2O)_4$-Ar complex, alongside simulated IR spectra from calculated singlet and triplet isomers. Typical of a low-spin d^8 electron configuration, a square-planar $^1Rh^+N^4$

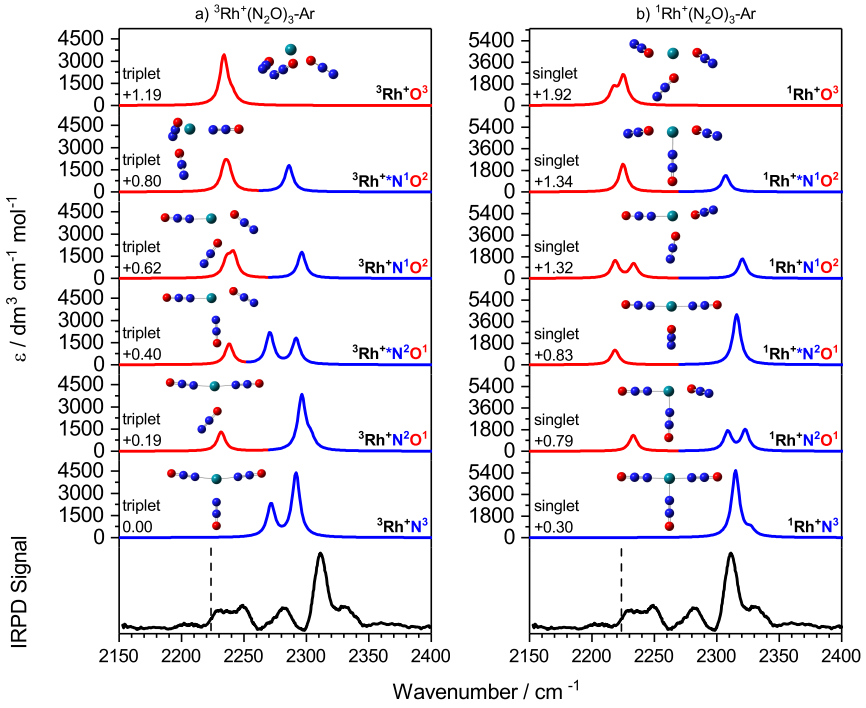

Figure 4.14: Experimental IRPD spectrum of the $Rh^+(N_2O)_3$-Ar complex along with simulated IR spectra of low-lying: a) triplet-state isomers, and b) singlet-state isomers in the region of the N_2O asymmetric (N=N) stretch. Simulated IR bands corresponding to N-bound and O-bound ligands are indicated in blue and red, respectively. The relative energies of the isomers concerned are given in eV. The vertical dashed line indicates the wavenumber of the ν_3(N=N) mode in isolated N_2O at 2223.5 cm^{-1}.[151] Figure reproduced with permission from *Phys. Chem. Chem. Phys.*, **2019**, 21, 13959-13967.

isomer is the calculated global minimum, with the $^3Rh^+N^4$ counterpart 0.63 eV higher in energy.

It is not uncommon for the global minimum spin state to change upon increasing ligation. This was found to be the case for $V^+(CO)_n$ complexes,[173,174] where a change from quintet to a lower (triplet) multiplicity appears for $n \geqslant 4$. For the $Rh^+(N_2O)_n$ complexes, the switch to the lower multiplicity, singlet state at $n = 4$ is consistent with the adoption of square-planar geometries, typical of low-spin d^8 complexes. In this case, $n = 4$ represents the coordination number. Just as with the $n = 3$ case, a combination of multiple isomers of both spin states (*i.e.* triplet and singlet) provides a satisfactory understanding of the

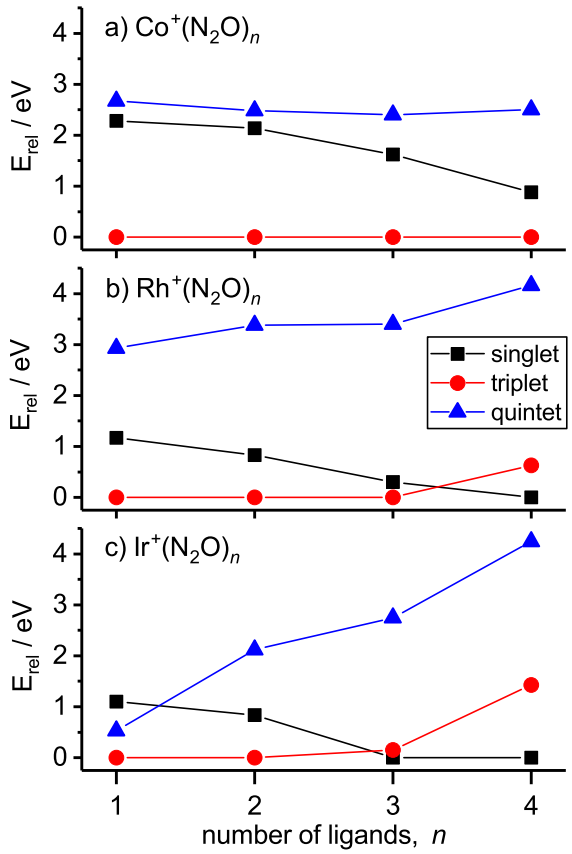

Figure 4.15: Calculated lowest energy isomers of singlet (black squares), triplet (red circles) and quintet (blue triangles) states of: a) $Co^+(N_2O)_n$, b) $Rh^+(N_2O)_n$, and $Ir^+(N_2O)_n$ as a function of ligand number. Energies are relative to the global minimum structure for each n. Figure reproduced with permission from *Phys. Chem. Chem. Phys.*, **2019**, 21, 13959-13967.

observed spectrum (see figure 4.16). The intense band at 2333 cm^{-1} can be assigned to the N-bound ligand in a singlet isomer. This band is markedly blue-shifted from the strongest feature in the $n = 3$ spectra (figure 4.14), reflecting the change in structure and spin state upon sequential addition of N_2O ligands. The weaker band at 2302 cm^{-1} is most likely due to an N-bound ligand bound strongly in a triplet isomer ($^3Rh^+N^3O^1$, $^3Rh^+N^2O^2$ or $^3Rh^+N^1O^3$), but could be a weakly-interacting N-bound ligand in a singlet isomer.

Once the singlet state is assigned as the lowest energy multiplicity for $n > 4$, interpretation of the spectra for the $Rh^+(N_2O)_n$-Ar complexes becomes simpler and less complex. By contrast with $Co^+(N_2O)_n$ and the coinage metal complexes, the blue-shift in the N-bound

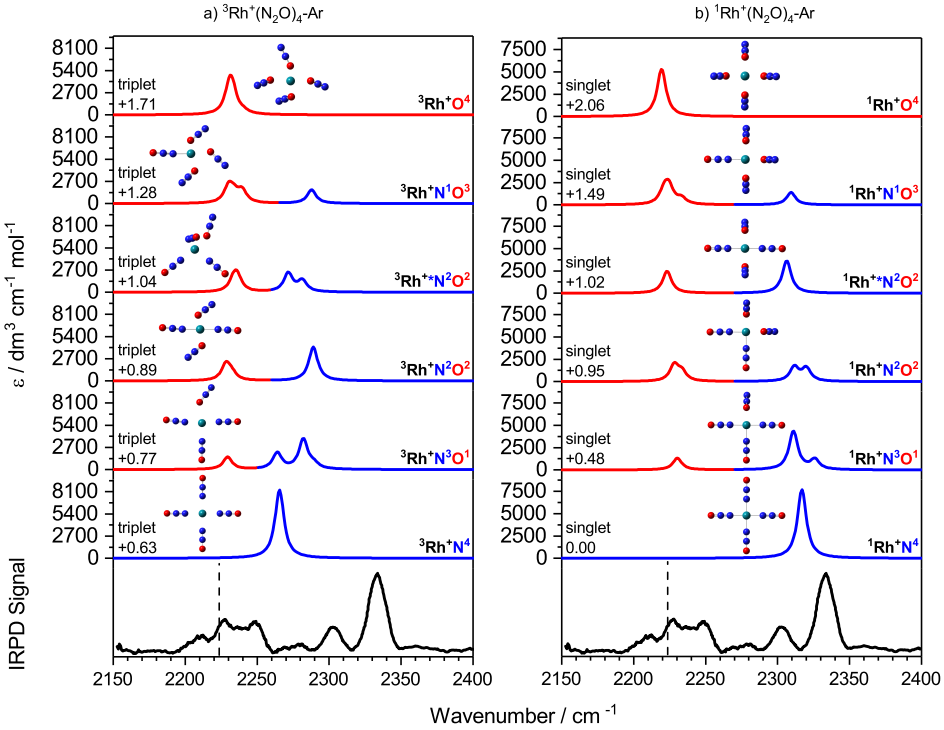

Figure 4.16: Experimental IRPD spectrum of the $Rh^+(N_2O)_4$-Ar complex along with simulated IR spectra of low-lying: a) triplet-state isomers, and b) singlet-state isomers in the region of the N_2O asymmetric (N=N) stretch. Simulated IR bands corresponding to N-bound and O-bound ligands are indicated in blue and red, respectively. The relative energies of the isomers concerned are given in eV. The vertical dashed line indicates the wavenumber of the ν_3(N=N) mode in isolated N_2O at 2223.5 cm^{-1}.[151] Figure reproduced with permission from *Phys. Chem. Chem. Phys.*, **2019**, 21, 13959-13967.

band increases further with n, reflecting more σ-donation from the N_2O ligands to the metal centre. $n = 4$ represents a complete coordination shell, adopting a square-planar geometry. Upon the addition of N_2O ligands to the $n = 4$ complex, the four metal-ligand (M^+-N) bond distances in the "core" shorten. Consequently, this increases the σ-donation and as such, leads to a more blue-shifted band, as observed in the experimental spectra (figure 4.17).

It is possible to assign bands in these $Rh^+(N_2O)_n$-Ar spectra as arising from N-bound N_2O ligands from singlet and triplet isomers, as shown in figure 4.17. At $n = 4$, where the global minimum spin configuration changes from triplet to singlet, the singlet remains

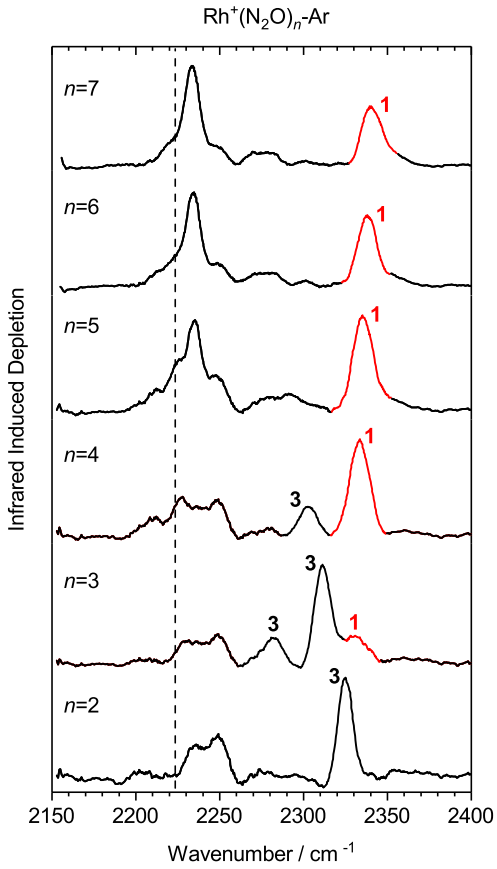

Figure 4.17: Experimental IRPD spectra of the $Rh^+(N_2O)_n$-Ar (n = 2-7) complexes in the region of the N_2O asymmetric (N=N) stretch. For comparison, the depletion intensity for each complex size was normalised with the maximum value in this region. N-bound bands are assigned to either a singlet isomer (1), or a triplet isomer (3). The vertical dashed line indicates the wavenumber of the ν_3(N=N) mode in isolated N_2O at 2223.5 cm^{-1}.[151] Figure reproduced with permission from *Phys. Chem. Chem. Phys.*, **2019**, 21, 13959-13967.

the lowest energy multiplicity calculated for higher order complexes (*i.e.* for n = 5-7) and dominate the IRPD spectra.

Table 4.3: Zero-point corrected energies of structural isomers of $Rh^+(N_2O)_n$ (n = 1-4) complexes calculated at the B3P86/Def2TZVP level of theory. Energies are relative to the global minimum geometry and electronic state for each complex.

Species	Isomer	$E_{rel.}$ / eV	Species	Isomer	$E_{rel.}$ / eV
$^3Rh^+(N_2O)$	N^1	0.00	$^3Rh^+(N_2O)_3$	N^3	0.00
	O^1	0.62		N^2O^1	0.19
$^1Rh^+(N_2O)$	N^1	1.17		$*N^2O^1$	0.40
	O^1	1.63		N^1O^2	0.62
$^5Rh^+(N_2O)$	N^1	2.93		$*N^1O^2$	0.80
	O^1	3.48		O^3	1.92
			$^1Rh^+(N_2O)_3$	N^3	0.30
				N^2O^1	0.79
				$*N^2O^1$	0.83
				N^1O^2	1.32
				$*N^1O^2$	1.34
				O^3	1.92
			$^5Rh^+(N_2O)_3$	N^3	3.40
				N^2O^1	3.52
				N^1O^2	3.61
				O^3	3.70
$^3Rh^+(N_2O)_2$	N^2	0.00	$^1Rh^+(N_2O)_4$	N^4	0.00
	N^1O^1	0.48		N^3O^1	0.48
	O^2	1.16		N^2O^2	0.95
$^1Rh^+(N_2O)_2$	N^2	0.83		$*N^2O^2$	1.02
	N^1O^1	1.36		N^1O^3	1.49
	O^2	1.93		O^4	2.06
$^5Rh^+(N_2O)_2$	N^2	3.38	$^3Rh^+(N_2O)_4$	N^4	0.63
	N^1O^1	3.65		N^3O^1	0.77
	O^2	3.52		N^2O^2	0.89
				$*N^2O^2$	1.04
				N^1O^3	1.28
				O^4	1.71
			$^5Rh^+(N_2O)_4$	N^4	4.16
				N^3O^1	4.21
				$*N^3O^1$	4.27
				N^2O^2	4.27
				N^1O^3	4.48
				O^4	4.42

4.4.3 $Ir^+(N_2O)_n$-Ar IRPD Spectra

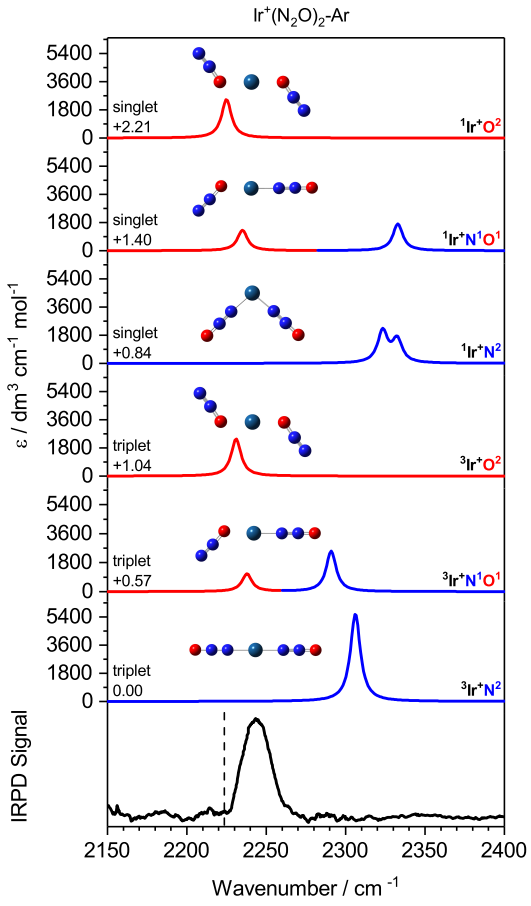

Figure 4.18: Experimental IRPD spectrum of the $Ir^+(N_2O)_2$-Ar complex along with simulated IR spectra of low-lying triplet- and singlet-state isomers in the region of the N_2O asymmetric (N=N) stretch. Simulated IR bands corresponding to N-bound and O-bound ligands are indicated in blue and red, respectively. The relative energies of the isomers concerned are given in eV. The vertical dashed line indicates the wavenumber of the ν_3(N=N) mode in isolated N_2O at 2223.5 cm^{-1}.[151] Figure reproduced with permission from *Phys. Chem. Chem. Phys.*, **2019**, 21, 13959-13967.

The IRPD spectra for the $Ir^+(N_2O)_n$-Ar (n = 2-7) complexes are shown in figure 4.5c and are unlike those of any other $M^+(N_2O)_n$ systems studied previously. Only a single, partially resolved feature is observed, slightly blue-shifted from the isolated N_2O asymmetric (N=N) stretch, previously interpreted as arising from O-bound ligands.

The ground state of the Ir cation (Ir^+) is a $5d^7(^4F)6s$ ^5F state with a $5d^8$ ^3F state *ca.*

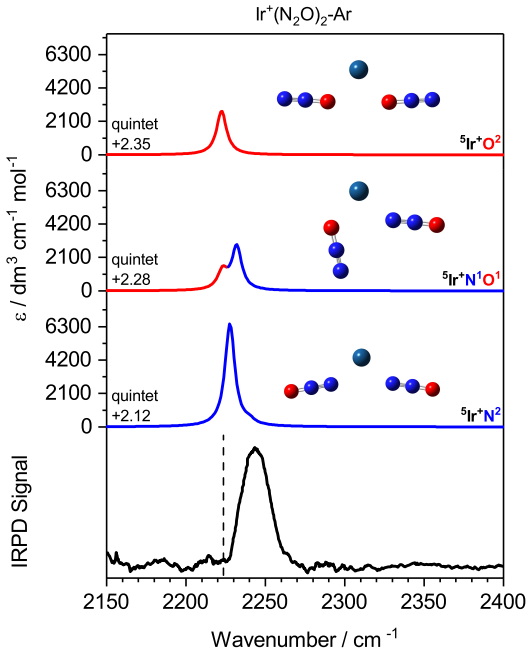

Figure 4.19: Experimental IRPD spectrum of the $Ir^+(N_2O)_2$-Ar complex along with simulated IR spectra of low-lying quintet isomers in the region of the N_2O asymmetric (N=N) stretch. Simulated IR bands corresponding to N-bound and O-bound ligands are indicated in blue and red, respectively. The relative energies of the isomers concerned are given in eV. The vertical dashed line indicates the wavenumber of the ν_3(N=N) mode in isolated N_2O at 2223.5 cm^{-1}.[151]

0.25 eV higher.[175] Complexation with even a single N_2O ligand stabilises the ^3F state of the ion relative to the ^5F ground state, resulting in a triplet lowest energy entrance-channel structure, $^3Ir^+N^2$ (see figures 4.4 and 4.18).

Figure 4.18 shows a comparison of the observed IRPD spectrum of $Ir^+(N_2O)_2$-Ar with calculated spectra of low-lying isomers. The simulated spectra for the triplet and singlet isomers (in particular the $^3Ir^+N^2$, $^3Ir^+N^1O^1$ and $^1Ir^+N^2$, $^1Ir^+N^1O^1$ isomers) agree very poorly with the observed spectrum in which there is no evidence of a band in the N-bound region around 2300 cm^{-1}. The simulated O-bound bands agree well with the observed band at 2244 cm^{-1}. However, since the $^3Ir^+O^2$ isomer lies > 1 eV above the ground state, it is highly unlikely that a pure distribution of this species is formed (indeed the same is true for the $^1Ir^+O^2$ isomer).

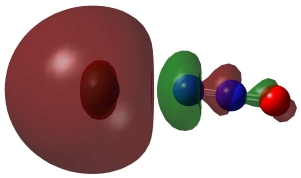

Figure 4.20: Molecular orbital of the $^5Ir^+N^1$ isomer of $Ir^+(N_2O)$ calculated at the B3P86/Def2TZVP level of theory showing the interaction of the $6s$ orbital on the Ir^+ with the 7σ orbital from N_2O, forming a non-linear complex.

Despite lying considerably higher in energy, the simulated spectra of the quintet state isomers agree well with the experimental IRPD spectrum (figure 4.19), as no significant blue-shift is predicted for the N-bound ligands. In the quintet isomers, higher population of strongly antibonding orbitals, including a $6s$-7σ interaction (figure 4.20), weakens the N-bound metal-N_2O interaction, reflected in the non-linear structures observed in figure 4.19. As there are no strong N-bound ligands present in the quintet isomers, the predicted bands in both N- and O-bound ligands appear in the region 2220-2240 cm^{-1}. The observed spectral band is notably broader when compared to the $Co^+(N_2O)_2$-Ar and $Rh^+(N_2O)_2$-Ar spectra. This band is thus assigned as a convolution of the three quintet isomers, $^5Ir^+N^2$, $^5Ir^+N^1O^1$ and $^5Ir^+O^2$. Table 4.4 presents the calculated relative energies of the $Ir^+(N_2O)_n$ structural isomers.

The IRPD spectrum for $Ir^+(N_2O)_3$-Ar along with low-lying structures of simulated singlet and triplet isomers is presented in figure 4.21. Both the singlet and triplet isomers present simulated N-bound bands significantly blue-shifted from the isolated N_2O asymmetric stretch and thus, agree poorly with the observed IRPD spectrum. Just as with n = 2, the simulated spectra from the quintet-state isomers present bands in which there is little difference between N- and O-bound bands, and so agree well with the experimental spectrum. Interestingly, for the $^5Ir^+N^1O^2$ and $^5Ir^+N^2O^1$ isomers, the ligands no longer act

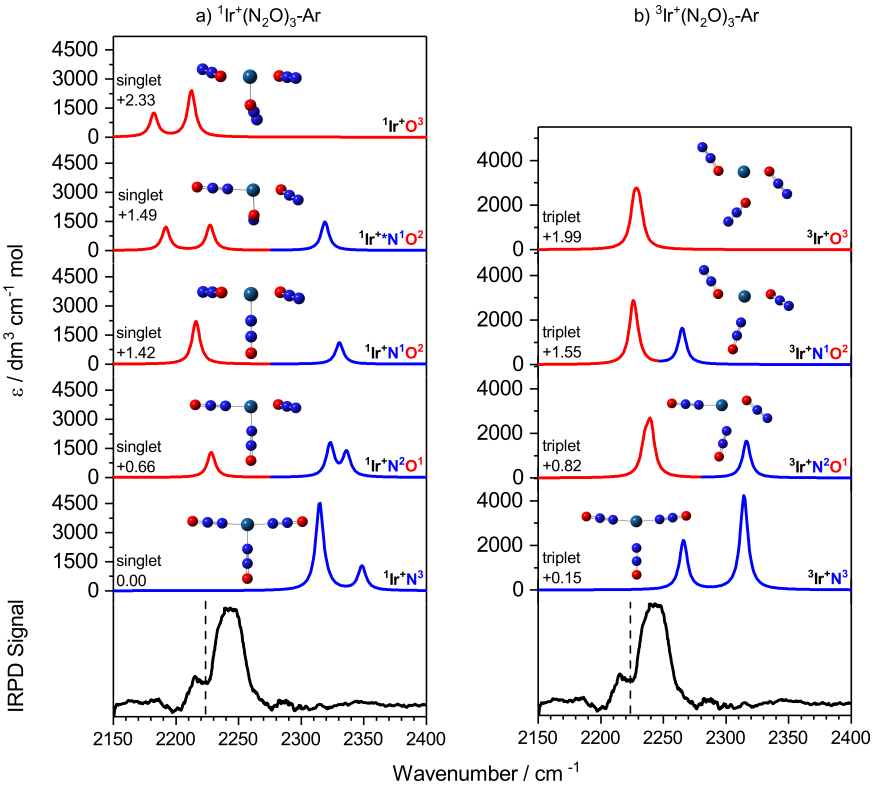

Figure 4.21: Experimental IRPD spectrum of the $Ir^+(N_2O)_3$-Ar complex along with simulated IR spectra of low-lying: a) singlet-state isomers, and b) triplet-state isomers in the region of the N_2O asymmetric (N=N) stretch. Simulated IR bands corresponding to N-bound and O-bound ligands are indicated in blue and red, respectively. The relative energies of the isomers concerned are given in eV. The vertical dashed line indicates the wavenumber of the ν_3(N=N) mode in isolated N_2O at 2223.5 cm^{-1}.[151]

as independent N- and O-bound ligands but instead act as coupled vibrational modes and so overlap. These bands are indicated in black in figure 4.22.

Another possible explanation for the absence of triplet isomers is clear from the calculated M^+ + N_2O reaction pathways shown in figure 4.4. On the triplet-state surface, the barrier to the O-atom transfer reaction is submerged, hence any reaction on the triplet surface can be assumed to proceed to completion resulting in the sequential production of IrO_m^+. This is consistent with the single-collision reaction studies of Böhme and cowork-

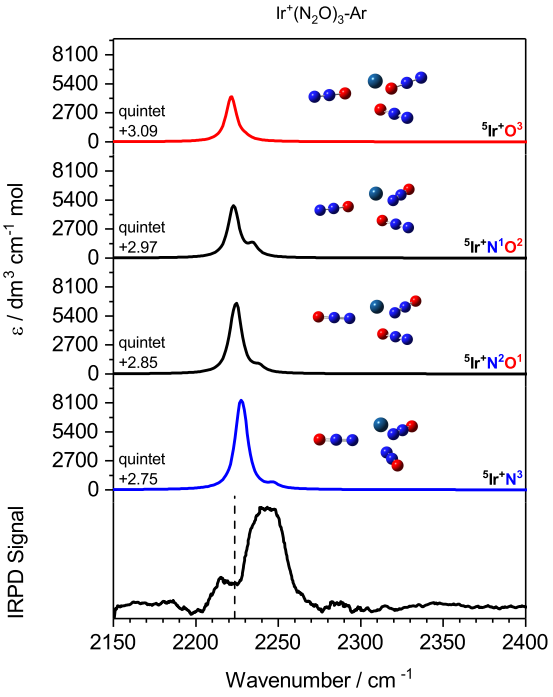

Figure 4.22: Experimental IRPD spectrum of the $Ir^+(N_2O)_3$-Ar complex along with simulated IR spectra of low-lying quintet isomers in the region of the N_2O asymmetric (N=N) stretch. Simulated IR bands corresponding to N-bound and O-bound ligands are indicated in blue and red, respectively. Bands in which N- and O-bound bands become vibrationally-coupled are indicated in black. The relative energies of the isomers concerned are given in eV. The vertical dashed line indicates the wavenumber of the ν_3(N=N) mode in isolated N_2O at 2223.5 cm^{-1}.[151]

ers,[100] as well as the complete loss of the Ir^+ signal observed in the time-of-flight mass spectrum (figure 4.3).

Contrastingly, a small (0.19 eV) but real barrier to the O-atom transfer reaction exists on the quintet surface and, under the rapid quenching conditions of the expansion, reactants could easily become trapped behind this small barrier as weakly-bound entrance-channel structures. These complexes could then form seeds for subsequent clustering and, if no change in spin was induced, then the only complexes observed would be quintet states with spectra as shown in figures 4.19 and 4.22, which agree well with the observed IRPD spectra. This interpretation would imply highly inefficient surface-crossings between quintet and triplet surfaces for all $Ir^+(N_2O)_n$-Ar complexes.

Table 4.4: Zero-point corrected energies of structural isomers of $Ir^+(N_2O)_n$ (n = 1-4) complexes calculated at the B3P86/Def2TZVP level of theory. Energies are relative to the global minimum geometry and electronic state for each complex.

Species	Isomer	$E_{rel.}$ / eV	Species	Isomer	$E_{rel.}$ / eV
$^3Ir^+(N_2O)$	N^1	0.00	$^1Ir^+(N_2O)_3$	N^3	0.00
	O^1	0.36		N^2O^1	0.66
$^5Ir^+(N_2O)$	N^1	0.53		N^1O^2	1.42
	O^1	0.63		$^*N^1O^2$	1.49
$^1Ir^+(N_2O)$	N^1	1.10		O^3	2.33
	O^1	1.35			
$^3Ir^+(N_2O)_2$	N^2	0.00	$^3Ir^+(N_2O)_3$	N^3	0.15
	N^1O^1	0.57		N^2O^1	0.82
	O^2	1.04		N^1O^2	1.55
$^1Ir^+(N_2O)_2$	N^2	0.84		O^3	1.99
	N^1O^1	1.40	$^5Ir^+(N_2O)_3$	N^3	2.75
	O^2	2.21		N^2O^1	2.85
$^5Ir^+(N_2O)_2$	N^2	2.12		N^1O^2	2.97
	N^1O^1	2.28		O^3	3.09
	O^2	2.35			
			$^1Ir^+(N_2O)_4$	N^4	0.00
				N^3O^1	0.64
				N^2O^2	1.28
				$^*N^2O^2$	1.38
				N^1O^3	2.08
				O^4	2.94
			$^3Ir^+(N_2O)_4$	N^4	1.43
				N^3O^1	1.61
				$^*N^3O^1$	2.00
				N^2O^2	1.85
				N^1O^3	2.45
				O^4	3.48
			$^5Ir^+(N_2O)_4$	N^4	4.24
				N^3O^1	4.28
				N^2O^2	4.37
				N^1O^3	4.49
				O^4	4.54

4.5 Discussion

The most striking aspect of this study is the difference observed in the spectra for each of the group 9 transition metals. This contrasts the coinage metal-N_2O complexes where only subtle differences in the structures and spectra were observed (see chapter 3). The differences in the group 9 N_2O complexes appear to correlate with the importance of low-lying excited electronic states and, in particular, the differing effects successive ligation has on the ground and excited states of the metal cations.

The first row group 9 metal cation, Co^+, when complexed with N_2O presents the simplest IRPD spectra, behaving similarly to the coinage metal ions. A satisfactory understanding of the spectra, in terms of N- and O-bound ligands, is achieved when considering only the ground electronic state. The excited states were calculated to lie significantly higher in energy. A smooth red-shift in the N-bound spectral band is observed with successive ligation as incoming ligands impair the efficiency of σ-donation by the two core ligands.

The second and third row group 9 metal cations, Rh^+ and Ir^+, present qualitatively different IRPD spectra when complexed with N_2O. Particularly in the case of the $Rh^+(N_2O)_n$-Ar complexes, the IR spectra contain evidence for the role of excited electronic states, with new bands appearing in the spectra at n = 3,4 just as the singlet state is calculated to compete with the triplet state as the ground state multiplicity. Such findings are not unprecedented, as it is this abundance of low-lying electronic states within the platinum group metals which make them so useful in catalysis.

It is worth noting that for the group 9 transition metal-ligand complexes studied here, a satisfactory understanding of the observed spectra is achieved when compared to the calculated low-lying spin states and structures predicted by density functional theory. This contrasts with the naked metal clusters ($M_n^{+/0/-}$) of the platinum group elements, the

Table 4.5: Bond distances (nitrous oxide molecule along with M-X where X is the terminal atom, *i.e.* N or O), reduced masses, and force constants for the lowest energy N- and O-bound isomers of $M^+(N_2O)$ (M^+ = Co, Rh, Ir) complexes (along with quintet isomers for Ir) calculated at the B3P86/Def2TZVP level of theory.

Species	N=N / Å	N=O / Å	k / mDyn/Å	μ / Da	M-X / Å
N_2O	1.120	1.180	47.27	14.10	-
$^3Co^+NNO$	1.125	1.150	50.36	14.14	1.930
$^3Co^+ONN$	1.108	1.205	48.32	14.05	1.994
$^3Rh^+NNO$	1.122	1.154	51.15	14.12	2.040
$^3Rh^+ONN$	1.100	1.203	47.89	14.05	2.240
$^3Ir^+NNO$	1.122	1.154	52.49	14.12	1.936
$^3Ir^+ONN$	1.107	1.218	47.13	14.04	2.074
$^5Ir^+NNO$	1.126	1.150	49.02	14.14	2.322
$^5Ir^+ONN$	1.110	1.206	47.11	14.05	2.356

electronic and geometrical structures of which remain, in some cases, a matter of heated discussion.[176–180]

Table 4.5 presents the calculated bond distances, reduced masses, and force constants for the N- and O-bound isomers of the group 9 nitrous oxide complexes. Similar to the case of the coinage metals, the observed blue-shifts can be diagnosed from the force constant, k, rather than the nitrous oxide bond distances. Interestingly, for the $^5Ir^+NNO$ complex, there is a reduction in the force constant (when compared to the triplet complexes) and an increase in the M-X bond distance. Both effects, in addition to the molecular orbital interactions, figure 4.20, explain the weakly-interacting N-bound N_2O ligand and small blue-shift observed in the IRPD spectra.

4.6 Conclusions

The structures of gas-phase $M^+(N_2O)_n$ complexes (M = Co, Rh, Ir; n = 2-7) were studied using a combination of IRPD spectroscopy and density functional theory. The spectra of the complexes for the three group 9 transition metals are starkly different from one another

and evolve in contrasting ways with increasing ligand number, n.

Simulated IR spectra based on DFT calculated low-lying structures provide clear explanations for the observed IRPD spectra in terms of isomers with spectroscopically distinguishable N- and O-bound ligands. In all cases, the N-bound isomers represent the lower in energy with significant barriers to free internal rotation allowing for trapping of O-bound ligands. The IRPD spectra of the $Rh^+(N_2O)_n$ and $Ir^+(N_2O)_n$ complexes present additional evidence of low-lying excited electronic states including, in the case of the former, a switch in spin multiplicity of the ground state at $n = 4$.

The combination of multiple binding motifs and low-lying electronic states gives rise to a rich and diverse range of isomers. The presence of spectroscopically distinguishable N- and O-bound core ligands gives rise to the tantalising possibility of addressing individual ligands with known binding motifs. This in turn offers the possibility of controllable infrared excitation for the study of intra-complex chemistry.

Chapter 5

Infrared Spectroscopy of Closed *s*-Shell Gas-Phase $M^+(N_2O)_n$ (M = Li, Al) Ion-Molecule Complexes

This chapter presents a combined experimental and computational study of the structures of gas-phase $M^+(N_2O)_n$ (M = Li, Al) complexes. Unlike in previous chapters on coinage metal- and group 9-nitrous oxide complexes, N- and O-bound isomers in this case are essentially isoenergetic and cannot be distinguished spectroscopically at this resolution. However, in the case of the Li^+ complexes, there is evidence for the presence of N_2 moieties, indicating the presence of inserted, $OLi^+N_2(N_2O)$ type structures. The bound N_2 band lies to the blue of the signature of molecularly N- and O-bound ligands and is well-reproduced in the simulated spectra of energetically low-lying structures computed from density functional theory. Other explanations such as overtones or combination bands were calculated but did not present good agreement with the observed spectra. No such inserted isomers are observed in the case of $Al^+(N_2O)_n$ complexes, whose infrared spectra can be understood on

the basis of molecularly-bound N_2O ligands. The differences in the $M^+(N_2O)_n$ structures observed for these closed-shell, ns^2 metal centres relative to other metal cations (coinage and group 9) are discussed in terms of likely binding motifs. Much of the work presented in this chapter is based on the publication: Infrared spectroscopy of closed s-shell gas-phase $M^+(N_2O)_n$ (M = Li, Al) ion-molecule complexes, Cunningham, E. M.; Gentleman, A. S.; Beardsmore, P. W.; Mackenzie, S. R.; *Mol. Phys.*, DOI: 10.1080/00268976.2019.1595202.

5.1 Introduction

Kinetic reactivity studies of the reaction of Li + N_2O over a temperature range of 363 - 900 K has been carried out by Plane and coworkers.[181] The primary reaction observed was O-atom transfer:

$$Li + N_2O \longrightarrow LiO + N_2 \tag{5.1}$$

The concentration of metal atoms was monitored in real time using laser-induced fluorescence (LIF), with second order rate constants measured at nine different temperatures between 363 and 900 K. When the data was plotted in standard Arrhenius form, a strong departure from linearity was observed for temperatures above 600 K. The non-Arrhenius behaviour observed above 600 K was attributed to the involvement of vibrationally-excited N_2O, enabling the reaction to proceed *via* a close-range, charge-transfer mechanism, significantly enhancing the reaction cross section.

Reactions of the Al^+ ion with N_2O have been studied by Armentrout and coworkers using guided-ion-beam mass spectrometry.[182] The O-atom transfer reaction was also the primary reaction observed here:

$$Al^+ + N_2O \longrightarrow AlO^+ + N_2 \tag{5.2}$$

These studies were carried out to further confirm the thermochemistry of AlO^+. The measured thresholds for this reaction were significantly higher than the calculated thermodynamic values, suggesting a large activation barrier to O-atom transfer. The authors suggest this barrier is due to the spin-forbidden processes such as removing a ground-state oxygen atom from N_2O.

Relevant infrared studies on lithium/aluminium atom reactions with nitrous oxide have been performed in matrix isolation by Andrews[183,184] and Zhou.[185] Initial studies by Andrews found that Li atoms produced thermally would only react with N_2O to form LiO and Li_2O in a nitrogen gas matrix, but not in an argon matrix.[183] This was attributed to the reactions requiring energy assistance. A follow-up study was carried out investigating the efficacy of laser vaporisation in the O-atom transfer reaction.[184] Pulsed laser evaporation has been proven to be an efficient method in producing atoms with excess kinetic energy for reactions with small molecules. Li atoms produced from laser vaporisation were found to react with N_2O in an argon matrix forming the LiO product, in contrast to thermal Li atom reactions, excess kinetic energy in the laser evaporated Li atoms provides the activation energy for the O-atom transfer reaction.

Reactions of laser-ablated Al atoms with nitrous oxide in an argon matrix yielded exclusively AlNNO complexes, identified on the basis of isotopically-substituted infrared absorptions coupled with theoretical calculations.[185]

As outlined in chapter 1, it is well known that nitrous oxide is a potent greenhouse gas. However, metal cations, in particular the group 1 metals Na and K, are also atmospherically significant. Hundreds of tons of meteoritic material, rich in these lighter metals enter the

upper atmosphere every day. The metals become a sink for positive charge and have been proved useful as a tracer for the study of dynamics and the neutral/ion chemistry of the mesosphere and lower thermosphere (MLT).[73,186–191]

Beyond electrostatic interactions, the bonding within metal-nitrous oxide complexes has been well established in previous chapters and by Zhou,[98] and is dominated by electron donation from the N_2O HOMO-1, 7σ orbital to the metal ion (especially partially-filled M^+-centered sd_{z^2} hybrid orbitals). By way of testing this binding mechanism further, this chapter reports a combined experimental and quantum chemical study of $Li^+(N_2O)_n$ and $Al^+(N_2O)_n$ complexes, aiming to investigate the fundamental binding mechanisms associated with metals without any occupied *d* orbitals.

5.2 Experimental Methods

The instrument and technique have been described in detail in chapter two. Briefly, gas phase $M^+(N_2O)_n$ (M = Li, Al) complexes along with their argon-tagged (or N_2-tagged) counterparts are formed by 532 nm pulsed ablation of a rotating Li/Al alloy disc (composition 1:9) in the presence of argon (or nitrogen) carrier gas seeded with 0.6% (1.46%) N_2O. The resulting molecular beam is skimmed and positively charged species are detected by reflectron time-of-flight mass spectrometry.[129] Pulsed infrared radiation, tunable in the 2150-2350 cm^{-1} region covering the asymmetric ν_3(N=N) mode in nitrous oxide, is provided by an optical parametric oscillator/amplifier system (LaserVision). The infrared beam counter-propagates with the molecular beam and spectra are collected *via* the "inert messenger" technique.[132,160–164] Absorption of an infrared photon results in the loss of a weakly-bound Ar (or N_2) fragment from a photoexcited $M^+(N_2O)_n$-Ar (or $M^+(N_2O)_n$-N_2) complex, providing a mass spectrometric signature of this dissociative event. Monitoring

the fractional depletion of a $M^+(N_2O)_n$-Ar (or $M^+(N_2O)_n$-N_2) complex as a function of infrared photon energy yields the infrared spectrum of the $M^+(N_2O)_n$ complex of interest.

To aid in assigning and interpreting and experimental data, the structures and simulated spectra of energetically low-lying isomers were calculated using density functional theory (DFT). Calculations performed on the $M^+(N_2O)_n$ structures employed the B3PW91-D3 hybrid density functional[149,152] coupled with the aug-cc-pVDZ basis set.[153,154] All calculations were performed using the Gaussian09 suite of programs.[150]

5.3 Time-of-Flight Mass Spectra

Figure 5.1 shows the time-of-flight mass spectrum illustrating the production of $Li^+(N_2O)_n$ and $Al^+(N_2O)_n$ complexes following the ablation of a Li/Al alloy disc (composition 1:9) in the presence of a six bar pulse of argon carrier gas seeded with 0.6% N_2O. A range of $Li^+(N_2O)_n$ and $Al^+(N_2O)_n$ complexes, along with their argon-tagged counterparts, can be identified. Under the same experimental conditions, Li^+ clusters more effectively than Al^+, as reflected in the comparable signal intensities for the $Li^+(N_2O)_n$ and $Al^+(N_2O)_n$ complexes despite the 9:1 Al:Li alloy ratio. Similarly, the $Li^+(N_2O)_n$ complex distribution peaks at $n = 4$ under these conditions, whilst the $Al^+(N_2O)_n$ distribution peaks at $n = 1$ and falls monotonically with n thereafter.

5.4 $Li^+(N_2O)_n$-Ar IRPD Spectra

Figure 5.2 shows the IRPD spectra for the $Li^+(N_2O)_n$-Ar (n = 2-9) complexes. The spectrum for the $n = 2$ complex is dominated by a strong feature at 2267 cm^{-1} and weaker features around 2245 cm^{-1} and 2294 cm^{-1}. All three bands are blue-shifted from the ν_3(N=N) mode in isolated N_2O at 2223.5 cm^{-1}.[151] The spectra for the $n = 3$ and 4 com-

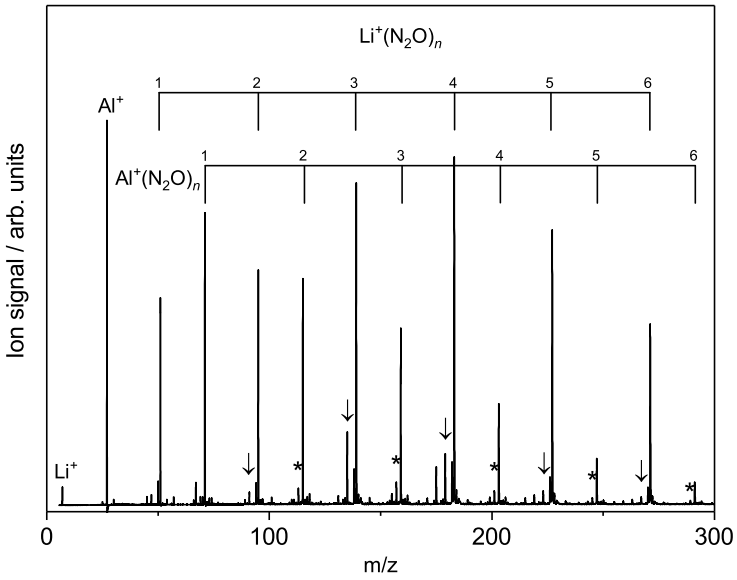

Figure 5.1: Time-of-flight mass spectrum of $Li^+(N_2O)_n$ and $Al^+(N_2O)_n$ complexes produced by laser ablation of a Li/Al (1:9) alloy disc in the presence of an argon carrier gas (6 bar backing pressure) seeded with 0.6% N_2O. $Li^+(N_2O)_n$-Ar ion signals are indicated by arrows with $Al^+(N_2O)_n$-Ar complexes indicated by asterisks (*). Figure reproduced with permission from *Mol. Phys.*, **2019**, DOI: 10.1080/00268976.2019.1595202.

plexes are qualitatively similar to that of $n = 2$ but red-shifted by 8 cm^{-1} and 14 cm^{-1}, respectively. The $n = 5$ and 6 spectra each exhibit one strong band centered at 2245 cm^{-1} and 2242 cm^{-1}, respectively. In addition to this main band, a new spectral feature appears in the spectra of the n = 7-9 complexes very close to the free N_2O stretch at 2223.5 cm^{-1}. The strongest band observed in the spectra for all complex sizes undergoes a smooth red-shift from 2267 cm^{-1} ($n = 2$) to 2242 cm^{-1} ($n = 6$) before blue-shifting very slightly to 2245 cm^{-1} by $n = 9$.

The evolution of the $Li^+(N_2O)_n$-Ar IRPD spectra with n exhibits marked similarity with that of the $Co^+(N_2O)_n$-Ar and coinage metal $M^+(N_2O)_n$-Ar (M = Cu, Ag, Au) complexes and, as such, a similar rationale can be applied to their understanding.[170,192] As before, it is informative to understand the binding of the Li^+N_2O complex. Figure 5.3a presents the calculated potential energy surface (PES), $V(R,\Theta)$, of the Li^+N_2O complex.

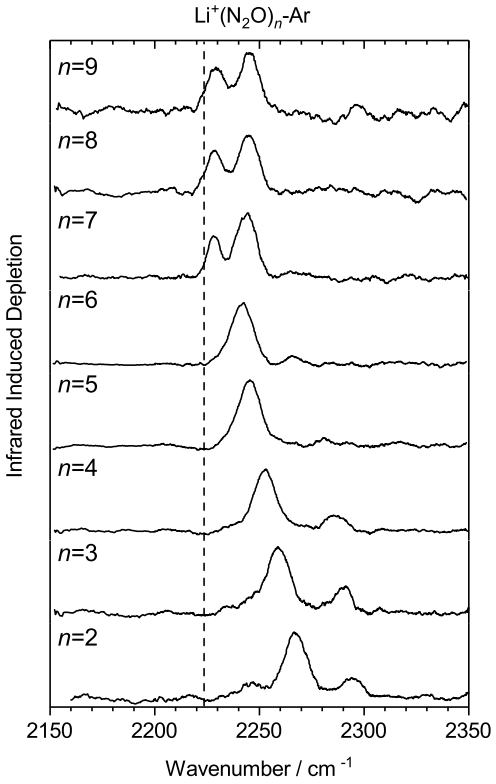

Figure 5.2: Experimental IRPD spectra of $Li^+(N_2O)_n$-Ar (n = 2-9) complexes in the region of the N_2O asymmetric (N=N) stretch. In each case depletion of the ion signal occurs due to the loss of the Ar messenger atom. For comparison the depletion intensity for each complex size was normalised with the maximum value in this region. The vertical dashed line indicates the wavenumber of the ν_3(N=N) mode in isolated N_2O at 2223.5 cm^{-1}.[151] Figure reproduced with permission from *Mol. Phys.*, **2019**, DOI: 10.1080/00268976.2019.1595202.

The putative global minimum structure is a linear Li^+NNO complex (*i.e.*, binding *via* the terminal N-atom). However, a deep secondary minimum, only *ca.* 0.1 eV above the global minimum is calculated corresponding to the near-linear Li^+ONN configuration, *i.e.*, bound *via* the terminal O-atom. These features are mirrored in figure 5.3b, showing a plot of energy vs. Li-N-N bond angle where the N_2O geometry was allowed to relax. As observed in previous chapters, O-bound N_2O binds to the Li^+ by electrostatic interactions, with the metal centre interacting directly with one of the lone pairs of electrons on the terminal O-atom, resulting in a non-linear structure. The O-bound minimum is broader than the N-bound minimum but wide amplitude motion is expected in each energy well.

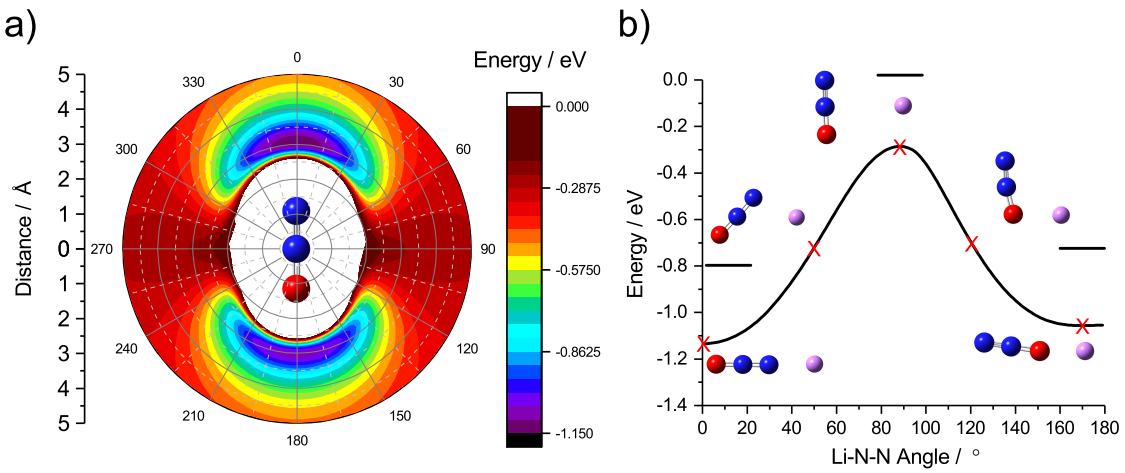

Figure 5.3: (a) PES for the Li^+N_2O complex showing one linear minimum, Li^+NNO, and one quasilinear minimum, Li^+ONN. This PES was generated by fixing the N_2O molecule at its equilibrium geometry. (b) Minimum energy pathway as a function of Li-N-N bond angle illustrating the relative energies of N- and O-bound minima. For this PES the N_2O geometry was allowed to relax. Horizontal lines indicate the energy of the respective geometry-optimised structures including zero-point correction. Figure reproduced with permission from *Mol. Phys.*, **2019**, DOI: 10.1080/00268976.2019.1595202.

The two minima are separated by a large barrier to internal rotation of > 0.8 eV with the zero-point energy of the T-shaped (90°) structure very close to the dissociation energy (*i.e.*, barely bound). As observed previously, the rapid cooling which occurs in the free-jet expansion facilitates the trapping of excited isomeric forms behind such barriers, leading to the possibility of a range of isomers with mixed N- and O-bound ligands. In previous chapters however, the N-bound potential minimum is significantly deeper than the O-bound giving rise to a clearly resolved spectral signature of each.

Just as in previous chapters, the following notation is adopted: $^{2S+1}M^+N^xO^y$, which represents a particular structure whereby x and y are integer values that indicate the number of N- and O-bound N_2O ligands, respectively, and as such: $x + y = n$. For example, $^1M^+N^1O^1$ represents a singlet state isomer of $M^+(N_2O)_2$, with one N-bound ligand and one O-bound ligand.

Figure 5.4 shows the experimental IRPD spectrum of $[LiN_4O_2Ar]^+$ together with the

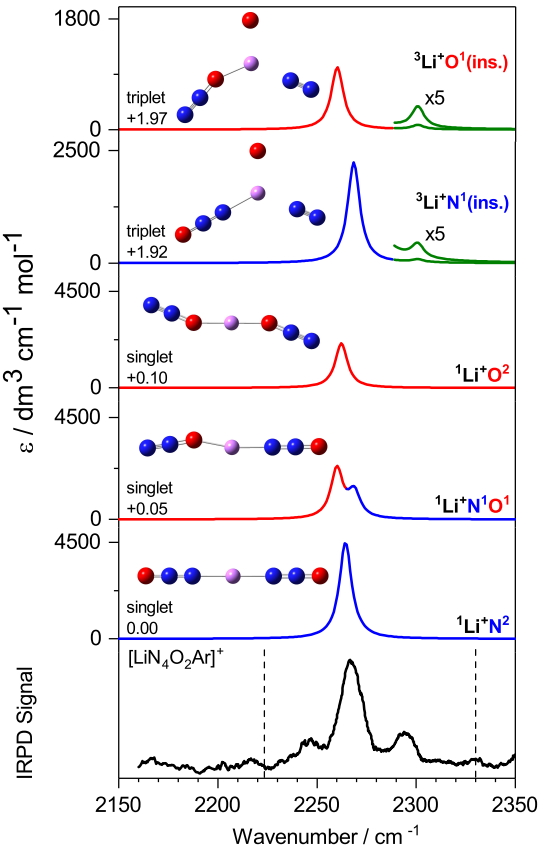

Figure 5.4: Experimental IRPD spectrum of $[LiN_4O_2Ar]^+$ in the region of the N_2O asymmetric (N=N) stretch, along with the simulated vibrational spectra of energetically low-lying isomers. Simulated IR bands corresponding to N-bound and O-bound ligands, and N≡N vibrations in insertion structures are indicated in blue, red and green respectively. The relative energies of the different calculated isomers are given in eV. The vertical dashed lines at 2223.5 cm^{-1} and 2330 cm^{-1} indicate the wavenumber of the ν_3(N=N) mode in isolated N_2O and the N≡N frequency in isolated N_2, respectively.[151] Figure reproduced with permission from *Mol. Phys.*, **2019**, DOI: 10.1080/00268976.2019.1595202.

simulated spectra of calculated energetically low-lying isomers. The molecular formula nomenclature is adopted to indicate that it is unclear whether the N_2O ligands bind molecularly and/or form inserted structures. The only energetically low-lying isomers of molecularly-bound isomers are singlet states. Other multiplicities are calculated to lie much higher in energy and are unlikely to be formed in our expansion. The $^1Li^+N^2$ isomer represents the global minimum structure, however $^1Li^+N^1O^1$ and $^1Li^+O^2$ lie very close at 0.05 and 0.10 eV, respectively reflecting the near isoenergetic nature of the N- and O-binding.

The $^1Li^+N^2$ structure cannot account for the three bands in the observed IRPD spectrum and it is inferred that the presence of O-bound ligands (in the form of $^1Li^+N^1O^1$ and $^1Li^+O^2$ isomers) account for the lower wavenumber band at 2245 cm^{-1}.

Unlike the coinage and group 9 metal complexes, in which the spectral signatures of N- and O-bound ligands were spectrally well-resolved (separated by 118 cm^{-1} in the case of $Au^+(N_2O)_2$-Ar), the $Li^+(N_2O)_n$-Ar complexes display two bands that lie close to each other in wavenumber. This is reflected in the almost isoenergetic nature of the $^1Li^+N^2$, $^1Li^+N^1O^1$ and $^1Li^+O^2$ structures. The binding mechanism for N-bound N_2O ligands has been well established[98] and is dominated by electron donation from the N_2O HOMO-1, 7σ orbital to the metal centre. The 7σ orbital is antibonding with respect to the N=N bond, which is thus strengthened by this donation resulting in a spectral blue-shift of the fundamental ν_3 mode. Unlike the group 9 and 11 cations, Li^+ has a $1s^2$ electron configuration and thus, s-d hybridisation is not energetically feasible. Therefore, any donation from the 7σ orbital is less efficient leading to a less pronounced blue-shift and reduced distinction between N- and O-bound ligands.

It is clear, however, that molecularly-bound isomers cannot fully account for the spectrum observed. Figure 5.4 also shows the lowest triplet state isomers, $^3Li^+N^1$(ins.) and $^3Li^+O^1$(ins.), in which the metal ion is inserted into the N_2O forming a $OLi^+N_2(N_2O)$ structure. The triplet state is the lowest energy multiplicity for all inserted isomers of all complex sizes, consistent with previous *ab initio* studies which concluded that the triplet state, $X^3\Sigma^-$, is the lowest energy term of the lithium monoxide cation.[193] The band at 2294 cm^{-1} agrees well with the simulated stretch of the N_2 moiety, which becomes infrared-allowed when N_2 binds to a metal ion.[194–196] The three bands in the observed spectrum are therefore assigned as a mixture of molecularly-adsorbed N- and O-bound N_2O ligands,

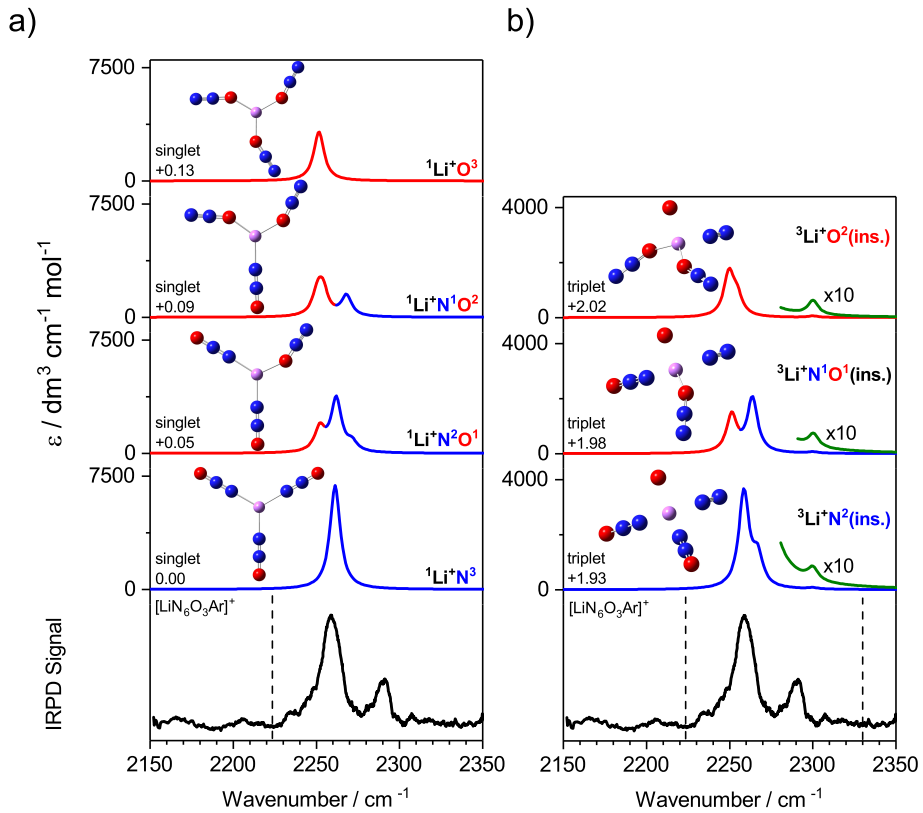

Figure 5.5: Experimental IRPD spectra of $[LiN_6O_3Ar]^+$ along with a) simulated vibrational spectra of energetically low-lying isomers of the ground, singlet state and b) simulated vibrational spectra of insertion isomers in the triplet state in the region of the N_2O asymmetric (N=N) stretch. Simulated IR bands corresponding to N-bound and O-bound ligands, and N≡N vibrations in insertion structures are indicated in blue, red and green respectively. The relative energies of the different calculated isomers are given in eV. The vertical dashed lines at 2223.5 cm^{-1} and 2330 cm^{-1} indicate the wavenumber of the ν_3(N=N) mode in isolated N_2O and the N≡N frequency in isolated N_2, respectively.[151] Figure reproduced with permission from *Mol. Phys.*, **2019**, DOI: 10.1080/00268976.2019.1595202.

together with inserted isomers.

A similar rationale can be applied when assigning the bands in the observed spectrum for $[LiN_6O_3Ar]^+$, figure 5.5. The strong band at 2259 cm^{-1} can be assigned as the signature of molecularly N-bound N_2O, with the weak shoulder to the red edge assigned to O-bound N_2O from low-lying isomers. Just as in the case for $[LiN_4O_2Ar]^+$, these structures alone cannot account for the feature at 2290 cm^{-1}, which is consistent with the N_2 stretch in the $^3Li^+N^2$(ins.), $^3Li^+N^1O^1$(ins.) and $^3Li^+O^2$(ins.) inserted structures, presented in figure

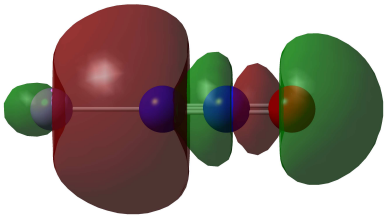

Figure 5.6: The HOMO-2 molecular orbital of N-bound $Li^+(N_2O)$ complex showing the 7σ orbital of N_2O binding to the metal-centred s-orbital.

5.5b. Although inserted structures were not observed in previous chapters of $M^+(N_2O)_n$ complexes, we cannot rule out the possibility that these N_2 bands were obscured by stronger features. This weak, blue-shifted band could also be assigned as an overtone or combination band. Anharmonic vibrational frequency calculations on molecularly-bound and inserted isomers were carried out on $n = 2$ and 3. From these calculations, combination bands were found to lie close to the observed bands at 2294 cm^{-1} and 2290 cm^{-1}, respectively. These bands, however, are on the order of 20 times weaker in intensity when compared to the calculated intensity of the N_2 stretch in inserted structures. The most plausible explanation for the observed bands at 2294 cm^{-1} and 2290 cm^{-1} (for $n = 2$ and 3, respectively) are therefore tentatively assigned to an N_2 stretch from an inserted complex.

Both Li^+ and N_2O are singlets in their ground state, whilst LiO^+ has a triplet ground state, thus the O-atom transfer reaction is spin forbidden (and endothermic). One possible explanation to explain the presence of inserted structures is that the $^3LiO^+(N_2)$ complex is formed during the laser ablation process in the source region, which is then the seed for subsequent N_2O ligation.

As observed in figure 5.2, as the number of ligands, n, increases, the main band (assigned to molecularly N-bound ligands) smoothly red-shifts, an observation that is ascribed to the proportionate reduction in σ-donation from each N-bound core ligand. Different

Table 5.1: Zero-point corrected energies of structural isomers of $Li^+(N_2O)_n$ (n = 1-3) complexes calculated at the B3PW91/aug-cc-pVDZ level of theory. Energies are relative to the global minimum geometry and electronic state for each complex.

Species	Isomer	$E_{rel.}$ / eV	Species	Isomer	$E_{rel.}$ / eV
$^1Li^+(N_2O)$	N^1	0.00	$^3LiO^+N_2(N_2O)$	N^1	0.00
	O^1	0.04		O^1	0.05
$^3Li^+(N_2O)$	N^1	2.84	$^1LiO^+N_2(N_2O)$	N^1	2.93
	O^1	3.16		O^1	2.99
$^3LiO^+N_2$	-	0.00	$^1Li^+(N_2O)_3$	N^3	0.00
$^1LiO^+N_2$	-	2.97		N^2O^1	0.05
				N^1O^2	0.09
				O^3	0.13
$^1Li^+(N_2O)_2$	N^2	0.00	$^3LiO^+N_2(N_2O)_2$	N^2	0.00
	N^1O^1	0.05		N^1O^1	0.05
	O^2	0.10		O^2	0.09

from the binding interactions observed in previous chapters, where the 7σ orbital of N_2O would interact with a metal-centred sd_{z^2} orbital, the N_2O instead σ donates to a metal-centred s orbital. Figure 5.6 shows the relevant molecular orbital (HOMO-2) of the N-bound $Li^+(N_2O)$ complex presenting such a binding interaction.

Overall, this red-shift ceases at n = 6, consistent with a complete coordination shell accordant with DFT calculated structures. The IRPD spectra for n = 7-9 present a new band at 2228 cm^{-1}, very close to the free N_2O stretch, signifying weakly-bound ligands in a second, outer coordination shell.

Table 5.1 presents the relative energies of the calculated structures of $Li^+(N_2O)_n$ and inserted $OLi^+N_2(N_2O)_n$ complexes (n = 1-3) in the lowest energy multiplicity.

5.5 $Li^+(N_2O)_n$-N_2 IRPD Spectra

Given the above interpretation that inserted isomers, $OLi^+N_2(N_2O)$, are present in the spectra of the $Li^+(N_2O)_n$-Ar (n = 2-4) complexes, experiments were performed replacing

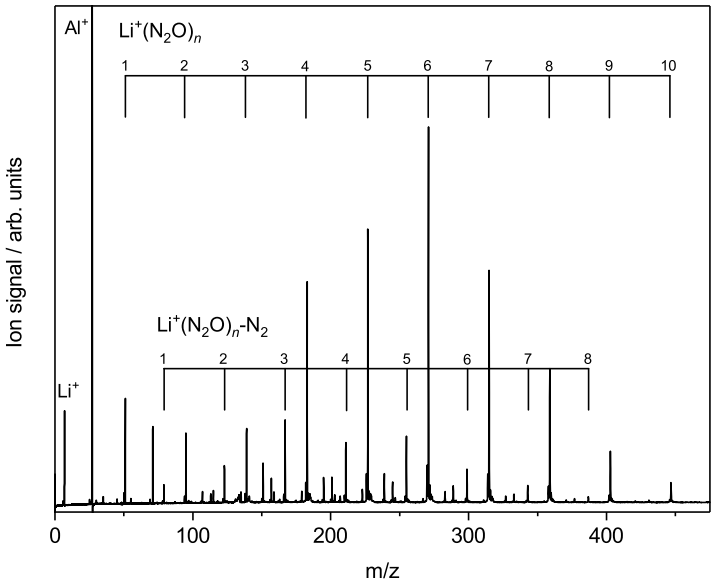

Figure 5.7: Time-of-flight mass spectrum of $Li^+(N_2O)_n$ and $Li^+(N_2O)_n$-N_2 complexes produced by laser ablation of a Li/Al (1:9) alloy disc in a nitrogen carrier gas seeded with 1.46% N_2O.

the carrier gas from argon to nitrogen. Figure 5.7 shows the time-of-flight mass spectrum showing the production of $Li^+(N_2O)_n$ and $Li^+(N_2O)_n$-N_2 complexes following the ablation of a Li/Al alloy disc (1:9) in the presence of a six bar pulse of nitrogen carrier gas seeded with 1.46% N_2O.

Figure 5.8 shows the IRPD spectra for the $Li^+(N_2O)_n$-N_2 (n = 2-8) complexes. The spectra for the n = 3-8 complexes show very similar band positions and relative band intensities to those of the $Li^+(N_2O)_n$-Ar (n = 3-8) complexes, figure 5.2. For n = 2, however, no discernible spectral features were observed in the IRPD spectrum.

A direct comparison between the messenger moieties is presented in figure 5.9. Figure 5.9a presents the experimental IRPD spectra of $Li^+(N_2O)_3$-N_2 along with that of $Li^+(N_2O)_3$-Ar. The spectra are very similar but both bands are somewhat broader in the N_2-tagged spectra, with slightly reduced separation when compared to the Ar-tagged complex. DFT calculated structures, together with their corresponding simulated spectra,

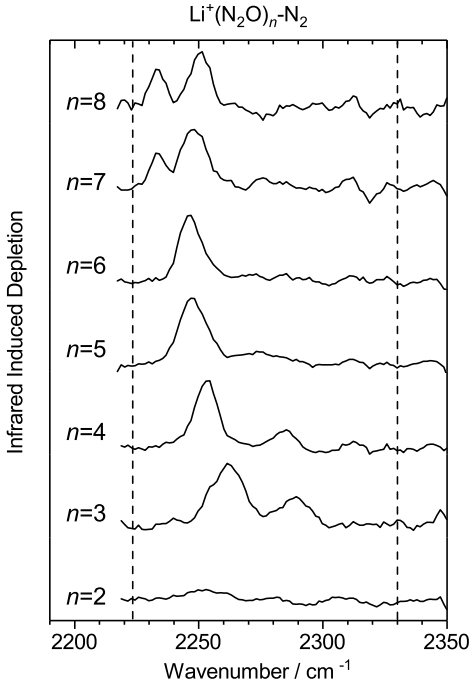

Figure 5.8: Experimental IRPD spectra of $Li^+(N_2O)_n$-N_2 (n = 2-8) complexes in the region of the (N=N) stretch in N_2O and in N_2. For ease of comparison the spectra for the $n \geqslant 3$ have been normalised. The vertical lines dashed at 2223.5 cm^{-1} and 2330 cm^{-1} indicate the wavenumber of the ν_3(N=N) mode in isolated N_2O and the N≡N frequency in isolated N_2, respectively.[151] Figure reproduced with permission from *Mol. Phys.*, **2019**, DOI: 10.1080/00268976.2019.1595202.

are consistent with this notion, presenting slight changes in vibrational modes when there is an Ar atom bound, or a N_2 ligand bound to the metal centre, figure 5.10.

Figure 5.9b presents the experimental IRPD spectra of $Li^+(N_2O)_2$-N_2 along with $Li^+(N_2O)_2$-Ar. The lack of discernible bands in the $Li^+(N_2O)_2$-N_2 spectrum indicates negligible photodissociation in this wavelength region, thus implying the N_2 moiety is bound relatively strongly. Calculated binding energies support this interpretation, with N_2 calculated to be bound by 0.32 eV to the $^1Li^+N^2$, $^1Li^+N^1O^1$ and $^1Li^+O^2$ isomers, and by 0.31 and 0.27 eV to the inserted isomers, $^3Li^+N^1$(ins.) and $^3Li^+O^1$(ins.), respectively. These energies are significantly higher than the calculated binding energy of the Ar atom, which is 0.14 eV for all isomers. Hence, any photon absorbed in this spectral region (*ca.* 0.28 eV) is sufficient to lead to Ar loss but not necessarily N_2 loss. For the n = 3 complexes, figure 5.9, the

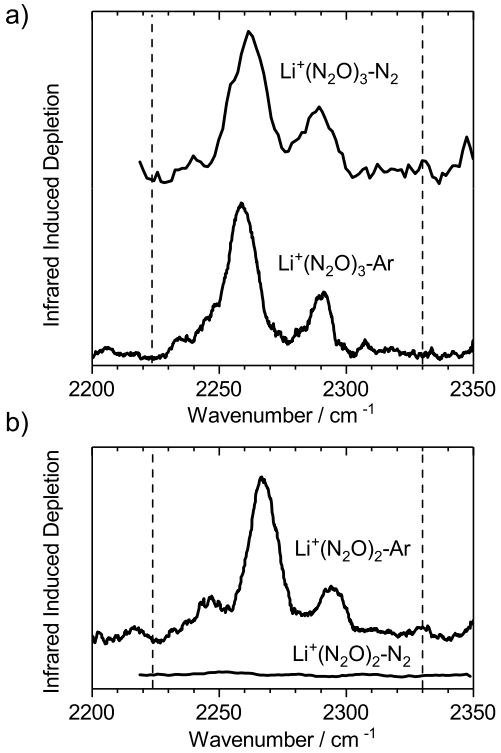

Figure 5.9: Experimental IRPD spectra of a) $Li^+(N_2O)_3$-N_2, $Li^+(N_2O)_3$-Ar and b) $Li^+(N_2O)_2$-N_2, $Li^+(N_2O)_2$-Ar complexes in the region of the N_2O asymmetric (N=N) stretch. In each case depletion of the ion signal occurs due to either the loss of the N_2 messenger molecule or the loss of the Ar messenger atom. For comparison the depletion intensity for each complex size has been approximately normalised with the maximum value in this region. The vertical lines dashed at 2223.5 cm^{-1} and 2330 cm^{-1} indicate the wavenumber of the ν_3(N=N) mode in isolated N_2O and the N≡N frequency in isolated N_2, respectively.[151] Figure reproduced with permission from *Mol. Phys.*, **2019**, DOI: 10.1080/00268976.2019.1595202.

N_2 moiety is bound to both the molecularly-bound and inserted isomers by 0.19 eV, whilst the Ar atom is bound by *ca.* 0.10 eV, thus one photon absorption brings about efficient messenger loss in both cases.

Using nitrogen as a carrier gas, it was hoped that the N_2 would provide an infrared signature of its vibrational stretch, predicted around the observed band at 2294 cm^{-1}, confirming the assignment of the bands in figures 5.4 and 5.5. Instead, the N_2 is itself bound too strongly to the $n = 2$ complex and a further weakly-bound messenger, such as Ar, would be needed for efficient photodissociation. In the case of $n = 3$, N_2 is weakly-bound and acts

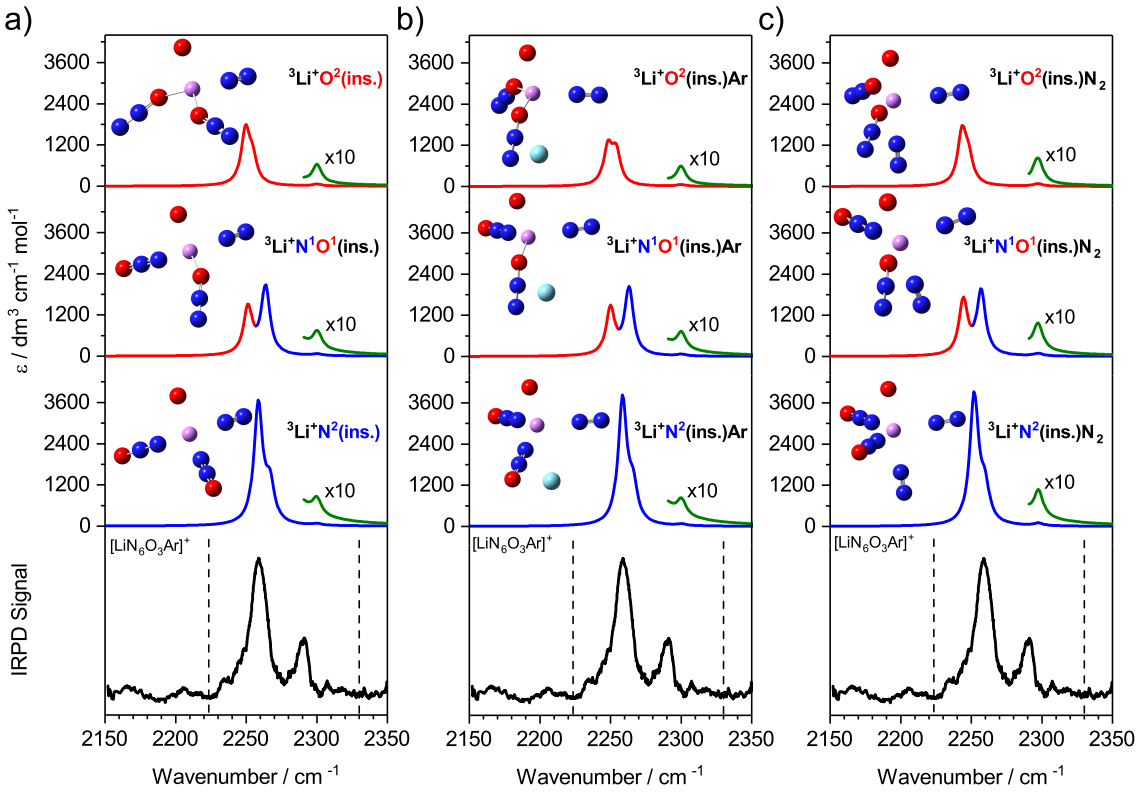

Figure 5.10: Experimental IRPD spectra of $[LiN_6O_3Ar]^+$ along with simulated spectra of a) insertion isomers, b) Ar-tagged insertion isomers, and c) N_2-tagged insertion isomers in the region of the N_2O asymmetric (N=N) stretch. Simulated IR bands corresponding to N-bound and O-bound ligands, and N≡N vibrations in insertion structures are indicated in blue, red and green respectively. The vertical lines dashed at 2223.5 cm^{-1} and 2330 cm^{-1} indicate the wavenumber of the ν_3(N=N) mode in isolated N_2O and the N≡N frequency in isolated N_2, respectively.[151]

as a messenger itself. As a result, although agreement with the simulated band positions is good, the bands at 2294 cm^{-1} (n = 2) and 2291 cm^{-1} (n = 3) cannot be conclusively assigned as an N_2 stretch. One method to carry out might be to employ a mass-selective technique which would observe photoinduced N_2 loss directly from $[LiN_{2n}O_n]^+$ complexes.

5.6 $Al^+(N_2O)_n$-Ar IRPD Spectra

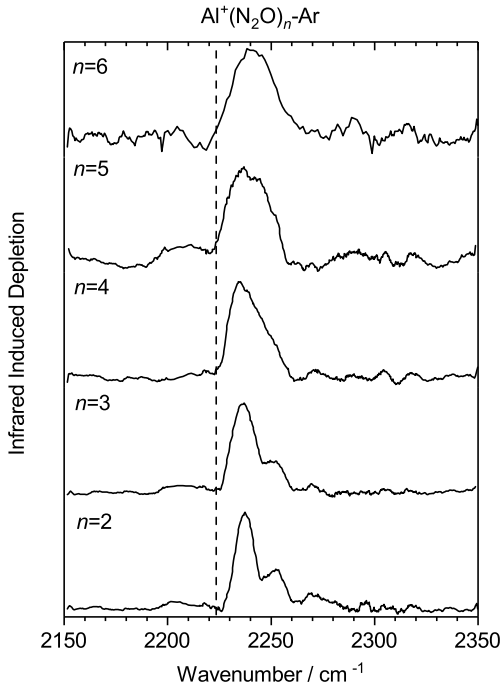

Figure 5.11: Experimental IRPD spectra of $Al^+(N_2O)_n$-Ar (n = 2-6) complexes in the region of the N_2O asymmetric (N=N) stretch. In each case depletion of the ion signal occurs due to the loss of the Ar messenger atom. For comparison the depletion intensity for each complex size was normalised with the maximum value in this region. The vertical dashed line indicates the wavenumber of the ν_3(N=N) mode in isolated N_2O at 2223.5 cm^{-1}.[151] Figure reproduced with permission from *Mol. Phys.*, **2019**, DOI: 10.1080/00268976.2019.1595202.

Figure 5.11 presents the IRPD spectra for $Al^+(N_2O)_n$-Ar (n = 2-6) complexes. The spectra for complexes n = 2,3 comprise a strong band at 2238 cm^{-1} and 2237 cm^{-1}, and a weaker band at 2251 cm^{-1} and 2250 cm^{-1}, respectively. These features become increasingly merged as n increases. As with Li^+N_2O, the calculated potential energy surface for Al^+N_2O supports two deep minima - a global Al^+NNO minimum and a secondary, slightly bent Al^+ONN minimum well (see figure 5.12a). Just as in the case for Li^+N_2O, the two potential minima are very close to isoenergetic (figure 5.12b), but the broader O-bound minimum leads to the zero-point energy here being lower than that in the deeper N-bound minimum. The barrier to internal rotation is, however, lower in this case (*ca.* 0.50 eV) than in the

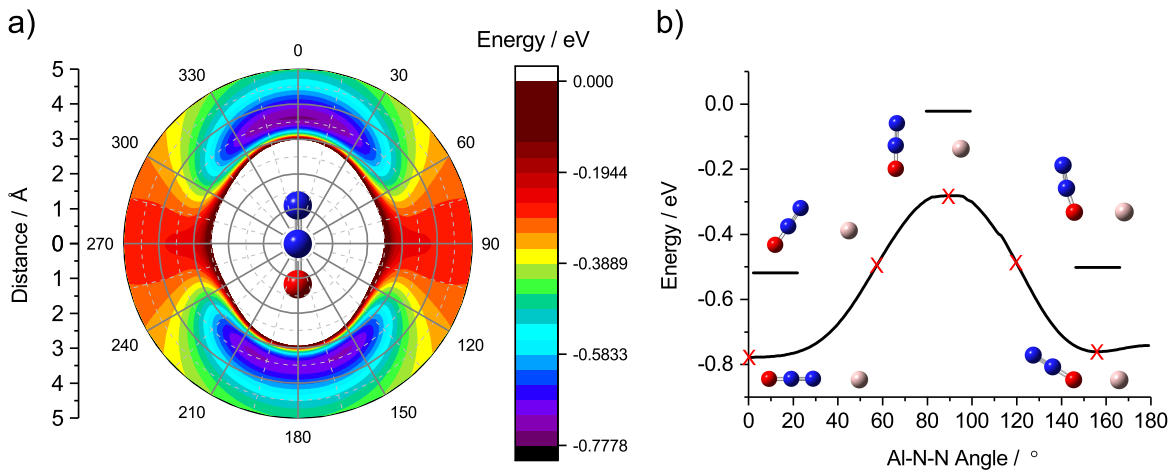

Figure 5.12: (a) PES for the Al^+N_2O complex showing a linear, ground state minimum, Al^+NNO and a secondary non-linear minimum, Al^+ONN. This PES was generated by fixing the N_2O molecule at its equilibrium geometry. (b) Minimum energy pathway as a function of Al-N-N bond angle illustrating the relative energies of N- and O-bound minima. For this PES the N_2O geometry was allowed to relax. Horizontal lines indicate the energy of the respective geometry-optimised structures including zero-point correction. Figure reproduced with permission from *Mol. Phys.*, **2019**, DOI: 10.1080/00268976.2019.1595202.

Li^+N_2O complex (*ca.* 0.80 eV) and the T-shaped intermediate structure is calculated to be barely bound.

Figure 5.13 shows the IRPD spectrum of $[AlN_4O_2Ar]^+$ along with simulated vibrational spectra of energetically low-lying molecularly-bound isomers. The energetic ordering of the different structures is in stark contrast with those of $[LiN_4O_2Ar]^+$. For $[AlN_4O_2Ar]^+$, the calculated structures of the inserted isomers, $^1Al^+N^1$(ins.) and $^1Al^+O^1$(ins.), are markedly lower in energy than the molecularly-bound structures, $^1Al^+N^2$, $^1Al^+N^1O^1$, and $^1Al^+O^2$. The simulated spectra corresponding to the inserted isomers, however, agree poorly with the observed IRPD spectrum, which is well-reproduced by the molecularly-bound structures. This implies a significant barrier to insertion which cannot be efficiently surmounted under the conditions of the molecular beam.

Different from any of the previous $M^+(N_2O)_n$ complexes studied in this thesis, N- and O-bound ligands in $[AlN_4O_2Ar]^+$ are not spectrally distinguishable. Indeed, analysis of the

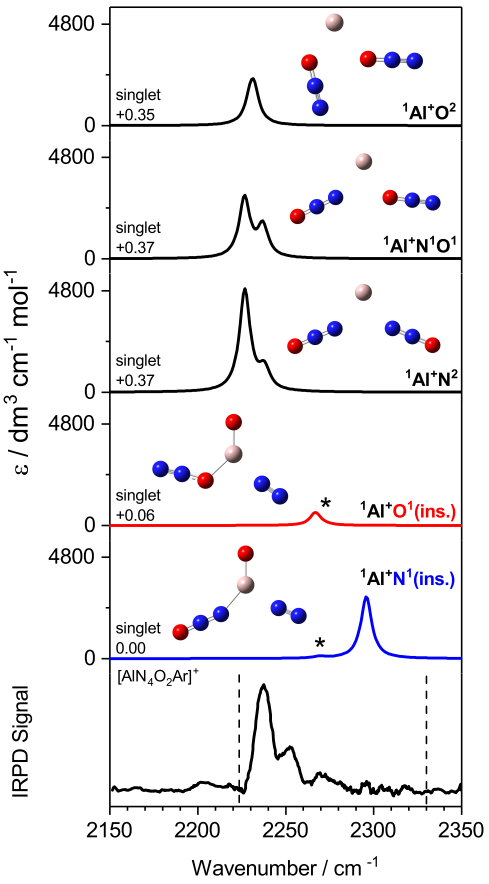

Figure 5.13: Experimental IRPD spectrum of $[AlN_4O_2Ar]^+$ in the region of the N_2O asymmetric (N=N) stretch along with the simulated vibrational spectra of energetically low-lying isomers. Simulated IR bands corresponding to N-bound and O-bound ligands are indicated in blue and red, respectively. Simulated IR bands corresponding to the N_2 moiety are indicated by an asterisk (*). The relative energies of the different calculated isomers are given in eV. The vertical dashed lines at 2223.5 cm^{-1} and 2330 cm^{-1} indicate the wavenumber of the ν_3(N=N) mode in isolated N_2O and the N≡N frequency in isolated N_2, respectively.[151] Figure reproduced with permission from *Mol. Phys.*, **2019**, DOI: 10.1080/00268976.2019.1595202.

predicted motions show that the N_2O vibrations are highly coupled and less localised on individual ligands. In this sense, the ligand vibrations in the molecularly-bound $Al^+(N_2O)_2$ isomers act similarly to the CO_2 ligands in $Al^+(CO_2)_n$ observed by Duncan and coworkers.[197] For $Al^+(CO_2)_n$ complexes, non-linear structures were attributed to the sequential CO_2 binding at the $3s^2$ Al^+ centre. The CO_2 ligands do not add to the metal centre according to VSEPR (for e.g. $n = 2$, a linear structure is expected), but instead bind to the same side of the metal ion. As explained by Bauschlicher and coworkers[198,199] and then by

Duncan[197] to rationalise the structure of $Mg^+(CO_2)_2$, as the first CO_2 ligand binds to the cationic metal centre, the ligand polarises the valence electron distribution inducing a partial negative charge on the opposite side of the metal ion. As such, the second CO_2 ligand avoids this negative charge by binding to the same side as the first ligand. The similarity of structures calculated here for $Al^+(N_2O)_2$ isomers when compared to those observed for $Al^+(CO_2)_n$[197] suggests the same polarisation effect dominates.

For $Al^+(N_2O)_n$ complexes, the coupled N_2O ligand vibrations behave similarly to CO_2 ligands. For the $n = 2$ complexes, both the in-phase and out-of-phase combinations of the two ligand ν_3 stretches must be considered, which is manifested by two bands at 2238 and 2251 cm^{-1}, respectively. By considering the calculated vibrational behaviour of the N_2O ligands, the stronger band at 2238 cm^{-1} is assigned to the out-of-phase asymmetric (N=N) combination, with the 2251 cm^{-1} weaker band assigned to the in-phase combination (with this combination displaying a reduced change in dipole moment relative to the out-of-phase combination). These combinations are present in the simulated spectra of all three molecularly-bound isomers, $^1Al^+N^2$, $^1Al^+N^1O^1$, and $^1Al^+O^2$ and it seems likely that the observed IRPD spectrum comprises a mixture of all three. Table 5.2 presents the relative energies of the calculated structures of $Al^+(N_2O)_n$ and inserted $OAl^+N_2(N_2O)_n$ complexes (n = 1-3) in the lowest energy multiplicity.

Similar to the Li^+ complexes, σ-donation is inefficient and thus, the observed vibrational bands are only slightly blue-shifted from those in isolated N_2O. As n increases, the number of possible combinations of ligand stretches increases, leading to a broader spread of the simulated stretches which is reflected in the spectral broadening of the IRPD bands as n increases.

Table 5.2: Zero-point corrected energies of structural isomers of $Al^+(N_2O)_n$ (n = 1-3) complexes calculated at the B3PW91/aug-cc-pVDZ level of theory. Energies are relative to the global minimum geometry and electronic state for each complex.

Species	Isomer	$E_{rel.}$ / eV	Species	Isomer	$E_{rel.}$ / eV
$^1Al^+(N_2O)$	N^1	0.00	$^1AlO^+N_2(N_2O)$	N^1	0.00
	O^1	0.00		O^1	0.06
$^3Al^+(N_2O)$	N^1	2.37	$^3AlO^+N_2(N_2O)$	N^1	0.56
	O^1	3.58		O^1	0.61
$^1AlO^+N_2$	-	0.00	$^1Al^+(N_2O)_3$	N^3	0.02
$^3AlO^+N_2$	-	0.32		N^2O^1	0.02
				N^1O^2	0.03
				O^3	0.00
$^1Al^+(N_2O)_2$	N^2	0.02			
	N^1O^1	0.02			
	O^2	0.00			

5.7 Discussion

A plot of IRPD peak positions as a function of complex size is illustrated in figure 5.14. The observed spectral bands were fitted to sums of Gaussian functions to extract the exact band positions. The peak positions in the $Al^+(N_2O)_n$-Ar series show little variation with increasing complex size; as n increases the main band broadens and blue-shifts slightly. From the calculated structures, as the ligand number increases beyond $n = 2$, the inner two ligands move closer to the Al^+ centre, leading to more σ-donation and a slightly enhanced blue-shift.

The peak positions in the $Li^+(N_2O)_n$-Ar series are more clearly assigned, with bands arising from N- and O-bound ligands, together with inserted structures. The weaker, highest frequency band (observed for n = 2-4 (5,6)) is tentatively assigned as an N_2 stretch within inserted, $OLi^+N_2(N_2O)_{n-1}$ isomers. The strong band in the spectra of all complex sizes is due to the molecularly-bound N- or O-bound isomers. Confirmed by DFT calculations,

the coordination number of the $Li^+(N_2O)_n$ series is six, explaining the discontinuity in the trend in frequency with $n = 6$. The new band, appearing at *ca.* 2228 cm^{-1} for $n > 6$ arises from weakly-bound N_2O ligands in an outer coordination shell.

Li^+ and Al^+ metal centres were chosen to determine the effect of the closed-shell s^2 configuration ion on the structures generated and how they might differ from other metal centres studied in previous chapters. The differences observed are marked. First, molecularly N- and O-bound ligands are almost spectrally indistinguishable. Second, in the case of the $Al^+(N_2O)_n$-Ar complexes, the N_2O ligand vibrations are no longer local modes and act collectively in a similar way to CO_2 ligands within $Al^+(CO_2)_n$ complexes yielding IRPD

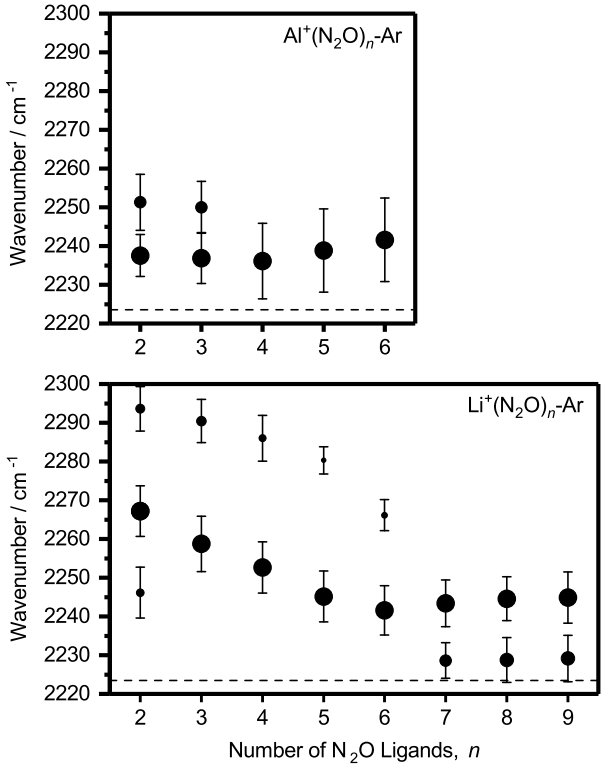

Figure 5.14: Experimental resolved peak positions displayed as a function of cluster size for $Li^+(N_2O)_n$-Ar (n = 2-9) and $Al^+(N_2O)_n$-Ar (n = 2-6). The size of each point represents the intensity relative to the maximum band in each complex size. Uncertainties correspond to the full-width-half-maximum (FWHM) of fitted Gaussian functions used to determine the exact position of each band. The horizontal dashed line indicates the wavenumber of the ν_3(N=N) mode in isolated N_2O at 2223.5 cm^{-1}.[151] Figure reproduced with permission from *Mol. Phys.*, **2019**, DOI: 10.1080/00268976.2019.1595202.

spectra which are similar for each complex, and broaden as complex size increases. In the case of the group 9 and 11 cations, σ-donation from the N_2O 7σ orbital into a partially-filled sd_{z^2} hybrid orbital on the metal ion leads to significant stabilisation of the N-bound ligands relative to the O-bound equivalents. In this case, with $1s^2$ and $3s^2$ configurations, s-d hybridisation is not energetically feasible and as such, donation is much less efficient. Hence, the two binding motifs are effectively isoenergetic and spectrally indistinguishable at this level. Previous investigations of group 13 cations interacting with rare-gases also concluded no significant s-d hybridisation, consistent with the study presented here.[200–202]

Comparing the Li^+ and Al^+ metal centres, the blue-shift in N-bound bands for $n = 2$ is more pronounced for Li^+ than for Al^+, with the N-bound band for Li^+ blue-shifted by 29 cm^{-1} higher than for the N-bound band in Al^+. The size/charge ratio for Li^+ is smaller when compared to Al^+ so it would be expected to form stronger electrostatic interactions with N_2O, reflected in the observed blue-shift. Calculated bond distances, reduced masses, and force constants for the N- and O-bound isomers of $^1Li^+(N_2O)$ and $^1Al^+(N_2O)$ are presented in table 5.3. Considering the N-bound isomers, the force constant is increased further for Li^+ than Al^+ when compared to k for isolated N_2O, which is reflected in the more pronounced blue-shift for $Li^+(N_2O)_2$ in the IRPD spectra. The force constants for N- and O-bound isomers, for both metals, are similar (when compared to the calculated force constants of group 11 and group 9 metals, tables 3.5 and 4.5, respectively) which can explain why the two binding motifs are spectrally indistinguishable at this resolution.

Despite lying much higher in energy than molecularly-bound ligands, the spectra for the $Li^+(N_2O)_n$-Ar complexes exhibit some evidence of insertion into the N_2O molecule, with an N_2 stretch indicating the presence of such isomers. This band is blue-shifted from the molecularly-bound ligands, with the N- and O-bound isomers of the insertion

Table 5.3: Bond distances (nitrous oxide molecule along with M-X where X is the terminal atom, *i.e.* N or O), reduced masses, and force constants for the lowest energy N- and O-bound isomers of $M^+(N_2O)$ (M^+ = Li, Al) complexes calculated at the B3PW91/aug-cc-pVDZ level of theory.

Species	N=N / Å	N=O / Å	k / mDyn/Å	μ / Da	M-X / Å
N_2O	1.132	1.185	47.03	14.10	-
$^1Li^+NNO$	1.136	1.160	49.90	14.14	1.983
$^1Li^+ONN$	1.122	1.201	49.58	14.08	1.877
$^1Al^+NNO$	1.138	1.161	48.75	14.14	2.470
$^1Al^+ONN$	1.122	1.210	48.01	14.05	2.329

complexes being spectrally overlapped. Contrastingly, in the case of the $Al^+(N_2O)_n$-Ar complexes, the inserted structures are calculated to be clearly the lowest in energy and yet, the experimental spectra show little evidence for them. Instead, the spectra are well-reproduced by molecularly-bound isomers.

5.8 Conclusions

The structures of gas-phase $M^+(N_2O)_n$ complexes (M = Li, Al) have been studied using a combined approach of IRPD action spectroscopy coupled with density functional theory. Spectral simulations based on calculated molecularly-bound structures show little energetic and spectral difference between N- and O-bound ligands. However, large barriers to internal rotation are predicted, resulting in the trapping of both N- and O-bound ligands leading to a wide range of potential isomers. The spectral widths observed for larger complexes are consistent with this concept.

Uniquely amongst the $M^+(N_2O)_n$ complexes studied in this thesis, the IRPD spectra of the $Li^+(N_2O)_n$ complexes (n = 2-6) show some evidence of an N_2 moiety, tentatively assigned as arising from inserted, $OLi^+N_2(N_2O)_{n-1}$ isomers. The N_2 band arising from this moiety is spectrally distinct and blue-shifted from the molecularly bound N- and O-bound ligands and is well reproduced when compared to the simulated spectra of low-lying isomers

calculated using density functional theory. In the case of the $Al^+(N_2O)_n$ complexes there is no such evidence of inserted $OAl^+N_2(N_2O)_{n-1}$ isomers as the N_2 band, which is also predicted to be blue-shifted in this case, does not agree with the experimental spectra. The IRPD spectra are, however, well represented by molecularly-bound N_2O ligands.

Chapter 6

Adsorption of Nitrous Oxide on Gold and Cobalt Cationic Clusters

This chapter presents the first study of nitrous oxide binding to isolated Au_n^+, and Co_n^+ clusters. Utilising infrared multi-photon dissociation (IRMPD) spectroscopy and density funtional theory, the binding motifs of N_2O on these clusters can be ascertained. Infrared spectra were collected in both the region of the symmetric and asymmetric stretching modes of nitrous oxide and, for the smaller clusters, present evidence of both N- and O-bound ligands. In the case of the gold clusters, the energy difference between electronic states was large enough for only the lowest energy electronic state to be considered. The spectra for cobalt, however, presents evidence of low-lying electronic states, particularly for larger clusters. For both metals, as the cluster size increases, the spectra show evidence for N_2O to bind preferentially *via* the terminal N-atom. This is attributed to a larger cluster size representing a more effective energy "bath", facilitating annealing to the lowest energy structure.

6.1 Introduction

6.1.1 Gold

It was first demonstrated by Haruta that gold, one of the most inert metals, is transformed into an active catalyst by reducing its dimensions to a few nanometres.[203] These gold nanoparticles, when supported on a metal oxide surface, are found to be as active as present-day catalysts, particularly for the oxidation of CO.[204] The oxidation reactions were, however, found to operate at much lower temperatures when employing the gold nano-particles and, as such, are considered a more energy efficient (*i.e.* greener) alternative when compared to Pd and Pt catalysts.[205] As a consequence, gold nano-particles are one of the best studied catalytic systems.[205,206]

This catalytic activity, as is the case for many transition metal clusters, has been elucidated in many experimental and theoretical studies and is found to depend on the complex interplay of a range of physical factors such as size, geometry, charge, dimensionality, chemical composition, substrate composition, and the presence, or absence, of defect sites.[207–210] Studies of gold clusters supported on metal oxide surfaces revealed that the support played an active part and by manipulating the substrate, the catalytic activity could be controlled.[211–213] Thus, the catalytic activity is dependent on the properties of both the metal cluster and the support and by studying the properties of either of these independently, elucidating the catalytic activity is greatly simplified. Many experimental studies have been performed to investigate the structural evolution of isolated gold clusters with increasing atom number. Early investigations utilised ion mobility mass spectrometry which, when combined with quantum chemical calculations, is a powerful tool for structure determination of metal cluster ions.[214] Kappes and coworkers performed studies on both Au_n^+ and Au_n^-

for n up to 14 and 13, respectively.[48,49] In the case of Au_n^+, unexpected planar structures were found for n = 3-7, with 3-dimensional structures appearing at n = 8. Contrastingly, for Au_n^-, n = 3-11 occupy planar structures with the first 3-dimensional anionic cluster introduced at n = 12.

Neutral gold clusters have been probed using photoelectron spectroscopy[215] and vibrational spectroscopy,[216] revealing that the Au_{20} cluster is highly stable and chemically inert, suggesting a highly symmetrical geometry. Indeed, coupled with DFT calculations, Au_{20} was found to occupy a tetrahedral geometry.

Isolated clusters represent well-defined model systems, whereby proposed reaction pathways can be tested, yielding a wealth of insight. In rare cases, clusters themselves can act as catalysts; the catalytic cycle of low-temperature CO oxidation by small gold cluster anions was elucidated theoretically[217] and later experimentally using pulsed flow reactor and mass spectrometric techniques.[218,219] Thus, understanding the structures of clusters is of paramount importance. As model systems, understanding the cluster morphology before and after a molecule is attached, the entrance-channel species for certain catalytic reactions can be ascertained.

Relevant structural information on nitrogen oxides adsorbed to gold clusters is limited to IRMPD studies of Au_n^+(NO) by Fielicke and coworkers.[220] In this study, the degree of activation of nitric oxide (NO) when adsorbed to small Au_n^+ clusters was investigated by measuring ν(NO) as a function of cluster size, n. Since ν is directly related to the force constant, and hence the NO bond strength, the shift in ν(NO) band position correlates with the degree of bond activation. The authors found an alternating dependence on ν(NO); with even n, a lower ν(NO) (and hence, weaker NO bond) is observed, in contrast to odd n, presenting a higher ν(NO). Reproduced from density functional theory, molecular orbital

analysis revealed that the low ν(NO) on even n clusters correlates with double occupancy of the antibonding NO $2\pi^*$ orbital, whereas the odd n clusters, with a high ν(NO), correlate to a single occupancy. NO was found to bind exclusively in atop arrangements, tending to favour low coordinated gold atoms, bound in a non-linear fashion.

6.1.2 Cobalt

Cobalt nanoparticles have been shown to catalyse the production of long-chain hydrocarbons in the Fischer-Tropsch process.[221] Since Fischer-Tropsch synthesis converts CO and H_2 into these hydrocarbons, there is much interest in the chemistry and chemisorption of CO onto transition metal surfaces, particularly cobalt. Catalytic activity has been predicted using density functional theory, indicating the cobalt particle size, on both face centered cubic and icosahedral structures, strongly influences activity.[222] This find was also verified experimentally.[223] Given that the CO binding, and hence, the overall activity, depends on the cobalt structure,[224,225] understanding metal surfaces on the nanoscale is imperative to both fundamental understanding and the development of more efficient catalysts in technology.

Various experimental techniques have been carried out to elucidate the structures of cobalt clusters. Early attempts involved flow tube reaction methods, whereby bare cobalt clusters were reacted with ammonia, with the degree of saturation determining the number of binding sites on the cluster surface, of which structural information can be extrapolated.[226] The authors found particularly high abundances at n = 55, 71, 101, 116, 131, and 147. These "magic numbers" are consistent with high-symmetry, icosahedral structures. In the n = 55 case, shells of 12, and 42 atoms surround a central atom forming a Mackay icosahedron. Trapped ion electron diffraction measurements also show that Co_n^+ clusters

present a magic number at $n = 55$, exhibiting a highly symmetrical, closed-shell, Mackay icosahedron.[227]

Co_n^- (n = 1-108) clusters have been extensively investigated using photoelectron spectroscopy by Liu *et al.*[228] Clusters $n < 20$ were found to behave more molecularly, displaying discrete transitions and dramatic size variations, whereas $n \geqslant 20$ clusters behaved more like bulk cobalt presenting broad spectral features together with smooth-size evolution. However, discrete and well-resolved spectral features were observed at $n = 55$, consistent with a highly symmetric, Co_{55}^- icosahedral structure.

Infrared-multiple photon dissociation (IRMPD) measurements coupled with density functional theory calculations were carried out in order to identify the structures of Co_n^+-Ar (n = 4-8) clusters.[157] All clusters are in high spin states and exhibit sizeable Jahn-Teller distortion. Contrary to studies on other metal clusters, (e.g. group 5, V_n^+, Nb_n^+, and Ta_n^+), the vibrational spectra of Co_n^+ are strongly dependent on the number of adsorbed Ar atoms.

The structures of neutral Co_n clusters (n = 4-10,13) have been studied using two-colour IR-UV spectroscopy.[229] Combined with DFT calculations the authors tentatively assign: Co_4 as a rhombus, Co_5 a trigonal bipyramid, Co_6 a tetragonal bipyramid, Co_8 a bicapped tetrahedron, Co_9 a tricapped tetrahedron, and Co_{13} an icosahedron. The structures of Co_7 and Co_{10}, however, unfortunately could not be assigned with certainty.

Size-specific activation of CO_2 has been reported for Co_n^- clusters.[230] Utilising mass spectrometry, it was shown that the reactivity is strongly dependent on cluster size; at n = 7 the reactivity emerges, peaking at n = 8-10, and gradually decreasing as n increases. Recording the IRMPD spectra of these clusters each exhibited a single band at *ca.* 1870 cm^{-1}. DFT calculations revealed that dissociative adsorption of CO_2 (into CO and O) was more energetically favourable when compared with non-dissociative (molecular) adsorption.

In addition, simulated vibrational spectra for dissociated isomers, e.g. $Co_7^-(CO)O$, agreed well with the experimental spectra, whereas those of non-dissociated (molecularly-bound) isomers, e.g. $Co_7^-(CO_2)$, agreed poorly. In the same study, photoelectron spectra were recorded on the $Co_n^-(CO_2)$ clusters, presenting a dramatic blue-shift to higher electron binding energies relative to spectra of the bare, Co_n^- clusters. This suggests effective electron transfer from Co_n^- to CO and O ligands, once more indicating that the CO_2 ligand adsorbs dissociatively to Co_n^- clusters.

Reactions of Co_n^+ (n = 4-30) clusters with nitric oxide, NO, and nitrous oxide, N_2O, have been performed using Fourier transform ion cyclotron resonance (FT-ICR) mass spectrometry under single-collision conditions.[231] Reaction rates with N_2O proceed slower than the calculated collision rate, resulting in the formation of oxides. Contrastingly, chemisorption of NO occurs at, or faster, than the calculated collision rate. For both reactions there is evidence for reaction-induced cluster fragmentation, characterised by Co atom evaporation. The fragmentation observed was found to decrease upon increasing cluster size. Storing the clusters for extended periods allowed for multiple reactions to occur, whereby interesting chemistry was observed, including the formation of stable oxide clusters and/or decomposition of NO on the cluster leading to loss of molecular nitrogen.

Studying the physical and chemical properties of isolated transition-metal clusters is of great importance, particularly in the fields of heterogeneous catalysis, solid-state physics, surface chemistry, and organometallic chemistry. Gas-phase metal clusters represent model systems from which molecular level insight of the thermodynamics and kinetics of catalytic reactions can be gained. This chapter presents an IRMPD study of an N_2O ligand adsorbed to Au_n^+ and Co_n^+ clusters, whereby structural isomers, the emergence of low-lying electronic states, and cluster size effects are elucidated. These findings can then be compared to the

single cation $Au^+(N_2O)_n$ and $Co^+(N_2O)_n$ complexes in chapters 3 and 4, respectively.

6.2 Experimental and Theoretical Methods

The instrument at the Fritz-Haber Institute along with the technique employed (IRMPD) have been described in chapter 2, section 2.6, so only brief details will be given. Gas-phase $M_n^+(N_2O)$ (M = Co, Au) clusters are formed by entraining the products of focussed 532 nm pulsed laser ablation of a rotating metal rod in a dense pulse of helium carrier gas (10 bar backing pressure), with N_2O introduced *via* a late mixing valve. As the gas pulse moves through the clustering channel, neutral and ionic clusters are formed. The resultant molecular beam is skimmed and positively-charged clusters are detected using reflectron time-of-flight mass spectrometry.[129] Tunable pulsed infrared radiation is provided by the free electron laser (FEL) at the Fritz-Haber Institute in the region of 2100-2450 cm^{-1}, and 1100-1400 cm^{-1}, covering the ν_3 and ν_1 (stretching) modes of N_2O, respectively.[151] The infrared radiation counter-propagates with the molecular beam, and IRMPD spectra are collected employing the messenger technique.[132,160–164] The messenger used in this case is the N_2O ligand itself, with loss of N_2O from a $M_n^+(N_2O)$ cluster providing the signature of IR photon absorption as a function of wavenumber.

To better understand and interpret the experimental spectra, quantum chemical calculations were performed yielding structures along with simulated infrared spectra of low-lying isomers. Since the computational complexity, along with cost, increases with cluster size, calculations performed were limited to the smaller clusters studied: $M_n^+(N_2O)$ (n = 2-5). Calculations were performed using density functional theory (DFT) employing the hybrid version of the meta-GGA functional TPSS, with 10% exact exchange included (termed TPSSh),[155] together with the Def2TZVP basis set.[147,148] Relativistic effects prominent in

gold chemistry[144–146] were approximated using an effective core potential (ECP) accounting for all but the valence 19 electrons of each gold atom. Starting structures were generated from existing geometries of cationic gold[48] and cobalt[157] clusters in the literature. Using chemical intuition, the location of N_2O binding sites was established with atop, bridge, and three body binding sites investigated. N_2O was found to bind exclusively in an atop arrangement, favouring low coordinated gold/cobalt atoms. Calculations were performed with starting geometries of N_2O in μ^2 and μ^3 arrangements, but upon geometry optimisation of these starting structures converged to atop structures. The simulated spectra are scaled by a factor of 0.955, derived from the calculated ν_3 stretch of isolated N_2O.[151] All calculations were performed using the Gaussian09 suite of programs.[150]

6.3 Results and Discussion

6.3.1 $Au_n^+(N_2O)$ Clusters

Figure 6.1 presents the time-of-flight mass spectrum showing the production of Au_n^+ (n = 1-8) clusters along with attached adsorbates. Figure 6.2 shows a more detailed time-of-flight mass spectrum illustrating the production of $Au_n^+O_m(N_2O)_p$ (n = 1-3; m = 0,1; p = 0-2). In both cases, the time-of-flight mass spectra were obtained following the ablation of a gold rod in the presence of a helium carrier gas (10 bar backing pressure) and reaction gas of N_2O delivered in the reaction channel *via* a solenoid valve.

Interestingly, production of gold-oxide clusters can be clearly identified in figure 6.2. The equivalent clusters were not observed using the experimental set-up in Oxford (chapter 3) and these differences in mass spectra can be attributed to the different source conditions in the Oxford and Berlin experimental set-ups (see chapter 1, figure 1.4b and chapter 2,

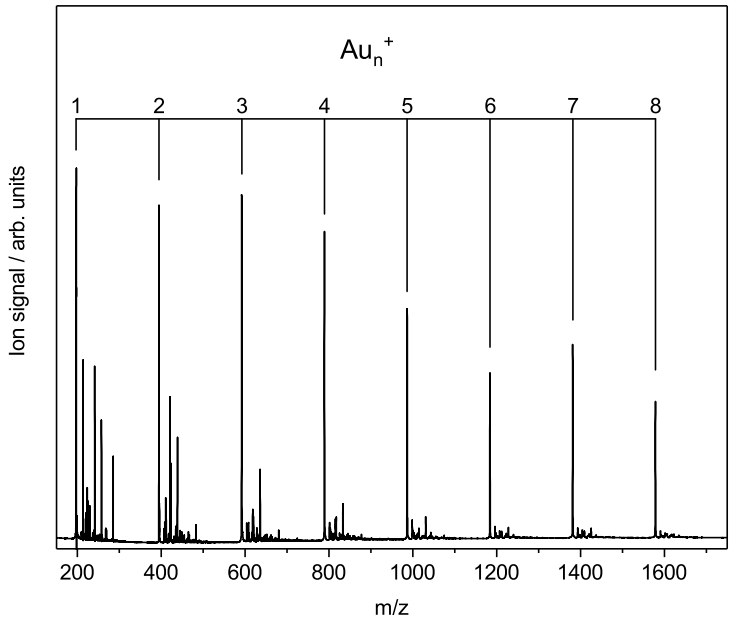

Figure 6.1: Time-of-flight mass spectrum of Au_n^+ clusters produced by laser ablation of a gold rod in the presence of a helium carrier gas (10 bar backing pressure) and reaction gas of N_2O delivered externally into the source *via* the reaction channel.

figure 2.5).

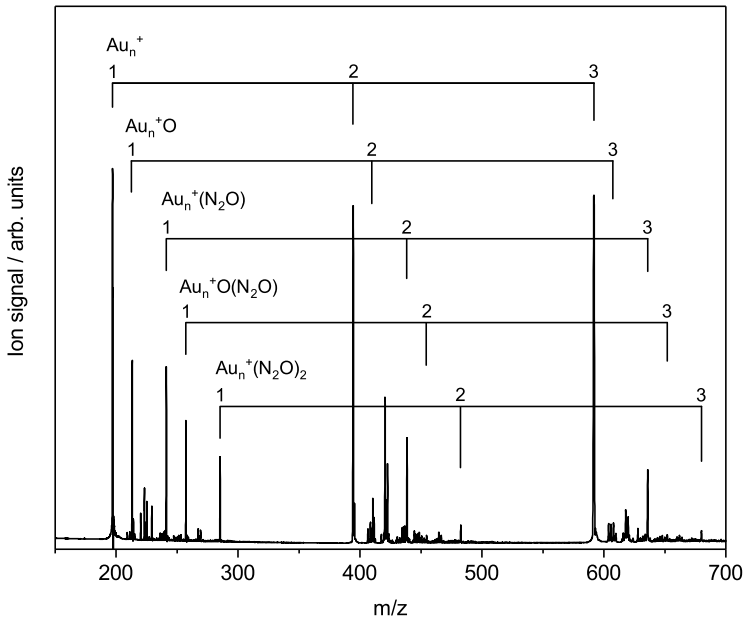

Figure 6.2: Time-of-flight mass spectrum illustrating the production of Au_n^+ and Au_n^+O (n = 1-3) clusters with attached nitrous oxide obtained following laser ablation of a gold rod in the presence of a helium carrier gas (10 bar backing pressure) and reaction gas of N_2O delivered externally into the source *via* the reaction channel.

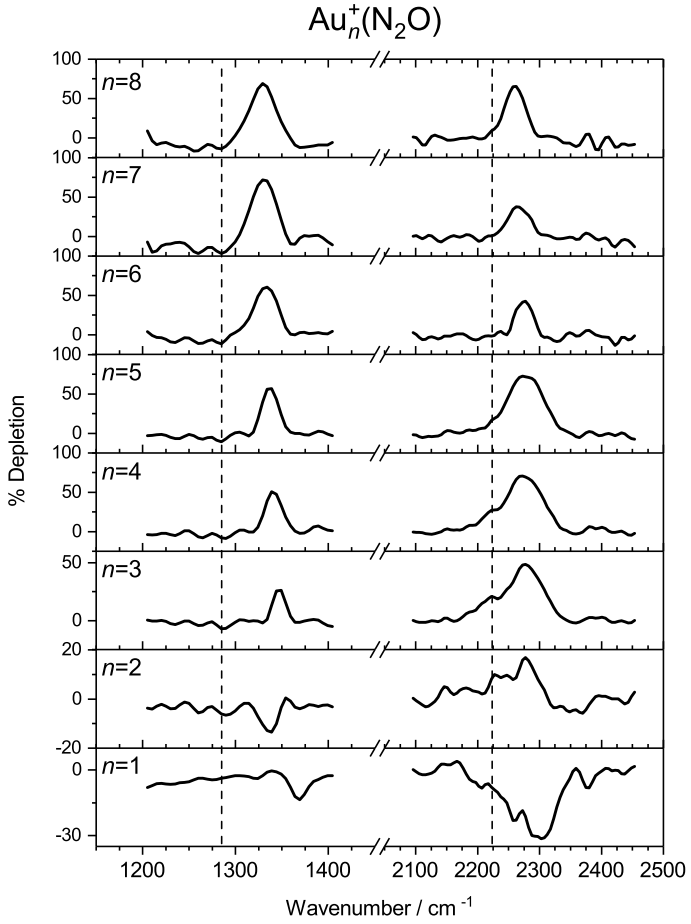

Figure 6.3: IRMPD depletion spectra of $Au_n^+(N_2O)$ (n = 1-8) clusters in the symmetric and asymmetric regions of N_2O with depletion given as a percentage of ion signal. In each case, the depletion of the ion signal is due to loss of the N_2O molecule. The vertical dashed lines at 1285 and 2223.5 cm^{-1} indicate the wavenumber of the ν_1(N=O) and ν_3(N=N) modes in isolated N_2O, respectively.[151]

The IRMPD spectra of an attached N_2O ligand to cationic gold clusters, $Au_n^+(N_2O)$ (n = 1-8) in both the symmetric (1200 - 1400 cm^{-1}) and asymmetric (2100 - 2450 cm^{-1}) regions of N_2O are presented in figure 6.3. In the symmetric region for n = 1,2 the depletion in signal is negative (*i.e.* the ion signal enhances), which is likely to arise from higher-order complexes (e.g. $Au_1^+(N_2O)_2$ and $Au_2^+(N_2O)_2$) losing one N_2O ligand upon absorption of IR photons. This leads to an enhancement in ion signal for the n = 1,2 channels. This observation is also found in the asymmetric region for n = 1 and the same reasoning can

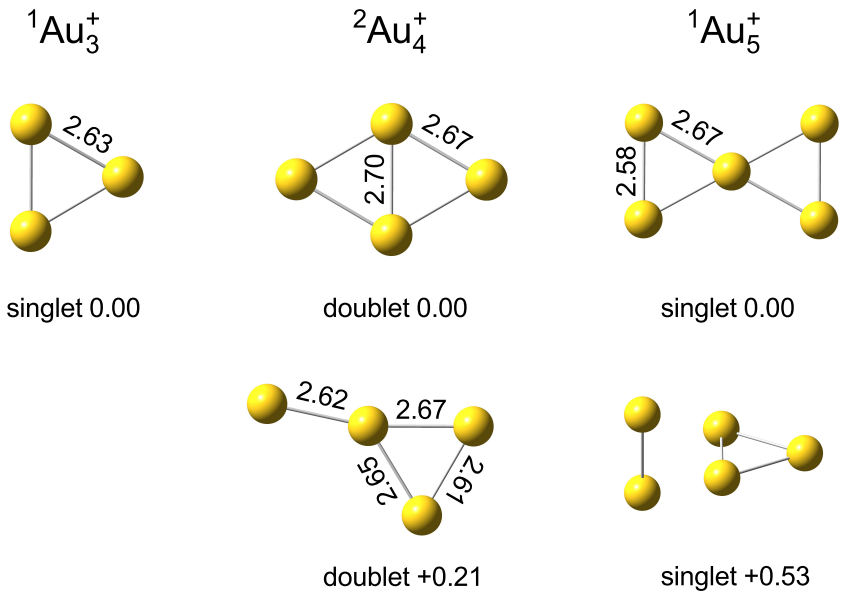

Figure 6.4: Geometry-optimised structures of the lowest energy forms for Au_n^+ (n = 3-5) calculated at the TPSSh/Def2TZVP level of theory. Bond lengths are provided (in Å) along with relative energies (in eV). Cartesian coordinates of these optimised structures, for all cluster sizes, can be found in the appendix.

be applied. For all other gold cluster sizes, the IRMPD spectra present a depletion in ion signal. In the symmetric region, the IRMPD spectra present one band, blue-shifted from the ν_1 mode of N_2O at 1285 cm^{-1},[151] which undergoes a smooth reduction in blue-shift with increasing gold cluster size from 1369 cm^{-1} for n = 1, to 1329 cm^{-1} for n = 8. However, the (enhancement) band for n = 2 does not strictly follow this trend and sharply red-shifts by 34 cm^{-1} from n = 1.

For all cluster sizes, a similar trend is observed in the asymmetric region; the main band is blue-shifted from the ν_3 mode of N_2O,[151] and reduces in blue-shift from 2299 cm^{-1} for n = 1, to 2260 cm^{-1} for n = 8. Cluster sizes n = 1 and 2 present a shoulder at 2261 cm^{-1} and 2243 cm^{-1}, respectively. This shoulder is also present for clusters n = 3-5 and, for all three cluster sizes, has a band centre at 2222 cm^{-1}. For n = 6,7, and 8, this shoulder is not present and only one band is observed at 2275 cm^{-1}, 2267 cm^{-1}, and 2260 cm^{-1}, respectively.

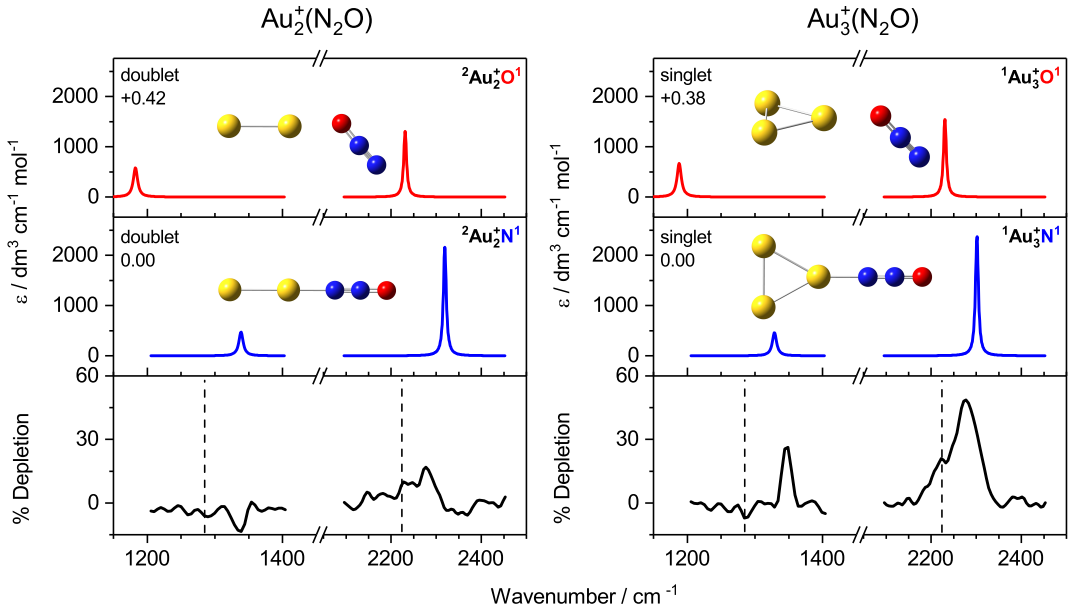

Figure 6.5: IRMPD depletion spectra of $Au_2^+(N_2O)$ and $Au_3^+(N_2O)$, along with simulated IR spectra of low-lying doublet-state isomers ($n = 2$) and singlet-state isomers ($n = 3$) in the region of the N_2O symmetric (N=O) and asymmetric (N=N) stretch. Simulated IR bands corresponding to N-bound and O-bound ligands are indicated in blue and red, respectively. The relative energies of different isomers are given in eV. The vertical dashed lines at 1285 and 2223.5 cm^{-1} indicate the wavenumber of the ν_1(N=O) and ν_3(N=N) modes in isolated N_2O, respectively.[151]

Just as in previous chapters, interpretation of the IRMPD spectra is supported by DFT calculations identifying low-lying isomers along with their simulated spectra. Figure 6.4 shows the calculated Au_n^+ structures, which are in excellent agreement with those reported previously by Kappes and coworkers using ion mobility measurements complemented with DFT calculations.[48] The observed spectra of $Au_2^+(N_2O)$ and $Au_3^+(N_2O)$, along with low-lying structural isomers together with simulated vibrational spectra, are presented in figure 6.5. Similar to before, each structure adopts the following notation: $^{2S+1}M_n^+N^x$ or $^{2S+1}M_n^+O^y$, in which x and y are integer values indicating the number of N_2O molecules. In this case there is one N_2O molecule, with n representing the number of metal atoms. As an example, $^2Au_2^+N^1$ represents a doublet state of $Au_2^+(N_2O)$ with one N-bound N_2O ligand.

The signal-to-noise ratio in the observed spectrum for $Au_2^+(N_2O)$ is low. However, in the symmetric region there is a clear enhancement band at 1335 cm^{-1}, which is in good agreement with the simulated spectrum of $^2Au_2^+N^1$. The observed spectrum in the asymmetric region is more ambiguous, presenting a lower signal-to-noise ratio, with evidence of a bands centred at 2279 cm^{-1} and 2243 cm^{-1}. Given this observation, these bands agree with the simulated spectra of both $^2Au_2^+N^1$ and $^2Au_2^+O^1$ and so both N- and O-bound ligands are likely to be present in the experiment.

This observation is mirrored in the observed spectrum for $Au_3^+(N_2O)$. The asymmetric region presents a band at 2277 cm^{-1} with a shoulder at 2222 cm^{-1}, in good agreement with the simulated spectra of $^1Au_3^+N^1$ and $^1Au_3^+O^1$. The spectrum in the symmetric region presents a band at 1347 cm^{-1}, in good agreement with the simulated spectrum of $^1Au_3^+N^1$. However, the simulated spectrum for $^1Au_3^+O^1$ presents a band at 1188 cm^{-1}, outside the range of the observed spectrum. Unfortunately, as this data was recorded at a national facility, the Fritz Haber Institute in Berlin, the spectra, once recorded, could not be easily re-recorded in the lower range of the symmetric region (1000 - 1200 cm^{-1}). Since the signature for an O-bound ligand is found in the asymmetric region of the observed spectrum of $Au_3^+(N_2O)$, it is expected that the same signature will be observed in the symmetric region. However, the IRMPD spectrum needs to be extended to the red to strengthen and secure this assignment. The simulated spectra in the symmetric region for O-bound isomers of all cluster sizes present a band red-shifted out of the range in the recorded spectra. Therefore, the IRMPD spectra will need to be re-recorded in this region for all cluster sizes in order to fully interpret the structural isomers present.

For all cluster sizes, the lowest electronic state calculated for each isomer is given (singlet for odd n, doublet for even n). Other electronic states were calculated to lie much higher

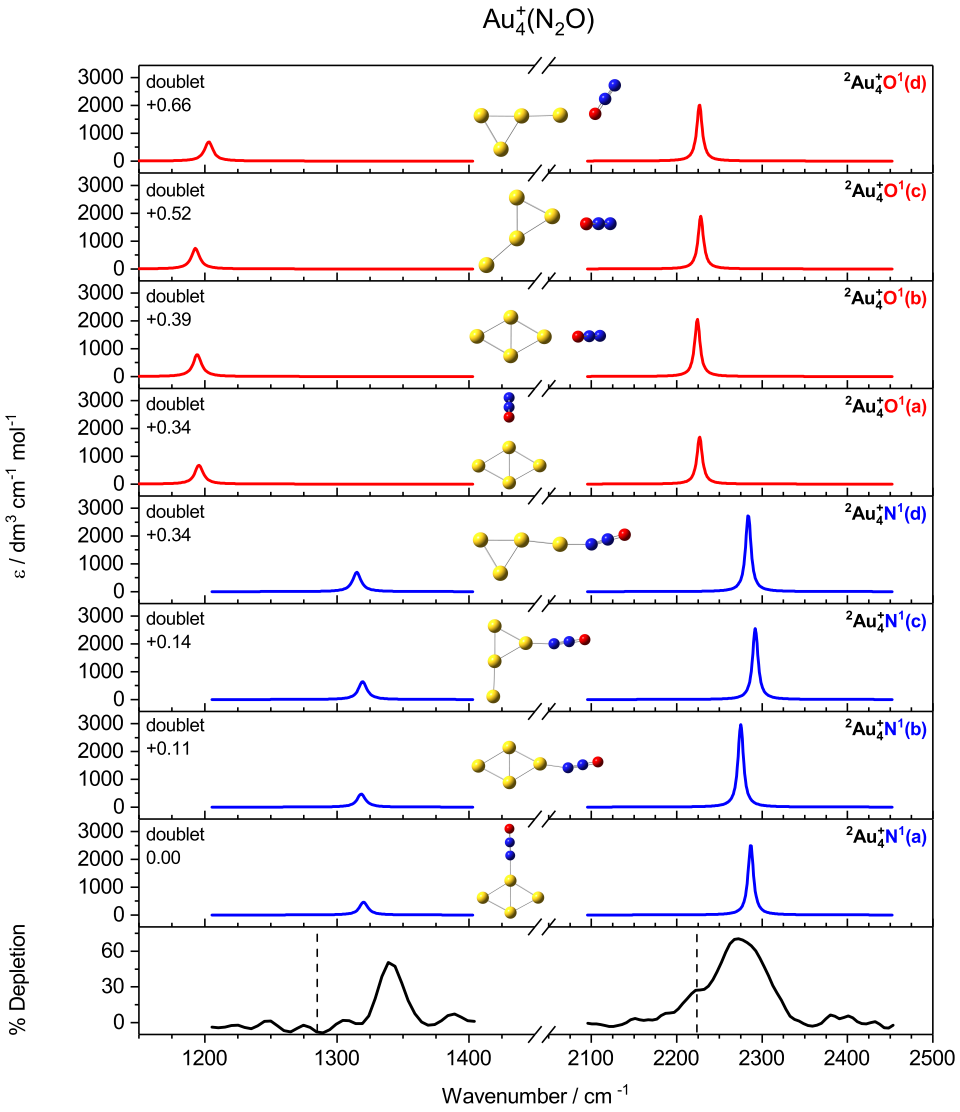

Figure 6.6: IRMPD depletion spectrum of $Au_4^+(N_2O)$, along with simulated IR spectra of low-lying doublet-state isomers in the region of the N_2O symmetric (N=O) and asymmetric (N=N) stretch. Simulated IR bands corresponding to N-bound and O-bound ligands are indicated in blue and red, respectively. The relative energies of different isomers are given in eV. The vertical dashed lines at 1285 and 2223.5 cm^{-1} indicate the wavenumber of the ν_1(N=O) and ν_3(N=N) modes in isolated N_2O, respectively.[151]

in energy and so are unlikely to be present in the experiment.

Figure 6.6 presents the IRMPD spectrum for $Au_4^+(N_2O)$ together with calculated low-lying structures and simulated spectra. Two different isomers of Au_4^+ were found to be very

close in energy, each occupying two binding sites for the N_2O to adsorb. With the N_2O able to bind *via* either the terminal N or O atom, this results in eight structural isomers.

A similar interpretation given for $Au_2^+(N_2O)$ and $Au_3^+(N_2O)$ can be applied here; the observed spectrum in the symmetric region presents one band at 1341 cm^{-1}, which can be assigned to the N-bound N_2O ligand adsorbed to a Au_4^+ cluster. For all N-bound isomers, the simulated spectra present one band in each region, blue-shifted from the isolated N_2O modes. The degree of blue-shift is similar for all isomers. In the asymmetric region, the observed spectrum presents a broad band centred at 2275 cm^{-1}, which is not well-resolved. There is also a shoulder at 2222 cm^{-1}, which is assigned to O-bound isomers. The N-bound isomers, $^2Au_4^+N^1$(a-d), and O-bound isomers, $^2Au_4^+O^1$(a-d), present simulated spectra which are very similar. The observed spectrum is unable to distinguish between: i) the four N-bound isomers, and ii) the four O-bound isomers. The N_2O bands are not diagnostic of the gold cluster structure and it is difficult to conclude much about the distribution of the isomers present.

A similar interpretation can be applied to the IRMPD spectra of $Au_5^+(N_2O)$, shown in figure 6.7. The degree of blue-shift for all N-bound isomers (*i.e.* $^1Au_5^+N^1$(a-c)) is similar in both the symmetric and asymmetric regions, accounting for the broadness of the observed bands at 1337 cm^{-1} and 2277 cm^{-1}. However, the increased spectral width of the bands is also mostly due to power broadening from the FEL. The shoulder at 2222 cm^{-1} accounts for an O-bound N_2O, however since all O-bound isomers in the asymmetric region present similar spectra, one cannot distinguish between either of the three isomers. As evidenced from the interpretation of $Au_4^+(N_2O)$ and $Au_5^+(N_2O)$ in figures 6.6 and 6.7, IRMPD is not an accurate way of discerning between the different N-bound or O-bound structural isomers. Argon-tagging these clusters along with reducing the FEL power would lead to

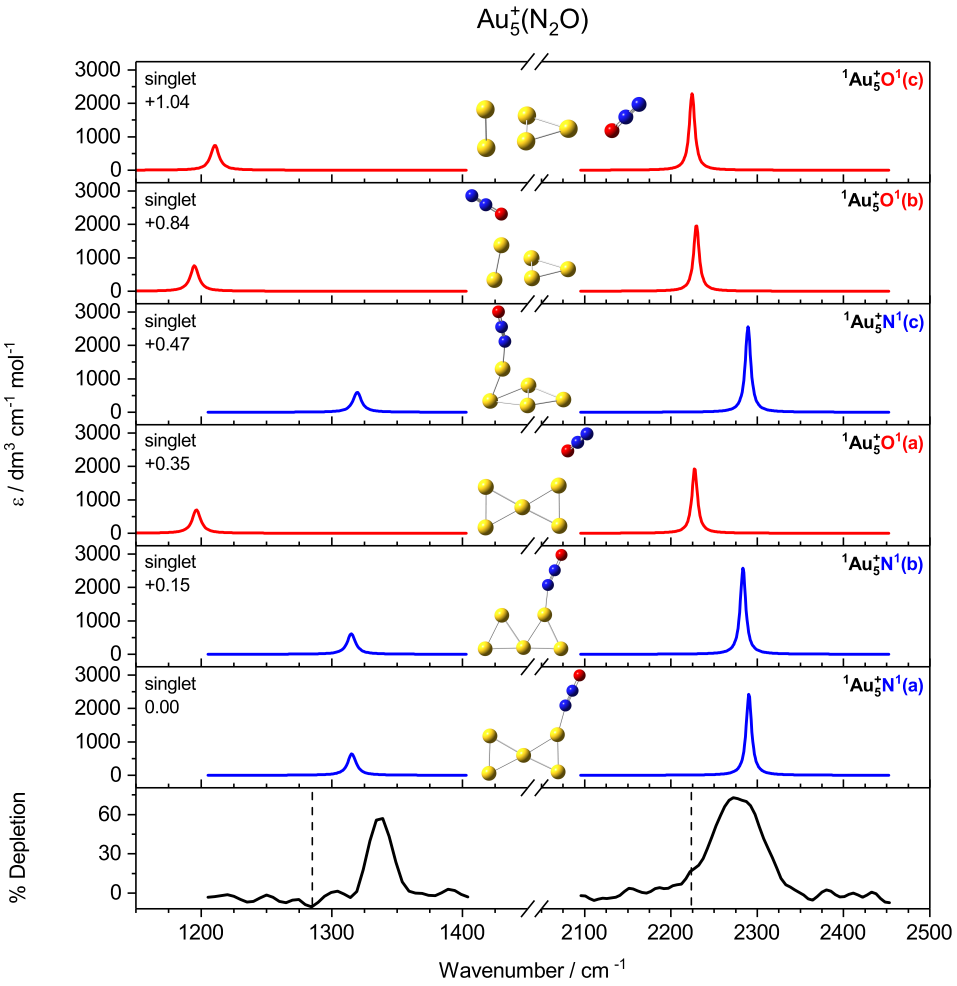

Figure 6.7: IRMPD depletion spectrum of $Au_5^+(N_2O)$, along with simulated IR spectra of low-lying singlet-state isomers in the region of the N_2O symmetric (N=O) and asymmetric (N=N) stretch. Simulated IR bands corresponding to N-bound and O-bound ligands are indicated in blue and red, respectively. The relative energies of different isomers are given in eV. The vertical dashed lines at 1285 and 2223.5 cm^{-1} indicate the wavenumber of the ν_1(N=O) and ν_3(N=N) modes in isolated N_2O, respectively.[151]

better resolved spectra, which might reveal the N- and O-bound isomer signatures.

Higher cluster sizes, n = 6-8, present a narrow band in the asymmetric region when compared to the cluster size n = 5 and below. This could indicate the presence of exclusively N-bound N_2O to the cluster. One band is also observed in the spectra covering the symmetric region. However, to secure this assignment, the spectra in the symmetric region needs to be extended to the red to observe any presence of O-bound ligands, which

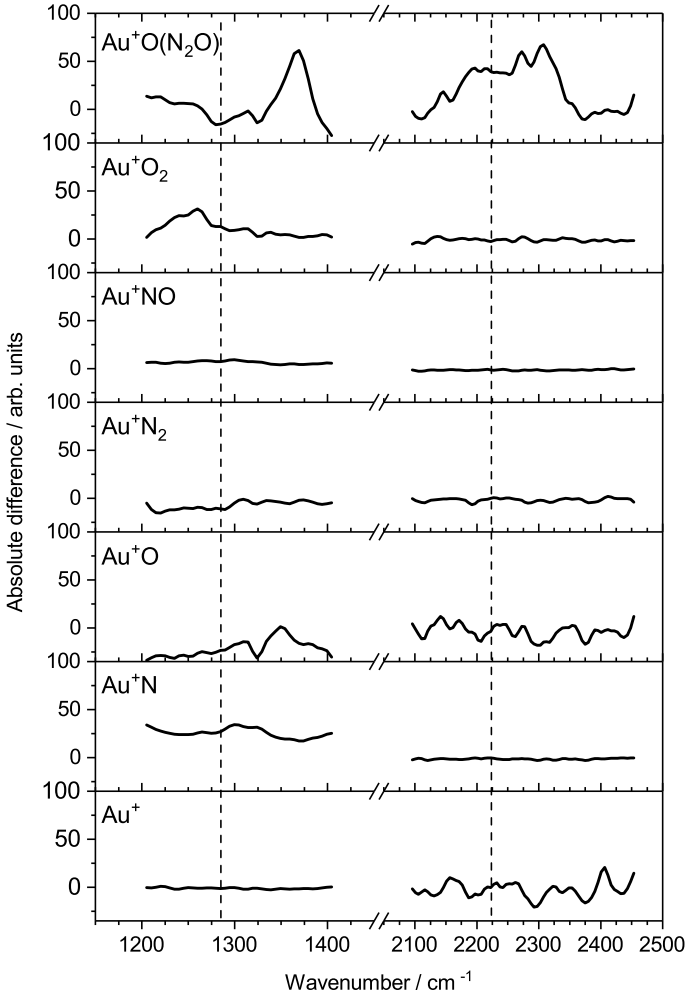

Figure 6.8: IRMPD depletion spectra of $AuO^+(N_2O)$ showing a strong depletion upon excitation in both the region of the N_2O symmetric (N=O) and asymmetric (N=N) stretch, with depletion given as an absolute difference. Accompanying are lower-mass signals representing product channels which could show corresponding enhancement features. The vertical dashed lines at 1285 and 2223.5 cm^{-1} indicate the wavenumber of the ν_1(N=O) and ν_3(N=N) modes in isolated N_2O, respectively.[151]

would absorb at *ca.* 1180 cm^{-1}. Further calculations generating the structures together with simulated spectra on these larger clusters is also required.

Figure 6.8 presents the IRMPD spectra (depletion given as an absolute difference) of $AuO^+(N_2O)$ in the ν_1(N=O) and ν_3(N=N) stretching regions along with spectra of lower-mass signals, which represent product channels. Within the ν_3(N=N) stretching region, there is a broad band between *ca.* 2330 and 2150 cm^{-1} for the $AuO^+(N_2O)$ complex. A

strong band at *ca.* 1370 cm^{-1} is also present in the ν_1(N=O) region for the $AuO^+(N_2O)$ complex. However, the corresponding enhancement signal for these features is not present in any of the oxide, nitrosyl, or nitride channels, and the spectra for these product channels instead all present a flat line. We tentatively assign this observation to an infrared-induced reaction, whereby the infrared radiation (resonant with either N_2O mode within the $AuO^+(N_2O)$ complex) is absorbed and induces a chemical reaction. In this case, the reactions produce *either* two NO molecules, or an O_2 molecule and an N_2 molecule. Either case will result in an enhancement in the Au^+ ion signal, however because this signal is so large when compared to the $AuO^+(N_2O)$ ion signal, small fluctuations in the Au^+ ion signal are not likely to result in an observable IRMPD spectrum. This assignment is speculative and further calculations generating the potential energy surfaces for these reactions are being performed to strengthen this assignment.

6.3.2 $Co_n^+(N_2O)$ Clusters

The time-of-flight mass spectrum illustrating the production of Co_n^+ clusters (n = 1-6) along with $Co_n^+(N_2O)$ clusters (n = 1-5) is presented in figure 6.9. Figure 6.10 shows a magnified time-of-flight mass spectrum presenting Co_n^+ clusters (n = 1-3) with attached N_2O ligands and $Co_n^+O_m$ clusters (n = 1-3; m = 1-2). In each case, mass spectra were obtained by entraining the plume of focussed laser ablation of a cobalt rod in a pulse of helium carrier gas (10 bar backing pressure) with a reaction gas pulse of N_2O delivered into the reaction channel *via* a solenoid valve.

Production of Co^+O was observed using the Oxford experiment (chapter 4, figure 4.1). However, as is clear from figure 6.10, the Berlin experiment is capable of producing cationic cobalt clusters along with multiple oxides. This is most likely due to the difference in designs of the cluster sources, *i.e.* the design employed in Oxford facilitates the production

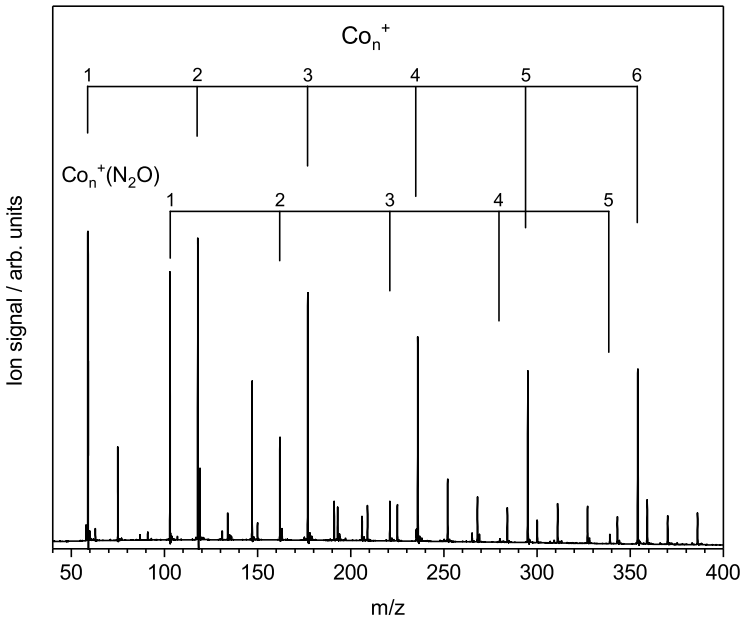

Figure 6.9: Time-of-flight mass spectrum of Co_n^+ (n = 1-6) and $Co_n^+(N_2O)$ (n = 1-5) clusters produced by laser ablation of a cobalt rod in the presence of a helium carrier gas (10 bar backing pressure) and reaction gas of N_2O delivered externally into the source *via* the reaction channel.

of $M^+(L)_n$ ion-molecule complexes, whereas the Berlin source is designed for the production of $M_n^+(L)$ cluster-molecule complexes.

Figure 6.11 shows the IRMPD spectra of cationic cobalt clusters (n = 1-5) with an attached N_2O ligand in both the symmetric and asymmetric regions of nitrous oxide. Just as in the case for the $Au_n^+(N_2O)$ (n = 1,2) clusters, the spectra for $n = 1$ (apart from the band at 1192 cm^{-1}) show a negative depletion (*i.e.* an enhancement in ion signal) likely due to the $Co_1^+(N_2O)_2$ complex losing an N_2O ligand upon absorption of infrared photons, falling into the $n = 1$ channel leading to an enhancement in ion signal. The IRMPD spectra for n = 3-5 all present depletion in ion signal. Fortunately, for this data set, the IRMPD spectra obtained in the symmetric region was extended to 1100 cm^{-1} in an attempt to observe bands attributed to O-bound N_2O ligands.

Considering the IRMPD spectra in the symmetric region, all cluster sizes present two bands; one red-shifted from the ν_1 band of N_2O at 1285 cm^{-1} and another blue-shifted.

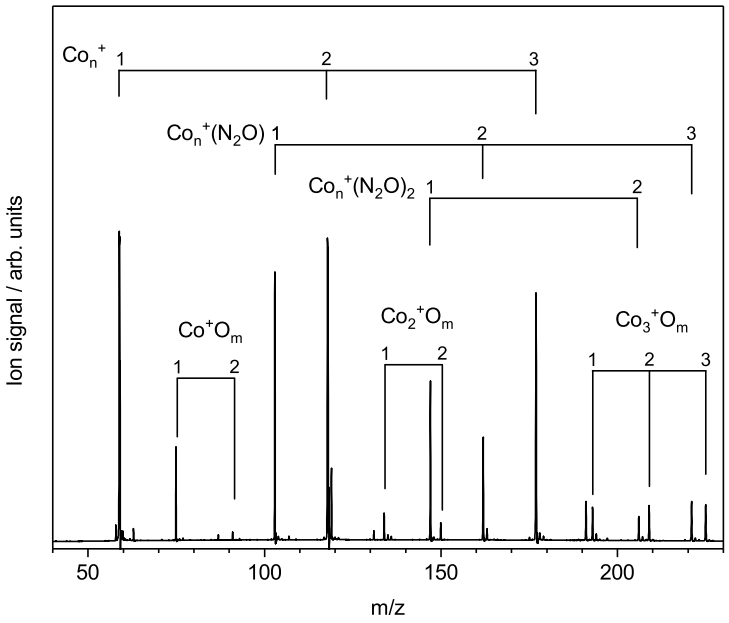

Figure 6.10: Time-of-flight mass spectrum illustrating the production of Co_n^+ clusters (n = 1-3) with attached nitrous oxide and $Co_n^+O_m$ (n = 1-3; m = 1-3) obtained following laser ablation of a cobalt rod in the presence of a helium carrier gas (10 bar backing pressure) and reaction gas of N_2O delivered externally into the source *via* the reaction channel.

The blue-shifted band for the n = 1,2 shows a negative depletion (*i.e.* signal enhancement) likely due to the depletion of higher-order complexes falling into these mass channels. Nevertheless, the band positions of these features can be considered when following the trends upon increasing metal cluster size. This band is the most blue-shifted for n = 1 at 1345 cm^{-1}, undergoing a smooth reduction in blue-shift to 1323 cm^{-1} for n = 5.

Upon inspection of the spectra in the N_2O asymmetric region, all clusters present one main band blue-shifted from the ν_3 band of N_2O at 2223.5 cm^{-1}, with another, weaker band, close to the ν_3 stretch. Similar to the symmetric region, this main band is the most blue-shifted for the smallest cluster, n = 1, at 2280 cm^{-1} and undergoes a smooth red-shift to 2271 cm^{-1} for n = 5. The weaker band also follows this trend starting at 2230 cm^{-1} for n = 1 and ending at 2204 cm^{-1} for n = 5.

The DFT calculated low-lying structures for the Co_n^+ (n = 3-5) clusters are shown in

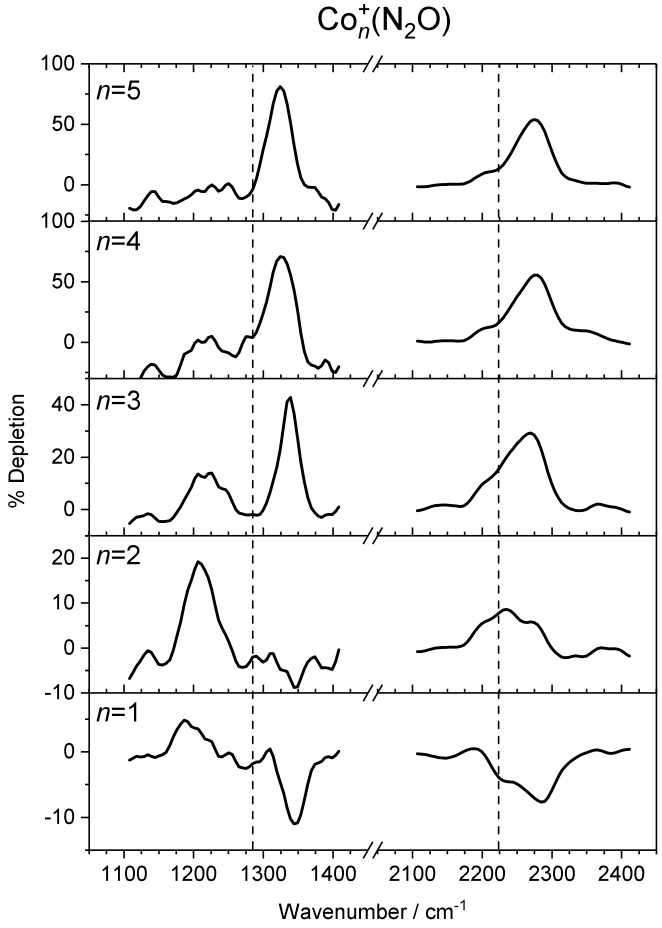

Figure 6.11: IRMPD depletion spectra of $Co_n^+(N_2O)$ (n = 1-5) clusters in the symmetric and asymmetric regions of N_2O, with depletion given as a percentage. In each case, the depletion of the ion signal is due to loss of the N_2O molecule. The vertical dashed lines at 1285 and 2223.5 cm^{-1} indicate the wavenumber of the ν_1(N=O) and ν_3(N=N) modes in isolated N_2O, respectively.[151]

figure 6.12. The structures here agree well those identified using far-infrared vibrational spectroscopy by Gehrke *et al.*[157]

The IRMPD spectra of $Co_2^+(N_2O)$ together with calculated low-lying sextet, quartet, and doublet structures with simulated spectra are shown in figure 6.13. In the symmetric region, the global-minimum $^6Co_2^+N^1$ structure presents a weak band which is in excellent agreement with the enhancement band at 1345 cm^{-1} in the observed spectrum. As discussed earlier, this enhancement is likely due to depletion of a higher-order (e.g. $Co_2^+(N_2O)_2$) complex. The band at 1210 cm^{-1} agrees well with all O-bound isomers presented in figure

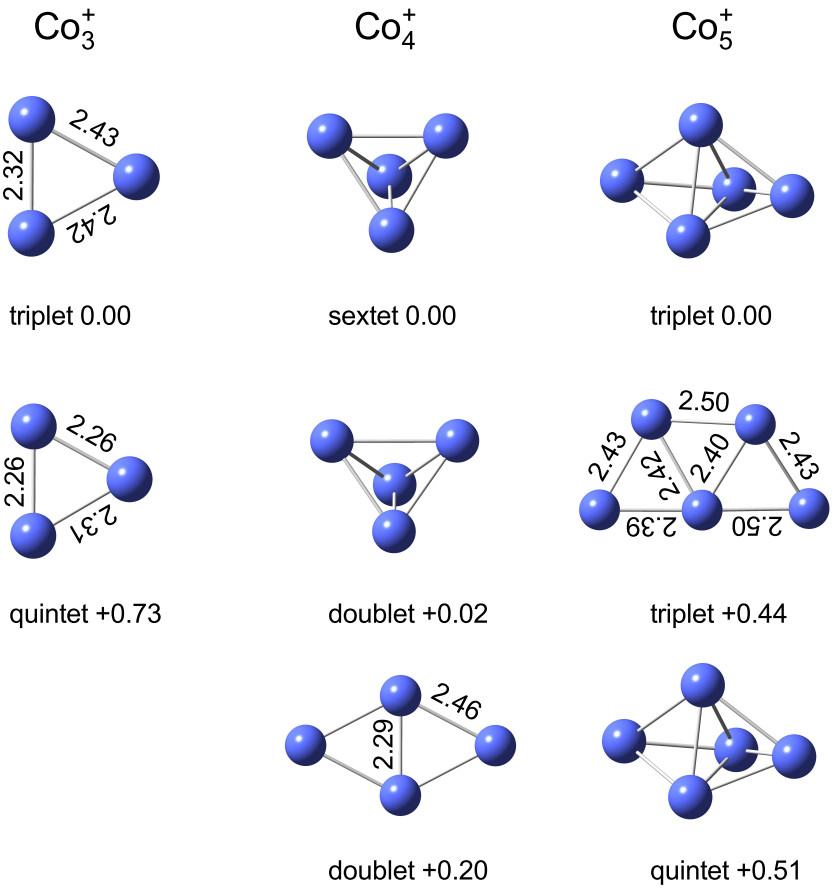

Figure 6.12: Geometry-optimised structures of the lowest energy isomers and electronic states for Co_n^+ (n = 3-5) calculated at the TPSSh/Def2TZVP level of theory. Bond lengths are provided (in Å) along with relative energies (in eV). Cartesian coordinates of these optimised structures, for all cluster sizes, can be found in the appendix.

6.13. For both Co_2^+ and $Co_2^+(N_2O)$, the sextet multiplicity was found to be the lowest electronic state, consistent with previous experimental and theoretical studies on Co_2^+.[232] The global minimum structure, $^6Co_2^+N^1$, presents an intense band in the asymmetric region assigned as the asymmetric stretch of N_2O, when bound to Co_2^+ *via* the terminal N-atom. The combination of the N_2O vibrating asymmetrically, together with the N_2O bound in close proximity to the charge on Co_2^+, results in a large change to the dipole moment, and thus, an intense band. Contrastingly, the symmetric region presents one weak band, assigned as the symmetric stretch of N_2O, when bound to Co_2^+ *via* the terminal N-atom. As the stretch is symmetric, together with the N_2O bound linearly to Co_2^+, this results in a small change

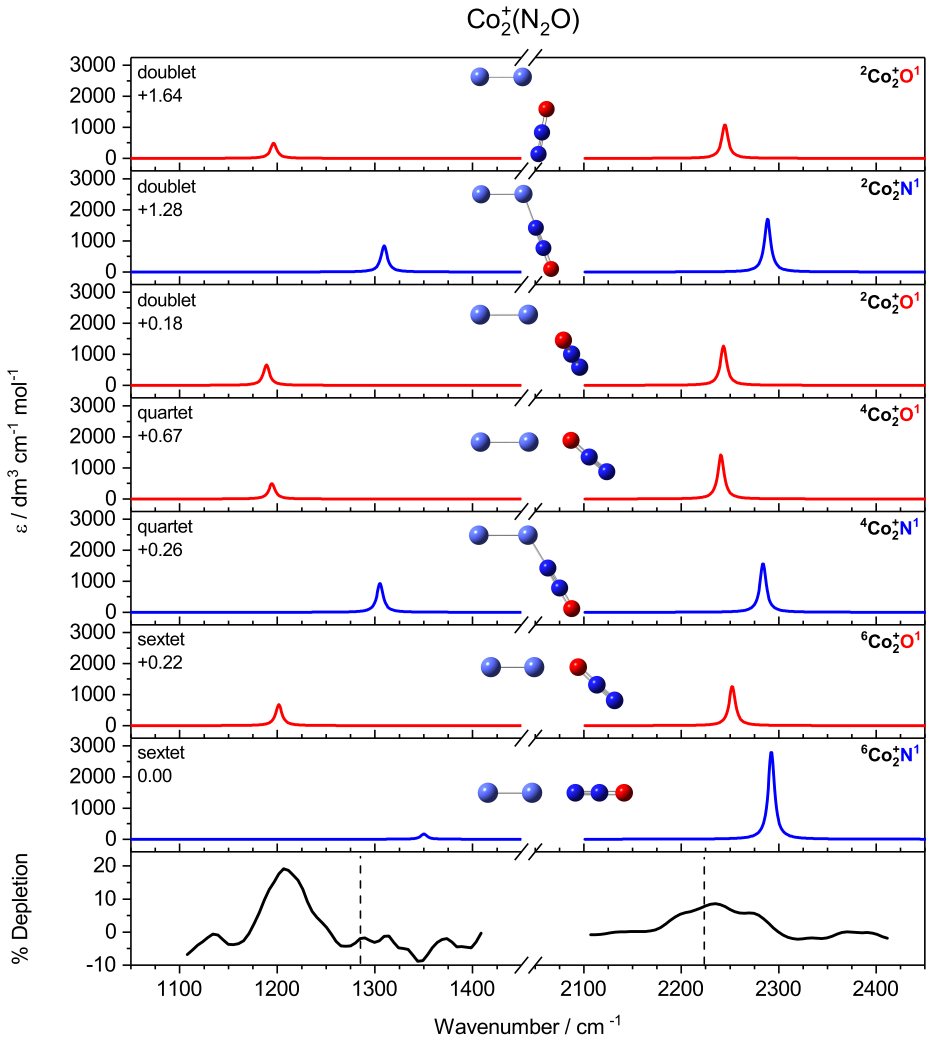

Figure 6.13: IRMPD depletion spectrum of $Co_2^+(N_2O)$ along with simulated IR spectra of low-lying sextet-, quartet-, and doublet-state isomers in the region of the N_2O symmetric (N=O) and asymmetric (N=N) stretch. Simulated IR bands corresponding to N-bound and O-bound ligands are indicated in blue and red, respectively. The relative energies of different isomers are given in eV. The vertical dashed lines at 1285 and 2223.5 cm^{-1} indicate the wavenumber of the ν_1(N=O) and ν_3(N=N) modes in isolated N_2O, respectively.[151]

in the dipole moment of N_2O, resulting in a band with low intensity, meaning in this case, the charge from Co_2^+ has little effect on the overall dipole moment. This argument can be extended when considering the symmetric simulated spectra of $^4Co_2^+N^1$ and $^2Co_2^+N^1$, which present a stronger N-bound band relative to $^6Co_2^+N^1$. In both cases, the N_2O binds in a non-linear fashion to the Co_2^+, resulting in a larger change to the dipole moment, resulting

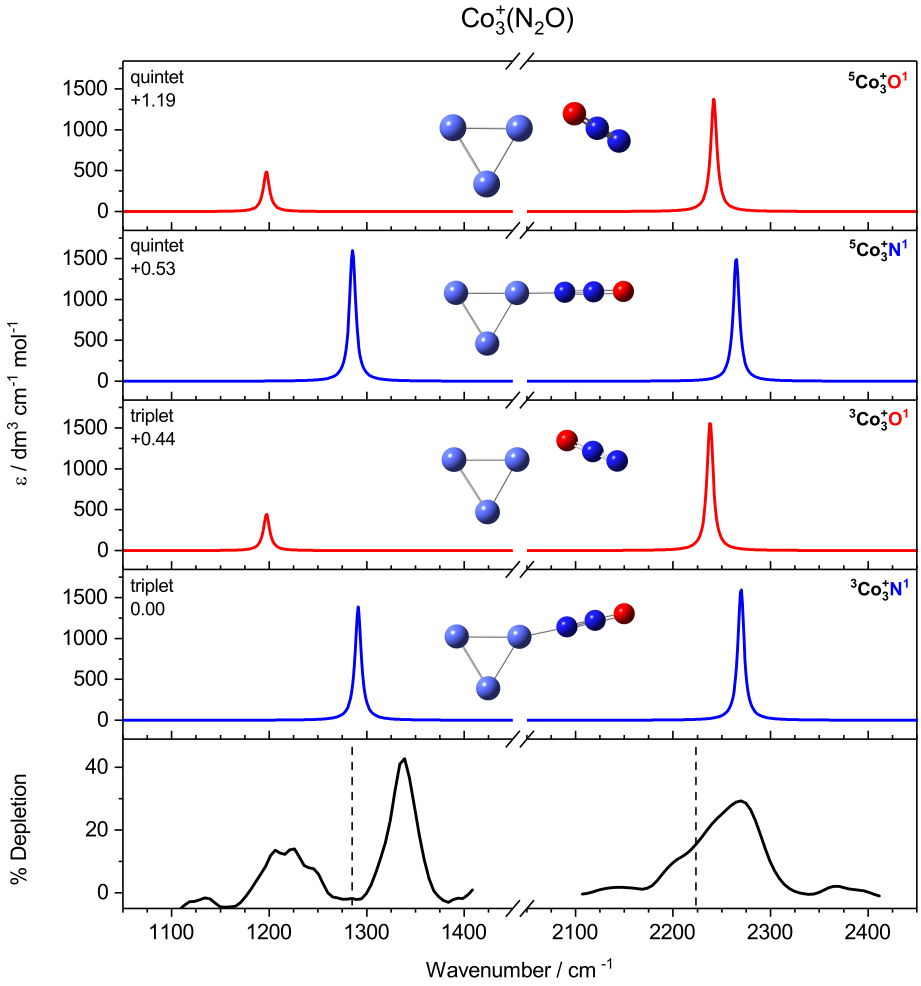

Figure 6.14: IRMPD depletion spectrum of $Co_3^+(N_2O)$ along with simulated IR spectra of low-lying triplet- and quintet-state isomers in the region of the N_2O symmetric (N=O) and asymmetric (N=N) stretch. Simulated IR bands corresponding to N-bound and O-bound ligands are indicated in blue and red, respectively. The relative energies of different isomers are given in eV. The vertical dashed lines at 1285 and 2223.5 cm^{-1} indicate the wavenumber of the ν_1(N=O) and ν_3(N=N) modes in isolated N_2O, respectively.[151]

in a more intense band.

The spectrum in the asymmetric region shows a weak, unresolved feature, likely due to N- and O-bound isomers. As in the case for the $Au_n^+(N_2O)$ clusters, IRMPD spectroscopy is unable to unambiguously distinguish between the three N-bound ($^{6/4/2}Co_2^+N^1$) and four O-bound ($^{6/4/2}Co_2^+O^1$) isomers present in figure 6.13.

Figure 6.14 shows the IRMPD spectra of $Co_3^+(N_2O)$ together with low-lying triplet and

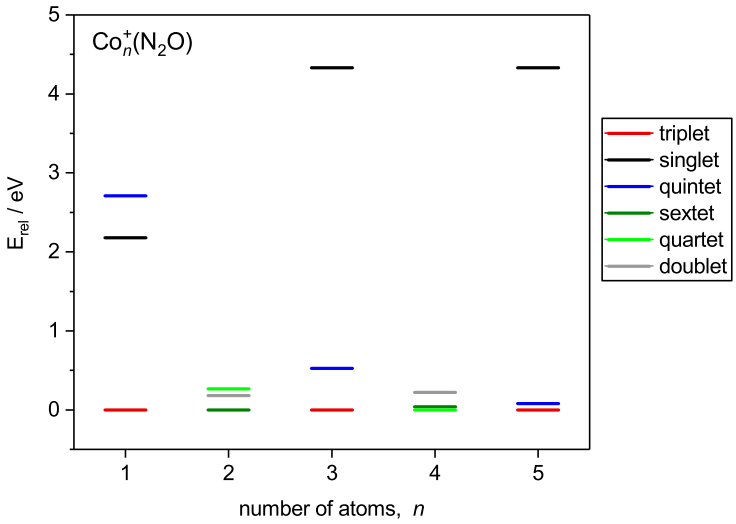

Figure 6.15: Calculated lowest energy isomers of triplet, singlet, and quintet states for $Co_n^+(N_2O)$, n = 1,3,5, along with sextet, quartet, and doublet states for $Co_n^+(N_2O)$, n = 2 and 4. Energies are relative to the global minimum structure for each n.

quintet isomers, along with their simulated spectra. In the symmetric region, the strong band at 1337 cm^{-1} is in good agreement with the N-bound band in $^3Co_3^+N^1$, but also with the N-bound band in $^5Co_3^+N^1$. Similarly, the unresolved feature around 1219 cm^{-1} agrees well with both O-bound bands in $^3Co_3^+O^1$ and $^5Co_3^+O^1$. The asymmetric region presents a broad feature, with a band centre at 2270 cm^{-1} and a shoulder at 2209 cm^{-1}. Again, the band centre can be assigned as arising from N-bound isomers of both multiplicity, with the shoulder arising from O-bound isomers of both multiplicity. There is no reason to infer that the IRMPD spectrum comprises both the triplet and higher-lying quintet isomers. However, there is also no evidence to suggest the quintet isomers are not present in the experiment. IRMPD is therefore, in this case, not diagnostic in distinguishing between the triplet and quintet structural isomers of $Co_3^+(N_2O)$.

The global minimum, sextet structure of Co_4^+ is shown in figure 6.12. Upon addition of an N_2O molecule, the difference in energy between the electronic states reduces. Thus,

the sextet, quartet, and doublet state N-bound isomers of $Co_4^+(N_2O)$ are all within 0.22 eV of each other. The calculated lowest energy isomers of $Co_n^+(N_2O)$ (n = 1-5) along with multiplicity are presented in figure 6.15. For clusters n = 1, 3, and 5, the lowest energy multiplicities are triplet, singlet, and quintet. For n = 1, the difference between the triplet ground state and singlet/quintet states is large. However, this difference reduces upon increasing atom number. By n = 3, the difference between triplet and quintet reduces significantly and at n = 5 these states are almost isoenergetic. Contrastingly, the energy of the singlet isomers increases upon increasing atom number. For clusters n = 2 and 4, the difference in energy between the lowest energy multiplicities (sextet, quartet, and doublet) is low.

The structures of $Co_n^+(N_2O)$, n = 4,5, are formed of isomers with low-lying electronic states, which all present qualitatively similar spectra and so only the sextet (n = 4) and triplet (n = 5) isomers shall be discussed (figures 6.16 and 6.17). As before, the symmetric region presents a strong band at 1324 cm^{-1} and 1323 cm^{-1} for n = 4 and 5, respectively, which can be attributed to an N-bound isomer. However in these cases the N-bound isomers present similar spectra and the IRMPD spectra cannot distinguish between them. The same is true for the strong band in the asymmetric region at 2274 cm^{-1} and 2271 cm^{-1} for n = 4 and 5, respectively.

Interestingly, for both cluster sizes, there is weak contribution from O-bound isomers. In the symmetric region, there are weak features at 1221 cm^{-1} and 1226 cm^{-1} and shoulder bands in the asymmetric region at 2204 cm^{-1} for both n = 4, and 5, respectively. This could be due to the increase in energy difference between N- and O-bound isomers upon increasing cluster size. This observation could also be due to a reduced barrier to internal rotation with increasing cluster size. An increased cluster size also represents a more effective energy

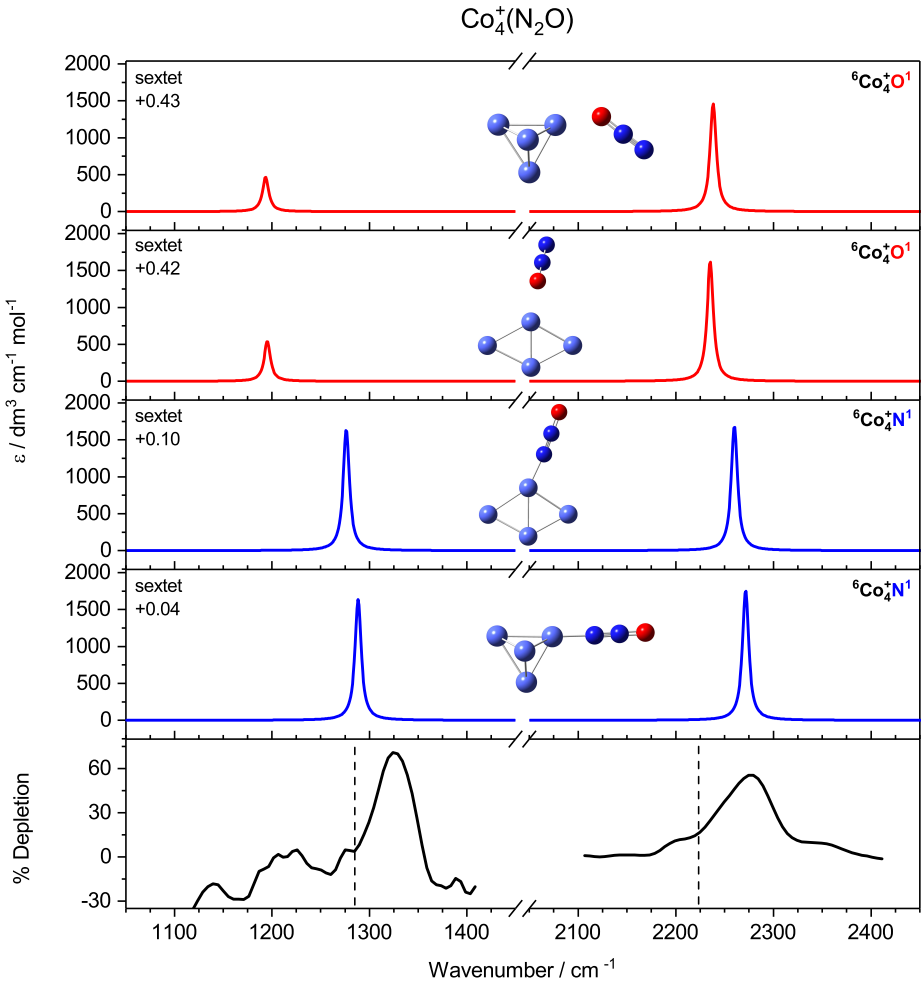

Figure 6.16: IRMPD depletion spectrum of $Co_4^+(N_2O)$ along with simulated IR spectra of low-lying sextet-state isomers in the region of the N_2O symmetric (N=O) and asymmetric (N=N) stretch. Simulated IR bands corresponding to N-bound and O-bound ligands are indicated in blue and red, respectively. The relative energies of different isomers are given in eV. The vertical dashed lines at 1285 and 2223.5 cm^{-1} indicate the wavenumber of the ν_1(N=O) and ν_3(N=N) modes in isolated N_2O, respectively.[151]

"bath", which can facilitate annealing to the lowest energy structure.

Figure 6.18 shows the relative energies between the N- and O-bound isomers of $Co_n^+(N_2O)$ (n = 1-5), inclusive of multiplicity. For all cluster sizes, the N-bound isomers (blue) present the global minimum structure. The relative energies of the O-bound isomers (red) however vary with cluster size. The $n = 2$ cluster presents the smallest difference at 0.18 eV, increasing to 0.44 eV at $n = 3$. The relative difference then decreases slightly to 0.36 eV

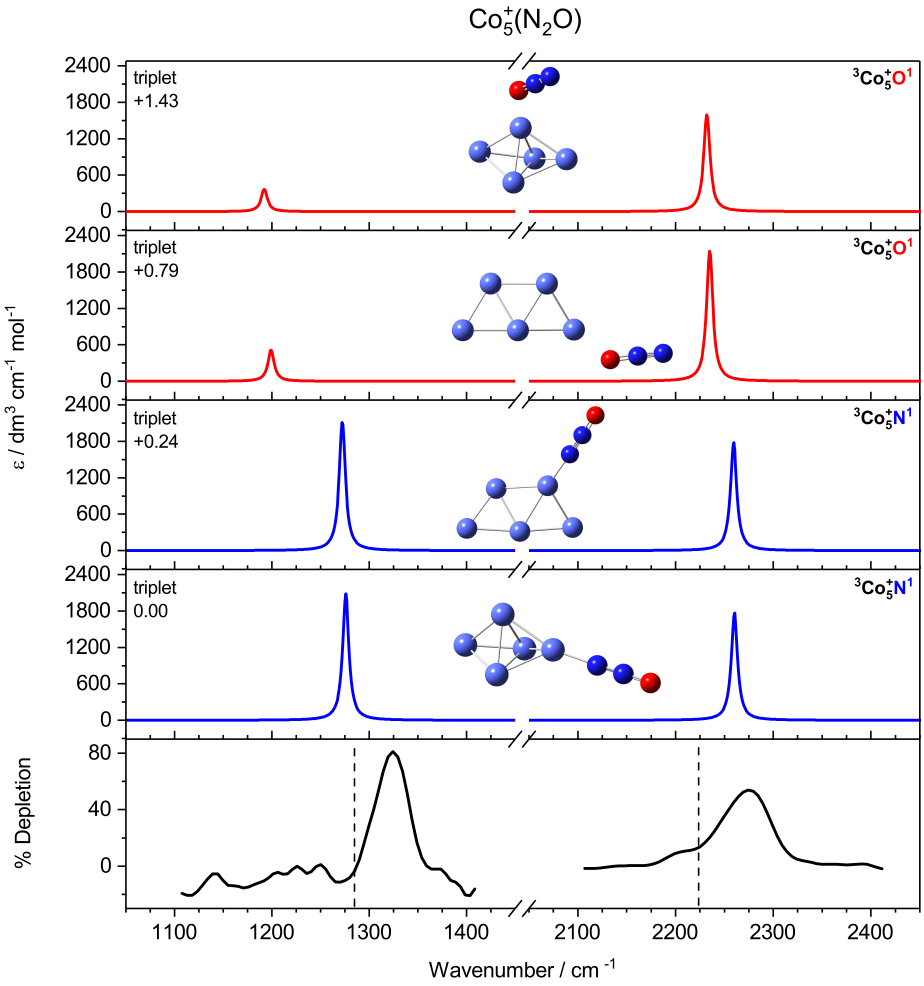

Figure 6.17: IRMPD depletion spectrum of $Co_5^+(N_2O)$ along with simulated IR spectra of low-lying triplet-state isomers in the region of the N_2O symmetric (N=O) and asymmetric (N=N) stretch. Simulated IR bands corresponding to N-bound and O-bound ligands are indicated in blue and red, respectively. The relative energies of different isomers are given in eV. The vertical dashed lines at 1285 and 2223.5 cm^{-1} indicate the wavenumber of the ν_1(N=O) and ν_3(N=N) modes in isolated N_2O, respectively.[151]

at $n = 4$ before increasing drastically to 0.72 eV at $n = 5$. From this, it is expected that n = 1,3,4, and 5 should not present bands which would indicate the presence of O-bound isomers. However, the observed spectra of $Co_1^+(N_2O)$ and $Co_3^+(N_2O)$, figure 6.11, present bands in both the symmetric and asymmetric regions which are attributed to O-bound ligands. Conversely, the observed spectra for $Co_4^+(N_2O)$ and $Co_5^+(N_2O)$ present weak features attributed to O-bound ligands, and N-bound features dominate the IRMPD spectra. One

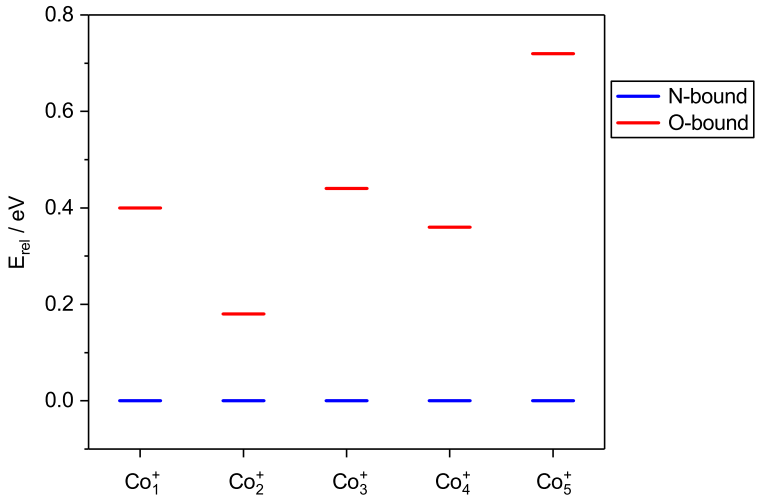

Figure 6.18: Calculated lowest energy N- and O-bound isomers for $Co_n^+(N_2O)$ (n = 1-5), relative to the (inclusive) lowest energy multiplicity. Energies are relative to the global minimum structure for each n.

possible explanation is that upon increasing cluster size, there are more available binding sites for the N_2O ligand to arrange itself to the lowest energy N-bound geometry. Another explanation is that upon increasing the number of atoms in the cluster leads to a more effective thermal bath for annealing over any barrier towards the global minimum structure. IRMPD studies on $Rh_6^+(N_2O)$ observed the N_2O ligand binding exclusively in atop arrangements, *via* the terminal N-atom,[113,114] and the same N_2O binding effects in larger Co_n^+ clusters are mirrored here.

6.4 Conclusions

Small gas-phase $Au_n^+(N_2O)$ and $Co_n^+(N_2O)$ clusters (n = 1-5) have been investigated using infrared multi-photon photodissociation spectroscopy in both the ν_1(N=O) and ν_3(N=N) regions of N_2O. Coupled with density functional theory, the simulated spectra of these clusters can be compared with the observed spectra.

In the case of $Au_n^+(N_2O)$, the asymmetric region presents a blue-shifted band for n =

1-5, assigned as N-bound N_2O, along with a shoulder band assigned to O-bound N_2O. The symmetric spectra also present a blue-shifted band. However the signature of an O-bound ligand, as observed in the simulated spectra, is red-shifted and lies outside of the wavelength range of the spectra recorded. Therefore, the spectra in the symmetric region need to be re-recorded and extended to lower wavenumber to secure the assignments and arguments presented. Larger clusters, *i.e.* n = 6-8, present one blue-shifted band in the asymmetric region. This is most likely an N-bound ligand, which infers that for these cluster sizes, N_2O binds exclusively *via* the terminal N atom. However, further calculations on the structural isomers, together with simulated spectra, are required to strengthen this assignment. For all cluster sizes, N-bound geometries are the lower in energy, when compared to O-bound geometries, and only the lowest electronic state is considered as others lie much higher in energy.

For $Co_n^+(N_2O)$, the interpretation is similar; the spectra in the asymmetric region all present a blue-shifted band (N-bound) along with a shoulder band (O-bound). Fortunately, the spectra in the symmetric region were extended, and the clear signature of O-bound ligands was observed. For cluster sizes n = 1-3, there is evidence of both N- and O-bound ligands, in both the symmetric and asymmetric spectra. However, at n = 4,5, O-bound features become weaker, with N-bound bands dominating the spectra, similar to the higher-order $Au_n^+(N_2O)$ clusters. This observation has been tentatively attributed to more binding sites, and/or a more effective thermal bath, which larger clusters provide, whereby the N_2O molecule can more readily rearrange to the lowest energy, N-bound geometry. In contrast to gold, the calculations for $Co_n^+(N_2O)$ present evidence of low-lying electronic states, especially for larger clusters. Unfortunately, the simulated spectra for these different electronic states are similar, which can help explain the broad features in the observed spectra.

Thus, there is no clear fingerprint for each of the geometries occupying different electronic states. IRMPD is therefore not an effective method for the structure determination of these clusters. As such, a complementary technique, such as x-ray magnetic circular dichroism spectroscopy, which has been effective in determining electronic states of metal cations,[232] should be implemented to discern the specific multiplicities (along with the respective geometries) of these clusters.

Chapter 7

Conclusions

The thesis presents the first experimental studies on $M^+(N_2O)_n$ ion-molecule complexes. These complexes represent model entrance-channel species for the metal-centred nitrous oxide reduction reaction. The results presented form a systematic study comparing N_2O bound to a range of metals across the periodic table in an attempt to draw differences and comparisons between them, elucidating behavioural trends.

IRPD and IRMPD spectroscopy complemented with simulated spectra obtained from density functional theory offers a powerful tool for elucidating the structures of metal-ligand ion-molecule complexes. The complexes in chapters 3-5 were studied using IRPD in the region of the ν_3(N=N) mode of N_2O. Chapter 3 presents the first study, investigating coinage (Cu, Ag, Au) metals. These metals were chosen as they offer a closed-shell d^{10} electron configuration in their cationic form, and thus, simpler ion-N_2O interactions are expected. The spectra reveal clear evidence for structural isomers containing both N- and O-bound ligands, each with a spectral signature. N-bound ligands are significantly more blue-shifted when compared to O-bound ligands, with blue-shifts the most pronounced for Au, followed by Cu, and then Ag. Based on these shifts, a coordination number of

four was found for the $Cu^+(N_2O)_n$ and $Ag^+(N_2O)_n$ complexes, whereas for $Au^+(N_2O)_n$, the coordination number was two. These trends are interpreted from a molecular orbital approach to the binding interaction, whereby the N_2O induces s-d_{z^2} hybridisation of the metal cation.

Following these studies, open-shell group 9, d^8 ions were complexed with nitrous oxide (chapter 4). The spectra reveal that the $Co^+(N_2O)_n$ complexes behave similarly to the coinage metals, however are markedly different for Rh and Ir, and evolve in contrasting ways upon increasing ligand number, n. Similar to the coinage metal complexes, the spectra for all three metals present evidence for N- and O-bound signatures, however the $Rh^+(N_2O)_n$ and $Ir^+(N_2O)_n$ complexes also present additional evidence of low-lying electronic states. In the case of $Rh^+(N_2O)_n$, a switch in ground-state multiplicity, from triplet to singlet, occurs at $n = 4$.

To compare with these transition metal ions, closed s-shell ions, Li^+ and Al^+, were ligated with N_2O (chapter 5). Contrastingly, there is little energetic or spectral difference between N- and O-bound ligands. Uniquely amongst these $M^+(N_2O)_n$ complexes presented in this thesis, the IRPD spectra of the $Li^+(N_2O)_n$ show evidence of an N_2 moiety, tentatively assigned as arising from inserted, $OLi^+N_2(N_2O)_{n-1}$ isomers. The N_2 moiety is spectrally distinct and blue-shifted from the molecularly bound N- and O-bound ligands and is well-reproduced when compared to simulated spectra.

Summarising the behaviour for each of the metal-nitrous oxide complexes: $\mathbf{Li^+(N_2O)}_n$ complexes are similar to Co^+ as each has a coordination number of six, and similar to $Al^+(N_2O)_n$ as in each case, N- and O-bound isomers cannot be distinguished spectroscopically. Different from any of the other metal-nitrous oxide complexes however, the spectra for Li^+ present evidence of an N_2 moiety, arising from inserted complexes. $\mathbf{Al^+(N_2O)}_n$

complexes are different from any of the other metal-nitrous oxide complexes as the N_2O ligand vibrations do not act as local modes, instead acting collectively in a similar way to CO_2 ligands within $Al^+(CO_2)_n$ complexes. $\mathbf{Co^+(N_2O)}_n$ complexes are similar to the group 11 metal-nitrous oxide complexes presenting spectral signatures for N- and O-bound N_2O ligands. Co^+ is different however from Rh^+ and Ir^+ as only one electronic state (triplet) is considered when interpreting the observed IRPD spectra. $\mathbf{Rh^+(N_2O)}_n$ complexes are similar to $Ir^+(N_2O)_n$, both presenting evidence of low-lying electronic states and in the case of Rh^+, a switch in spin multiplicity of the ground state at $n = 4$. $\mathbf{Ir^+(N_2O)}_n$ complexes are different from all metal-nitous oxide complexes with respect to the electronic state. The lowest energy electronic state (triplet) does not agree with the recorded IRPD spectra, with higher lying quintet isomers instead presenting a better agreement. Similar to the $Al^+(N_2O)_n$ complexes, the N_2O ligands in the $Ir^+(N_2O)_n$ complexes act collectively, and not as local modes. $\mathbf{Cu^+(N_2O)}_n$ complexes are similar to Al^+, Ag^+, and Au^+ as only the ground state electronic state (singlet) contributes to the observed IRPD spectrum. $\mathbf{Ag^+(N_2O)}_n$ complexes are similar to Cu^+ as both have a coordination number of four. $\mathbf{Au^+(N_2O)}_n$ complexes are different from Cu^+ and Ag^+ as Au^+ has a coordination number of two. Au^+ is similar to the other group 11 and group 9 metal-nitrous oxide complexes as incoming N-bound N_2O ligands donate σ electron character to the metal centre, reflected in a blue-shift. The degree of blue-shift is the highest for the $Au^+(N_2O)_2$ complex.

By comparison with the single metal-cation $M^+(N_2O)_n$ complexes, chapter 6 presents an IRMPD study of nitrous oxide binding to cationic gold and cobalt clusters ($M_n^+(N_2O)$, M = Au, Co) utilising the FEL facility at the Fritz-Haber Institute in Berlin. Infrared spectra were recorded in both the ν_1(N=O) and ν_3(N=N) stretching regions of N_2O. In the case of the $Au_n^+(N_2O)$ clusters (n = 1-5), the asymmetric region presents evidence

of N- and O-bound spectral signatures. However, the symmetric spectral region needs to be re-recorded and extended to a lower wavenumber to secure assignments of O-bound ligands. Larger clusters, n = 6-8, show one blue-shifted band, likely due to exclusively N-bound ligands. Future work involves performing calculations generating low-lying structural isomers, together with simulated spectra to secure these assignments.

The spectra for the $Co_n^+(N_2O)$ clusters also show N- and O-bound signatures, in this case both in the asymmetric and symmetric stretching regions. Similar to the case of Au^+, as the metal cluster size increases the N-bound bands dominate the spectra. This observation is tentatively explained as the larger cluster size representing a more effective energy "bath", facilitating annealing to the lowest energy structure. In contrast to Au^+, calculated structures for the $Co_n^+(N_2O)$ complexes present evidence of low-lying electronic states, especially for larger clusters. However, the simulated spectra for these different electronic states are all similar. The IRMPD spectra can therefore not distinguish between the different electronic states of the larger $Co_n^+(N_2O)$ complexes.

All complexes studied in this thesis were cationic. For an interesting comparison, future work on equivalent anionic, $M^-(N_2O)_n$, complexes could be carried out in order to observe any N_2O activation caused by the M^- centre. The laboratory is set up for anion detection with initial success detecting $Au^-(CO_2)_n$ complexes. In addition to spectroscopic measurements for structure determination, the ultimate goal in IRPD measurements is to observe infrared-induced chemical reactivity involving a metal-ligand complex. Utilising N_2O as the ligand, which provides different binding arrangements together with a spectral signature, offers the prospect of initiating infrared-driven isomer-selective chemistry in size-selected complexes.

One future direction involves mixed-ligand complexes. For example, two different lig-

ands, N_2O and CO, could be adsorbed to a metal centre forming $M^+(N_2O)_n(CO)_m$ complexes. These complexes could potentially offer three distinct bands within the 2000 - 2500 cm^{-1} region: i) an N-bound N_2O band, ii) an O-bound N_2O band, and iii) a CO band. The behaviour of such a complex is unknown with one important question being what happens when *either* of these ligands absorbs an infrared photon. Does the most weakly-bound ligand always desorb from the complex? Are there co-adsorption effects leading to differences in spectral shift? IRPD measurements on such systems is a viable method in approaching such questions.

However, in order to accurately determine the branching ratios of such experiments, mass-selectivity should be introduced. The experiment has recently been upgraded with the addition of a quadrupole ion guide in order to perform such mass-selective measurements. Initial experiments are promising, with successful production and mass selection of various $M^+(N_2O)_n(CO)_m$ complexes achieved. Initial spectroscopic measurements, along with simulated spectra from DFT calculations, show that the N_2O and CO bands are decoupled and act as local modes. Thus, IRPD measurements on size-selected complexes offer the prospect of: i) using infrared spectroscopy to introduce a known amount of energy into a known part of the complex (*i.e.* into one of the adsorbed ligands), and ii) using fragmentation to observe where the energy has been spent (*i.e.* loss/desorption of an adsorbed ligand). These experiments not only address some of the fundamental processes involved in IRPD spectroscopy but also offer the tantalising prospect of observing different product branching ratios for infrared-driven mode-selective reactivity in different isomers.

Appendix A

Appendix

Table A.1: Cartesian coordinates of the geometry-optimised structures of the lowest energy forms for Au_n^+ (n = 3 and 4) calculated at the TPSSh/Def2TZVP level of theory. Relative energies are given in eV and coordinate distances in Å.

Species	Atom	x	y	z	$E_{rel.}$ / eV
$^1Au_3^+$	Au	1.25837600	0.16380200	0.00000000	0.00
	Au	-1.37385200	0.10415300	0.00000000	
	Au	-0.00593800	-2.14576200	0.00000000	
$^2Au_4^+$	Au	-1.57909700	-0.01930100	1.67277200	0.00
	Au	0.98152700	0.00633300	0.92672100	
	Au	-0.98155100	-0.00602400	-0.92684800	
	Au	1.57912000	0.01899300	-1.67264600	
$^2Au_4^+$	Au	0.20253200	0.00000000	3.08686600	0.21
	Au	-0.25738100	0.00000000	0.50562600	
	Au	1.32026500	0.00000000	-1.62532000	
	Au	-1.26541500	0.00000000	-1.96717200	

Table A.2: Cartesian coordinates of the geometry-optimised structures of the lowest energy forms for Au_n^+ ($n = 5$) calculated at the TPSSh/Def2TZVP level of theory. Relative energies are given in eV and coordinate distances in Å.

Species	Atom	x	y	z	$E_{rel.}$ / eV
$^1Au_5^+$	Au	1.30262500	0.10375400	-0.00884200	0.00
	Au	-1.37187100	0.13595500	-0.00409700	
	Au	0.02928600	-2.14220200	0.01072800	
	Au	-2.77285500	2.41418900	-0.01909000	
	Au	-4.04640900	0.16831500	0.00085500	
$^1Au_5^+$	Au	-0.03120400	0.02299500	-2.73975500	0.53
	Au	-0.02102700	1.31538100	-0.41020400	
	Au	0.01304900	-1.30755100	-0.43331400	
	Au	-1.27078800	-0.03062800	1.80402400	
	Au	1.30997000	-0.00019800	1.77925000	

Table A.3: Cartesian coordinates of the geometry-optimised structures of the lowest energy forms for Co_n^+ ($n = 3$) calculated at the TPSSh/Def2TZVP level of theory. Relative energies are given in eV and coordinate distances in Å.

Species	Atom	x	y	z	$E_{rel.}$ / eV
$^3Co_3^+$	Co	0.02092500	1.41858300	0.00000000	0.00
	Co	1.15057100	-0.72438900	0.00000000	
	Co	-1.17149700	-0.69419400	0.00000000	
$^5Co_3^+$	Co	0.00277800	1.32370100	0.00000000	0.73
	Co	1.12799000	-0.69144900	0.00000000	
	Co	-1.13076800	-0.63225300	0.00000000	

Table A.4: Cartesian coordinates of the geometry-optimised structures of the lowest energy forms for Co_n^+ ($n = 4$) calculated at the TPSSh/Def2TZVP level of theory. Relative energies are given in eV and coordinate distances in Å.

Species	Atom	x	y	z	$E_{rel.}$ / eV
$^6Co_4^+$	Co	-0.79375100	1.21987500	0.05718600	0.00
	Co	0.75780000	0.00726700	1.21635900	
	Co	0.88713200	-0.02461200	-1.22896100	
	Co	-0.85118000	-1.20252900	-0.04458400	
$^2Co_4^+$	Co	1.29018900	-0.23547300	-0.39674700	0.02
	Co	-0.69781200	1.12497200	-0.56494900	
	Co	0.00494500	0.34552900	1.60999800	
	Co	-0.90436800	-1.27859900	-0.39338900	
$^2Co_4^+$	Co	0.00002700	1.14421800	0.00000000	0.20
	Co	-0.00002700	0.00016600	2.17807300	
	Co	-0.00002700	0.00016500	-2.17807200	
	Co	0.00002800	-1.14454800	-0.00000100	

Table A.5: Cartesian coordinates of the geometry-optimised structures of the lowest energy forms for Co_n^+ ($n = 5$) calculated at the TPSSh/Def2TZVP level of theory. Relative energies are given in eV and coordinate distances in Å.

Species	Atom	x	y	z	$E_{rel.}$ / eV
$^3Co_5^+$	Co	0.07615000	-0.14984900	1.45156800	0.00
	Co	-2.02076200	0.06355600	0.00269900	
	Co	-0.07988500	-1.10684200	-0.74889400	
	Co	2.00697900	-0.10682800	-0.11861800	
	Co	0.01752000	1.29996500	-0.58675500	
$^3Co_5^+$	Co	-3.41189400	1.73702100	-0.29054300	0.44
	Co	-4.73922700	-0.26233200	0.11207900	
	Co	-2.35683300	-0.41112700	0.09964800	
	Co	-0.99643200	1.54966900	0.33382700	
	Co	0.12729000	-0.54921900	-0.13426500	
$^5Co_5^+$	Co	-2.20648500	1.88720000	-0.32555300	0.51
	Co	-0.00074400	2.51000300	0.29886600	
	Co	-2.70409900	-0.35156300	0.29723900	
	Co	-0.43843900	0.21715600	-0.26271200	
	Co	-1.27193700	1.00239500	1.88228800	

Bibliography

[1] Santen, R. A. v. *Modern Heterogeneous Catalysis: An Introduction;* Wiley VCH: Weinheim, 2017.

[2] Milina, M.; Mitchell, S.; Crivelli, P.; Cooke, D.; Pérez-Ramírez, J. *Nature Communications* **2014**, *5*, 3922.

[3] Moulijn, J. A.; van Diepen, A. E.; Kapteijn, F. *Applied Catalysis A: General* **2001**, *212*(1), 3–16.

[4] Goldman, A. S.; Roy, A. H.; Huang, Z.; Ahuja, R.; Schinski, W.; Brookhart, M. *Science* **2006**, *312*(5771), 257–261.

[5] Cue, B. W.; Zhang, J. *Green Chemistry Letters and Reviews* **2009**, *2*(4), 193–211.

[6] Cadierno, V.; Francos, J.; García-Garrido, S. E.; Gimeno, J. *Green Chemistry Letters and Reviews* **2011**, *4*(1), 55–61.

[7] Yeap, E. W. Q.; Acevedo, A. J.; Khan, S. A. *Organic Process Research and Development* **2019**, *23*(3), 375–381.

[8] Jia, X.; Qin, C.; Friedberger, T.; Guan, Z.; Huang, Z. *Science Advances* **2016**, *2*(6), e1501591.

[9] Serrano, D. P.; Aguado, J.; Escola, J. M. *ACS Catalysis* **2012**, *2*(9), 1924–1941.

[10] Kašpar, J.; Fornasiero, P.; Graziani, M. *Catalysis Today* **1999**, *50*(2), 285–298.

[11] Kašpar, J.; Fornasiero, P.; Hickey, N. *Catalysis Today* **2003**, *77*(4), 419–449.

[12] Lee, K.; Kosaka, H.; Sato, S.; Yokoi, T.; Choi, B. *Chemical Engineering Science* **2019**, *203*, 28–42.

[13] Zhang, N.; Xian, G.; Li, X.; Zhang, P.; Zhang, G.; Zhu, J. *Frontiers in Chemistry* **2018**, *6*.

[14] Descorme, C. *Catalysis Today* **2017**, *297*, 324–334.

[15] Smil, V. *Enriching the Earth: Fritz Haber, Carl Bosch, and the Transformation of World Food Production;* MIT Press: Cambridge, MA, 2001.

[16] Herzing, A. A.; Kiely, C. J.; Carley, A. F.; Landon, P.; Hutchings, G. J. *Science* **2008**, *321*(5894), 1331–1335.

[17] Binnig, G.; Quate, C. F.; Gerber, C. *Physical Review Letters* **1986**, *56*(9), 930–933.

[18] Binnig, G.; Rohrer, H.; Gerber, C.; Weibel, E. *Physical Review Letters* **1982**, *49*(1), 57–61.

[19] Ertl, G. *Reactions at Solid Surfaces;* Wiley: Hoboken, NJ, 2009.

[20] Somorjai, G. A.; Li, Y. *Introduction to Surface Chemistry and Catalysis, 2nd Edition;* Wiley: Hoboken, NJ, 2010.

[21] Taylor Hugh, S.; Armstrong Edward, F. *Proceedings of the Royal Society of London. Series A, Containing Papers of a Mathematical and Physical Character* **1925**, *108*(745), 105–111.

[22] Castleman, A. W. *Catalysis Letters* **2011**, *141*(9), 1243.

[23] Dietz, T. G.; Duncan, M. A.; Powers, D. E.; Smalley, R. E. *The Journal of Chemical Physics* **1981**, *74*(11), 6511–6512.

[24] Haberland, H. *Clusters of Atoms and Molecules - Theory, Experiment, and Clusters of Atoms;* Berlin ; New York : Springer-Verlag: Berlin, Heidelberg, 1994.

[25] Haberland, H. *Clusters of atoms and molecules II : solvation and chemistry of free clusters, and embedded, supported, and compressed clusters;* Berlin ; New York : Springer-Verlag, 1994.

[26] Jortner, J. *Zeitschrift für Physik D Atoms, Molecules and Clusters* **1992**, *24*(3), 247–275.

[27] Hashmi, A. S. K.; Hutchings, G. J. *Angewandte Chemie International Edition* **2006**, *45*(47), 7896–7936.

[28] Meyer, R.; Lemire, C.; Shaikhutdinov, S. K.; Freund, H. J. *Gold Bulletin* **2004**, *37*(1), 72–124.

[29] Haruta, M.; Kobayashi, T.; Sano, H.; Yamada, N. *Chemistry Letters* **1987**, *16*(2), 405–408.

[30] Foster, P. J.; Leckenby, R. E.; Robbins, E. J. *Journal of Physics B: Atomic and Molecular Physics* **1969**, *2*(4), 478–483.

[31] Larsen, R. A.; Neoh, S. K.; Herschbach, D. R. *Review of Scientific Instruments* **1974**, *45*(12), 1511–1516.

[32] Knight, W. D.; Clemenger, K.; de Heer, W. A.; Saunders, W. A.; Chou, M. Y.; Cohen, M. L. *Physical Review Letters* **1984**, *52*(24), 2141–2143.

[33] Ganteför, G.; Siekmann, H. R.; Lutz, H. O.; Meiwes-Broer, K. H. *Chemical Physics Letters* **1990**, *165*(4), 293–296.

[34] Katakuse, I.; Ichihara, T.; Fujita, Y.; Matsuo, T.; Sakurai, T.; Matsuda, H. *International Journal of Mass Spectrometry and Ion Processes* **1985**, *67*(2), 229–236.

[35] Fayet, P.; Wolf, J. P.; Wöste, L. *Physical Review B* **1986**, *33*(10), 6792–6797.

[36] Ho, J.; Ervin, K. M.; Lineberger, W. C. *The Journal of Chemical Physics* **1990**, *93*(10), 6987–7002.

[37] Lincoln, K. A. *International Journal of Mass Spectrometry and Ion Physics* **1969**, *2*(1), 75–83.

[38] Bondybey, V. E.; English, J. H. *The Journal of Chemical Physics* **1981**, *74*(12), 6978–6979.

[39] Duncan, M. A. *Review of Scientific Instruments* **2012**, *83*(4), 041101.

[40] Knickelbein, M. B.; Yang, S.; Riley, S. J. *The Journal of Chemical Physics* **1990**, *93*(1), 94–104.

[41] Fielicke, A.; Kirilyuk, A.; Ratsch, C.; Behler, J.; Scheffler, M.; von Helden, G.; Meijer, G. *Physical Review Letters* **2004**, *93*(2), 023401.

[42] Nonose, S.; Sone, Y.; Onodera, K.; Sudo, S.; Kaya, K. *The Journal of Physical Chemistry* **1990**, *94*(7), 2744–2746.

[43] Kishi, R.; Iwata, S.; Nakajima, A.; Kaya, K. *The Journal of Chemical Physics* **1997**, *107*(8), 3056–3070.

[44] Pramann, A.; Nakajima, A.; Kaya, K. *The Journal of Chemical Physics* **2001**, *115*(12), 5404–5410.

[45] Koyasu, K.; Mitsui, M.; Nakajima, A.; Kaya, K. *Chemical Physics Letters* **2002**, *358*(3), 224–230.

[46] Weis, P.; Gilb, S.; Gerhardt, P.; Kappes, M. M. *International Journal of Mass Spectrometry* **2002**, *216*(1), 59–73.

[47] Weis, P.; Bierweiler, T.; Gilb, S.; Kappes, M. M. *Chemical Physics Letters* **2002**, *355*(3), 355–364.

[48] Gilb, S.; Weis, P.; Furche, F.; Ahlrichs, R.; Kappes, M. M. *The Journal of Chemical Physics* **2002**, *116*(10), 4094–4101.

[49] Furche, F.; Ahlrichs, R.; Weis, P.; Jacob, C.; Gilb, S.; Bierweiler, T.; Kappes, M. M. *The Journal of Chemical Physics* **2002**, *117*(15), 6982–6990.

[50] Maier-Borst, M.; Cameron, D. B.; Rokni, M.; Parks, J. H. *Physical Review A* **1999**, *59*(5), R3162–R3165.

[51] Rapps, T.; Ahlrichs, R.; Waldt, E.; Kappes, M. M.; Schooss, D. *Angewandte Chemie International Edition* **2013**, *52*(23), 6102–6105.

[52] Cai, M.; Carter, C. C.; Miller, T. A.; Bondybey, V. E. *The Journal of Chemical Physics* **1991**, *95*(1), 73–79.

[53] Merritt, J. M.; Bondybey, V. E.; Heaven, M. C. *The Journal of Physical Chemistry A* **2009**, *113*(47), 13300–13309.

[54] Matsuda, Y.; Bernstein, E. R. *The Journal of Physical Chemistry A* **2005**, *109*(17), 3803–3811.

[55] Bellert, D.; Breckenridge, W. H. *The Journal of Chemical Physics* **2001**, *114*(7), 2871–2874.

[56] Bellert, D.; Winn, D. K.; Breckenridge, W. H. *The Journal of Chemical Physics* **2002**, *117*(7), 3139–3148.

[57] Antonov, I. O.; Barker, B. J.; Heaven, M. C. *The Journal of Chemical Physics* **2011**, *134*(4), 044306.

[58] Bieske, E. J.; Maier, J. P. *Chemical Reviews* **1993**, *93*(8), 2603–2621.

[59] Duncan, M. A. *International Journal of Mass Spectrometry* **2000**, *200*(1), 545–569.

[60] Okumura, M.; Yeh, L. I.; Lee, Y. T. *The Journal of Chemical Physics* **1985**, *83*(7), 3705–3706.

[61] Liu, W.; Lisy, J. M. *The Journal of Chemical Physics* **1988**, *89*(1), 605–606.

[62] Brümmer, M.; Kaposta, C.; Santambrogio, G.; Asmis, K. R. *The Journal of Chemical Physics* **2003**, *119*(24), 12700–12703.

[63] Asmis, K. R.; Meijer, G.; Brümmer, M.; Kaposta, C.; Santambrogio, G.; Wöste, L.; Sauer, J. *The Journal of Chemical Physics* **2004**, *120*(14), 6461–6470.

[64] Santambrogio, G.; Janssens, E.; Li, S.; Siebert, T.; Meijer, G.; Asmis, K. R.; Döbler, J.; Sierka, M.; Sauer, J. *Journal of the American Chemical Society* **2008**, *130*(45), 15143–15149.

[65] Jiang, L.; Wende, T.; Claes, P.; Bhattacharyya, S.; Sierka, M.; Meijer, G.; Lievens, P.; Sauer, J.; Asmis, K. R. *The Journal of Physical Chemistry A* **2011**, *115*(41), 11187–11192.

[66] Burow, A. M.; Wende, T.; Sierka, M.; Włodarczyk, R.; Sauer, J.; Claes, P.; Jiang, L.; Meijer, G.; Lievens, P.; Asmis, K. R. *Physical Chemistry Chemical Physics* **2011**, *13*(43), 19393–19400.

[67] Asmis, K. R. *Physical Chemistry Chemical Physics* **2012**, *14*(26), 9270–9281.

[68] Holm, R. H.; Kennepohl, P.; Solomon, E. I. *Chemical Reviews* **1996**, *96*(7), 2239–2314.

[69] Kilpin, K. J.; Dyson, P. J. *Chemical Science* **2013**, *4*(4), 1410–1419.

[70] Andreini, C.; Bertini, I.; Cavallaro, G.; Holliday, G. L.; Thornton, J. M. *JBIC Journal of Biological Inorganic Chemistry* **2008**, *13*(8), 1205–1218.

[71] Pluth, M. D.; Bergman, R. G.; Raymond, K. N. *Science* **2007**, *316*(5821), 85–88.

[72] Duncan, M. A. *International Reviews in Physical Chemistry* **2003**, *22*(2), 407–435.

[73] Plane, J. M. C.; Feng, W.; Dawkins, E. C. M. *Chemical Reviews* **2015**, *115*(10), 4497–4541.

[74] Noll, K. S.; McGrath, M. A.; Trafton, L. M.; Atreya, S. K.; Caldwell, J. J.; Weaver, H. A.; Yelle, R. V.; Barnet, C.; Edgington, S. *Science* **1995**, *267*(5202), 1307–1313.

[75] Castleman, A. W.; Keesee, R. G. *Accounts of Chemical Research* **1986**, *19*(12), 413–419.

[76] Castleman, A. W.; Bowen, K. H. *The Journal of Physical Chemistry* **1996**, *100*(31), 12911–12944.

[77] Böhme, D. K.; Schwarz, H. *Angewandte Chemie International Edition* **2005**, *44*(16), 2336–2354.

[78] Reddic, J. E.; Duncan, M. A. *The Journal of Chemical Physics* **1999**, *110*(20), 9948–9955.

[79] Bersenkowitsch, N. K.; Ončák, M.; Linde, C. v. d.; Herburger, A.; Beyer, M. K. *Physical Chemistry Chemical Physics* **2018**, *20*(12), 8143–8151.

[80] Prather, M. J. *Science* **1998**, *279*(5355), 1339–1341.

[81] Ravishankara, A. R.; Daniel, J. S.; Portmann, R. W. *Science* **2009**, *326*(5949), 123–125.

[82] WMO. Scientific assessment of ozone depletion: 2014, world meteorological organization, global ozone research and monitoring project-report Report, No. 55, 416 pp., **2014**.

[83] Tolman, W. *Angewandte Chemie International Edition* **2010**, *49*(6), 1018–1024.

[84] Chen, P.; Gorelsky, S. I.; Ghosh, S.; Solomon, E. I. *Angewandte Chemie International Edition* **2004**, *43*(32), 4132–4140.

[85] Rosca, V.; Duca, M.; de Groot, M. T.; Koper, M. T. M. *Chemical Reviews* **2009**, *109*(6), 2209–2244.

[86] Otten, E.; Neu, R. C.; Stephan, D. W. *Journal of the American Chemical Society* **2009**, *131*(29), 9918–9919.

[87] Piro, N. A.; Lichterman, M. F.; Harman, W. H.; Chang, C. J. *Journal of the American Chemical Society* **2011**, *133*(7), 2108–2111.

[88] Zhuravlev, V.; Malinowski, P. J. *Angewandte Chemie International Edition* **2018**, *57*(36), 11697–11700.

[89] Delabie, A.; Vinckier, C.; Flock, M.; Pierloot, K. *The Journal of Physical Chemistry A* **2001**, *105*(22), 5479–5485.

[90] Stirling, A. *Journal of the American Chemical Society* **2002**, *124*(15), 4058–4067.

[91] Kryachko, E. S.; Tishchenko, O.; Nguyen, M. T. *International Journal of Quantum Chemistry* **2002**, *89*(4), 329–340.

[92] Rondinelli, F.; Russo, N.; Toscano, M. *Journal of Chemical Theory and Computation* **2008**, *4*(11), 1886–1890.

[93] Rondinelli, F.; Russo, N.; Toscano, M. *Inorganic Chemistry* **2007**, *46*(18), 7489–7493.

[94] Chiodo, S.; Rondinelli, F.; Russo, N.; Toscano, M. *Journal of Chemical Theory and Computation* **2008**, *4*(2), 316–321.

[95] Alikhani, M. E.; Michelini, M. d. C.; Russo, N.; Silvi, B. *The Journal of Physical Chemistry A* **2008**, *112*(50), 12966–12974.

[96] Michelini, M. D. C.; Russo, N.; Alikhani, M. E.; Silvi, B. *Journal of Computational Chemistry* **2005**, *26*(12), 1284–1293.

[97] Lin, T.-S.; Chen, H.-T. *The Journal of Physical Chemistry C* **2015**, *119*(1), 449–455.

[98] Jin, X.; Wang, G.; Zhou, M. *The Journal of Physical Chemistry A* **2006**, *110*(26), 8017–8022.

[99] Wang, G.; Jin, X.; Chen, M.; Zhou, M. *Chemical Physics Letters* **2006**, *420*(1–3), 130–134.

[100] Lavrov, V. V.; Blagojevic, V.; Koyanagi, G. K.; Orlova, G.; Böhme, D. K. *The Journal of Physical Chemistry A* **2004**, *108*(26), 5610–5624.

[101] Dietrich, G.; Lutzenkirchen, K.; Becker, S.; Hasse, H. U.; Kluge, H. J.; Lindinger, M.; Schweikhard, L.; Ziegler, J.; Kuznetsov, S. *Berichte Der Bunsen-Gesellschaft-Physical Chemistry* **1994**, *98*(12), 1608–1612.

[102] Hintz, P. A.; Ervin, K. M. *Journal of Chemical Physics* **1995**, *103*(18), 7897–7906.

[103] Balaj, O. P.; Balteanu, I.; Rossteuscher, T. T. J.; Beyer, M. K.; Bondybey, V. E. *Angewandte Chemie-International Edition* **2004**, *43*(47), 6519–6522.

[104] Balteanu, I.; Balaj, O. P.; Beyer, M. K.; Bondybey, V. E. *Physical Chemistry Chemical Physics* **2004**, *6*(11), 2910–2913.

[105] Harding, D.; Ford, M. S.; Walsh, T. R.; Mackenzie, S. R. *Physical Chemistry Chemical Physics* **2007**, *9*(17), 2130–2136.

[106] Anderson, M. L.; Lacz, A.; Drewello, T.; Derrick, P. J.; Woodruff, D. P.; Mackenzie, S. R. *The Journal of Chemical Physics* **2009**, *130*(6), 064305.

[107] Parry, I. S.; Kartouzian, A.; Hamilton, S. M.; Balaj, O. P.; Beyer, M. K.; Mackenzie, S. R. *J. Phys. Chem. A* **2013**, *117*(36), 8855–8863.

[108] Beyer, M. K.; Berg, C. B.; Bondybey, V. E. *Physical Chemistry Chemical Physics* **2001**, *3*(10), 1840–1847.

[109] Rodgers, M. T.; Walker, B.; Armentrout, P. B. *International Journal of Mass Spectrometry* **1999**, *182*, 99–120.

[110] Yamamoto, H.; Miyajima, K.; Yasuike, T.; Mafuné, F. *The Journal of Physical Chemistry A* **2013**, *117*(47), 12175–12183.

[111] Inokuchi, Y.; Matsushima, R.; Kobayashi, Y.; Ebata, T. *The Journal of Chemical Physics* **2009**, *131*(4), 044325.

[112] Thompson, M. C.; Weber, J. M. *The Journal of Chemical Physics* **2016**, *144*(10), 104302.

[113] Hamilton, S. M.; Hopkins, W. S.; Harding, D. J.; Walsh, T. R.; Gruene, P.; Haertelt, M.; Fielicke, A.; Meijer, G.; Mackenzie, S. R. *J. Am. Chem. Soc.* **2010**, *132*(5), 1448–1449.

[114] Hamilton, S. M.; Hopkins, W. S.; Harding, D. J.; Walsh, T. R.; Haertelt, M.; Kerpal, C.; Gruene, P.; Meijer, G.; Fielicke, A.; Mackenzie, S. R. *J. Phys. Chem. A* **2011**, *115*(12), 2489–2497.

[115] Hermes, A. C.; Hamilton, S. M.; Hopkins, W. S.; Harding, D. J.; Kerpal, C.; Meijer, G.; Fielicke, A.; Mackenzie, S. R. *Journal of Physical Chemistry Letters* **2011**, *2*(24), 3053–3057.

[116] Parry, I. S.; Kartouzian, A.; Hamilton, S. M.; Balaj, O. P.; Beyer, M. K.; Mackenzie, S. R. *Angewandte Chemie-International Edition* **2015**, *54*(4), 1357–1360.

[117] Jellinek, J.; Guvenc, Z. B. In *Mode Selective Chemistry*; Jortner, J., Levine, R. D., Pullman, B., Eds.; Kluwer Academic Publ: Dordrecht, 1991; Vol. 24; pages 153–164.

[118] Duncan, M. A. *Annual Review of Physical Chemistry* **1997**, *48*(1), 69–93.

[119] Dodson, L. G.; Thompson, M. C.; Weber, J. M. *Annual Review of Physical Chemistry* **2018**, *69*(1), 231–252.

[120] Lisy, J. M. *International Reviews in Physical Chemistry* **1997**, *16*(3), 267–289.

[121] Morse, P. M. *Physical Review* **1929**, *34*(1), 57–64.

[122] Banwell. *Fundamentals of Molecular Spectroscopy;* McGraw-Hill Education (India) Pvt Limited, 2001.

[123] Hollas, J. M. *High Resolution Spectroscopy;* Butterworth-Heinemann, 2013.

[124] Berden, G.; Peeters, R.; Meijer, G. *International Reviews in Physical Chemistry* **2000**, *19*(4), 565–607.

[125] Scherer, J. J.; Paul, J. B.; Collier, C. P.; O'Keefe, A.; Saykally, R. J. *The Journal of Chemical Physics* **1995**, *103*(21), 9187–9192.

[126] Kraus, D.; Saykally, R. J.; Bondybey, V. E. *Chemical Physics Letters* **1998**, *295*(4), 285–288.

[127] Iskra, A.; Gentleman, A. S.; Kartouzian, A.; Kent, M. J.; Sharp, A. P.; Mackenzie, S. R. *The Journal of Physical Chemistry A* **2017**, *121*(1), 133–140.

[128] Wiley, W. C.; McLaren, I. H. *Review of Scientific Instruments* **1955**, *26*(12), 1150–1157.

[129] Mamyrin, B. A.; Karataev, V. I.; Shmikk, D. V.; Zagulin, V. A. *Journal of Experimental and Theoretical Physics* **1973**, *37*(1), 45.

[130] Menezes, W. J. C.; Knickelbein, M. B. *The Journal of Chemical Physics* **1993**, *98*(3), 1856–1866.

[131] Nesbitt, D. J.; Hynes, J. T. *The Journal of Chemical Physics* **1982**, *76*(12), 6002–6014.

[132] Rodriguez, O.; Lisy, J. M. *The Journal of Physical Chemistry A* **2011**, *115*(7), 1228–1233.

[133] Li, Y.; Wang, L.; Qu, H.; Wang, G.; Zhou, M. *The Journal of Physical Chemistry A* **2015**, *119*(15), 3577–3586.

[134] Wang, L.; Wang, G.; Qu, H.; Li, Z. H.; Zhou, M. *Physical Chemistry Chemical Physics* **2014**, *16*(22), 10788–10798.

[135] O'Shea, P. G.; Freund, H. P. *Science* **2001**, *292*(5523), 1853–1858.

[136] Harding, D. J.; Fielicke, A. *Chemistry – A European Journal* **2014**, *20*(12), 3258–3267.

[137] Schöllkopf, W.; Gewinner, S.; Junkes, H.; Paarmann, A.; Helden, G. v.; Bluem, H. P.; Todd, A. M. M. In *Advances in X-ray Free-Electron Lasers Instrumentation III*, Vol. 9512, page 95121L. International Society for Optics and Photonics.

[138] Perdew, J. P. *Physical Review B* **1986**, *33*(12), 8822–8824.

[139] Becke, A. D. *Physical Review A* **1988**, *38*(6), 3098–3100.

[140] Burke, K.; Ernzerhof, M.; Perdew, J. P. *Chemical Physics Letters* **1997**, *265*(1), 115–120.

[141] Perdew, J. P.; Ernzerhof, M.; Burke, K. *The Journal of Chemical Physics* **1996**, *105*(22), 9982–9985.

[142] Perdew, J. P.; Burke, K.; Ernzerhof, M. *Physical Review Letters* **1996**, *77*(18), 3865–3868.

[143] Tao, J.; Perdew, J. P.; Staroverov, V. N.; Scuseria, G. E. *Physical Review Letters* **2003**, *91*(14), 146401.

[144] Pyykkö, P. *Angewandte Chemie International Edition* **2004**, *43*(34), 4412–4456.

[145] Pyykkö, P. *Inorganica Chimica Acta* **2005**, *358*(14), 4113–4130.

[146] Pyykkö, P. *Chemical Society Reviews* **2008**, *37*(9), 1967–1997.

[147] Weigend, F. *Physical Chemistry Chemical Physics* **2006**, *8*(9), 1057–1065.

[148] Weigend, F.; Ahlrichs, R. *Physical Chemistry Chemical Physics* **2005**, *7*(18), 3297–3305.

[149] Becke, A. D. *The Journal of Chemical Physics* **1993**, *98*, 5648.

[150] Frisch, M. J.; Trucks, G. W.; Schlegel, H. B.; Scuseria, G. E.; Robb, M. A.; Cheeseman, J. R.; Scalmani, G.; Barone, V.; Mennucci, B.; Petersson, G. A.; Nakatsuji, H.; Caricato, M.; Li, X.; Hratchian, H. P.; Izmaylov, A. F.; Bloino, J.; Zheng, G.; Sonnenberg, J. L.; Hada, M.; Ehara, M.; Toyota, K.; Fukuda, R.; Hasegawa, J.; Ishida, M.; Nakajima, T.; Honda, Y.; Kitao, O.; Nakai, H.; Vreven, T.; Montgomery, J. A.; Peralta, J. E.; Ogliaro, F.; Bearpark, M.; Heyd, J. J.; Brothers, E.; Kudin, K. N.; Staroverov, V. N.; Kobayashi, R.; Normand, J.; Raghavachari, K.; Rendell, A.; Burant, J. C.; Iyengar, S. S.; Tomasi, J.; Cossi, M.; Rega, N.; Millam, J. M.; Klene, M.; Knox, J. E.; Cross, J. B.; Bakken, V.; Adamo, C.; Jaramillo, J.; Gomperts, R.; Stratmann, R. E.; Yazyev, O.; Austin, A. J.; Cammi, R.; Pomelli, C.; Ochterski, J. W.; Martin, R. L.; Morokuma, K.; Zakrzewski, V. G.; Voth, G. A.; Salvador, P.; Dannenberg, J. J.; Dapprich, S.; Daniels, A. D.; Farkas, O.; Foresman, J. B.; Ortiz, J. V.; Cioslowski, J.; Fox, D. J. *Gaussian 09, Revision D.01, Gaussian, Inc., Wallingford CT* **2009**.

[151] Herzberg, G. *Molecular Spectra and Molecular Structure: II Infrared and Raman Spectra of Polyatomic Molecules*, Vol. 2; Krieger: Malabar, Florida, 1991.

[152] Perdew, J. P. *Electronic Structure of Solids;* Akademie Verlag: Berlin, 1991.

[153] Davidson, E. R. *Chemical Physics Letters* **1996**, *260*(3), 514–518.

[154] Dunning, T. H. *The Journal of Chemical Physics* **1989**, *90*(2), 1007–1023.

[155] Staroverov, V. N.; Scuseria, G. E.; Tao, J.; Perdew, J. P. *The Journal of Chemical Physics* **2003**, *119*(23), 12129–12137.

[156] Pal, R.; Wang, L.-M.; Pei, Y.; Wang, L.-S.; Zeng, X. C. *Journal of the American Chemical Society* **2012**, *134*(22), 9438–9445.

[157] Gehrke, R.; Gruene, P.; Fielicke, A.; Meijer, G.; Reuter, K. *The Journal of Chemical Physics* **2009**, *130*(3), 034306.

[158] Orgel, L. E. *Journal of the Chemical Society* **1958**, pages 4186–4190.

[159] Jiang, L.; Kohyama, M.; Haruta, M.; Xu, Q. *The Journal of Physical Chemistry A* **2008**, *112*(51), 13495–13499.

[160] Rodriguez Jr, O.; Lisy, J. M. *Chemical Physics Letters* **2011**, *502*(4–6), 145–149.

[161] Ayotte, P.; Weddle, G. H.; Kim, J.; Johnson, M. A. *Journal of the American Chemical Society* **1998**, *120*(47), 12361–12362.

[162] Okumura, M.; Yeh, L. I.; Myers, J. D.; Lee, Y. T. *The Journal of Physical Chemistry* **1990**, *94*(9), 3416–3427.

[163] Okumura, M.; Yeh, L. I.; Myers, J. D.; Lee, Y. T. *The Journal of Chemical Physics* **1986**, *85*(4), 2328–2329.

[164] Knickelbein, M. B.; Menezes, W. J. C. *The Journal of Physical Chemistry* **1992**, *96*(16), 6611–6616.

[165] Pickering, J. C.; Raassen, A. J. J.; Uylings, P. H. M.; Johansson, S. *The Astrophysical Journal Supplement Series* **1998**, *117*(1), 261.

[166] Armentrout, P. B.; Halle, L. F.; Beauchamp, J. L. *The Journal of Chemical Physics* **1982**, *76*(5), 2449–2457.

[167] Jiang, L.; Xu, Q. *The Journal of Physical Chemistry A* **2009**, *113*(19), 5620–5624.

[168] Citra, A.; Andrews, L. *The Journal of Physical Chemistry A* **2000**, *104*(51), 11897–11908.

[169] Zhou, M.; Andrews, L. *The Journal of Physical Chemistry A* **2000**, *104*(17), 3915–3925.

[170] Cunningham, E. M.; Gentleman, A. S.; Beardsmore, P. W.; Iskra, A.; Mackenzie, S. R. *The Journal of Physical Chemistry A* **2017**, *121*(40), 7565–7571.

[171] Sancho, F. J. *An. Fis. Quim., Ser. A* **1958**, *54*(1-2), 41–64.

[172] Shadmi, Y. *Bulletin of the Research Council Israel* **1961**, *9F(4)*, 141–170.

[173] Sievers, M. R.; Armentrout, P. B. *The Journal of Physical Chemistry* **1995**, *99*(20), 8135–8141.

[174] Ricks, A. M.; Brathwaite, A. D.; Duncan, M. A. *The Journal of Physical Chemistry A* **2013**, *117*(6), 1001–1010.

[175] van Kleef, T. A. M.; Metsch, B. C. *Physica B+C* **1978**, *95*(2), 251–265.

[176] Harding, D. J.; Walsh, T. R.; Hamilton, S. M.; Hopkins, W. S.; Mackenzie, S. R.; Gruene, P.; Haertelt, M.; Meijer, G.; Fielicke, A. *J. Chem. Phys.* **2010**, *132*(1), 011101.

[177] Harding, D. J.; Gruene, P.; Haertelt, M.; Meijer, G.; Fielicke, A.; Hamilton, S. M.; Hopkins, W. S.; Mackenzie, S. R.; Neville, S. P.; Walsh, T. R. *J. Chem. Phys.* **2010**, *133*(21), 214304.

[178] Chaves, A. S.; Piotrowski, M. J.; Da Silva, J. L. F. *Physical Chemistry Chemical Physics* **2017**, *19*(23), 15484–15502.

[179] Da Silva, J. L. F.; Piotrowski, M. J.; Aguilera-Granja, F. *Physical Review B* **2012**, *86*(12), 6.

[180] Navarro-Ibarra, D. C.; Aguilera-Granja, J. F.; Guirado-Lopez, R. A. *European Physical Journal D* **2018**, *72*(7), 11.

[181] Plane, J. M. C. *The Journal of Physical Chemistry* **1987**, *91*(26), 6552–6557.

[182] Clemmer, D. E.; Weber, M. E.; Armentrout, P. B. *The Journal of Physical Chemistry* **1992**, *96*(26), 10888–10893.

[183] Jr, R. C. S.; Andrews, L. *The Journal of Chemical Physics* **1973**, *58*(2), 702–712.

[184] Andrews, L.; Saffell, W.; Yustein, J. T. *Chemical Physics* **1994**, *189*(2), 343–349.

[185] Wang, G.; Zhou, M. *Chemical Physics* **2007**, *342*(1), 90–94.

[186] Dawkins, E. C. M.; Plane, J. M. C.; Chipperfield, M. P.; Feng, W. *Journal of Geophysical Research: Atmospheres* **2015**, *120*(15), 7975–7987.

[187] Gómez Martín, J. C.; Garraway, S. A.; Plane, J. M. C. *The Journal of Physical Chemistry A* **2016**, *120*(9), 1330–1346.

[188] Marsh, D. R.; Janches, D.; Feng, W.; Plane, J. M. C. *Journal of Geophysical Research: Atmospheres* **2013**, *118*(19), 11,442–11,452.

[189] Plane, J. M. C.; Feng, W.; Dawkins, E.; Chipperfield, M. P.; Höffner, J.; Janches, D.; Marsh, D. R. *Geophysical Research Letters* **2014**, *41*(13), 4753–4760.

[190] Collins, S. C.; Plane, J. M. C.; Kelley, M. C.; Wright, T. G.; Soldán, P.; Kane, T. J.; Gerrard, A. J.; Grime, B. W.; Rollason, R. J.; Friedman, J. S.; González, S. A.; Zhou, Q.; Sulzer, M. P.; Tepley, C. A. *Journal of Atmospheric and Solar-Terrestrial Physics* **2002**, *64*(7), 845–860.

[191] Plane, J. M. C.; Plowright, R. J.; Wright, T. G. *The Journal of Physical Chemistry A* **2006**, *110*(9), 3093–3100.

[192] Cunningham, E. M.; Gentleman, A. S.; Beardsmore, P. W.; Mackenzie, S. R. *Physical Chemistry Chemical Physics*.

[193] Lee, E. P. F.; Soldán, P.; Wright, T. G. *Chemical Physics Letters* **2001**, *347*(4), 481–486.

[194] Pillai, E. D.; Jaeger, T. D.; Duncan, M. A. *The Journal of Physical Chemistry A* **2005**, *109*(16), 3521–3526.

[195] Pillai, E. D.; Jaeger, T. D.; Duncan, M. A. *Journal of the American Chemical Society* **2007**, *129*(8), 2297–2307.

[196] Brathwaite, A. D.; Abbott-Lyon, H. L.; Duncan, M. A. *The Journal of Physical Chemistry A* **2016**, *120*(39), 7659–7670.

[197] Walters, R. S.; Brinkmann, N. R.; Schaefer, H. F.; Duncan, M. A. *The Journal of Physical Chemistry A* **2003**, *107*(38), 7396–7405.

[198] Bauschlicher, C. W.; Partridge, H. *The Journal of Physical Chemistry* **1991**, *95*(24), 9694–9698.

[199] Sodupe, M.; Bauschlicher, C. W. *Chemical Physics Letters* **1991**, *181*(4), 321–326.

[200] Gardner, A. M.; Gutsmiedl, K. A.; Wright, T. G.; Lee, E. P. F.; Breckenridge, W. H.; Rajbhandari, S.; Chapman, C. Y. N.; Viehland, L. A. *The Journal of Physical Chemistry A* **2011**, *115*(25), 6979–6985.

[201] Harris, J. P.; Gardner, A. M.; Wright, T. G.; Breckenridge, W. H.; Viehland, L. A. *The Journal of Physical Chemistry A* **2012**, *116*(20), 4995–5007.

[202] Gardner, A. M.; Gutsmiedl, K. A.; Wright, T. G.; Breckenridge, W. H.; Chapman, C. Y. N.; Viehland, L. A. *The Journal of Chemical Physics* **2010**, *133*(16), 164302.

[203] Haruta, M. *Catalysis Today* **1997**, *36*(1), 153–166.

[204] Haruta, M.; Yamada, N.; Kobayashi, T.; Iijima, S. *Journal of Catalysis* **1989**, *115*(2), 301–309.

[205] Haruta, M. *Nature* **2005**, *437*(7062), 1098.

[206] Valden, M.; Lai, X.; Goodman, D. W. *Science* **1998**, *281*(5383), 1647–1650.

[207] Sanchez, A.; Abbet, S.; Heiz, U.; Schneider, W. D.; Häkkinen, H.; Barnett, R. N.; Landman, U. *The Journal of Physical Chemistry A* **1999**, *103*(48), 9573–9578.

[208] Lang, S. M.; Bernhardt, T. M.; Barnett, R. N.; Yoon, B.; Landman, U. *Journal of the American Chemical Society* **2009**, *131*(25), 8939–8951.

[209] Landman, U.; Yoon, B.; Zhang, C.; Heiz, U.; Arenz, M. *Topics in Catalysis* **2007**, *44*(1), 145–158.

[210] Yoon, B.; Häkkinen, H.; Landman, U.; Wörz, A. S.; Antonietti, J.-M.; Abbet, S.; Judai, K.; Heiz, U. *Science* **2005**, *307*(5708), 403–407.

[211] Harding, C.; Habibpour, V.; Kunz, S.; Farnbacher, A. N.-S.; Heiz, U.; Yoon, B.; Landman, U. *Journal of the American Chemical Society* **2009**, *131*(2), 538–548.

[212] Roldán, A.; Ricart, J. M.; Illas, F.; Pacchioni, G. *The Journal of Physical Chemistry C* **2010**, *114*(40), 16973–16978.

[213] Nilius, N.; Risse, T.; Schauermann, S.; Shaikhutdinov, S.; Sterrer, M.; Freund, H. J. *Topics in Catalysis* **2011**, *54*(1), 4–12.

[214] Kemper, P. R.; Bowers, M. T. *The Journal of Physical Chemistry* **1991**, *95*(13), 5134–5146.

[215] Li, J.; Li, X.; Zhai, H.-J.; Wang, L.-S. *Science* **2003**, *299*(5608), 864–867.

[216] Gruene, P.; Rayner, D. M.; Redlich, B.; Meer, A. F. G. v. d.; Lyon, J. T.; Meijer, G.; Fielicke, A. *Science* **2008**, *321*(5889), 674–676.

[217] Häkkinen, H.; Landman, U. *Journal of the American Chemical Society* **2001**, *123*(39), 9704–9705.

[218] Socaciu, L. D.; Hagen, J.; Bernhardt, T. M.; Wöste, L.; Heiz, U.; Häkkinen, H.; Landman, U. *Journal of the American Chemical Society* **2003**, *125*(34), 10437–10445.

[219] Wallace, W. T.; Whetten, R. L. *Journal of the American Chemical Society* **2002**, *124*(25), 7499–7505.

[220] Fielicke, A.; Helden, G. v.; Meijer, G.; Simard, B.; Rayner, D. M. *Physical Chemistry Chemical Physics* **2005**, *7*(23), 3906–3909.

[221] Tsakoumis, N. E.; Rønning, M.; Borg, y.; Rytter, E.; Holmen, A. *Catalysis Today* **2010**, *154*(3), 162–182.

[222] Reboredo, F. A.; Galli, G. *The Journal of Physical Chemistry B* **2006**, *110*(15), 7979–7984.

[223] den Breejen, J. P.; Radstake, P. B.; Bezemer, G. L.; Bitter, J. H.; Frøseth, V.; Holmen, A.; de Jong, K. P. *Journal of the American Chemical Society* **2009**, *131*(20), 7197–7203.

[224] Zeinalipour-Yazdi, C. D.; van Santen, R. A. *The Journal of Physical Chemistry C* **2012**, *116*(15), 8721–8730.

[225] McNary, C. P.; Armentrout, P. B. *Physical Chemistry Chemical Physics* **2014**, *16*(48), 26467–26477.

[226] Winter, B. J.; Klots, T. D.; Parks, E. K.; Riley, S. J. *Zeitschrift für Physik D Atoms, Molecules and Clusters* **1991**, *19*(4), 375–380.

[227] Schooss, D.; Blom, M. N.; Parks, J. H.; Issendorff, B. v.; Haberland, H.; Kappes, M. M. *Nano Letters* **2005**, *5*(10), 1972–1977.

[228] Liu, S.-R.; Zhai, H.-J.; Wang, L.-S. *Physical Review B* **2001**, *64*(15), 153402.

[229] Bakker, J. M.; Jalink, J.; Dieleman, D.; Kirilyuk, A. *Journal of Physics: Condensed Matter* **2018**, *30*(49), 494003.

[230] Yanagimachi, A.; Koyasu, K.; Valdivielso, D. Y.; Gewinner, S.; Schöllkopf, W.; Fielicke, A.; Tsukuda, T. *The Journal of Physical Chemistry C* **2016**, *120*(26), 14209–14215.

[231] Anderson, M. L.; Lacz, A.; Drewello, T.; Derrick, P. J.; Woodruff, D. P.; Mackenzie, S. R. *Journal of Chemical Physics* **2009**, *130*(6), 064305.

[232] Zamudio-Bayer, V.; Hirsch, K.; Langenberg, A.; Ławicki, A.; Terasaki, A.; v. Issendorff, B.; Lau, J. T. *The Journal of Chemical Physics* **2015**, *143*(24), 244318.